Mathematical Modelling of Electrohydrodynamic Flows

Matthew S. Keith

Department of Mathematics and Statistics
University of Strathclyde

A thesis submitted in fulfilment of the requirements for the degree of Doctor of Philosophy

September 2021

This thesis is the result of the author's original research. It has been composed by the author and has not been previously submitted for examination which has led to the award of a degree.

Abstract

This thesis concerns the analytical and numerical investigation of a bilayer of liquid and gas contained between two electrodes. The work contained in this thesis uses the Taylor–Melcher leaky dielectric model to describe electrostatic effects, which are coupled with the hydrodynamic effects through the normal and tangential stresses. The long-wave approximation is used to obtain a model that consists of two coupled, nonlinear partial differential equations for the interfacial height and the charge density. Several limiting cases of this long-wave model are considered. The first limiting case is when the liquid is perfectly conducting, the second limiting case is when the liquid and gas have high conductivities, and the third limiting case is when the liquid and gas are both perfect dielectrics. The first two limiting cases and the full long-wave model are investigated in detail. This analysis shows that a variety of different behaviours can occur, i.e. levelling, upper contact, thinning, and touchdown behaviour, which are explored, both analytically and numerically. In particular, levelling behaviour is described by linear stability theory, similarity solutions are found for the interface during the upper contact and thinning behaviours, and an extensive numerical investigation of touchdown behaviour is performed. A systematic numerical investigation of parameter space for the long-wave model and the limiting cases is performed. In particular, the regions of parameter space in which each behaviour occurs, and the transitions between these regions, are investigated. Coupled with an investigation of the interfacial dynamics of the different behaviours, this work allows for a more complete understanding of the behaviour of electrohydrodynamic flows.

Acknowledgements

First and foremost, I am indebted to my supervisors Prof Stephen Wilson and Dr Alexander Wray for their continued advice and support. This thesis would not be possible without their expertise, guidance and critique throughout my post-graduate studies.

I also owe a huge thanks to Mr Greg McDowall, my high school Mathematics teacher, who saw my potential and passion for the subject and encouraged me to pursue it further. I certainly wouldn't be where I am today without his guidance.

I'm grateful to have shared an office with Michael and Daryl. Their friendship made my studies more enjoyable and the challenging times more bearable.

Finally, I would like to thank the University of Strathclyde for funding my post-graduate studies.

Contents

Chapter 1

Introduction

1.1 Thin-film flows

Thin films of fluid are ubiquitous in nature, are commonplace in our daily lives, and occur in many physical contexts such as rain draining down a window and the formation of polymer fibres. The behaviour of thin films has been the subject of many analytical, numerical, and experimental investigations. The free surface of a fluid film is, in general, deformable, which can lead to a range of interesting behaviours, such as pattern formation phenomena, which involve the formation of chaotic or regular structures [1, 2, 3, 4], and film rupture [5, 6, 7, 8]. Thin-film flows occur, and have been studied, in a host of different situations, which include (but are not limited to) geophysical settings, from lava flows [9, 10] to gravity currents [11, 12], a range of biological scenarios, from the airways and lining of the lung [13] to tear films in the eye [14, 15], and in engineering, where thin films are used in heat and mass transfer processes [16, 17]. Oron *et al.* [18], Craster and Matar [19], and Davis [20] give extensive reviews on thin-film flows in many situations. As these reviews describe, low-order modelling has been applied to thin-film flows, and elucidating their behaviour has involved a variety of analytical and numerical techniques, many of which are surveyed in these reviews.

Specifically, low-order modelling typically exploits the presence of small parameters in problems, using techniques such as asymptotic or perturbation methods to obtain approximate and asymptotic solutions to problems that are otherwise very difficult or impossible to solve. Studies using low order techniques will be explored further in Section 1.2.

The interfacial patterns that arise from instabilities of thin-film flows have important technological applications as mentioned earlier and have received considerable attention [21, 22, 23, 24, 25]. Electric fields can be used to induce electrohydrodynamic (EHD) instabilities and control how fluids behave, and this has led to a wide range of practical applications. In particular, electric fields have been used for pattern formation in electronic devices at the micro- or nano- scale [26, 3, 23], micro-fluidic mixing [3, 27, 28, 29], and electrospinning [30, 31, 32] (a cheap method of producing thin fibres). Specifically, pattern formation applications that use EHD instabilities include Lithographically Induced Self Assembly (LISA) and Lithographically Induced Self Construction (LISC) [26, 3, 33, 34]. LISA and LISC are processes where a uniform film self-assembles into a periodic array of pillars that bridge a lower substrate and upper mask (LISA), or the film assembles into a replica of an upper mask (LISC). Electric fields are the driving force behind these instabilities, and Figure 1.1(a) shows the setup of LISA/LISC applications, and Figure 1.1(b) shows a micrograph of pillars formed from a poly(methyl methacrylate) film.

In Section 1.2, we will outline the low-order modelling techniques that can be used to simplify the governing equations of a wide range of different systems, involving thin and/or slender films of fluid, by utilising the disparities in lengthscales that arise in thin-film flows. We then discuss numerical schemes used to investigate thin-film flows in Section 1.3. In Section 1.4, we will review previous studies of thin-film flows in a range of different coating and draining problems, as well as film or jet rupture problems in Section 1.5. In Section 1.6.1, we will introduce the

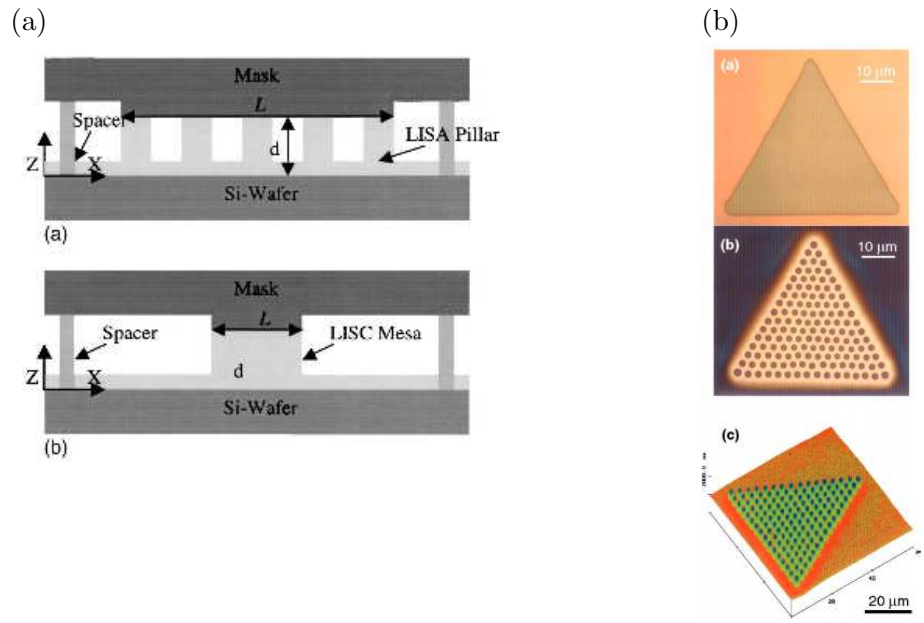

Figure 1.1: Part (a) shows the setup of LISA/LISC applications, reproduced with permission from [37], and part (b) shows a micrograph of pillars formed from a poly(methyl methacrylate) film, reproduced with permission from [26]

Taylor–Melcher leaky dielectric model [35, 36] which couples electrostatic effects with the hydrodynamics of a fluid. This model will be appropriate for the system we are studying (introduced in Section 2.1). In Section 1.7, we will review relevant previous studies that include electrostatic effects, before concluding with an outline of the contents of this thesis in Section 1.8.

1.2 Low-order modelling

Interfacial flows involve the flow of two or more fluids bounded by one or more interfaces. Hence, when studying these flows, the presence of one or more deformable interfaces makes the situation complicated (and interesting) as the locations of the interfaces are unknown a priori and have to be determined as part of the solution to the problem. The motion of interfaces can be determined as part of the solution of the governing equations and boundary conditions of the system under investigation. For viscous fluids, the governing equations are the

Navier–Stokes equations, which are a set of nonlinear partial differential equations (PDEs). There are challenges in solving the full Navier–Stokes equations in general: performing direct numerical simulations (DNS) is costly (as it can take weeks to months of processing time to solve some problems) and it is difficult to make any analytical progress [18, 19]. However, there are situations (e.g. thin-film and slender-body flows) where the disparities between the lateral and transverse lengthscales give rise to one or more small parameters, which can be used to simplify the governing equations. For example, the disparity between a characteristic film thickness H to a characteristic lateral lengthscale L (such as the characteristic wavelength) gives the small aspect ratio $\epsilon = H/L \ll 1$. Quantities (such as the derivatives and the components of the velocity) are typically found to scale with powers of ϵ, allowing for an asymptotic reduction of the problem: this is referred to as a thin-film or long-wave (LW) approximation. These techniques, in which an approximate or asymptotic solution to the problem under investigation is found by using asymptotic and perturbation methods, are known as low-order modelling techniques, as previously described in Section 1.1. The terms "thin film" and "long wave" are interchangeable here as we are working in a planar context (this would not be the case, for example, when working on a curved substrate). The consequence of this LW approximation is generally to remove the dependence of the problem on the transverse coordinate, reducing the dimensionality of the problem by one. The LW approximation is a powerful tool that has been used to study the dynamics of thin fluid films driven to flow by various forces, such as gravity, capillarity, thermocapillarity, and intermolecular forces [18, 19, 20].

In his classical work, Benney [38] investigated a two-dimensional fluid film flowing down an inclined plane, using a Cartesian coordinate system (x, y), and he used the LW approximation to derive a nonlinear equation for the thickness of the fluid film $y = h(x, t)$. This has come to be known as the Benney equation,

which is, in its dimensionless form,

$$\frac{\partial h}{\partial t} + \frac{\partial}{\partial x}\left(\frac{2}{3}h^3 + \epsilon\left[\left(\frac{16Re}{15}h^6 - \frac{2}{3}h^3\cot\theta\right)\frac{\partial h}{\partial x} + \frac{1}{Ca}h^3\frac{\partial^3 h}{\partial x^3}\right]\right) = 0, \qquad (1.1)$$

where $Re = gH^3\sin\theta/\nu^2$ and $Ca = \rho g H^2/\sigma\epsilon^2$ are the Reynolds and capillary numbers, respectively, g is acceleration due to gravity, H is the mean film thickness, ρ is the density of the fluid, ν is the kinematic viscosity of the fluid, ϵ is the small aspect ratio, and θ is the angle of inclination of the plane to the horizontal. Re and Ca represent the relative significance of inertial forces to viscous forces, and of viscous forces to surface tension forces, respectively. Note that the surface tension term was not present in the original equation investigated by Benney [38] since this term enters at higher-order unless the capillary number is rescaled in ϵ, as is given by (2.24). The leading-order terms in ϵ of equation (1.1) are linearly neutrally stable and form a shock in finite time [39]. The destabilising inertia term and the stabilising hydrostatic pressure and surface tension terms (the third, fourth, and fifth terms, respectively, in equation (1.1)) enter at first order in ϵ. Finite-time "blowup" (where the interfacial height grows without bound) was found to occur [40, 41] for solutions of equation (1.1) for moderate to large Reynolds numbers. Hence, solutions to the Benney equation lose any physical relevance during blowup. Furthermore, it was found that blowup does not occur when DNS of the full Navier–Stokes equations are performed [42, 43, 44, 45].

The Benney equation (1.1) can be simplified by reducing it to a weakly nonlinear equation, as derived by Sivashinsky [46]. They perturbed the interfacial height h around some steady base state $y = \overline{h}$, namely, $h = \overline{h} + \delta\widetilde{h}$, where $\delta \ll 1$ and $\widetilde{h} = \widetilde{h}(x,t)$ are the size and shape of the perturbation, respectively. The perturbed solution was then substituted into equation (1.1), the x and t coordinates were rescaled, and the appropriate Galilean transformation was applied such that the system was expressed in a moving frame of reference (which removes convec-

tive terms and has no impact on the dynamics of the system). The first-order terms in δ give a weakly nonlinear equation for $\widetilde{h}$, namely,

$$\frac{\partial \widetilde{h}}{\partial t} + \widetilde{h}\frac{\partial \widetilde{h}}{\partial x} + \frac{\partial^2 \widetilde{h}}{\partial x^2} + \frac{\partial^4 \widetilde{h}}{\partial x^4} = 0, \tag{1.2}$$

where the second, third, and fourth terms correspond to inertial, gravitational, and surface tension effects, respectively. Equation (1.2) is known as the Kuramoto–Sivashinsky (KS) equation and is applicable to numerous other physical situations [47, 48, 49, 46]. Note that equation (1.2) is only valid for perturbations that are small compared to the base state $\overline{h}$. In equation (1.2), the gravitational term acts as an energy source and so has a destabilising effect, the stabilising inertial term transfers energy from small to large wavenumbers, where the stabilising $\partial^4 \widetilde{h}/\partial x^4$ term (which dissipates energy) dominates. Solutions to the KS equation give complicated behaviour, i.e. periodic, quasi-periodic, and chaotic solutions, as shown through previous analytical [50, 51] and computational [52, 53, 54, 55] studies.

Initial attempts at resolving the unphysical blowup phenomenon that occurs in the solution of the Benney equation (1.1) were performed [56, 57], but the results did not show good agreement with experimental results or with DNS of the full Navier–Stokes equations. One approach that did stop blowup from occurring was the weighted residual integral boundary-layer (WRIBL) method, introduced by Ruyer-Quil and Manneville [58]. We will use the WRIBL method in Appendix F. The WRIBL method was used to derive a model, using a Galerkin method, that is based on a LW approximation of the Navier–Stokes equations. For falling films, this method gives four governing equations for $h(x,t)$ and the depth-integrated flux $q(x,t) = \int_0^h u \, \mathrm{d}y$, where $u = u(x,y,t)$ is the velocity in the transverse direction. In addition, there are two subsidiary fields $s_1(x,t)$ and $s_2(x,t)$ that describe the deviation of the velocity profile from a parabolic velocity profile. Numerical

calculations using the WRIBL method have produced very good agreement with linear stability results of the full Navier–Stokes equations [59], as well as very good qualitative agreement with experimental results [60]. The WRIBL method has been extended to describe falling films with inertial effects [58, 59, 60, 61], as well as flows with other physical effects [62, 63, 64]. More recently, the WRIBL method has been used to study "thick-film flows" [65, 66], in which the radius of curvature of the substrate over which the fluid flows can be the same size as the thickness of the film.

1.3 Numerical schemes for thin-film flows

Models of thin-film flows derived using low-order modelling techniques can rarely be solved analytically to obtain explicit expressions for the variables, and so numerical schemes (that solve these models) have been used as a powerful way to complement the results from perturbation theory and asymptotic analysis. The numerical results are particularly useful in exploring the interfacial dynamics in the nonlinear regime, and for comparisons (both qualitatively and quantitatively) against experimental results. Numerical techniques have been used to study falling films [67, 68, 69, 70], finite-time singularity problems [71, 72, 73, 74], and pattern formation problems [75, 76, 77]. One commonly-used numerical technique for solving differential equations is the Finite-Difference Method, where both the spatial domain and the time interval are discretised into grid points. The Method of Lines allows us to convert the solution of a PDE to a system of nonlinear ordinary differential equations (ODEs) corresponding to each of the grid points. A time-stepping technique (such as the Backwards Euler or the Trapezium rule) can be applied and the resulting nonlinear algebraic expressions can then be solved using the Newton–Raphson (NR) method. We will use the Finite-Difference Method to investigate the problems tackled in this thesis, and

will discuss this method (and our numerical implementation of it) in more detail in Chapter 4.

1.4 Coating and draining flow problems

There have been extensive studies on coating and draining flow problems where instabilities in the system arise due to gravity and/or capillarity. Understanding these flows are important to numerous applications, such as microfluidic heat transfer problems [78], coating flow problems [79], and flows in the lungs [13], and low-order modelling has given a host of results through using both analytical and numerical methods. Jones and Wilson [80] used a thin-film approximation to investigate the Rayleigh–Taylor (RT) instability of a liquid film trapped beneath a sedimenting drop of fluid, finding that the height of the interface h was described by an equation of the form

$$\frac{\partial h}{\partial t} = -\frac{\partial}{\partial x}\left(\frac{h^3}{3}\left(A\frac{\partial h}{\partial x} + B\frac{\partial^3 h}{\partial x^3}\right)\right), \tag{1.3}$$

where A and B are constants. Note that the studies reviewed in this Section look at problems that are influenced by different physical mechanisms but are mathematically similar, i.e. are governed by equations of the form (1.3). These differences in the physics of the systems are incorporated into the constants A and B, which usually contain non-dimensional parameters such as Re and Ca. Jones and Wilson [80] found that, as the liquid drains from beneath the sedimenting drop, the height of the liquid film decreases like $h \sim t^{-1/2}$. In a later study, Hammond [81] investigated the axisymmetric case of a liquid coating a solid cylinder in the absence of gravity, and found h to be governed by (1.3). The liquid film evolved into a series of filling and draining lobes, separated by trough regions, as shown in Figure 1.2, and the liquid flowed from the draining lobe into the filling lobes. Figure 1.2 shows a plot of h as a function of x/L, highlighting the draining

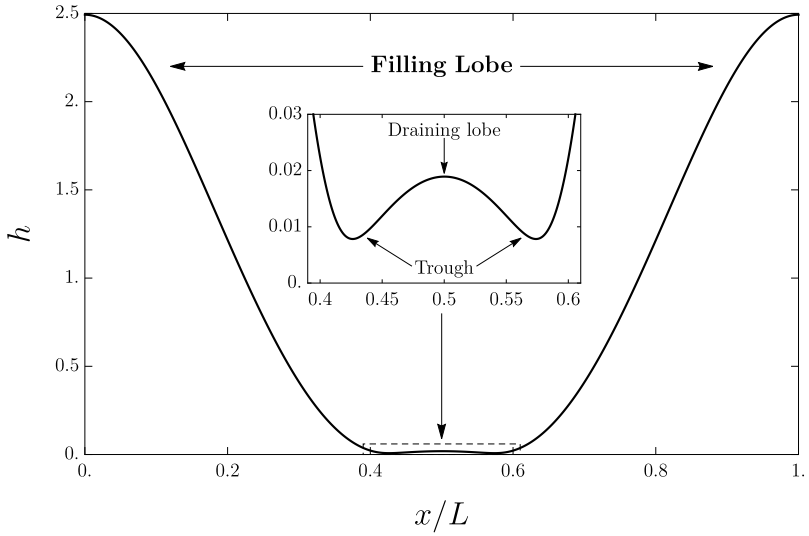

Figure 1.2: Plot of h as a function of x/L showing draining and filling lobe regions, and the trough region.

and filling lobe regions, as well as the trough region. Here, L is the length of the domain. A similarity solution for the interface in the trough region was found, for which the matching conditions onto the draining and filling lobes are linear and quadratic functions, respectively. This difference between the matching conditions at either side of a trough is what drives the drainage. Hammond [81] also found that, at late times, the height of the interface in the trough regions varied like $h \sim t^{-1/2}$, the same scaling law as that found by Jones and Wilson [80]. Later, Yiantsios and Higgins [82] investigated the RT instability of a liquid film coating the lower surface of a horizontal substrates (i.e. on the ceiling), and found that the interface again evolved into a series of filling and draining lobes. They found that for asymmetric (but, notably, not symmetric) initial conditions, a sliding phenomenon occurred, in which, at late times, the lobes translated to the left or right. In a later study, Lister *et al.* [83], confirmed Hammond's findings [81] that for sufficiently small domains, the height of the trough regions varied like $h \sim t^{-1/2}$ at late times. However, for longer domain lengths, Lister *et al.* [83] showed that the trough regions can be situated between two filling lobes (instead of between a filling and draining lobe), and in this case the height of the

trough regions varied like $h \sim t^{-1}$. Furthermore, Lister *et al.* observed a sliding phenomenon similar to that seen by Yiantsios and Higgins [82]. In particular, they found that the filling lobe can translate back and forward along the domain, where it consumes the draining lobe in its path and leaving a smaller daughter lobe behind it. In a companion paper, Lister *et al.* [84] investigated the drainage of a liquid trapped between a two-dimensional drop that settles towards a horizontal plane, in which filling and draining lobes formed. They found that the Bond number B, i.e. the measure of the relative importance between gravity and surface tension, controls the evolution of the liquid film. Specifically, when B is sufficiently small, all of the liquid ultimately drains from the draining lobe. When B is sufficiently large, permanent filling and draining lobes are formed, and the sliding dynamics seen by Lister *et al.* [83] were observed. Furthermore, for critical values of B, they also found cases where liquid is permanently trapped inside the draining lobe. Glasner [85] investigated the RT instability of a liquid film coating a porous ceiling, with a constant supply of liquid. Filling and draining lobes formed, and a sliding phenomena similar to that seen by Yiantsios and Higgins [82] and Lister *et al.* [84] was observed. Glasner [85] showed that it is energetically favourable for the liquid film to slide in the direction of the thicker (rather than the thinner) liquid film. Furthermore, the RT instability of a liquid film coating a ceiling was also investigated by Dietze *et al.* [86]. They investigated the onset of the sliding phenomena and showed that it can occur for both symmetric and asymmetric initial conditions, in contrast to that seen by Yiantsios and Higgins [82], who only observed sliding for asymmetric initial conditions. Dietze *et al.* [86] showed that, if the Yiantsios and Higgins [82] had performed their numerical calculations long enough in time, sliding would indeed be seen for symmetric initial conditions. They also showed that the sliding phenomenon arises from asymmetric instabilities, and, even though sliding is typically observed when the interface has reached a quasi-steady state, sliding can effectively occur at any

time after filling and draining lobes have formed. Furthermore, Dietze *et al.* [86] investigated this system with additional Marangoni stresses, which incorporated an extra tangential stress term to equation (1.3). They showed that this tangential stress term prevents the sliding phenomenon from occurring, and instead the troughs "buckle" into additional filling and draining lobes, and troughs. In fact, these buckling events occur indefinitely and are therefore referred to as a cascade of buckling events.

For steady flows, the fourth-order governing equation (1.3) can be simplified to a third-order equation of the form

$$\frac{\partial^3 h}{\partial x^3} = f(h), \tag{1.4}$$

where the function $f(h)$ varies for different systems. Equation (1.4) has been studied in many coating and draining problems, such as flows with high surface tension [87, 88] where $f(h) = -1 + 1/h^2$, free-surface flows with surface tension effects [89] where $f(h) = 1/h^2$, and thermally driven flows [90].

In all of the studies described above, the effects of gravity and/or surface tension control the evolution of the interface. However, the effect of an electric field can also be incorporated (in place or alongside gravity, surface tension, or other physical effects) into these coating and draining flow problems, which have applications in technology and engineering, such as in LISC/LISA applications, as discussed in Section 1.6.

1.5 Film or jet rupture problems

There has been a lot of attention on problems where rupture of liquid films or jets occur. Figure 1.3 shows experimental pictures of the process of droplet separation from a jet (reproduced from [91]) where panel (a) is at times before breakup of the jet, and panel (b) is at times after breakup of the jet. The arrows show where

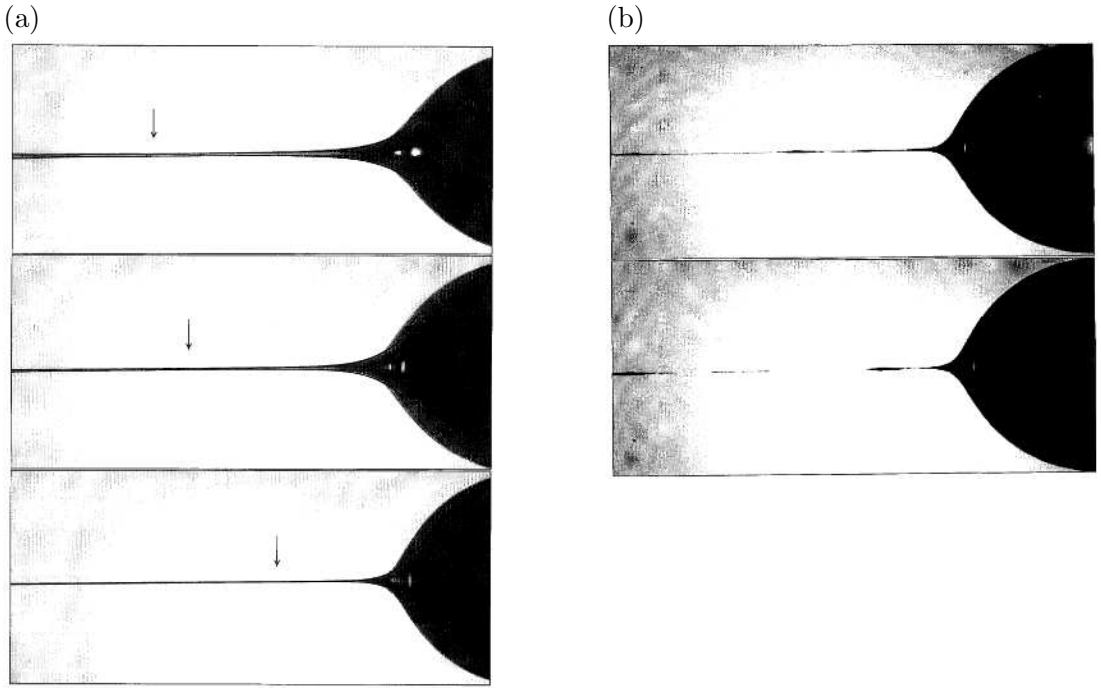

Figure 1.3: Experimental pictures of the process of droplet separation from a jet where (a) is at times before breakup of the jet and (b) is at times after breakup of the jet. The arrows show where the jet is thinning. Reproduced with permission from [91].

the thinning of the jet (and ultimately breakup) occurs. Film or jet rupture has a variety of engineering applications and has been the focus of experimental studies, for example, on droplet formation in a jet leaving an orifice at high speeds [92, 93, 91] and of a liquid being released very slowly from a nozzle (e.g. a dripping faucet) [94, 95, 96]. Mathematically, rupture is represented by a localised finite-time singularity of the governing equations, and the dynamics of the interface (close in space and time to the singularity) can often be described by self-similar solutions. This allows for more analytical insight into the dynamics of the interface close in space and time to the singularity. There has been extensive research on the breakup of fluid jets caused by surface tension [5, 6, 7, 8], the rupture of a fluid sheet by van der Waals forces [97, 73], and finite-time singularities in systems with variations in topology [98, 99, 100, 101]. In these systems, the thickness of

the liquid films $h = h(x, y, z)$ are typically governed by equations of the form

$$\frac{\partial h}{\partial t} = \nabla \cdot \left(A h^a \nabla h - B h^b \nabla \nabla^2 h \right), \tag{1.5}$$

where a, b, A and B are constants that are dependent on the system being investigated. In this Section, we will focus on the rupture of a thin liquid film on a solid substrate due to van der Waals forces. This problem was investigated by Williams and Davis [102], who derived a governing equation for h of the form (1.5) where $a = 3$ and $b = -1$. Burelbach *et al.* [103] proposed, after performing numerical simulations in two-dimensions, that surface tension is negligible near rupture, and that only van der Waals forces and viscous dissipation are important. However, Zhang and Lister [71] showed that, in fact, van der Waals forces, surface tension, and viscous dissipation are all important near rupture. Furthermore, for both the axisymmetric and two-dimensional situations, Zhang and Lister [71] obtained similarity solutions for the interface near to the time of rupture t_{R}, and these solutions predicted that $h \sim (t_{\mathrm{R}} - t)^{1/5}$ and $x \sim (t_{\mathrm{R}} - t)^{2/5}$. Zhang and Lister [96] also showed, using a numerical shooting method, that there is an infinite set of similarity solutions and that the profile seen in the solutions to the PDE corresponds to the similarity solution with the least oscillatory curvature profile, called the fundamental similarity solution. Witelski and Bernoff [72] investigated the stability of the similarity solutions of this system. Specifically, they introduced an alternative numerical approach for calculating the self-similar profiles that also enabled them to determine the stability of these solutions. They found that only the fundamental similarity solution is stable to linear perturbations. Hence, the fundamental similarity solution i.e. the stable similarity solution, corresponds to the solution to the PDE.

Finite-time singularities also occur in different systems when electric fields are present. In Section 1.7, we will provide an overview of the investigations into

finite-time singularity problems where electrostatic effects are present.

1.6 Modelling electrostatic effects

EHD flows have been studied experimentally since Gilbert's treatise *De Magnete* in the 1600s. Before the 1960's, most work focused on perfectly conducting fluids or perfect dielectrics (i.e. perfectly insulators) until the work of Allan and Mason [104] who studied leaky-dielectric (i.e. poorly conducting) fluids. For our study of leaky-dielectric fluids, we will use the Taylor–Melcher leaky dielectric model, which is the most commonly used model. In Section 1.6.1 we will outline this model, and in Section 1.7, we will discuss previous studies of EHD flows.

1.6.1 Taylor–Melcher leaky dielectric model

The leaky-dielectric model was first outlined in the work of Taylor on drop deformation [105] and the subsequent review of EHD flows by Melcher and Taylor [106]. The reviews by Saville [35] and Papageorgiou [36] give an overview of the pioneering and recent work on EHD instabilities, respectively.

Typically, systems are investigated where there are immiscible fluids separated by sharp interfaces subject to electrostatic forces. Under static conditions, the electric and magnetic fields are decoupled (Feynman *et al.* [107]), and in the absence of external magnetic fields, the magnetic effects can be neglected and the electrostatic approximation to Maxwell's equations is used. These state that, in the absence of magnetic effects, the divergence of the electric field is due to local free charge density, namely,

$$\nabla \cdot (\epsilon_0 \epsilon \mathbf{E}) = \rho^e, \tag{1.6}$$

where $\mathbf{E}$ is the electric field, ϵ_0 is the permittivity of free space, ϵ is the relative permittivity of the fluid, and ρ^e is the local free charge density. Note that for two

fluids (Fluid 1 and 2), $\mathbf{E}^1$ and $\mathbf{E}^2$ are the vectors describing the electric field in each fluid. Using the notation $\mathbf{E}$ means that the expression holds for the electric field in both fluids. Equation (1.6) is Gauss' law in the absence of magnetic fields. In addition, since magnetic effects are neglected, Faraday's law becomes

$$\nabla \times \mathbf{E} = \mathbf{0}, \tag{1.7}$$

i.e. the electric field is irrotational. Equations (1.6) and (1.7) can be used to show that the tangential component of the electric field is continuous at fluid-fluid interfaces (Landau and Lifshitz [108]) and its normal component jumps by a quantity proportional to the free charge per unit area q, namely,

$$\epsilon_0 \left[\epsilon_1 \mathbf{E}^1 - \epsilon_2 \mathbf{E}^2\right] \cdot \mathbf{n} = q, \tag{1.8}$$

where $\mathbf{n}$ is the normal vector to the interface between the two fluids, and ϵ_1 and ϵ_2 are the relative permittivities of each fluid. The electric field exerts a force through an additional contribution to the stress tensor, namely, the Maxwell stress tensor,

$$\mathbf{M} = \epsilon_{\mathrm{L,G}} \epsilon_0 \left(\mathbf{E} \otimes \mathbf{E} - \frac{1}{2} |\mathbf{E}|^2 \mathbf{I} \right), \tag{1.9}$$

and under circumstances where the permittivities are uniform, the conductivities are constant and charge is neglected in the bulk of the fluids [36], the hydrodynamics are coupled with the electrostatics only via the Maxwell stress at the interface.

Since there is free charge at the interface, an equation governing the evolution of this charge is required. This is given by the charge transport equation,

$$\frac{\partial q}{\partial t} + \mathbf{u} \cdot \nabla_{\mathrm{s}} q - q \mathbf{n} \cdot (\mathbf{n} \cdot \nabla) \mathbf{u} = \left[\sigma_2 \mathbf{E}^2 - \sigma_1 \mathbf{E}^1\right] \cdot \mathbf{n}, \tag{1.10}$$

where $\nabla_s = \nabla - \mathbf{n}(\mathbf{n} \cdot \nabla)$ is the surface gradient operator,u is the fluid velocity at the interface, and σ_1 and σ_2 are the conductivities of each fluid, and $\mathbf{n}$ and $\mathbf{t}$ are the normal and tangential vectors of the interface, respectively. The second and third terms on the left hand side correspond to convection and dilation of the free surface, respectively, and the term on the right hand side corresponds to ion conduction through the bulk. Equations (1.6)–(1.10) constitute the Taylor–Melcher leaky dielectric model which we will use in the present work.

1.7 Previous studies of EHD flows

There have been a vast range of experimental, analytical, and numerical studies performed on EHD flows. In this Section, we will discuss some of the previous studies on EHD instabilities and pattern formation, coating and draining flow problems, finite-time singularity problems, and other relevant studies on EHD flows.

1.7.1 EHD instability and pattern formation studies

There have been a host of linear stability studies and computational studies that have investigated EHD instabilities in systems with thin liquid films in two dimensional and axisymmetric geometries, where the system parameters are tuned to give structures of different wavelengths and heights (and this has applications to pattern formation technologies). Linear stability analyses of a bilayer of two fluids bounded by electrodes have shown that even the slightest conductivity in a fluid has a profound influence on the growth rates and characteristic lengthscale of EHD instabilities [109, 110]. Papageorgiou and Petropolous [111] studied the linear stability of a liquid film surrounded by a gas. They showed that (for arbitrary Reynolds numbers) a liquid film can become unstable when $\Sigma_R \epsilon_R > 1$ or $\Sigma_R \epsilon_R < 1$, and $(\Sigma_R - 1)(1 - \epsilon_R) < 0$, where Σ_R and ϵ_R are the conductivity and

permittivity ratios, respectively, of the liquid film and surrounding gas. Also, depending on the values of the system parameters, linear stability theory also showed that the electric field can be either stabilising or destabilising in a bilayer of leaky dielectric liquids [112, 113, 114]. Li *et al.* [114] showed that, for a bilayer of two perfectly dielectric viscous fluids in a two-dimensional channel, the electric field is always destabilising. In a later study by Uguz *et al.* [115], a system with a normal electric field was shown to have broader regions of parameter space that were destabilising compared to systems with a tangential electric field.

Numerical computations have allowed for the investigation of EHD instabilities in the nonlinear regime. Wu and Chou [37] investigated a two-dimensional bilayer of perfect dielectric liquid film and air contained between two electrodes, and found that the frequency of the pillars that formed are dependent on the ratio of the surface tension and electrostatic forces. Craster and Matar [75] studied a more general system of two viscous leaky dielectric fluid films, and found that varying the system parameters alters the shape and frequency of the pillars that form. Figure 1.4 is an example of the results obtained by Craster and Matar [75], and shows plots of h as a function of x for different values of the thickness ratio β (i.e. the ratio of the thickness of the lower and upper fluid films). Figure 1.4 illustrates the change in the shape and frequency of the pillars with a varying β. The enhancement and control of interfacial instabilities in the nonlinear regime was explored by Wray *et al.* [116], who investigated the evolution of the interface between a leaky dielectric liquid and gas contained between two concentric cylindrical electrodes in an axisymmetric geometry. They found that four behaviours can occur (depending on the values of the system parameters):

1. A stable regime in which the interface is uniform.

2. Nonlinear steady-state travelling waves.

3. Complex droplet-like behaviour that did not reach a steady state.

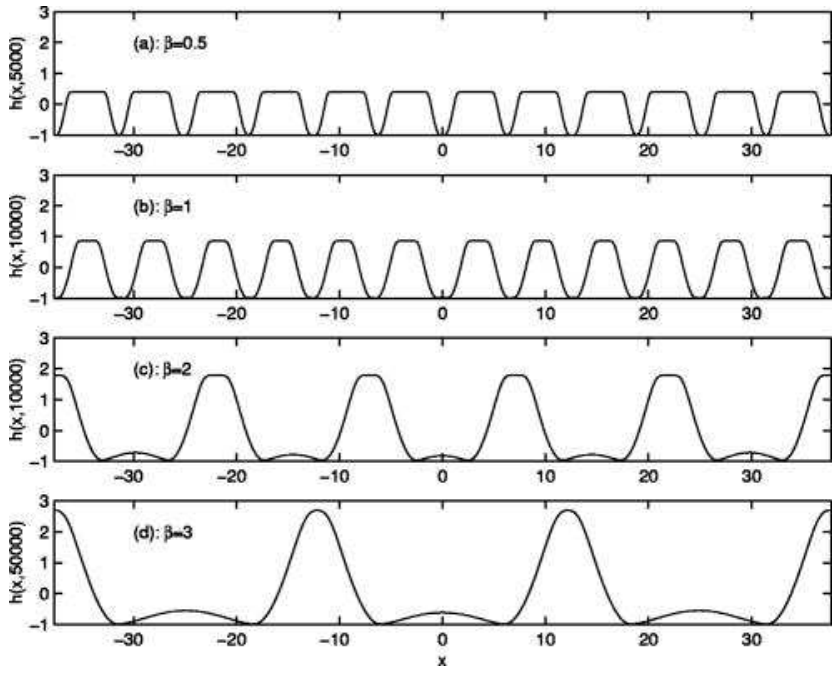

Figure 1.4: Plots of h as a function of x for varying values of the ratio of the lower to upper film thicknesses. Reproduced with permission from [75].

4. The formation of finite-time singularities.

Wray *et al.* [116] also performed a parametric investigation to determine where in parameter space each of the four behaviours occur.

Even though the studies discussed above investigate planar or axisymmetric geometries, there have also been studies exploring three dimensional systems [117, 76].

1.7.2 Coating and draining flow problems

Wang and Papageorgiou [74] investigated two immiscible perfect or leaky dielectric fluids in an axisymmetric geometry, that were confined between two concentric cylinders in the presence of a radial electric field. They showed that, for perfect dielectric fluids, filling and draining lobes (separated by troughs) formed, as described in Section 1.4. In particular, they found that $h \sim t^{-1/2}$ in the trough regions, the same scaling law as that seen in previous studies [80, 81, 83]. Also, Pillai and Narayanan [118] investigated the two-dimensional case of a bilayer

of perfectly conducting liquid below a passive gas, contained between two planar electrodes. They showed that the interface evolved into filling and draining lobes, and observed a sliding phenomena at late times. They stated that this sliding phenomenon must be facilitated by an asymmetric instability, as shown to be the case for the system investigated by Dietze *et al.* [86]. They also investigated the fast charge relaxation limiting case (i.e. when both the liquid and gas are highly conducting), and showed that a cascade of buckling events occurred in the trough regions, as also seen by Dietze *et al.* [86].

1.7.3 Film or jet rupture problems

There have been studies of finite-time singularities in systems with electric fields. The pinching or breakup of liquid jets or threads have been studied [119, 120], and also flows with charged surfactants [121, 122, 123, 124]. Barannyk *et al.* [125] observed finite-time singularities when investigating two perfect dielectric liquid films contained between two electrodes, where the electric field was applied parallel to the interface. Wray *et al.* [116] investigated finite-time interfacial touchdown and obtained similarity solutions for the interfacial height close to touchdown. Wang and Papageorgiou [74], who investigated the axisymmetric case of two viscous fluids contained between two concentric electrodes, found that finite-time touchdown can occur at either electrode for leaky dielectrics, and two-sided touchdown can occur for perfect dielectrics.

1.7.4 Other studies of EHD flows

Two and three-dimensional WRIBL models were derived by Wray *et al.* [70] to investigate gravity-driven, leaky-dielectric films with inertial effects. These models were validated against linear theories and DNS, and showed excellent agreement. A parametric study found that increasing the conductivity ratio and decreasing the permittivity ratio resulted in a disordered interface (i.e. there is

no clear order to the interfacial profile) and an increase in surface area. More recent studies have used WRIBL models to study flows with electrostatic effects [118, 126, 127, 128], and have shown them to be accurate in describing "thick-film flows" with electrostatic effects [129], showing both very good agreement with the linear stability results of the full Navier–Stokes equations, like accurately predicting the critical Reynolds number from stability to instability, as well as good qualitative agreement with DNS.

Furthermore, there have been studies of a thin, perfectly conducting or perfect dielectric liquid film below a passive, perfectly dielectric gas (which is not thin), that are only bounded below by an electrode [130, 131, 132, 133, 134]. However, there has been little attention paid to two-dimensional, thin, perfectly conducting liquid and perfectly insulating gas films that are bounded by two electrodes. These systems are singular (i.e. the denominators of the governing equations are zero) when the interface touches one of the electrodes [36]. Also, the situation in which a liquid flows over a corrugated electrode or wall has been investigated [68, 135, 136, 134, 137], and the results showed that the flows have nonuniform steady states.

The studies above investigated systems with DC electric fields, but the effect of AC electric fields have also been studied [138, 139, 140, 141, 142, 143, 118, 126]. It has been shown that the size and frequency of the interfacial patterns that form can be controlled by AC electric fields, and the subharmonic modes that arise may dominate depending on the imposed electric field.

Lastly, even though there have been extensive studies on varying the values of system parameters to investigate their effect on the stability of the system and on the evolution of different structures, there have been few parametric studies investigating where different behaviours occur [116]. In particular, there have been no systematic parametric investigations of the whole of parameter space to determine where different behaviours occur. In systems where the interface can

touch either electrode, it may be useful to know where in parameter space the interface approaches one electrode rather than the other. Also, knowledge of how behaviours change when a parameter (e.g. the conductivity or permittivity of a liquid) is varied will give a deeper insight into the effects of these parameters on the behaviour of flows. In this thesis, we will determine all possible behaviours that occur for the systems being investigated, and parametric studies will be performed that will determine where in the relevant parameter spaces the different behaviours occur.

1.8 Thesis outline

In Chapter 2, we derive the model used to describe the two-dimensional system we will investigate, namely a bilayer of liquid and gas contained between two planar electrodes. We derive the LW approximation to this model, as well as three limiting cases of the LW model, namely, when the liquid is perfectly conducting, the liquid and gas are both highly conducting, and when the liquid and gas are both perfect dielectrics. The case where the liquid and gas are perfect dielectrics is mathematically similar to the other limiting cases, and so, along with the time constraints of the PhD, we do not investigate this case in this thesis.

In Chapter 3, we perform a linear stability analysis of the perfectly conducting, highly conducting limiting cases, as well as the LW model. To validate these models in appropriate regime, the results are compared against the results of the full model. We then introduce and describe the numerical schemes used to perform our numerical calculations in Chapter 4. In particular, we explain the Matlab code that was used to perform these calculations, as well as additional code used to perform extra analyses.

The case where the liquid is perfectly conducting is then investigated in Chapter 5. We identify three possible behaviours and explore parameter space, indicating

where these behaviours occur, and investigate each behaviour further, both analytically and numerically.

In Chapter 6, we investigate the case where the liquid and gas are both highly conducting. Again, we identify the same three possible behaviours and explore parameter space, indicating where these behaviours occur, and investigate each behaviour further, both analytically and numerically.

We then investigate the LW model in Chapter 7, identifying four possible behaviours. We explore parameter space, indicating where these behaviours occur, and investigate the four behaviours further, both analytically and numerically.

In Chapter 8, we provide a summary of our analysis, draw conclusions, and highlight possible directions for future work.

1.9 Presentations and publications

The work contained in this thesis was presented at several local, national, and international conferences and meetings. Specifically, oral presentations of Chapters 3–7 were given at the following conferences and meetings: the British Applied Mathematics Colloquium 2019, Bath, the SIAM-IMA Student Chapter Conference 2019, University of Strathclyde, and the 8th International Symposium on Bifurcations and Instabilities in Fluid Dynamics 2019, University of Limerick. In addition, a poster presentation of Chapters 3–7 was given at the 32nd Scottish Fluid Mechanics Meeting 2019, Dundee. A virtual presentation of Chapters 3–7 was also given at the APS–DFD 2020, Chicago, and a short prerecorded presentation can still be viewed on YouTube (accessible via https://youtu.be/8q4TSyET1zc). Furthermore, Chapters 3–7 were also presented by Dr A.W. Wray at the Joint British Mathematical Colloquium / British Applied Mathematics Colloquium 2021 held virtually at the University of Glasgow. The work described in this thesis is currently being written up for publication in a peer-reviewed journal.

Chapter 2

Formulation of the mathematical model

In Section 2.1, we will introduce the system being investigated, describing the geometry setup and the coordinate system. In Sections 2.2 and 2.3, the hydrodynamic and electrostatic parts of the model, respectively, will be introduced and presented in more detail. In particular, the governing equations will be obtained, non-dimensionalised, and presented in coordinate form before deriving the LW version of the model. In Section 2.4, we will derive the governing equations for three limiting cases of the LW model.

2.1 System formulation

We consider a two-dimensional film of leaky dielectric liquid with constant density ρ and viscosity μ, and a hydrodynamically passive gas sandwiched between two impermeable, infinite electrodes. A potential difference is present across the two electrodes which induces electric fields $\mathbf{E}^{\mathrm{L}}$ and $\mathbf{E}^{\mathrm{G}}$ in the liquid and gas, respectively. The voltage potential in the liquid and gas are given by $\phi^{\mathrm{L}} = \phi^{\mathrm{L}}(x, y, t)$ and $\phi^{\mathrm{G}} = \phi^{\mathrm{G}}(x, y, t)$, respectively. The liquid has constant conductivity σ_{L} and permittivity $\epsilon_{\mathrm{L}}\epsilon_0$, where ϵ_{L} is the relative permittivity of the liquid and ϵ_0 is

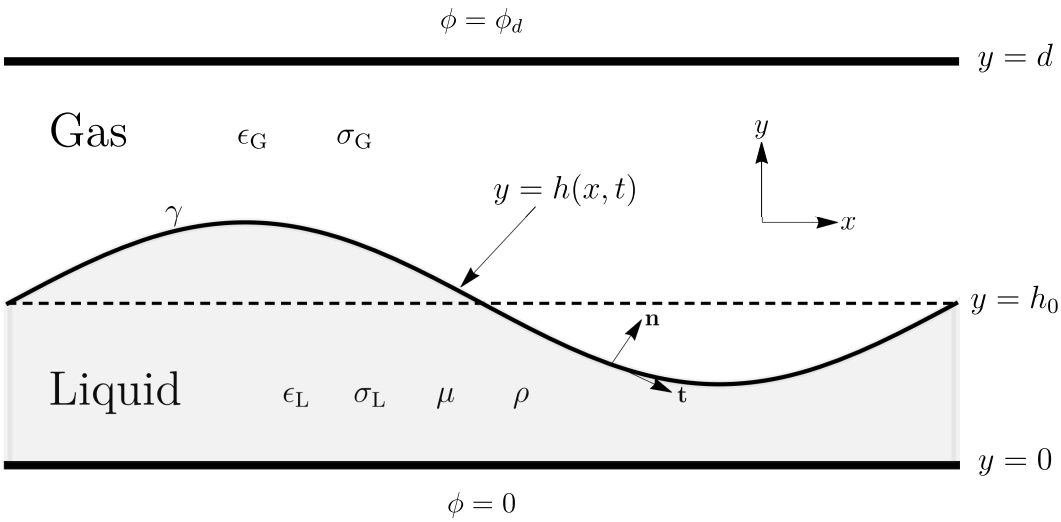

Figure 2.1: Schematic diagram of the system.

the permittivity of free space, and the gas has constant conductivity σ_G and permittivity $\epsilon_G\epsilon_0$, where ϵ_G is the relative permittivity of the gas. A Cartesian coordinate system (x, y) is used in which the velocity of the liquid $\mathbf{u}$ is described by

$$\mathbf{u} = (u, v) = (u(x, y, t), v(x, y, t)) , \tag{2.1}$$

where t denotes time. The lower electrode, located at $y = 0$, is held at zero voltage potential. The upper electrode is located at $y = d$ and has constant voltage potential $\phi = \phi_d$. The liquid-gas interface is located at $y = h(x, t)$ and has constant interfacial tension γ. Hence, the liquid and gas are located in the regions $0 < y < h(x, t)$ and $h(x, t) < y < d$, respectively. In the absence of perturbations, $y = h_0$ where h_0 is a constant, i.e. the interface is flat and parallel to the electrodes. The normal and tangential vectors of the interface are expressed as

$$\mathbf{n} = \frac{(-\partial h/\partial x, 1)}{\left(1 + (\partial h/\partial x)^2\right))^{1/2}}, \qquad \mathbf{t} = \frac{(1, \partial h/\partial x)}{\left(1 + (\partial h/\partial x)^2\right)^{1/2}},$$

respectively, in which $h = h(x, t)$. A schematic diagram of this system is shown in Figure 2.1.

2.2 Hydrodynamic part

We begin by formulating the hydrodynamic part of the model. The governing equations are presented in Section 2.2.1 before non-dimensionalising in Section 2.2.2. The equations are then expressed in coordinate form in Section 2.2.3 before a LW approximation is made in Section 2.2.4.

2.2.1 Governing equations

There is assumed to be no charge in the bulk of the liquid or gas which is in line with the Taylor–Melcher leaky dielectric model, which is a reasonable assumption to make for a small charge relaxation time [35, 36]. This assumption makes the analysis more tractable since the electrostatic effects are only incorporated into the model through the boundary conditions. Hence, the hydrodynamics of the liquid are governed by the Navier–Stokes and continuity equations,

$$\rho\left(\frac{\partial \mathbf{u}}{\partial t} + \mathbf{u}\cdot\nabla\mathbf{u}\right) = -\nabla p + \mu\nabla^2\mathbf{u}, \tag{2.2}$$

$$\nabla\cdot\mathbf{u} = 0, \tag{2.3}$$

respectively, which are subject to the standard no-slip and no-penetration on the lower electrode,

$$\mathbf{u} = \mathbf{0} \quad \text{on} \quad y = 0. \tag{2.4}$$

At the interface $y = h(x,t)$, there is the balance of normal and tangential stresses,

$$[\mathbf{n}\cdot\mathbf{T}\cdot\mathbf{n}]_{\mathrm{L}}^{\mathrm{G}} = \gamma\kappa \qquad [\mathbf{n}\cdot\mathbf{T}\cdot\mathbf{t}]_{\mathrm{L}}^{\mathrm{G}} = 0, \tag{2.5}$$

where

$$\kappa = -\frac{\partial^2 h/\partial x^2}{\left(1 + (\partial h/\partial x)^2\right)^{3/2}}, \tag{2.6}$$

is the interfacial curvature, $[\cdot]_{\mathrm{L}}^{\mathrm{G}}$ represents the jump in the value of a quantity from one side of the interface to the other, and $\mathbf{T}$ is the total stress tensor. In particular, the total stress tensor contains three components, $\mathbf{T} = -p\mathbf{I} + \mathbf{M} + \boldsymbol{\tau}$, where $p = p(x, y, t)$ is the pressure in the liquid, $\mathbf{M}$ is the Maxwell stress tensor, and $\boldsymbol{\tau}$ is the viscous stress tensor [39, 144]. The electrostatic effects are incorporated into the model through the Maxwell stress tensor $\mathbf{M}$ and will be described by equation (2.39) in Section 2.3.

Lastly, there is the kinematic boundary condition at the interface,

$$\frac{D}{Dt}\left(y - h(x,t)\right) = 0, \tag{2.7}$$

where $D/Dt = \partial/\partial t + \mathbf{u} \cdot \nabla$ is the material derivative, and equation (2.7) can be expressed as

$$\frac{\partial h}{\partial t} + u\frac{\partial h}{\partial x} = v, \tag{2.8}$$

evaluated at $y = h(x, t)$.

2.2.2 Non-dimensionalisation

The system is made non-dimensional using the following scalings,

$$(x, y, h) = h_0(x', y', h'), \quad (u, v) = V(u', v'), \quad p = \frac{V\mu}{h_0}p', \quad t = \frac{h_0}{V}t', \tag{2.9}$$

where the dashes denote dimensionless quantities and V is the characteristic velocity which will be defined in Section 2.2.4. The following non-dimensional

parameters arise,

$$d' = \frac{d}{h_0}, \quad Ca = \frac{\mu V}{\gamma}, \quad Re = \frac{\rho h_0 V}{\mu}, \tag{2.10}$$

where d' is the scaled position of the upper electrode, Ca is the capillary number, and Re is the Reynolds number.

Immediately dropping the dashes, the Navier–Stokes and continuity equations, (2.2) and (2.3), respectively, become

$$Re\left(\frac{\partial \mathbf{u}}{\partial t} + \mathbf{u}\cdot\nabla\mathbf{u}\right) = -\nabla p + \nabla^2\mathbf{u}, \tag{2.11}$$

$$\nabla\cdot\mathbf{u} = 0. \tag{2.12}$$

We will only consider flows in which liquid inertia is neglected, i.e. $Re = 0$, which corresponds to viscous forces being much greater than inertial forces. This regime is called Stokes flow (also called creeping flow or slow flow [39]) and in it equations (2.11) and (2.12) become the Stokes flow (SF) equations,

$$\mathbf{0} = -\nabla p + \nabla^2\mathbf{u}, \tag{2.13}$$

$$\nabla\cdot\mathbf{u} = 0. \tag{2.14}$$

The normal and tangential interfacial stresses (2.5) are

$$[\mathbf{n}\cdot\mathbf{T}\cdot\mathbf{n}]_{\mathrm{L}}^{\mathrm{G}} = \frac{\kappa}{Ca} \qquad [\mathbf{n}\cdot\mathbf{T}\cdot\mathbf{t}]_{\mathrm{L}}^{\mathrm{G}} = 0, \tag{2.15}$$

and the non-dimensional kinematic condition (2.23) is

$$\frac{\partial h}{\partial t} + u\frac{\partial h}{\partial x} = v. \tag{2.16}$$

2.2.3 Cartesian Coordinate form

The governing equations (2.13)-(2.16) are now presented in Cartesian coordinate form. The SF equations, (2.13) and (2.14), are

$$0 = -\frac{\partial p}{\partial x} + \left(\frac{\partial^2 u}{\partial x^2} + \frac{\partial^2 u}{\partial y^2}\right), \tag{2.17}$$

$$0 = -\frac{\partial p}{\partial y} + \left(\frac{\partial^2 v}{\partial x^2} + \frac{\partial^2 v}{\partial y^2}\right), \tag{2.18}$$

$$0 = \frac{\partial u}{\partial x} + \frac{\partial v}{\partial y}. \tag{2.19}$$

The no-slip and no-penetration boundary conditions (2.4) give

$$u = v = 0 \quad \text{on} \quad y = 0, \tag{2.20}$$

and the normal and tangential stress conditions (2.15), respectively, evaluated at $y = h(x,t)$, become

$$2\left(\frac{\partial v}{\partial y} + \frac{\partial u}{\partial x}\left(\frac{\partial h}{\partial x}\right)^2 - \frac{\partial h}{\partial x}\left(\frac{\partial u}{\partial y} + \frac{\partial v}{\partial x}\right)\right) - E^{\mathrm{N}} = \left[1 + \left(\frac{\partial h}{\partial x}\right)^2\right]\left(p - \frac{\kappa}{Ca}\right), \tag{2.21}$$

$$\left(1 - \left(\frac{\partial h}{\partial x}\right)^2\right)\left(\frac{\partial u}{\partial y} + \frac{\partial v}{\partial x}\right) + 2\frac{\partial h}{\partial x}\left(\frac{\partial v}{\partial y} - \frac{\partial u}{\partial x}\right) - E^{\mathrm{T}} = 0, \tag{2.22}$$

where

$$E^{\mathrm{N}} = \frac{h_0}{V\mu}\left(1 + \left(\frac{\partial h}{\partial x}\right)^2\right)\left[\mathbf{n}\cdot\mathbf{M}\cdot\mathbf{n}\right]_{\mathrm{L}}^{\mathrm{G}}, \qquad E^{\mathrm{T}} = \frac{h_0}{V\mu}\left(1 + \left(\frac{\partial h}{\partial x}\right)^2\right)\left[\mathbf{t}\cdot\mathbf{M}\cdot\mathbf{n}\right]_{\mathrm{L}}^{\mathrm{G}},$$

are the electrostatic contributions to the normal and tangential stresses, respectively, which describe the jump in value of the Maxwell stress across the interface, and will be given by equations (2.57) and (2.61) in Section 2.3.

After using the continuity equation (2.19) and the no-penetration condition (2.20),

the kinematic condition (2.16) in Cartesian coordinate form is given by

$$\frac{\partial h}{\partial t} + \frac{\partial}{\partial x} Q(x,t) = 0, \tag{2.23}$$

where $Q(x,t) = \int_0^h u dy$ is the volume flux of liquid across the line $x =$ constant.

2.2.4 Long-wave (LW) approximation

The LW version of the SF model is now derived, in which the analysis of the system becomes more tractable by reducing the system from two dimensions (x, y) to one dimension x. This allows for more progress to be made both analytically and numerically.

The following scalings are used:

- Assuming the characteristic length of the film is long relative to its thickness motivates the scaling $x = \widetilde{x}/\epsilon$, where $\epsilon = h_0/\lambda \ll 1$ is the small aspect ratio and λ is the characteristic wavelength of the system.
- To keep both terms of the continuity equation (2.19) (and ensure mass conservation) at leading-order in ϵ, the familiar LW scaling for the x- and y-component of the velocity, $u = \epsilon\widetilde{u}$ and $v = \epsilon^2\widetilde{v}$, are imposed.
- To retain the time dependence term in the kinematic condition (2.23) at leading-order, the scaling $t = \widetilde{t}/\epsilon^2$ is imposed.
- To keep the surface tension terms at leading-order in ϵ in (2.21), the scaling $Ca = \epsilon^2\widetilde{Ca}$ is imposed.

In summary, the LW version of the SF model is derived by imposing the following scalings:

$$x = \frac{1}{\epsilon}\widetilde{x}, \quad t = \frac{1}{\epsilon^2}\widetilde{t}, \quad u = \epsilon\widetilde{u}, \quad v = \epsilon^2\widetilde{v}, \quad Ca = \epsilon^2\widetilde{Ca}. \tag{2.24}$$

From here on, we set $\widetilde{Ca} = 1$ which fixes the characteristic velocity as $V = \gamma\epsilon^2/\mu$ through the definition of the capillary number (2.10).

2.2.4.a Leading-order equations

After introducing the scalings (2.24), and dropping the tildes immediately, the leading-order SF equations (2.17) and (2.18) become

$$0 = -\frac{\partial p}{\partial x} + \frac{\partial^2 u}{\partial y^2}, \tag{2.25}$$

$$0 = -\frac{\partial p}{\partial y}. \tag{2.26}$$

Equation (2.26) shows that the pressure is independent of y, i.e. $p = p(x,t)$. Furthermore, equation (2.25) is used with the no-slip (2.20) and the tangential stress (2.22) conditions to yield an expression for u,

$$u = \frac{1}{2}\frac{\partial p}{\partial x}\left(y^2 - 2hy\right) + E^{\mathrm{T}}_{\mathrm{LW}} y, \tag{2.27}$$

where the expression for p is obtained from the leading-order normal stress condition (2.21), namely,

$$p = -\frac{\partial^2 h}{\partial x^2} - E^{\mathrm{N}}_{\mathrm{LW}}, \tag{2.28}$$

where $E^{\mathrm{T}}_{\mathrm{LW}}$ and $E^{\mathrm{N}}_{\mathrm{LW}}$ are the leading-order electrostatic contributions to the tangential and normal stresses, respectively, which will be given in Section 2.3.4. The kinematic condition (2.23) is

$$\frac{\partial h}{\partial t} + \frac{\partial Q}{\partial x} = 0, \tag{2.29}$$

where $Q = Q(x,t)$ and substituting the expression for u (2.27) into (2.29) yields the governing equation for the interfacial height h,

$$\frac{\partial h}{\partial t} + \frac{\partial}{\partial x}\left(\frac{h^3}{3}\left(\frac{\partial^2 h}{\partial x^2} + E_{\mathrm{LW}}^{\mathrm{N}}\right) + \frac{h^2}{2}E_{\mathrm{LW}}^{\mathrm{T}}\right) = 0. \tag{2.30}$$

2.3 Electrostatic part

We now formulate the electrostatic part of the model. The governing equations are presented in Section 2.3.1 before non-dimensionalising in Section 2.3.2. The equations are expressed in coordinate form in Section 2.3.3 before a LW approximation is made in Section 2.3.4.

2.3.1 Governing equations

The electrostatic part of the model is described by the Taylor–Melcher leaky dielectric model [35, 36] introduced in Section 1.6.1. The electric field in the liquid and gas regions, $\mathbf{E}^{\mathrm{L}} = \mathbf{E}^{\mathrm{L}}(x,y,t)$ and $\mathbf{E}^{\mathrm{G}} = \mathbf{E}^{\mathrm{G}}(x,y,t)$, respectively, satisfy

$$\nabla \cdot \mathbf{E}^{\mathrm{L}} = 0, \qquad \nabla \times \mathbf{E}^{\mathrm{L}} = \mathbf{0}, \tag{2.31}$$

$$\nabla \cdot \mathbf{E}^{\mathrm{G}} = 0, \qquad \nabla \times \mathbf{E}^{\mathrm{G}} = \mathbf{0}. \tag{2.32}$$

Therefore, since the electric field in the liquid and gas have zero divergence and zero curl, they can be expressed in terms of the gradients of voltage potential according to $\mathbf{E}^{\mathrm{L}} = -\nabla\phi^{\mathrm{L}}(x,y,t)$ and $\mathbf{E}^{\mathrm{G}} = -\nabla\phi^{\mathrm{G}}(x,y,t)$, which satisfy Laplace's equation,

$$\nabla^2\phi^{\mathrm{L}} = 0, \qquad \nabla^2\phi^{\mathrm{G}} = 0. \tag{2.33}$$

At the interface $y = h(x,t)$, the electric field satisfies Gauss' law,

$$\epsilon_0 \left[\epsilon_{\mathrm{L}} \mathbf{E}^{\mathrm{L}} - \epsilon_{\mathrm{G}} \mathbf{E}^{\mathrm{G}}\right] \cdot \mathbf{n} = q, \tag{2.34}$$

where $q = q(x,t)$ is the interfacial charge density. The tangential component of the electric field is continuous across the interface so that

$$\left[\mathbf{E}^{\mathrm{L}} - \mathbf{E}^{\mathrm{G}}\right] \cdot \mathbf{t} = 0 \quad \text{at} \quad y = h(x,t). \tag{2.35}$$

Equations (2.34) and (2.35) may be rewritten as conditions for the voltage potential $\phi^{\mathrm{L}} = \phi^{\mathrm{L}}(x,y,t)$ and $\phi^{\mathrm{G}} = \phi^{\mathrm{G}}(x,y,t)$, evaluated at $y = h(x,t)$, specifically,

$$\epsilon_0 \left[\epsilon_{\mathrm{L}} \nabla\phi^{\mathrm{L}} - \epsilon_{\mathrm{G}} \nabla\phi^{\mathrm{G}}\right] \cdot \mathbf{n} = -q, \tag{2.36}$$

$$\phi^{\mathrm{L}} = \phi^{\mathrm{G}}, \tag{2.37}$$

where the voltage potential boundary conditions at the lower and upper electrodes are

$$\phi^{\mathrm{L}}|_{y=0} = 0, \quad \phi^{\mathrm{G}}|_{y=d} = \phi_{\mathrm{d}}. \tag{2.38}$$

The Maxwell stress tensor is defined as [35]

$$\mathbf{M} = \epsilon\epsilon_0 \left(\mathbf{E} \otimes \mathbf{E} - \frac{1}{2} |\mathbf{E}|^2 \mathbf{I}\right), \tag{2.39}$$

where $\mathbf{E} = \mathbf{E}^{\mathrm{L}}$ and $\epsilon = \epsilon_{\mathrm{L}}$, and $\mathbf{E} = \mathbf{E}^{\mathrm{G}}$ and $\epsilon = \epsilon_{\mathrm{G}}$ in the liquid and gas, respectively.

Lastly, the charge transport equation, evaluated at $y = h(x,t)$, which governs the evolution of charge q at the interface [35, 36], is given by

$$\frac{\partial q}{\partial t} + \mathbf{u} \cdot \nabla_{\mathrm{s}} q - q\mathbf{n} \cdot (\mathbf{n} \cdot \nabla)\, \mathbf{u} = -\left[\sigma_{\mathrm{L}} \mathbf{E}^{\mathrm{L}} - \sigma_{\mathrm{G}} \mathbf{E}^{\mathrm{G}}\right] \cdot \mathbf{n}, \tag{2.40}$$

where $\nabla_{\mathrm{s}} = \nabla - \mathbf{n}\,(\mathbf{n}\cdot\nabla)$ is the surface gradient operator. This can be recast so that the right hand side is expressed in terms of the voltage potentials ϕ^{L} and ϕ^{G}, evaluated at $y = h(x,t)$, namely,

$$\frac{\partial q}{\partial t} + \mathbf{u}\cdot\nabla_{\mathrm{s}} q - q\mathbf{n}\cdot(\mathbf{n}\cdot\nabla)\,\mathbf{u} = \left[\sigma_{\mathrm{L}}\nabla\phi^{\mathrm{L}} - \sigma_{\mathrm{G}}\nabla\phi^{\mathrm{G}}\right]\cdot\mathbf{n}. \tag{2.41}$$

Pillai and Narayanan [118, 126] included an additional diffusion term that incorporates the effects of the interfacial velocity $u|_h$ on the distribution of charge on the interface, as studied by Johns [145]. It is expected that this will occur over a much slower timescale that the other diffusion terms and so is neglected in this system [35].

2.3.2 Non-dimensionalisation

The system is made non-dimensional using the scalings (2.9) and

$$\left(\phi^{\mathrm{L}}, \phi^{\mathrm{G}}\right) = \phi_{\mathrm{d}}\left(\phi^{\mathrm{L}\prime}, \phi^{\mathrm{G}\prime}\right), \qquad q = \frac{\epsilon_{\mathrm{G}}\epsilon_0\phi_{\mathrm{d}}}{h_0}q'. \tag{2.42}$$

The following non-dimensional parameters arise,

$$E_{\mathrm{b}} = \frac{\epsilon_{\mathrm{G}}\epsilon_0\phi_{\mathrm{d}}^2}{\mu V h_0}, \qquad \Sigma_{\mathrm{L}} = \frac{\sigma_{\mathrm{L}}h_0}{\epsilon_{\mathrm{G}}\epsilon_0 V}, \qquad \Sigma_{\mathrm{G}} = \frac{\sigma_{\mathrm{G}}h_0}{\epsilon_{\mathrm{G}}\epsilon_0 V}, \qquad \epsilon_{\mathrm{R}} = \frac{\epsilon_{\mathrm{L}}}{\epsilon_{\mathrm{G}}}, \tag{2.43}$$

where E_{b} is a measure of the electric field strength, Σ_{L} and Σ_{G} are measures of the conductivities in the liquid and gas, respectively, and ϵ_{R} is the ratio of the permittivities between the liquid and gas.

Dropping the dashes immediately, the governing equations for the voltage potential (2.33) become

$$\nabla^2\phi^{\mathrm{L}} = 0, \qquad \nabla^2\phi^{\mathrm{G}} = 0. \tag{2.44}$$

The non-dimensionalisation applied to Gauss' law (2.36) and the continuity of voltage potential (2.37) at the interface $y = h(x,t)$ yields

$$\nabla\left(\phi^{\mathrm{G}} - \epsilon_{\mathrm{R}}\phi^{\mathrm{L}}\right)\cdot\mathbf{n} = -q, \tag{2.45}$$

$$\phi^{\mathrm{L}} = \phi^{\mathrm{G}}, \tag{2.46}$$

respectively, and the boundary conditions for the voltage potential at the electrodes (2.38) become

$$\phi^{\mathrm{L}}|_{y=0} = 0, \quad \phi^{\mathrm{G}}|_{y=d} = 1. \tag{2.47}$$

Lastly, the non-dimensionalised charge transport equation (2.41), evaluated at $y = h(x,t)$ is

$$\frac{\partial q}{\partial t} + \mathbf{u}\cdot\nabla_{\mathrm{s}} q - q\mathbf{n}\cdot(\mathbf{n}\cdot\nabla)\,\mathbf{u} = \left[\Sigma_{\mathrm{L}}\nabla\phi^{\mathrm{L}} - \Sigma_{\mathrm{G}}\nabla\phi^{\mathrm{G}}\right]\cdot\mathbf{n}. \tag{2.48}$$

2.3.3 Cartesian Coordinate form

The electrostatic part of the model is now presented in Cartesian coordinate form. The voltage potential governing equations (2.44) become

$$\frac{\partial^2\phi^{\mathrm{L}}}{\partial x^2} + \frac{\partial^2\phi^{\mathrm{L}}}{\partial y^2} = 0, \tag{2.49}$$

$$\frac{\partial^2\phi^{\mathrm{G}}}{\partial x^2} + \frac{\partial^2\phi^{\mathrm{G}}}{\partial y^2} = 0. \tag{2.50}$$

Gauss' law (2.45) and the continuity of voltage potential (2.46) in Cartesian coordinate form are

$$-\left(1 + \frac{\partial h}{\partial x}^2\right)^{\frac{1}{2}} q = \left(\frac{\partial\phi^{\mathrm{G}}}{\partial y} - \frac{\partial h}{\partial x}\frac{\partial\phi^{\mathrm{G}}}{\partial x}\right) - \epsilon_{\mathrm{R}}\left(\frac{\partial\phi^{\mathrm{L}}}{\partial y} - \frac{\partial h}{\partial x}\frac{\partial\phi^{\mathrm{L}}}{\partial x}\right), \tag{2.51}$$

$$\phi^{\mathrm{L}} = \phi^{\mathrm{G}}, \tag{2.52}$$

respectively, evaluated at $y = h(x,t)$, and the boundary conditions at the electrodes (2.47) are

$$\phi^{\mathrm{L}}|_{y=0} = 0, \quad \phi^{\mathrm{G}}|_{y=d} = 1. \tag{2.53}$$

The Maxwell stress tensor (2.39) in Cartesian coordinate form is

$$\mathbf{M} = \frac{\epsilon_{\mathrm{L,G}}\epsilon_0\phi_{\mathrm{d}}^2}{h_0^2}\left[\begin{pmatrix}\left(\frac{\partial\phi}{\partial x}\right)^2 & \frac{\partial\phi}{\partial x}\frac{\partial\phi}{\partial y}\\ \frac{\partial\phi}{\partial x}\frac{\partial\phi}{\partial y} & \left(\frac{\partial\phi}{\partial y}\right)^2\end{pmatrix} - \frac{1}{2}\left(\left(\frac{\partial\phi}{\partial x}\right)^2 + \left(\frac{\partial\phi}{\partial y}\right)^2\right)\mathbf{I}\right]. \tag{2.54}$$

We now calculate the electrostatic contribution to the normal and tangential stresses E^{N} and E^{T}, respectively. Firstly, the electrostatic contribution to the normal stress is

$$E^{\mathrm{N}} = \frac{h_0}{V\mu}\left(1 + \left(\frac{\partial h}{\partial x}\right)^2\right)\left[\mathbf{n}\cdot\mathbf{M}\cdot\mathbf{n}\right]_{\mathrm{L}}^{\mathrm{G}} \tag{2.55}$$

$$= \frac{\epsilon_{\mathrm{G}}\epsilon_0\phi_{\mathrm{d}}^2}{h_0 V\mu}M_{\mathrm{G}} - \frac{\epsilon_{\mathrm{L}}\epsilon_0\phi_{\mathrm{d}}^2}{h_0 V\mu}M_{\mathrm{L}} \tag{2.56}$$

$$= E_{\mathrm{b}}\left(M_{\mathrm{G}} - \epsilon_{\mathrm{R}}M_{\mathrm{L}}\right), \tag{2.57}$$

where

$$M_{\mathrm{L,G}} = \left[\frac{1}{2}\left(1 - \left(\frac{\partial h}{\partial x}\right)^2\right)\left(\left(\frac{\partial\phi}{\partial y}\right)^2 - \left(\frac{\partial\phi}{\partial x}\right)^2\right) - 2\frac{\partial h}{\partial x}\frac{\partial\phi}{\partial x}\frac{\partial\phi}{\partial y}\right]; \tag{2.58}$$

and the electrostatic contribution to the tangential stress is

$$E^{\mathrm{T}} = \frac{h_0}{V\mu}\left(1 + \left(\frac{\partial h}{\partial x}\right)^2\right)\left[\mathbf{t}\cdot\mathbf{M}\cdot\mathbf{n}\right]_{\mathrm{L}}^{\mathrm{G}} \tag{2.59}$$

$$= \frac{h_0}{V\mu}\left(\left[\epsilon\epsilon_0\,\mathbf{t}\cdot(\mathbf{E}\otimes\mathbf{E})\cdot\mathbf{n}\right]_{\mathrm{L}}^{\mathrm{G}} - \frac{1}{2}\left[\epsilon\epsilon_0\left|\mathbf{E}\right|^2\mathbf{t}\cdot\mathbf{n}\right]_{\mathrm{L}}^{\mathrm{G}}\right), \tag{2.60}$$

$$= -E_{\mathrm{b}}q\left(1 + \left(\frac{\partial h}{\partial x}\right)^2\right)^{\frac{1}{2}}\frac{\partial\phi|_{y=h}}{\partial x}, \tag{2.61}$$

where $\mathbf{E} = \mathbf{E}^{\mathrm{L}} = \mathbf{E}^{\mathrm{G}}$, $\phi = \phi^{\mathrm{L}} = \phi^{\mathrm{G}}$, and $\epsilon = \epsilon_{\mathrm{L}} = \epsilon_{\mathrm{G}}$ evaluated at $y = h(x,t)$, and we have used the fact that $\mathbf{t} \cdot \mathbf{n} = 0$ to remove the second term of (2.60) and have used Gauss' law (2.45) to obtain (2.61). The electrostatic stress terms (2.57) and (2.61) are then substituted into equations (2.21) and (2.22) for the normal and tangential stresses, respectively, to yield

$$2\left(\frac{\partial v}{\partial y} + \frac{\partial u}{\partial x}\left(\frac{\partial h}{\partial x}\right)^2 - \frac{\partial h}{\partial x}\left(\frac{\partial u}{\partial y} + \frac{\partial v}{\partial x}\right)\right) - \frac{1}{2}\left(1 - \frac{\partial h}{\partial x}^2\right)\left(\left(\frac{\partial \phi}{\partial y}\right)^2 - \left(\frac{\partial \phi}{\partial x}\right)^2\right) - 2\frac{\partial h}{\partial x}\frac{\partial \phi}{\partial x}\frac{\partial \phi}{\partial y} = \left[1 + \left(\frac{\partial h}{\partial x}\right)^2\right]\left(p - \frac{\kappa}{Ca}\right), \quad (2.62)$$

and

$$\left(1 - \left(\frac{\partial h}{\partial x}\right)^2\right)\left(\frac{\partial u}{\partial y} + \frac{\partial v}{\partial x}\right) + 2\frac{\partial h}{\partial x}\left(\frac{\partial v}{\partial y} - \frac{\partial u}{\partial x}\right) + E_{\mathrm{b}} q \left(1 + \left(\frac{\partial h}{\partial x}\right)^2\right)^{\frac{1}{2}} \frac{\partial \phi|_{y=h}}{\partial x} = 0. \quad (2.63)$$

The charge transport equation (2.48) in coordinate form becomes

$$\frac{\partial q}{\partial t}\left(1 + \left(\frac{\partial h}{\partial x}\right)^2\right) + \frac{\partial q}{\partial x}\left(u + v\frac{\partial h}{\partial x}\right) - q\left(\frac{\partial v}{\partial y} + \frac{\partial u}{\partial x}\left(\frac{\partial h}{\partial x}\right)^2 - \frac{\partial h}{\partial x}\left(\frac{\partial v}{\partial x} + \frac{\partial u}{\partial y}\right)\right) = \left(1 + \left(\frac{\partial h}{\partial x}\right)^2\right)^{1/2}\left[\Sigma_{\mathrm{L}}\left(\frac{\partial \phi^{\mathrm{L}}}{\partial y} - \frac{\partial h}{\partial x}\frac{\partial \phi^{\mathrm{L}}}{\partial x}\right) - \Sigma_{\mathrm{G}}\left(\frac{\partial \phi^{\mathrm{G}}}{\partial y} - \frac{\partial h}{\partial x}\frac{\partial \phi^{\mathrm{G}}}{\partial x}\right)\right]. \quad (2.64)$$

2.3.4 Long-wave (LW) approximation

The LW version of the model is derived by using the scalings (2.24) from Section 2.2.4. In addition, the following scalings are used (where the tilde variables are $O(1)$):

- Using the scalings (2.24), the electrostatic effects described in the normal and tangential stress conditions (2.21) and (2.22), respectively, are lost at

leading-order. To retain these effects, the scaling $E_\mathrm{b} = \widetilde{E_\mathrm{b}}/\epsilon$ is imposed.

- To keep the right hand side of the charge transport equation (2.64), i.e. the ion conduction terms, at leading-order, the scalings $\Sigma_\mathrm{L} = \epsilon^2\widetilde{\Sigma}_\mathrm{L}$ and $\Sigma_\mathrm{G} = \epsilon^2\widetilde{\Sigma}_\mathrm{G}$ are imposed.

In summary, the LW version of the model is derived by using the scalings (2.24) as well as the three additional scalings,

$$E_\mathrm{b} = \frac{1}{\epsilon}\widetilde{E_\mathrm{b}}, \qquad (\Sigma_\mathrm{L}, \Sigma_\mathrm{G}) = \epsilon^2\left(\widetilde{\Sigma}_\mathrm{L}, \widetilde{\Sigma}_\mathrm{G}\right). \tag{2.65}$$

2.3.4.a Leading-order equations

After introducing the scalings (2.24) and (2.65), and dropping the tildes immediately, the leading-order governing equations for the voltage potential in the liquid and gas, (2.49) and (2.50), respectively, are

$$\frac{\partial^2\phi^\mathrm{L}}{\partial y^2} = 0, \tag{2.66}$$

$$\frac{\partial^2\phi^\mathrm{G}}{\partial y^2} = 0. \tag{2.67}$$

Gauss' law (2.51) and the continuity of voltage potential (2.52) at leading order are

$$-q = \frac{\partial\phi^\mathrm{G}}{\partial y} - \epsilon_\mathrm{R}\frac{\partial\phi^\mathrm{L}}{\partial y}, \tag{2.68}$$

$$\phi^\mathrm{L} = \phi^\mathrm{G}, \tag{2.69}$$

respectively, evaluated at $y = h(x,t)$. Together with the boundary conditions at the lower and upper electrodes (2.53), equations (2.66) and (2.67) can be solved

to obtain the following expressions for ϕ^{L} and ϕ^{G},

$$\phi^{\mathrm{L}}(x,y,t) = \frac{((d-h)q+1)\,y}{\epsilon_{\mathrm{R}}(d-h)+h}, \qquad \phi^{\mathrm{G}}(x,y,t) = \frac{(\epsilon_{\mathrm{R}}-hq)(y-d)}{\epsilon_{\mathrm{R}}(d-h)+h} + 1. \tag{2.70}$$

The leading-order electrostatic contribution to the normal and tangential stresses, (2.57) and (2.61), respectively, are

$$E^{\mathrm{N}}_{\mathrm{LW}} = \frac{E_{\mathrm{b}}}{2}\left(\left(\frac{\partial\phi^{\mathrm{G}}}{\partial y}\right)^2 - \epsilon_{\mathrm{R}}\left(\frac{\partial\phi^{\mathrm{L}}}{\partial y}\right)^2\right), \tag{2.71}$$

$$E^{\mathrm{T}}_{\mathrm{LW}} = -E_{\mathrm{b}}q\frac{\partial\phi|_{y=h}}{\partial x}, \tag{2.72}$$

where $\phi = \phi^{\mathrm{L}} = \phi = \phi^{\mathrm{G}}$ evaluated at $y = h(x,t)$, and are then used in the governing equation for the interfacial height h (2.30). The expression for the pressure p (2.28) is

$$p = -\frac{\partial^2 h}{\partial x^2} - \frac{E_{\mathrm{b}}}{2}\left(\left(\frac{\partial\phi^{\mathrm{G}}}{\partial y}\right)^2 - \epsilon_{\mathrm{R}}\left(\frac{\partial\phi^{\mathrm{L}}}{\partial y}\right)^2\right). \tag{2.73}$$

The electrostatic terms (2.71) and (2.72) are used in the leading-order governing equation for the interfacial height h (2.30) to give

$$\frac{\partial h}{\partial t} - \frac{\partial}{\partial x}\left(\frac{h^3}{3}\frac{\partial p}{\partial x} + \frac{E_{\mathrm{b}}}{2}qh^2\frac{\partial\phi|_{y=h}}{\partial x}\right) = 0, \tag{2.74}$$

and the charge transport equation (2.64) at leading-order in ϵ becomes

$$\frac{\partial q}{\partial t} - \frac{\partial}{\partial x}\left(\frac{1}{2}qh^2\frac{\partial p}{\partial x} + E_{\mathrm{b}}q^2h\frac{\partial\phi|_{y=h}}{\partial x}\right) = \Sigma_{\mathrm{L}}\frac{\partial\phi^{\mathrm{L}}}{\partial y} - \Sigma_{\mathrm{G}}\frac{\partial\phi^{\mathrm{G}}}{\partial y}, \tag{2.75}$$

where expressions for the pressure p and the voltage potentials ϕ^{L} and ϕ^{G} are given by (2.73) and (2.70), respectively.

2.3.5 Recasting in canonical form

The following additional scalings are imposed:

$$x = \frac{1}{\Sigma_{\mathrm{G}}^{1/4}} x', \qquad t = \frac{1}{\Sigma_{\mathrm{G}}} t', \qquad E_{\mathrm{b}} = \Sigma_{\mathrm{G}}^{1/2} E_{\mathrm{b}}', \tag{2.76}$$

which reduces the number of dimensionless parameters by one. In particular, Σ_{L} and Σ_{G} are replaced with the new dimensionless parameter

$$\Sigma_{\mathrm{R}} = \frac{\Sigma_{\mathrm{L}}}{\Sigma_{\mathrm{G}}},$$

which is the ratio of the conductivities of the liquid and the gas. The right hand side of the charge transport equation (2.75) becomes an expression involving Σ_{R}, namely,

$$\frac{\partial q}{\partial t} - \frac{\partial}{\partial x}\left(\frac{1}{2} q h^2 \frac{\partial p}{\partial x} + E_{\mathrm{b}} q^2 h \frac{\partial \phi^{\mathrm{L,G}}|_{y=h}}{\partial x}\right) = \frac{\partial \phi^{\mathrm{G}}}{\partial y} - \Sigma_{\mathrm{R}} \frac{\partial \phi^{\mathrm{L}}}{\partial y}, \tag{2.77}$$

where the dashes are dropped immediately. The other equations in the LW model (2.70), (2.73), and (2.74) remain unchanged.

In Chapters 3 and 7, will use this version of the charge transport equation, i.e. equation (2.77) in place of (2.75), in which we will investigate $(\Sigma_{\mathrm{R}}, \epsilon_{\mathrm{R}})$ parameter space.

2.3.6 Typical parameter values

A bilayer of water or polymer (liquid) and air (gas) that are used in devices at the micro and nano scale for applications as discussed in Section 1.1. Hence, in

exploring these applications, we use the values [109, 110, 75, 146, 126]

$$\gamma = 0.03 \text{ N/m}, \quad \mu = 10 \text{ N s/m}^2, \quad \epsilon_0 = 8.85 \times 10^{-12} \text{ C}^2 \text{ s}^2 \text{ / kg m}^3, \quad h_0 = 1 \times 10^{-8} \text{ m},$$
$$\sigma_{\text{L}} = \left[10^{-13} - 10^{-9}\right] \text{ C}^2\text{s/(kg m}^2\text{)}, \quad \sigma_{\text{G}} = \left[10^{-15} - 10^{-9}\right] \text{ C}^2\text{s/(kg m}^2\text{)}. \tag{2.78}$$

The characteristic velocity $V = \gamma\epsilon^2/\mu$ is substituted into the non-dimensional conductivities (2.43), subject to (2.43) and (2.65), to give

$$\Sigma_{\text{L,G}} = \frac{\mu h_0 \sigma_{\text{L,G}}}{\gamma \epsilon_0 \epsilon_{\text{G}} \epsilon^4}. \tag{2.79}$$

and using (2.78) yields

$$\Sigma_{\text{L,G}} = \frac{1.88 \times 10^7}{\epsilon^4} \sigma_{\text{L,G}}. \tag{2.80}$$

The values for σ_{G} and σ_{L} were chosen to be

$$\sigma_{\text{G}} = 10^{-11} \text{ C}^2\text{s/(kg m}^2\text{)}, \quad \sigma_{\text{L}} = \left[10^{-11} - 1\right] \text{ C}^2\text{s/(kg m}^2\text{)}, \tag{2.81}$$

where the values inside the square brackets indicate a range of σ_{L} from 10^{-11} to 1, and using them in the conductivity ratio $\Sigma_{\text{R}} = \sigma_{\text{L}}/\sigma_{\text{G}}$ gives the range

$$\Sigma_{\text{R}} = \left[1 - 10^{11}\right] \text{ C}^2\text{s/(kg m}^2\text{)}. \tag{2.82}$$

Furthermore, the conductivities and permittivities of liquids are typically greater than those of gases [110, 75, 126], and so, throughout this thesis, we will investigate systems where $\Sigma_{\text{R}} \geq 1$ and $\epsilon_{\text{R}} \geq 1$.

Furthermore, we use (2.43) subject to (2.65) to give

$$E_{\mathrm{b}} = \left(\frac{\epsilon^2 \epsilon_{\mathrm{G}}^3 \epsilon_0^3}{\mu \gamma h_0^3 \sigma_{\mathrm{G}}} \right)^{1/2} . \tag{2.83}$$

Using (2.78) yields $E_{\mathrm{b}} = 15.2\epsilon$, and for values of $\epsilon = [0.1 - 0.5]$, we obtain

$$E_{\mathrm{b}} = [1.52 - 7.6] . \tag{2.84}$$

2.4 Electrostatic limiting cases

In many cases, models can be simplified by exploring approximations in particular regimes that are typical of what occurs physically. The limiting cases of these models allow for even greater analytical and numerical progress. In this Section, three commonly studied limiting cases of the LW model, given in Sections 2.2.4.a and 2.3.4.a, are now derived. Specifically, these are the perfectly conducting (PC) case, the highly-conducting (HC) case, and the perfectly dielectric (PD) case. These approximations all lead to useful simplifications of the LW model as it is reduced from two coupled governing equations for h and q to a single governing equation for the interfacial height h.

2.4.1 Perfectly conducting (PC) case

Many common liquids have a high conductivity (e.g. brine water [116] and ultrapure water [118]), and a commonly studied system is when the conductivity of the liquid is much greater than the conductivity of the overlying gas. For example, we choose the liquid to be ultrapure water which has conductivity $\sigma_{\mathrm{L}} = 5.5 \times 10^{-6}$ $\mathrm{C^2 s/(kg\ m^2)}$ [126], and the gas to be air with conductivity $\sigma_{\mathrm{G}} = 10^{-13}$ $\mathrm{C^2 s/(kg}$

m^2). Together with the parameter values (2.78), we obtain

$$\Sigma_{\mathrm{R}} = \frac{\sigma_{\mathrm{L}}}{\sigma_{\mathrm{G}}} = 5.5 \times 10^7. \tag{2.85}$$

Hence, we will explore the limit where the conductivity ratio of the liquid and gas is large, i.e. the limit $\Sigma_{\mathrm{R}} \to \infty$. Taking this limit yields a single governing equation for the interfacial height h and we will call this the perfectly conducting (PC) case.

2.4.1.a Derivation of the governing equation

In the limit $\Sigma_{\mathrm{R}} \to \infty$, the charge transport equation (2.77) simplifies to

$$\frac{\partial \phi^{\mathrm{L}}}{\partial y} = 0, \tag{2.86}$$

and, together with the governing equation for the voltage potential in the liquid (2.66) and the boundary condition at the lower electrode (2.53), the voltage potential in the liquid is $\phi^{\mathrm{L}} \equiv 0$. This means that everywhere in the liquid takes the value of the potential of the lower electrode.

The continuity of voltage potential at the interface (2.69) simplifies to $\phi^{\mathrm{G}}\big|_{y=h} = 0$, and, together with the voltage potential boundary condition at the upper electrode (2.53) and governing equation for the voltage potential (2.67), the voltage potential in the gas has the simple linear form,

$$\phi^{\mathrm{G}}(x, y, t) = \frac{y - h}{d - h}. \tag{2.87}$$

Using (2.86) and (2.87), the charge density q may now be explicitly determined from Gauss' law (2.68),

$$q = -\left.\frac{\partial \phi^{\mathrm{G}}}{\partial y}\right|_{y=h} = -\frac{1}{d - h}. \tag{2.88}$$

Owing to the continuity of voltage potential at the interface, i.e. $\phi^{\mathrm{G}}\big|_{y=h} = \phi^{\mathrm{L}}\big|_{y=h} = 0$, the tangential electric stress terms drop out of the governing equation for the interfacial height h (2.74), and, using (2.86), (2.87) and (2.88), the governing equation for h is reduced to

$$\frac{\partial h}{\partial t} + \frac{\partial}{\partial x}\left(\frac{h^3}{3}\left(\frac{\partial^3 h}{\partial x^3} + \frac{E_{\mathrm{b}}}{(d-h)^3}\frac{\partial h}{\partial x}\right)\right) = 0. \tag{2.89}$$

Equation (2.89) may be rendered into canonical form via the scalings

$$x = E_{\mathrm{b}}^{-1/2} x', \qquad t = E_{\mathrm{b}}^{-2} t', \tag{2.90}$$

where the non-dimensional parameter E_{b} is scaled out of (2.89). Hence, after dropping the dashes, the governing equation for h (2.89) is

$$\frac{\partial h}{\partial t} + \frac{\partial}{\partial x}\left(\frac{h^3}{3}\left(\frac{\partial^3 h}{\partial x^3} + \frac{1}{(d-h)^3}\frac{\partial h}{\partial x}\right)\right) = 0. \tag{2.91}$$

2.4.1.b Summary of PC case

As we have shown, in the PC case, the LW model consisting of two coupled nonlinear governing equations for h and q, (2.74) and (2.77), respectively, is simplified to one governing equation for h (2.91). We will perform both analytical and numerical investigations of equation (2.91) in Chapter 5. We are also interested in the parameter space of this system, which has two parameters, namely, d and the computational domain length L, which will be introduced in Chapter 4.

2.4.2 Highly conducting (HC) case

Another common problem [70, 111, 126] is when the non-dimensional conductivities of both the liquid and gas are large. For example, we choose the liquid to be water which has conductivity $\sigma_{\mathrm{L}} = 1 \times 10^{-2}$ C^{2}s/(kg m^2), and the gas to be air

with conductivity $\sigma_{\mathrm{G}} = 10^{-10}$ C^{2}s/(kg m^2) [146]. Together with the parameter values

$$\gamma = 0.03 \text{ N/m}, \quad \mu = 10 \text{ N s/m}^2, \quad \epsilon_0 = 8.85 \times 10^{-12} \text{ C}^2 \text{ s}^2 \text{ / kg m}^3, \\ h_0 = 10^{-3} \text{ m}, \quad \epsilon = 0.1, \tag{2.92}$$

we obtain

$$\Sigma_{\mathrm{L}} = 3.76 \times 10^{12}, \quad \Sigma_{\mathrm{G}} = 1 \times 10^{4}. \tag{2.93}$$

Hence, we will explore the limit where the conductivity of both the liquid and gas are large i.e. the limits $\Sigma_{\mathrm{L}} \to \infty$ and $\Sigma_{\mathrm{G}} \to \infty$, and will consequently call this the highly conducting (HC) case.

2.4.2.a Derivation of the governing equation

In the limit $\Sigma_{\mathrm{L,G}} \to \infty$ with $\Sigma_{\mathrm{L}} = O(\Sigma_{\mathrm{G}})$, the interfacial charge transport equation (2.75) simplifies to

$$\phi_y^{\mathrm{G}} = \Sigma_{\mathrm{R}} \phi_y^{\mathrm{L}}. \tag{2.94}$$

Using (2.94) together with the governing equations for the voltage potential, (2.66) and (2.67), the continuity of voltage potential at the interface (2.69), and the voltage potential boundary conditions at the lower and upper electrodes (2.53), solutions for ϕ^{L} and ϕ^{G} are obtained,

$$\phi^{\mathrm{L}}(x,y,t) = \frac{y}{\Sigma_{\mathrm{R}}(d-h)+h}, \qquad \phi^{\mathrm{G}}(x,y,t) = \frac{\Sigma_{\mathrm{R}}(y-h)+h}{\Sigma_{\mathrm{R}}(d-h)+h}. \tag{2.95}$$

Using (2.95), the charge density q may now be explicitly determined from Gauss' law (2.68),

$$q = \frac{\epsilon_{\mathrm{R}} - \Sigma_{\mathrm{R}}}{\Sigma_{\mathrm{R}}(d-h)+h}. \tag{2.96}$$

The expressions (2.95) and (2.96) are used in the governing equation for h (2.74) to yield

$$\frac{\partial h}{\partial t} = -\frac{\partial}{\partial x}\left[\frac{h^3}{3}\left(\frac{\partial^3 h}{\partial x^3} + \frac{E_{\mathrm{b}}(\Sigma_{\mathrm{R}}-1)(\Sigma_{\mathrm{R}}^2-\epsilon_{\mathrm{R}})}{(\Sigma_{\mathrm{R}}(d-h)+h)^3}\frac{\partial h}{\partial x}\right) + \frac{h^2}{2}\frac{E_{\mathrm{b}} d(\Sigma_{\mathrm{R}}-\epsilon_{\mathrm{R}})\Sigma_{\mathrm{R}}}{(\Sigma_{\mathrm{R}}(d-h)+h)^3}\frac{\partial h}{\partial x}\right]. \tag{2.97}$$

Equation (2.97) may be rendered into canonical form via the scalings

$$x = E_{\mathrm{b}}^{-1/2} x', \qquad t = E_{\mathrm{b}}^{-2} t', \tag{2.98}$$

where the non-dimensional parameter E_{b} is scaled out of (2.97). Hence, after dropping the dashes, the governing equation for h (2.97) becomes

$$\frac{\partial h}{\partial t} = -\frac{\partial}{\partial x}\left[\frac{h^3}{3}\left(\frac{\partial^3 h}{\partial x^3} + \frac{(\Sigma_{\mathrm{R}}-1)(\Sigma_{\mathrm{R}}^2-\epsilon_{\mathrm{R}})}{(\Sigma_{\mathrm{R}}(d-h)+h)^3}\frac{\partial h}{\partial x}\right) + \frac{h^2}{2}\frac{d(\Sigma_{\mathrm{R}}-\epsilon_{\mathrm{R}})\Sigma_{\mathrm{R}}}{(\Sigma_{\mathrm{R}}(d-h)+h)^3}\frac{\partial h}{\partial x}\right]. \tag{2.99}$$

Note that, by taking the limit $\Sigma_{\mathrm{R}} \to \infty$, the governing equation (2.99) simplifies to that of the PC model (2.91), as expected.

2.4.2.b Summary of the HC case

As we have shown, in the HC case, the LW model consisting of two coupled non-linear governing equations for h and q, (2.74) and (2.75), respectively, is simplified to one governing equation for h (2.99). We will perform both analytical and numerical investigations to equation (2.99) in Chapter 6. We are also interested in the parameter space of this system, which has four parameters, namely, d, Σ_{R},

ϵ_{R}, and L.

2.4.3 Perfectly dielectric (PD) case

Another commonly studied problem [37, 109] is when both the liquid and gas are perfect dielectrics (perfect insulators). For example, we choose the liquid to be water with conductivity $\sigma_{\mathrm{L}} = 1 \times 10^{-11}$ $\mathrm{C^2 s/(kg\ m^2)}$, and the gas to be air with conductivity $\sigma_{\mathrm{G}} = 10^{-13}$ $\mathrm{C^2 s/(kg\ m^2)}$ [118, 146]. Together with the parameter values

$$\begin{aligned} &\gamma = 0.03 \text{ N/m}, \quad \mu = 10 \text{ N s/m}^2, \quad \epsilon_0 = 8.85 \times 10^{-12} \text{ C}^2 \text{ s}^2 \text{ / kg m}^3, \\ &h_0 = 0.5 \times 10^{-6} \text{ m}, \quad \epsilon = 0.5, \end{aligned} \tag{2.100}$$

we obtain

$$\Sigma_{\mathrm{L}} = 3 \times 10^{-3}, \quad \Sigma_{\mathrm{G}} = 3 \times 10^{-5}. \tag{2.101}$$

Hence, we will explore the case when the conductivities of the liquid and gas are zero, i.e. $\Sigma_{\mathrm{L,G}} = 0$, and call this the perfectly dielectric (PD) limiting case.

2.4.3.a Governing equation/system

In the PD limiting case, $\Sigma_{\mathrm{L,G}} = 0$ and it is assumed that, as well as no charge in the bulk, there is no charge on the interface, i.e. $q \equiv 0$. Hence the interfacial charge transport equation (2.75) is automatically satisfied.

Since $q \equiv 0$, Gauss' law (2.68) becomes a statement of the continuity of current across the interface,

$$\phi_y^{\mathrm{G}} = \epsilon_{\mathrm{R}} \phi_y^{\mathrm{L}}, \tag{2.102}$$

and together with the governing equations for the voltage potential, (2.66) and (2.67), its boundary conditions at the upper and lower electrodes (2.53), and the continuity of voltage potential across the interface (2.69), the expressions for ϕ^{L} and ϕ^{G} are obtained,

$$\phi^{\mathrm{L}}(x,y,t) = \frac{y}{h-\epsilon_{\mathrm{R}}}, \qquad \phi^{\mathrm{G}}(x,y,t) = \frac{\epsilon_{\mathrm{R}}(y-d)}{(h-\epsilon_{\mathrm{R}})(h-d)} + 1. \tag{2.103}$$

The absence of charge on the interface means that the tangential electric stress terms drop out of the governing equation for the interfacial height h (2.74), and the expressions for the potentials in the liquid and gas (2.103) are used in (2.74) to give

$$\frac{\partial h}{\partial t} + \frac{\partial}{\partial x}\left(\frac{h^3}{3}\left(\frac{\partial^3 h}{\partial x^3} + \frac{E_{\mathrm{b}}\epsilon_{\mathrm{R}}(\epsilon_{\mathrm{R}}-1)^2}{(\epsilon_{\mathrm{R}}(d-h)+h)^3}\frac{\partial h}{\partial x}\right)\right) = 0. \tag{2.104}$$

Equation (2.104) may be rendered into canonical form via the scalings

$$x = E_{\mathrm{b}}^{-1/2}x', \qquad t = E_{\mathrm{b}}^{-2}t', \tag{2.105}$$

where the non-dimensional parameter E_{b} is scaled out of (2.97). Hence, after dropping the dashes, the governing equation for h (2.104) becomes,

$$\frac{\partial h}{\partial t} + \frac{\partial}{\partial x}\left(\frac{h^3}{3}\left(\frac{\partial^3 h}{\partial x^3} + \frac{\epsilon_{\mathrm{R}}(\epsilon_{\mathrm{R}}-1)^2}{(\epsilon_{\mathrm{R}}(d-h)+h)^3}\frac{\partial h}{\partial x}\right)\right) = 0. \tag{2.106}$$

2.4.3.b Summary of the PD case

As we have shown, in the HC case, the LW model consisting of two coupled nonlinear governing equations for h and q, (2.74) and (2.75), respectively, is simplified to one governing equation for h (2.106). Specifically, these parameters are d, ϵ_{R} and L. We will not explore this limiting case further, firstly, due to time constraints and secondly, the PD case is mathematically similar to both PC and

HC limiting cases (there is no tangential component to the governing equation, like the PC case, but there is no singularity at $y = h$, like the HC case), and so we believe the PD model will exhibit the similar qualitative behaviours to the PC and HC models. Hence, we concentrate our attention on the PC and HC limiting cases.

2.5 Summary

In this Chapter, we have introduced and described the system under investigation in Section 2.1, as illustrated by Figure 2.1. Specifically, we formulated a SF model described in Sections 2.2.3 and 2.3.3. A LW approximation was then performed, which provides a useful simplification by reducing the system from two dimensions (x, y) to one dimension x, which is described by two coupled nonlinear equations for h and q, specifically,

$$\frac{\partial h}{\partial t} - \frac{\partial}{\partial x}\left(\frac{h^3}{3}\frac{\partial p}{\partial x} + \frac{E_\mathrm{b}}{2}qh^2\frac{\partial \phi^{\mathrm{L,G}}|_{y=h}}{\partial x}\right) = 0 \tag{2.107}$$

$$\frac{\partial q}{\partial t} - \frac{\partial}{\partial x}\left(\frac{1}{2}qh^2\frac{\partial p}{\partial x} + E_\mathrm{b}q^2h\frac{\partial \phi^{\mathrm{L,G}}|_{y=h}}{\partial x}\right) = \Sigma_\mathrm{L}\frac{\partial \phi^\mathrm{L}}{\partial y} - \Sigma_\mathrm{G}\frac{\partial \phi^\mathrm{G}}{\partial y}, \tag{2.108}$$

where

$$p = -\frac{\partial^2 h}{\partial x^2} - \frac{E_\mathrm{b}}{2}\left(\left(\frac{\partial \phi^\mathrm{G}}{\partial y}\right)^2 - \epsilon_\mathrm{R}\left(\frac{\partial \phi^\mathrm{L}}{\partial y}\right)^2\right), \tag{2.109}$$

and ϕ^L and ϕ^G are given by

$$\phi^\mathrm{L}(x, y, t) = \left(\frac{(d-h)q + 1}{\epsilon_\mathrm{R}(d-h) + h}\right)y, \tag{2.110}$$

$$\phi^\mathrm{G}(x, y, t) = \frac{(\epsilon_\mathrm{R} - hq)(y-d)}{\epsilon_\mathrm{R}(d-h) + h} + 1. \tag{2.111}$$

Furthermore, we imposed the additional scalings (2.76), where the parameters Σ_{L} and Σ_{G} are replaced by Σ_{R}, thereby reducing the number of parameters in the system by one. Hence, the system (2.107)-(2.111) remains unaltered other than the charge transport equation (2.108) which becomes

$$\frac{\partial q}{\partial t} - \frac{\partial}{\partial x}\left(\frac{1}{2}qh^2\frac{\partial p}{\partial x} + E_{\mathrm{b}}q^2h\frac{\partial \phi^{\mathrm{L,G}}|_{y=h}}{\partial x}\right) = \frac{\partial \phi^{\mathrm{G}}}{\partial y} - \Sigma_{\mathrm{R}}\frac{\partial \phi^{\mathrm{L}}}{\partial y}. \tag{2.112}$$

In Chapters 3 and 7, we will use the charge transport equation (2.112). Lastly, we looked at limiting cases of the LW model, and derived the PC, HC, and PD models. The PC and HC models contain single governing equations for h, that is, equations (2.91) and (2.99), respectively. We also derived the PD model which contains a single governing equation for h (2.106). However, due to time constraints and that equation (2.106) is mathematically similar to equations (2.91) and (2.99), we will not explore the PD model further. We will investigate the PC and HC models further in Chapters 5 and 6, respectively.

Chapter 3

Linear stability analysis

Performing a linear stability analysis involves perturbing the system variables around a steady configuration, i.e. a base state, to determine whether it is stable or not. This allows us to obtain the growth rate of the system in which we can determine the relative importance of different physical mechanisms and obtain an insight into the mechanisms stabilising and destabilising the flow. In Section 3.1, a simple uniform base state will be formulated, and in Section 3.2, a linear stability analysis of the SF model will be performed in which the results of this analysis are exact for this system. In Sections 3.3, 3.5, and 3.7, a linear stability analysis of the LW, PC, and HC models, respectively, will be performed, and in Sections 3.4, 3.6, and 3.8, the linear stability results of the LW, HC, and PC models, respectively, will be compared with the linear stability results of the SF model for a range of parameter values. This allows us to compare the agreement in the appropriate parts of parameter space which can be used towards validating the LW, HC, and PC models.

3.1 Base state

The SF model admits a base state with a flat interface and no flow, given by $\overline{h} = 1$ and $\overline{u} = \overline{v} = 0$, where the bars denote base state quantities.

The governing equations for ϕ^{L} and ϕ^{G},

$$\frac{\partial^2 \phi^{\mathrm{L}}}{\partial x^2} + \frac{\partial^2 \phi^{\mathrm{L}}}{\partial y^2} = 0, \qquad \frac{\partial^2 \phi^{\mathrm{G}}}{\partial x^2} + \frac{\partial^2 \phi^{\mathrm{G}}}{\partial y^2} = 0,$$

were solved subject to the voltage potential boundary conditions at the electrodes (2.53), the charge transport equation (2.64), and the continuity of voltage potential across the interface (2.69), to give base state solutions for the voltage potential in the liquid and gas, $\overline{\phi}^{\mathrm{L}} = \overline{\phi}^{\mathrm{L}}(y)$ and $\overline{\phi}^{\mathrm{G}} = \overline{\phi}^{\mathrm{G}}(y)$, respectively, namely,

$$\overline{\phi}^{\mathrm{L}} = \frac{y}{\Sigma_{\mathrm{R}}(d-1)+1}, \qquad \overline{\phi}^{\mathrm{G}} = \frac{\Sigma_{\mathrm{R}}(y-1)+1}{\Sigma_{\mathrm{R}}(d-1)+1}, \tag{3.1}$$

which are both simple linear functions of y. These base state quantities were used in Gauss' law (2.51) to find the constant base state solution for the interfacial charge density $\overline{q}$, namely,

$$\overline{q} = \frac{\epsilon_{\mathrm{R}} - \Sigma_{\mathrm{R}}}{\Sigma_{\mathrm{R}}(d-1)+1}, \tag{3.2}$$

and the above base state quantities were used in the normal stress condition (2.62) to find the constant base state solution for the pressure $\overline{p}$, namely,

$$\overline{p} = \frac{E_{\mathrm{b}}\left(\epsilon_{\mathrm{R}} - \Sigma_{\mathrm{R}}^2\right)}{2\left(\Sigma_{\mathrm{R}}(d-1)+1\right)^2}. \tag{3.3}$$

Furthermore, the stream function $\psi(x, y, t)$ was introduced such that the stream function to the base state $\overline{\psi}$ gives

$$\overline{u} = \frac{\partial \overline{\psi}}{\partial y} = 0, \qquad \overline{v} = -\frac{\partial \overline{\psi}}{\partial x} = 0, \tag{3.4}$$

which satisfies the continuity equation (2.19), and this yields

$$\overline{\psi} = C_{\mathrm{S}}, \tag{3.5}$$

where C_{S} is an irrelevant constant that we set to zero without loss of generality. The base state described above will be used to perform the linear stability calculations throughout Chapter 3.

3.2 Stokes flow (SF) model

A linear stability analysis of the SF model was performed by perturbing around the base state according to

$$(h, q, u, v, \phi^{\mathrm{L}}, \phi^{\mathrm{G}}, p) = \left(1, \overline{q}, 0, 0, \overline{\phi}^{\mathrm{L}}, \overline{\phi}^{\mathrm{G}}, \overline{p}\right) + \delta\left[\left(\widetilde{h}, \widetilde{q}, \widetilde{u}, \widetilde{v}, \widetilde{\phi}^{\mathrm{L}}, \widetilde{\phi}^{\mathrm{G}}, \widetilde{p}\right) \mathrm{e}^{st+ikx} + \mathrm{c.c.}\right], \tag{3.6}$$

where $\delta \ll 1$ is the linearisation parameter, the tilde variables are the amplitudes of the perturbation of the different variables, s is the (complex) growth rate, c.c. denotes the complex conjugate, and k is the (real) wavenumber of the perturbation. Also, note that

$$\left(\widetilde{u}, \widetilde{v}, \widetilde{\phi}^{\mathrm{L}}, \widetilde{\phi}^{\mathrm{G}}, \widetilde{p}\right) = \left(\widetilde{u}(y), \widetilde{v}(y), \widetilde{\phi}^{\mathrm{L}}(y), \widetilde{\phi}^{\mathrm{G}}(y), \widetilde{p}(y)\right).$$

The perturbation of the stream function $\widetilde{\psi} = \widetilde{\psi}(y)$ was introduced such that

$$\psi = \overline{\psi} + \delta\widetilde{\psi}\mathrm{e}^{st+ikx}, \tag{3.7}$$

and

$$\widetilde{u} = \frac{\partial\widetilde{\psi}}{\partial y}, \qquad \widetilde{v} = -ik\widetilde{\psi}, \tag{3.8}$$

and so ψ satisfies the continuity equation (2.19).

The perturbations (3.6) were substituted into the Stokes equations, (2.17) and

(2.18), and equations were linearised to give

$$0 = -ik\widetilde{p} - k^2\widetilde{u} + \frac{\partial^2\widetilde{u}}{\partial y^2}, \tag{3.9}$$

$$0 = -\frac{\partial\widetilde{p}}{\partial y} - k^2\widetilde{v} + \frac{\partial^2\widetilde{v}}{\partial y^2}. \tag{3.10}$$

Equations (3.9) and (3.10) were differentiated with respect to y and multiplied by ik, respectively, and the expressions (3.8) were used to obtain expressions in terms of $\widetilde{\psi}$, namely,

$$0 = -ik\frac{\partial\widetilde{p}}{\partial y} - k^2\frac{\partial^2\widetilde{\psi}}{\partial y^2} + \frac{\partial^4\widetilde{\psi}}{\partial y^4}, \tag{3.11}$$

$$0 = -ik\frac{\partial\widetilde{p}}{\partial y} - k^4\widetilde{\psi} + ik\frac{\partial^2\widetilde{\psi}}{\partial y^2}. \tag{3.12}$$

Subsequently, to remove the $\widetilde{p}$ term, equation (3.12) was subtracted from equation (3.11), giving

$$0 = \frac{\partial^4\psi}{\partial y^4} - 2k^2\frac{\partial^2\psi}{\partial y^2} + k^4\psi, \tag{3.13}$$

and this was solved for $\widetilde{\psi}$ to give

$$\widetilde{\psi} = (C_1 + C_2y)\mathrm{e}^{ky} + (C_3 + C_4y)\mathrm{e}^{-ky}, \tag{3.14}$$

where the C_i $(i = 1, 2, 3, 4)$ are constants of integration. Hence, using (3.8), expressions for $\widetilde{u}$ and $\widetilde{v}$ in terms of $\widetilde{\psi}$ were found, namely,

$$\widetilde{u} = k\left[(C_1 + C_2y)\,\mathrm{e}^{ky} - (C_3 + C_4y)\,\mathrm{e}^{-ky}\right], \tag{3.15}$$

$$\widetilde{v} = -ik\left[(C_1 + C_2y)\mathrm{e}^{ky} + (C_3 + C_4y)\mathrm{e}^{-ky}\right]. \tag{3.16}$$

The Stokes equation (3.9) was multiplied by $-i/k$ and rearranged to obtain an expression for $\widetilde{p}$, namely,

$$\widetilde{p} = \frac{i}{k}\left(k^2\widetilde{u} - \frac{\partial^2\widetilde{u}}{\partial y^2}\right), \tag{3.17}$$

where $\widetilde{u}$ is given by (3.15), and for consistency, (3.17) also satisfies equation (3.11).

Furthermore, the perturbations were substituted into the governing equations for ϕ^{L} and ϕ^{G}, (2.49) and (2.50), respectively, and linearised to give

$$\frac{\partial^2\widetilde{\phi}^{\mathrm{L}}}{\partial y^2} - k^2\widetilde{\phi}^{\mathrm{L}} = 0, \tag{3.18}$$

$$\frac{\partial^2\widetilde{\phi}^{\mathrm{G}}}{\partial y^2} - k^2\widetilde{\phi}^{\mathrm{G}} = 0, \tag{3.19}$$

and these equations were solved for $\widetilde{\phi}^{\mathrm{L}}$ and $\widetilde{\phi}^{\mathrm{G}}$ to yield

$$\widetilde{\phi}^{\mathrm{L}} = C_{\mathrm{L}}\mathrm{e}^{-ky} + D_{\mathrm{L}}\mathrm{e}^{ky}, \tag{3.20}$$

$$\widetilde{\phi}^{\mathrm{G}} = C_{\mathrm{G}}\mathrm{e}^{-ky} + D_{\mathrm{G}}\mathrm{e}^{ky}, \tag{3.21}$$

where C_i, D_i $(i = \mathrm{L}, \mathrm{G})$ are additional constants of integration.

Using the expressions for $\widetilde{\phi}^{\mathrm{L}}$ and $\widetilde{\phi}^{\mathrm{G}}$, given by (3.20) and (3.21), respectively, the linearised form of Gauss' law (2.51) yields an expression for $\widetilde{q}$, namely,

$$\widetilde{q} = \left[C_{\mathrm{G}}\mathrm{e}^{-k} - D_{\mathrm{G}}\mathrm{e}^{k} + \epsilon_{\mathrm{R}}\left(-C_{\mathrm{L}}\mathrm{e}^{-k} + D_{\mathrm{L}}\mathrm{e}^{k}\right)\right]k. \tag{3.22}$$

We also obtained the linearised form of the boundary conditions at the electrodes, (2.20) and (2.53), namely,

$$\widetilde{u} = \widetilde{v} = 0, \tag{3.23}$$

$$\widetilde{\phi}^{\mathrm{L}} = \widetilde{\phi}^{\mathrm{G}} = 0, \tag{3.24}$$

evaluated at $y = 1$, where $\widetilde{u}$, $\widetilde{v}$, $\widetilde{\phi}^{\mathrm{L}}$, and $\widetilde{\phi}^{\mathrm{G}}$ are given by (3.15), (3.16), (3.20), and (3.21), respectively.

Furthermore, the linearised form of the normal stress (2.62), tangential stress (2.63), the kinematic condition (2.23), the continuity of voltage potential (2.52), and the charge transport equation (2.64) were obtained, namely,

$$0 = 2\frac{\partial \widetilde{v}}{\partial y} - E_{\mathrm{b}}\left(\frac{\partial \overline{\phi}^{\mathrm{G}}}{\partial y}\frac{\partial \widetilde{\phi}^{\mathrm{G}}}{\partial y} - \epsilon_{\mathrm{R}}\frac{\partial \overline{\phi}^{\mathrm{L}}}{\partial y}\frac{\partial \widetilde{\phi}^{\mathrm{L}}}{\partial y}\right) + \frac{i}{k}\left(\frac{\partial^2 \widetilde{u}}{\partial y^2} - k^2\widetilde{u}\right) + k^2\widetilde{h}, \tag{3.25}$$

$$0 = \frac{\partial \widetilde{u}}{\partial y} + ik\widetilde{v} + iE_{\mathrm{b}}k\overline{q}\left(\widetilde{h}\frac{\partial \overline{\phi}}{\partial y} + \widetilde{\phi}\right), \tag{3.26}$$

$$0 = s\widetilde{h} - \widetilde{v}, \tag{3.27}$$

$$0 = \widetilde{\phi}^{\mathrm{L}} + \widetilde{h}\frac{\partial \overline{\phi}^{\mathrm{L}}}{\partial y} - \widetilde{\phi}^{\mathrm{G}} - \widetilde{h}\frac{\partial \overline{\phi}^{\mathrm{G}}}{\partial y}, \tag{3.28}$$

$$0 = s\widetilde{q} - \overline{q}\frac{\partial \widetilde{v}}{\partial y} - \Sigma_{\mathrm{G}}\frac{\partial \widetilde{\phi}^{\mathrm{G}}}{\partial y} + \Sigma_{\mathrm{L}}\frac{\partial \widetilde{\phi}^{\mathrm{L}}}{\partial y}, \tag{3.29}$$

evaluated at $y = 1$, where $\phi = \phi^{\mathrm{G}} = \phi^{\mathrm{L}}$, the expression (3.17) for $\widetilde{p}$ was used in the normal stress condition, and $\widetilde{u}$, $\widetilde{v}$, $\widetilde{\phi}^{\mathrm{L}}$, $\widetilde{\phi}^{\mathrm{G}}$ and $\widetilde{q}$ are given by (3.15), (3.16), (3.20), (3.21) and (3.22) respectively.

The boundary conditions and interfacial conditions (3.23)–(3.29) were expressed as the matrix equation $A\mathbf{x} = \mathbf{0}$, where $\mathbf{x} = \left(\widetilde{h}, C_1, C_2, C_3, C_4, C_{\mathrm{L}}, C_{\mathrm{G}}, D_{\mathrm{L}}, D_{\mathrm{G}}\right)^{\mathrm{T}}$ is the vector of unknowns and A is the 9×9 stability matrix. The elements of the stability matrix A are given in Appendix A. To obtain a non-trivial solution

to this problem, we set $\det(A)= 0$ and obtained the dispersion relation for the growth rate s in terms of the wavenumber k and the other parameters in the problem, namely, E_b, Σ_G, Σ_L, ϵ_R, and d.

The dispersion relation is a quadratic equation that has two roots, $s = s_1$ and $s = s_2$, which arise from the two governing equations for h and q, (2.29) and (2.64), respectively, and correspond to different modes of behaviour. The general expressions for s_1^{SF} and s_2^{SF} are rather complicated, so we obtained their small-k expansions, namely,

$$s_1^{\mathrm{SF}} = \frac{E_\mathrm{b}\Sigma_\mathrm{G}(\Sigma_\mathrm{R} - \epsilon_\mathrm{R})\left(\mathscr{N}_1^{\mathrm{SF}} + \mathscr{T}_1^{\mathrm{SF}}\right)}{6\left(\Sigma_\mathrm{R}(d-1)+1\right)^3}k^2 + O(k^4) \tag{3.30}$$

as $k \to 0$, where

$$\mathscr{N}_1^{\mathrm{SF}} = 2(\Sigma_\mathrm{R}^2 - \epsilon_\mathrm{R}), \qquad \mathscr{T}_1^{\mathrm{SF}} = 3\Sigma_\mathrm{R} d,$$

and

$$s_2^{\mathrm{SF}} = -\frac{\Sigma_\mathrm{G}\left(\Sigma_\mathrm{R}(d-1)+1\right)}{\epsilon_\mathrm{R}(d-1)+1} + O(k^2) \tag{3.31}$$

as $k \to 0$. Here, $\mathscr{N}_1^{\mathrm{SF}}$ and $\mathscr{T}_1^{\mathrm{SF}}$ are the normal and tangential contributions of the electrical stress, respectively. At leading-order in the small-k limit, the sign of the s_1^{SF} term (and so the stability of the flow) is dependent on the groupings $\Sigma_\mathrm{R} - \epsilon_\mathrm{R}$ and $\Sigma_\mathrm{R}^2 - \epsilon_\mathrm{R}$. The leading-order term for s_2^{SF} is always negative. Furthermore, when $E_\mathrm{b} = 0$, i.e. there is no electric field, s_1^{SF} is always negative as capillarity is now the only force present in the system and it is stabilising in a planar geometry. These small-k expansions will be used, along with plots of s_1^{SF} and s_2^{SF} as functions of k and other parameters, to compare the linear stability predictions of the SF model with those of the LW, HC and PC models.

3.3 Long-wave (LW) model

A linear stability analysis of the LW mode (derived in Sections 2.2.4.a and 2.3.4.a) was performed by perturbing the interfacial height h and charge density q around the uniform base state according to

$$(h, q) = (1, \overline{q}) + \delta \left[\left(\widetilde{h}, \widetilde{q} \right) \mathrm{e}^{st+ikx} + \text{c.c.} \right], \tag{3.32}$$

where $\overline{q}$ is the base state quantity for q given by (3.2).

These perturbations were substituted into the governing equation h (2.107) and q (2.112), which were then linearised. The resulting system is expressed as the matrix equation $B\mathbf{x} = 0$, where B is the 2×2 stability matrix whose elements are given in Appendix B, and $\mathbf{x} = \left(\widetilde{h}, \widetilde{q} \right)^{\mathrm{T}}$. As before, we set $\det(B) = 0$ and solved it to obtain the dispersion relation describing the growth rate s in terms of the wavenumber k and the other parameters in the problem, namely, E_{b}, d, Σ_{R}, and ϵ_{R}.

The dispersion relation is a quadratic equation that has two roots, $s = s_1^{\mathrm{LW}}$ and $s = s_2^{\mathrm{LW}}$, which arise from the two evolution equations for h and q, (2.107) and (2.112), respectively, and correspond to different modes of behaviour. As was the case for the SF model, the general expressions for s_1^{LW} and s_2^{LW} are rather complicated, so we obtained their small-k expansions to elucidate behaviour in this limit, namely,

$$s_1^{\mathrm{LW}} = \frac{E_{\mathrm{b}}(\Sigma_{\mathrm{R}} - \epsilon_{\mathrm{R}}) \left(\mathscr{N}_1^{\mathrm{LW}} + \mathscr{T}_1^{\mathrm{LW}} \right)}{6 \left(\Sigma_{\mathrm{R}}(d-1) + 1 \right)^3} k^2 + O(k^4) \tag{3.33}$$

as $k \to 0$, where

$$\mathscr{N}_1^{\mathrm{LW}} = 2(\Sigma_{\mathrm{R}}^2 - \epsilon_{\mathrm{R}}), \qquad \mathscr{T}_1^{\mathrm{LW}} = 3\Sigma_{\mathrm{R}} d,$$

and

$$s_2^{\mathrm{LW}} = -\frac{\Sigma_{\mathrm{R}}(d-1)+1}{\epsilon_{\mathrm{R}}(d-1)+1} + \frac{E_{\mathrm{b}}(\Sigma_{\mathrm{R}}-\epsilon_{\mathrm{R}})\left(\mathscr{N}_2^{\mathrm{LW}}+\mathscr{T}_2^{\mathrm{LW}}\right)}{6\left(\Sigma_{\mathrm{R}}(d-1)+1\right)^3\left(\epsilon_{\mathrm{R}}(d-1)+1\right)}k^2 + O(k^4) \quad (3.34)$$

as $k \to 0$, where

$$\mathscr{N}_2^{\mathrm{LW}} = (\Sigma_{\mathrm{R}} + \epsilon_{\mathrm{R}}(d-1))(\Sigma_{\mathrm{R}}(3d-5)+5),$$
$$\mathscr{T}_2^{\mathrm{LW}} = (d-1)(\Sigma_{\mathrm{R}} - \epsilon_{\mathrm{R}})(\Sigma_{\mathrm{R}}(2d-3)+3).$$

Here, $\mathscr{N}_1^{\mathrm{LW}}$ and $\mathscr{N}_2^{\mathrm{LW}}$, and $\mathscr{T}_1^{\mathrm{LW}}$ and $\mathscr{T}_2^{\mathrm{LW}}$ are the normal and tangential contributions of the electrical stress, respectively. Specifically, (3.33) and (3.34) show that, at leading-order in the small-k limit, the sign of s_1^{LW} depends on the groupings $\Sigma_{\mathrm{R}} - \epsilon_{\mathrm{R}}$ and $\Sigma_{\mathrm{R}}^2 - \epsilon_{\mathrm{R}}$, whereas the leading-order term for s_2^{LW} is always $O(1)$ and negative, and hence this mode is always linearly stable at leading order. Additionally, as in the SF case, s_2^{LW} is most unstable at $k = 0$ where it is neutrally stable. Therefore, this small-k limit suggests that s_1^{LW} is the most unstable mode and that the values of Σ_{R} and ϵ_{R} are crucial to determining the linear stability of the system. As in the SF case, when $E_{\mathrm{b}} = 0$, s_1^{LW} is negative as capillarity is the only force present in the system which is stabilising.

Furthermore, we performed a large-k expansion of s_1^{LW} and s_2^{LW}. Even though this is the short-wave limit of the LW model, it is useful to show that the LW model is stable to short-wave perturbations, i.e. short waves decay. The large-k expansions are

$$s_1^{\mathrm{LW}} = -\frac{1}{3}k^4 + O\left(k^2\right) \quad (3.35)$$

as $k \to \infty$, and

$$s_2^{\mathrm{LW}} = -\frac{E_{\mathrm{b}}\left(d-1\right)\left(\Sigma_{\mathrm{R}}-\epsilon_{\mathrm{R}}\right)^2}{4\left(\epsilon_{\mathrm{R}}\left(d-1\right)+1\right)\left(\Sigma_{\mathrm{R}}\left(d-1\right)+1\right)^2}k^2 + O\left(1\right) \quad (3.36)$$

as $k \to \infty$. For $E_\mathrm{b} > 0$, $d > 1$, $\Sigma_\mathrm{R} > 0$, and $\epsilon_\mathrm{R} > 0$, the leading order terms for both s_1^{LW} and s_2^{LW} are always negative, which suggests that the LW model is always stable to short-wave perturbations. Also, the stabilising effect of capillary forces is characterised by the negative leading-order term of the unstable mode s_1 given by (3.35).

3.4 Comparison of the linear stability results of the LW model with the SF model

The linear stability results of the LW model given above were compared with the corresponding results of the SF model. Firstly, the small-k expansions of the growth rates were compared. Using the scalings (2.24) and (2.65), we obtained the following relationship for the growth rates and wavenumbers between the SF and LW models,

$$s^{\mathrm{SF}} = \Sigma_\mathrm{G} s^{\mathrm{LW}}, \qquad k^{\mathrm{SF}} = \Sigma_\mathrm{G}^{1/4} k^{\mathrm{LW}}, \tag{3.37}$$

where the SF and LW subscripts denote variables in the SF and LW models, respectively, and Σ_G is defined by (2.43). Using (3.37), we found that the small-k expansions of the growth rates in the SF and LW models are the same at leading-order which we expected as long wavelengths correspond to small wavenumbers, i.e. $\lambda \gg 1$ corresponds to $k \ll 1$. Furthermore, we compared the growth rates s as a function of the wavenumber k according to the SF and LW models using a range of system parameters. Figure 3.1 shows plots of the two modes of s as a function of k for the SF model (solid line) and the LW model (dashed line). Figure 3.1 shows that the agreement between the linear stability predictions of the SF and LW models improves as $k \to 0$, and the curves show good qualitative agreement for $k < 1$. Additionally, when d becomes large, we expect the agreement between

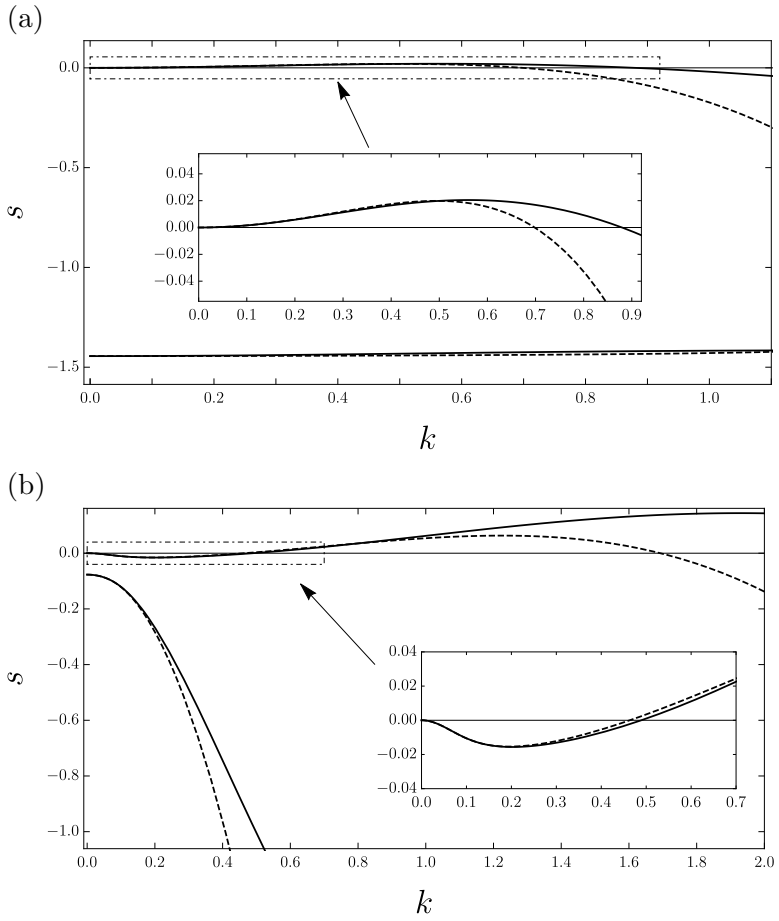

Figure 3.1: Plots of s as a function of k for the SF model (solid line) and the LW model (dashed line) where (a) $E_\mathrm{b} = 5$, $d = 3$, $\Sigma_\mathrm{G} = 1$, $\Sigma_\mathrm{L} = 6$, $\epsilon_\mathrm{R} = 4$, and $\epsilon = 1$, and (b) $E_\mathrm{b} = 5$, $d = 4$, $\Sigma_\mathrm{G} = 1$, $\Sigma_\mathrm{L} = 2$, $\epsilon_\mathrm{R} = 30$, and $\epsilon = 1$. The inserts show a magnified view of the most unstable modes.

the SF and LW models to decrease as the system is no longer thin. Indeed, this is what is observed when the parameter d is increased. Furthermore, as $k \to \infty$ there is a deterioration in agreement between the SF and LW models. These results are expected as variation in the x-direction is expected to become more important as k increases, which cannot be described by the LW model as it assumes that the flow is slowly-varying in the x-direction.

3.5 Highly conducting (HC) model

A linear stability analysis of the HC model (derived in Section 2.4.2) was performed by perturbing the interfacial height h around the uniform base state according to

$$h(x,t) = 1 + \delta\widetilde{h}\mathrm{e}^{st+ikx}. \tag{3.38}$$

This perturbation was substituted into the governing equation for h (2.99) and linearised to yield an expression for the growth rate s as a function of k, d, Σ_{R}, and ϵ_{R}, namely,

$$s = -\frac{1}{3}k^4 + \left(\frac{(\Sigma_{\mathrm{R}}-1)(\Sigma_{\mathrm{R}}^2-\epsilon_{\mathrm{R}})}{3(\Sigma_{\mathrm{R}}(d-1)+1)^3} + \frac{d(\Sigma_{\mathrm{R}}-\epsilon_{\mathrm{R}})\Sigma_{\mathrm{R}}}{2(\Sigma_{\mathrm{R}}(d-1)+1)^3}\right)k^2, \tag{3.39}$$

which is the expression found by Pillai and Narayanan [126] who investigated the linear stability of the same system in the HC case. The first term of (3.39) corresponds to the stabilising effect of capillary forces, and the second and third terms corresponds to the effect of the normal and tangential components of the electrical stress, respectively. Note that in the limit $\Sigma_{\mathrm{R}} \to \infty$, the tangential electrical stress terms vanish and the expression for s (3.39) simplifies to that of the PC case (3.43), as expected. As noted in Section 2.3.6, we assume that $\Sigma_{\mathrm{R}} \geq 1$ and so three terms determine the linear stability of the system, namely, $\Sigma_{\mathrm{R}} - 1$, $\Sigma_{\mathrm{R}}^2 - \epsilon_{\mathrm{R}}$, $\Sigma_{\mathrm{R}} - \epsilon_{\mathrm{R}}$, and d. The system is neutrally stable when the linear stability of the electrostatic terms, i.e. the second and third terms of (3.39) are zero. Hence, by solving

$$\frac{(\Sigma_{\mathrm{R}}-1)(\Sigma_{\mathrm{R}}^2-\epsilon_{\mathrm{R}})}{3(\Sigma_{\mathrm{R}}(d-1)+1)^3} + \frac{d(\Sigma_{\mathrm{R}}-\epsilon_{\mathrm{R}})\Sigma_{\mathrm{R}}}{2(\Sigma_{\mathrm{R}}(d-1)+1)^3} = 0,$$

for the value of ϵ_{R} when the system is neutrally stable yields

$$\epsilon_{\mathrm{R}} = \frac{\Sigma_{\mathrm{R}}^2 \left(2\Sigma_{\mathrm{R}} + 3d - 2\right)}{\Sigma_{\mathrm{R}} \left(3d + 2\right) - 2}. \tag{3.40}$$

We produced a figure which examines the linear stability of the HC model in $(\Sigma_{\mathrm{R}}, \epsilon_{\mathrm{R}})$ parameter space, similar to that produced by Pillai and Narayanan [126]. Figure 3.2 shows a plot of $(\Sigma_{\mathrm{R}}, \epsilon_{\mathrm{R}})$ parameter space which shows the regions in which the system is linearly stable or unstable. Specifically, the system is always stable above the solid grey line and unstable below the solid black line. Additionally, the dashed, dot-dashed, and dotted lines show plots of (3.40) where $d = 2$, $d = 5$, and $d = 8$, respectively. The system is stable and unstable above and below these lines, respectively. This makes sense physically since the destabilising influence of the electric field becomes less important as d increases, and so the region of stability should increase. Note that the maximum region of stability occurs in the limit $d \to \infty$, where the expression (3.40) simplifies to $\epsilon_{\mathrm{R}} = \Sigma_{\mathrm{R}}$ and this corresponds to the region above the solid black line in Figure 3.2 being stable.

Furthermore, the most unstable wavenumber $k_{\max}$ (i.e. the value of k corresponding to the largest positive value of s) was found by solving $\partial s/\partial k = 0$ for $k = k_{\max}$, which yields

$$k_{\max} = \sqrt{\frac{\Sigma_{\mathrm{R}}^2 \left(2\Sigma_{\mathrm{R}} + 3d - 2\right) + \epsilon_{\mathrm{R}} \left(2 - \left(2 + 3d\right) \Sigma_{\mathrm{R}}\right)}{4 \left(\Sigma_{\mathrm{R}} \left(d - 1\right) + 1\right)^3}}, \tag{3.41}$$

which is the same expression found by Pillai and Narayanan [126], and substituting $k = k_{\max}$ into (3.39) gives the most unstable growth rate $s_{\max}$, namely,

$$s_{\max} = \frac{1}{4} \left(\frac{\Sigma_{\mathrm{R}}^2 \left(2 - 3d - 2\Sigma_{\mathrm{R}}\right) + \epsilon_{\mathrm{R}} \left(\Sigma_{\mathrm{R}} \left(3d + 2\right) - 2\right)}{3(\Sigma_{\mathrm{R}}(d - 1) + 1)^3} \right)^2. \tag{3.42}$$

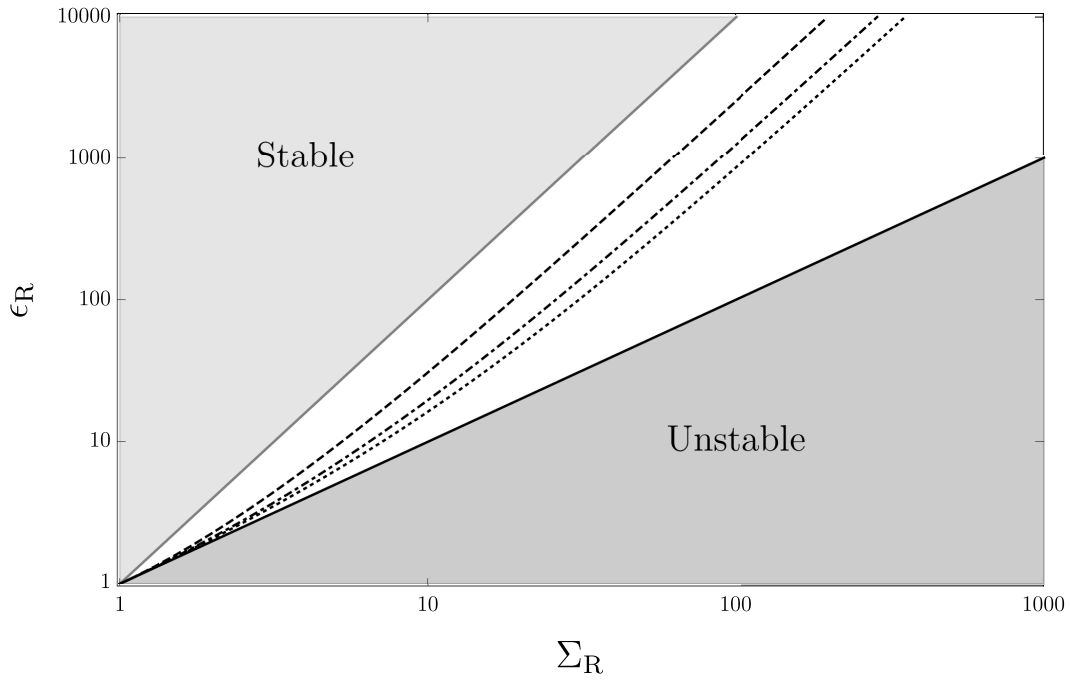

Figure 3.2: Plot of (Σ_R, ϵ_R) parameter space which describes the stability of the system. The solid black and grey lines are plots of $\epsilon_R = \Sigma_R$ and $\epsilon_R = \Sigma_R^2$, respectively. The dashed, dot-dashed, and dotted lines are plots of (3.40) in which $d = 2$, $d = 5$, and $d = 8$, respectively, where the system is stable above these lines and unstable below these lines. Note that the horizontal and vertical axes are logarithmically scaled.

Expressions (3.39) and (3.42) show that s and $s_{\max}$ decrease for increasing d, highlighting that the destabilising effect of the electric field decreases for increasing distance between electrodes, as expected.

3.6 Comparison of the linear stability results of the HC model with the SF and LW models

The linear stability results of the HC model given above were compared with the corresponding results of the SF and LW models. Figure 3.3 shows plots of the unstable growth rate s as a function of k for the SF model (thick solid line), the LW model (dashed, dotted, and dot-dashed lines), and the HC model (solid line) for a range of parameter values. Figure 3.3 shows that the agreement of the linear stability predictions between the LW and HC models improves as Σ_G and

Σ_{L} increase in the LW model, as expected, corresponding to the system moving into the HC regime. We also found that the two modes of behaviour present in the LW model reduce to one in the HC model which is characterised by the presence of a single growth rate (3.39) in the HC model. Considering the stable growth rate s_4 (3.34) of the LW model, we found that $s_4 \to -\infty$ in the HC limit which corresponds to the loss of one mode in this limit (where all waves are infinitely damped). Furthermore, we also found that the agreement between the linear stability results of the SF model and the LW and HC models improves as $k \to 0$. This is expected since both the LW and HC models are both LW approximations to the SF model.

3.7 Perfectly conducting (PC) model

A linear stability analysis of the PC model (derived in Section 2.4.1) was performed by perturbing the interfacial height h around the uniform base state according to (3.38). This perturbation was then substituted into the governing equation for h (2.91) and linearised to yield an expression for the growth rate s as a function of k and d, namely,

$$s = \frac{1}{3}\left(-k^4 + \frac{1}{(d-1)^3}k^2\right), \tag{3.43}$$

which is the expression found by Pillai and Narayanan [126] who investigated the linear stability of this PC case. The first term of (3.43) corresponds to the stabilising effect of capillary forces on the system and the second term corresponds to the effect of electrostatic forces. Note that the second term of (3.43) is always positive which corresponds to the electrostatic forces always being destabilising in the PC case and so the system is always unstable. Also, there is a range of unstable wavenumbers with $s > 0$ between $k = 0$ and a cutoff wavenumber $k = k_{\mathrm{c}}$, in which $s = 0$ at both $k = 0$ and $k = k_{\mathrm{c}}$. The cutoff wavenumber k_{c} was

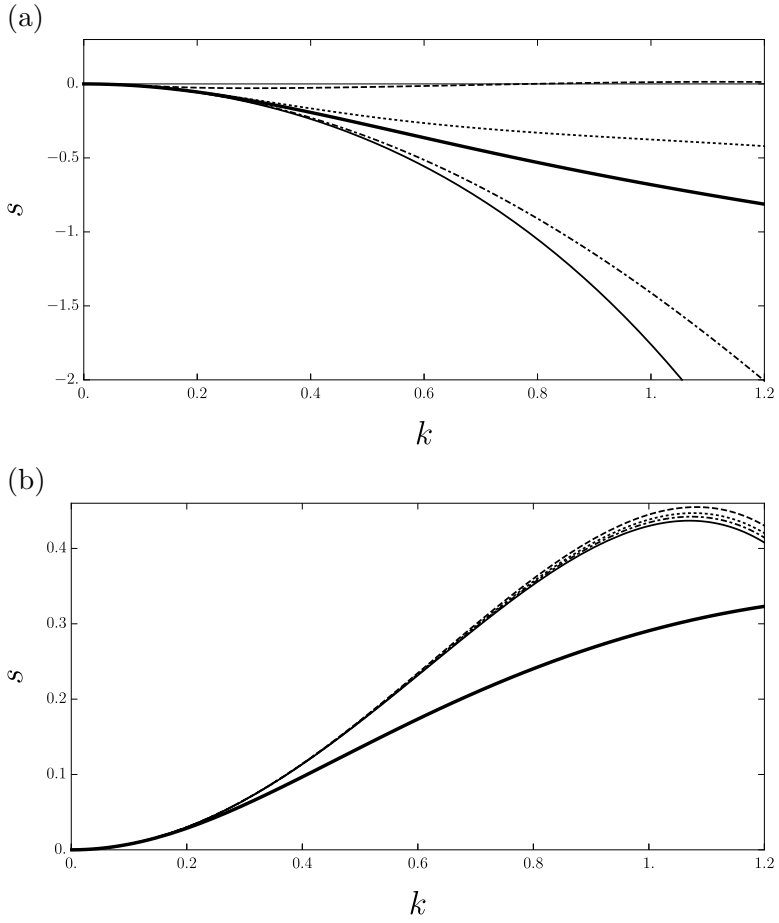

Figure 3.3: Plots of the unstable growth rate s as a function of k in which (a) $E_{\rm b} = 10$, $d = 4$, and $\epsilon_{\rm R} = 25$, where $\Sigma_{\rm G} = 10^6$ and $\Sigma_{\rm L} = 3 \times 10^6$ for the SF model (thick solid line), $\Sigma_{\rm R} = 3$ for the HC model (solid line) and, for the LW model, $\Sigma_{\rm G} = 1$ and $\Sigma_{\rm L} = 3$ (dashed line), $\Sigma_{\rm G} = 10$ and $\Sigma_{\rm L} = 30$ (dotted line), and $\Sigma_{\rm G} = 100$ and $\Sigma_{\rm L} = 300$ (dot-dashed line); and (b) $E_{\rm b} = 10$, $d = 2.5$, and $\epsilon_{\rm R} = 5$, where $\Sigma_{\rm G} = 10^6$ and $\Sigma_{\rm L} = 8 \times 10^6$ for the SF model (thick solid line), $\Sigma_{\rm R} = 8$ for the HC model (solid line) and, for the LW model, $\Sigma_{\rm G} = 1$ and $\Sigma_{\rm L} = 8$ (dashed line), $\Sigma_{\rm G} = 2$ and $\Sigma_{\rm L} = 16$ (dotted line), and $\Sigma_{\rm G} = 4$ and $\Sigma_{\rm L} = 32$ (dot-dashed line).

obtained by setting $s = 0$ in (3.43) and solving for k, which yields

$$k_{\mathrm{c}} = \frac{1}{(d-1)^{3/2}}, \tag{3.44}$$

which is the same expression found by Pillai and Narayanan [126]. Since $d > 1$, it is clear from (3.44) that $k_{\mathrm{c}} > 0$, i.e. for all values of d, there exists a range of unstable wavenumbers between $k = 0$ and $k = k_{\mathrm{c}}$, and hence this also shows that the system is always linearly unstable. Also, k_{c} decreases as d increases, i.e. the range of unstable wavenumbers decreases as the electrodes move further apart. This makes sense physically since the destabilising effect of the electric field decreases for increasing d.

The most unstable wavenumber $k_{\max}$ (i.e. the value of k corresponding to the largest positive value of s) was found by solving $\partial s/\partial k = 0$ for $k = k_{\max}$, which gives

$$k_{\max} = \frac{1}{\sqrt{2}(d-1)^{3/2}}, \tag{3.45}$$

and substituting $k = k_{\max}$ into (3.43) gives the most unstable growth rate $s_{\max}$, namely,

$$s_{\max} = \frac{1}{12(d-1)^{6}}. \tag{3.46}$$

This shows that the maximum growth rate decreases for increasing d, i.e. increasing d weakens the destabilising effect of the electric field.

3.8 Comparison of the linear stability results of the PC model with the SF and LW models

The linear stability results of the PC model given above were compared with the corresponding results of the SF and LW models. Figure 3.4 shows plots of the unstable growth rate s as a function of the wavenumber k for the SF model (thick solid line), the LW model (dashed, dotted, and dot-dashed lines), and the PC model (solid line). Figure 3.4 shows that the agreement of the linear stability predictions between the LW and PC models improves as Σ_{R} increases in the LW model, corresponding to the system moving into the PC regime, as expected. Specifically, the dot-dashed lines in Figures 3.4(a) and (b), corresponding to $\Sigma_{\mathrm{R}} = 1000$, are virtually indistinguishable from the solid line which highlights the excellent agreement of the linear stability results between the LW and PC models as Σ_{R} becomes large. Additionally, the two modes of behaviour present in the LW model reduce to one in the PC model, which is characterised by the presence of a single growth rate (3.43) in the PC model. Considering the stable growth rate s_4 given by (3.34) of the LW model, we found that $s_4 \to -\infty$ in the PC limit, which corresponds to the loss of one mode in this limit (where all waves are infinitely damped). Furthermore, we also found that as $k \to 0$ the agreement of the linear stability results between the SF model and the LW and PC models improves, as expected since the LW and PC models are both LW approximations to the SF model.

3.9 Summary

In summary, a uniform base state to the system (introduced in Section 2.1) was given, and we performed a linear stability analysis of the SF, LW, HC, and PC models by perturbing around this base state. For both the SF and LW models,

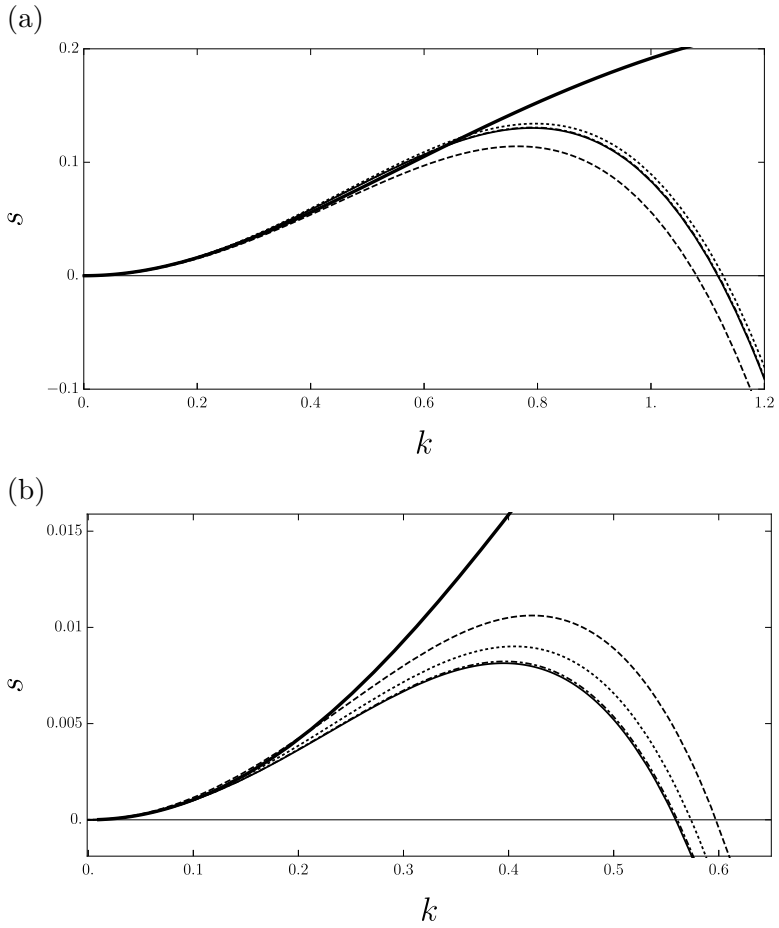

Figure 3.4: Plots of the unstable growth rate s as a function of k where (a) $E_{\rm b} = 10$, $d = 3$, and $\epsilon_{\rm R} = 5$, where $\Sigma_{\rm G} = 1$ and $\Sigma_{\rm L} = 10^6$ for the SF model (thick solid line) and PC model (solid line) and, for the LW model, $\Sigma_{\rm R} = 10$ (dashed line), $\Sigma_{\rm R} = 100$ (dotted line), and $\Sigma_{\rm R} = 1000$ (dot-dashed line); and (b) $E_{\rm b} = 20$, $d = 5$, and $\epsilon_{\rm R} = 5$, where $\Sigma_{\rm G} = 1$ and $\Sigma_{\rm L} = 10^6$ for the SF model (thick solid line) and PC model (solid line) and, for the LW model, $\Sigma_{\rm R} = 10$ (dashed line), $\Sigma_{\rm R} = 100$ (dotted line), and $\Sigma_{\rm R} = 1000$ (dot-dashed line). The dot-dashed lines are virtually indistinguishable.

we obtained implicit expressions for the two different modes of the growth rate s, which are functions of the wavenumber of the perturbation k and other system parameters, and are given in Appendices A and B, respectively. We also obtained the small-k expansions for s, namely, (3.30) and (3.31) for the SF model, and (3.33) and (3.34) for the LW model, to gain more insight into the linear stability of the system in the long-wave limit. We also obtained an expression for s as a function of k and other parameters for the PC and HC models, (3.43) and (3.39), respectively, which corresponds to the most unstable mode in the SF and LW models, (3.30) and (3.33), respectively. In addition, the most unstable growth rate $s_{\max}$ for the PC and HC models, (3.46) and (3.42), respectively, was obtained. We found that, for both limiting cases, $s_{\max}$ decreases for increasing d, making physical sense as the effect of the destabilising electric field should decrease for increasing distance between the two electrodes. The linear stability predictions of the SF model were compared with the predictions of the LW, HC, and PC models, and we found that their agreement improves as k decreases, as expected. Similarly, we compared plots of s as a function of k for the HC model against the SF and LW models, and found that for increasing Σ_{G} and Σ_{L} in the LW model, its agreement with the HC model improves. Lastly, plots of s as a function of k for the PC model were compared with the corresponding plots for the SF and LW models. We found that for increasing Σ_{R} in the LW model, its agreement with the PC model improves. Therefore, the linear stability results throughout this Chapter are important to the work throughout this thesis for two main reasons. Firstly, it shows that in the appropriate ranges of parameter space, and for sufficiently long waves, the SF model agrees with the LW, HC and PC models. Secondly, the regions of parameter space that are linearly stable or unstable have been located, and, for the limiting cases, analytical expressions have been obtained that separate these regions.

Chapter 4

Numerical schemes

This Chapter introduces and discusses the numerical schemes that we use solve the PDEs and ODEs considered in this work. In Section 4.1, a numerical scheme is introduced which solves the governing equations for the LW (2.107)–(2.108), HC (2.99) and PC (2.91) models, using the Method of Lines. Specifically, in Section 4.1.1 the theoretical approach is introduced and discussed, and in Section 4.1.2 a Matlab code is discussed that solves the LW model. This code imposes periodic boundary conditions on the system and, unless otherwise stated, they are used in the calculations throughout this thesis. In Section 4.1.3, a simplified Matlab code that solves the HC and PC models is discussed, and in Section 4.1.4, additional code which is used to perform extra analysis of the systems is introduced. Specifically, we discuss code that calculates $\partial^2 h/\partial x^2|_{x=x_{\min}}$ and the minimum points of the interfacial height $h_{\min} = h_{\min}(t)$ at each time step of our numerical calculations, as well as introducing code that imposes symmetric boundary conditions in the system. In Section 4.1.5, this Matlab code is validated by comparing the numerically calculated growth rates with the theoretical predictions of the linear theory, and the numerical results obtained compared with those obtained with other numerical solvers. Furthermore, in Section 4.2, a shooting method is introduced which solves the boundary value problem (BVP)

(4.20)–(4.23). In Section 4.2.1, the theoretical framework for solving this BVP is introduced and subsequently, in Section 4.2.2, the Matlab code which implements this theory is discussed.

4.1 Numerical scheme using the Method of Lines

The Method of Lines was used to solve the governing equations of the LW model, i.e. (2.107)–(2.108) for h and q, and the HC and PC models, i.e. (2.99) and (2.91), respectively, for h. This involves discretising the PDEs into a system of nonlinear ODEs which are then solved using the backwards Euler method, as described in Section 4.1.1. There is also extensive literature on the use of finite difference methods to solve ODEs and PDEs [147, 148, 149, 150]. The implementation of this bespoke code using Matlab, and the reasons for doing so, is then discussed in Section 4.1.2.

4.1.1 Theoretical approach

We consider a PDE of the form

$$\frac{\partial u}{\partial t} = F, \tag{4.1}$$

on the domain $0 < x < L$, where $u = u(x,t)$, L is the domain length, and

$$F = F\left(u, \frac{\partial u}{\partial x}, \frac{\partial^2 u}{\partial x^2}, \frac{\partial^3 u}{\partial x^3}, \frac{\partial^4 u}{\partial x^4}\right),$$

is a (nonlinear) function of u and its first to fourth x-derivatives. Equation (4.1) is subject to the initial condition

$$u_{x,t=0} = u_{\mathrm{IC}}(x), \tag{4.2}$$

and periodic boundary conditions, i.e.

$$\frac{\partial^k u(0,t)}{\partial x^k} = \frac{\partial^k u(L,t)}{\partial x^k} \tag{4.3}$$

for $k = 0, 1, 2, ...$

The numerical method for solving the system (4.1)–(4.3) is now introduced. Firstly, the independent variable x is discretised onto a uniform, one-dimensional grid, namely,

$$0 = x_0 < x_1 < ... < x_{M-1} < x_M = L - \Delta x,$$

where $M + 1$ is the number of grid points and, since it is a uniform grid, the grid step-size Δx is

$$\Delta x = \frac{x_M - x_0}{M + 1} = \frac{L}{M + 1}.$$

The time variable t is discretised as $t = t_j$ $(j = 0, 1, 2..., N - 1, N)$, where $t_0 = 0$, and the approximate discretised solution corresponding to u evaluated at $x = x_i$ and $t = t_j$ is denoted as

$$u_i^j = u(x_i, t_j),$$

where $i = 0, 1, ..., M - 1, M$ and $j = 0, 1, ..., N - 1, N$.

The x-derivatives are calculated using centred finite-difference approximations, namely,

$$\frac{\partial u_i^j}{\partial x} = \frac{u_{i+1}^j - u_{i-1}^j}{2\Delta x}, \tag{4.4}$$

$$\frac{\partial^2 u_i^j}{\partial x^2} = \frac{u_{i+1}^j - 2u_i^j + u_{i-1}^j}{\Delta x^2}, \tag{4.5}$$

$$\frac{\partial^3 u_i^j}{\partial x^3} = \frac{u_{i+2}^j - 2u_{i+1}^j + 2u_{i-1}^j - u_{i-2}^j}{2\Delta x^3}, \tag{4.6}$$

$$\frac{\partial^4 u_i^j}{\partial x^4} = \frac{u_{i+2}^j - 4u_{i+1}^j + 6u_i^j - 4u_{i-1}^j + u_{i-2}^j}{\Delta x^4}, \tag{4.7}$$

and the periodic boundary conditions,

$$\frac{\partial^k u_1^j}{\partial x^k} = \frac{\partial^k u_M^j}{\partial x^k},$$

for $k = 0, 1, 2, ...$

The time derivative is calculated using the backwards Euler method, namely,

$$\frac{\partial u_i^j}{\partial t} = \frac{u_i^j - u_i^{j-1}}{\Delta t}, \tag{4.8}$$

where $\Delta t = t_j - t_{j-1}$ $(j = 1, 2, ..., N-1, N)$ is the time step size. The backwards Euler method was used due to its stability in solving stiff equations [148].

Hence, after discretising the variable u onto the grid $x = x_i$ $(i = 1, 2, ..., M-1, M)$, and applying the centred finite differences (4.4)–(4.7) and the backwards Euler method (4.8), equation (4.1) becomes

$$\frac{u_i^{j+1} - u_i^j}{\Delta t} = F\left(u_i^{j+1}\right), \tag{4.9}$$

for $j = 0, 1, ..., N-2, N-1$. This is rearranged to give

$$u_i^{j+1} - \Delta t F\left(u_i^{j+1}\right) = u_i^j, \tag{4.10}$$

where $i = 0, 1, ..., M-1, M$ and $j = 0, 1, ..., N-2, N-1$, which can be recast as

$$\mathbf{u}^{j+1} - \Delta t\ \mathbf{F}\left(\mathbf{u}^{j+1}\right) = \mathbf{u}^j, \tag{4.11}$$

for $j = 0, 1, ..., N-2, N-1$, where $\mathbf{u}^j = \left(u_0^j, u_1^j, ..., u_{M-1}^j, u_M^j\right)^{\mathrm{T}}$ and $\mathbf{F}^{j+1} = \mathbf{F}\left(\mathbf{u}^{j+1}\right)$ is a vector function with elements $F_i^{j+1} = F(u_i^{j+1})$ which, for our models investigated in this thesis, is nonlinear.

The aim is to solve equation (4.11) for $\mathbf{u}^{j+1}$ where $\mathbf{u}^j$ is known. Since the initial conditions $\mathbf{u} = \mathbf{u}^0$ are known, equation (4.11) can be solved to find $\mathbf{u}^1$, and

consequently, this can be used to find $\mathbf{u}^2$. This process can be used to find $\mathbf{u}^j$ $(j = 1, 2, ..., N-1, N)$.

For the LW, HC, and PC models, equation (4.11) is a nonlinear, implicit equation that cannot be solved explicitly, and so we use an iterative procedure to solve it. Hence, at each time step $t = t_j$ $(j = 0, 1, ..., N-2, N-1)$, we let $\mathbf{u}^* = \left(u_0^*, u_1^*, ..., u_{M-1}^*, u_M^*\right)^{\mathrm{T}}$ be a vector approximation to $\mathbf{u}^{j+1}$ which solves equation (4.11), and let $\Delta\mathbf{u}$ be the correction to this approximation. Substituting

$$\mathbf{u}^{j+1} = \mathbf{u}^* + \Delta\mathbf{u},$$

into equation (4.11) and linearising around $\Delta\mathbf{u}$ yields

$$\mathbf{u}^* + \Delta\mathbf{u} - \Delta t\left(\mathbf{F}\left(\mathbf{u}^*\right) + \mathrm{J}\Delta\mathbf{u}\right) = \mathbf{u}^j + O\left(\Delta\mathbf{u}^2\right), \tag{4.12}$$

where $\mathrm{J} = \partial\mathbf{F}\left(\mathbf{u}^*\right)/\partial\mathbf{u}$ is the Jacobian matrix which has elements $J_{ij} = \partial F\left(u_i^*\right)/\partial u_j$. Considering only the leading-order terms and rearranging gives

$$\left(\mathbf{I} - \mathrm{J}\right)\Delta\mathbf{u} = \mathbf{u}^j - \mathbf{u}^* + \Delta t\ \mathbf{F}\left(\mathbf{u}^*\right), \tag{4.13}$$

where $\mathbf{I}$ is the identity matrix.

Now $\mathbf{u}^{j+1}$ is calculated by firstly making an initial guess, namely,

$$\mathbf{u}^* = \mathbf{u}_{(0)}^*, \tag{4.14}$$

where $\mathbf{u}_{(0)}^*$ is chosen to be the solution at the previous time step, i.e. $\mathbf{u} = \mathbf{u}^j$ $(j = 0, 1, ..., N-2, N-1)$. Then (4.14) is substituted into equation (4.13) and solved for $\Delta\mathbf{u}$, which is used to find a new approximation for $\mathbf{u}^*$, namely,

$$\mathbf{u}_{(1)}^* = \mathbf{u}_{(0)}^* + \Delta\mathbf{u}. \tag{4.15}$$

These iterations are continued for $\upsilon = 1, 2, ...,$ where $\mathbf{u}^*_{(\upsilon)}$ is substituted into equation (4.13) and solved for $\Delta\mathbf{u}$, and $\mathbf{u}^*_{(\upsilon+1)}$ is calculated by

$$\mathbf{u}^*_{(\upsilon+1)} = \mathbf{u}^*_{(\upsilon)} + \Delta\mathbf{u}. \tag{4.16}$$

These iterations are repeated until $||\Delta\mathbf{u}|| < \Delta u_{\mathrm{c}}$ (where $||.||$ denotes the L_2 norm) when, say, $\upsilon = l$, where Δu_{c} is some (small) cutoff value. Hence, the numerically calculated solution to equation (4.1) at $t = t_{j+1}$ is

$$\mathbf{u}^{j+1} = \mathbf{u}^*_{(l+1)}.$$

4.1.2 Matlab scheme used to solve the LW model

Matlab was used to solve the LW model (2.107)–(2.108) using the Method of Lines introduced in Section 4.1.1. The code contained a main function with a number of nested functions, which are given by Listings C.1–C.5 in Appendix C. This bespoke code was chosen over other solvers, such as Matlab, Mathematica and COMSOL Multiphysics [151], to perform the numerical calculations. Firstly, as will be discussed, this code is time-adaptive which makes the analysis easier, since behaviours such as finite-time rupture occur. Secondly, this code only retains the interfacial profiles for the current and previous time steps, and the important information is extracted at each time step and retained. Since the number of grid points required throughout this thesis is very large, this is beneficial for two reasons: minimising the memory usage speeds up the calculations, and analysing large datasets once the numerical calculations are complete is not required.

The main function is given by Listing C.1, which begins by setting up the problem

and using the initial conditions

$$h = 1 + \delta\widetilde{h}\cos\left(\frac{2\pi x}{L}\right), \tag{4.17}$$

$$q = \overline{q} + \delta\widetilde{q}\cos\left(\frac{2\pi x}{L}\right), \tag{4.18}$$

where, typically, $\delta = 0.01$, $\overline{q}$ is the base state for charge density (3.2), and $\widetilde{h}$ and $\widetilde{q}$ are the eigenvectors of the linear stability matrix A (given in Appendix B). These initial conditions for h and q, (4.17) and (4.18), respectively, were chosen to represent a small perturbation to the base state of the system under investigation. The Jacobian matrix is calculated using the function which is described by Listing C.3. So long as each iteration of the NR method converges to the solution the Jacobian matrix is not recomputed and can also be used over numerous time steps. This is important since the number of grid points M used throughout this thesis are typically very large, and so computing the Jacobian can be a very computationally expensive process. Note that the Jacobian matrix is also quite sparse for the computations used throughout this thesis, with most entries occurring along the diagonal, and the code stores only the non-zero entries. This speeds up the computations due to the lower memory usage and Matlab is also very good with dealing with sparse matrices. Furthermore, the functions given by Listing C.2 in Appendix C compute the governing equations, as well as calculating the first and second x-derivatives. Lastly, the NR method is performed using the code given by Listing C.4. As discussed earlier, the NR method is made more efficient by not recomputing the Jacobian after every iteration, which would be computationally expensive and slow down the numerical calculations. Lastly, an adaptive time stepping method was also used. After each time step, if h changed by more than 2%, the time step size was reduced, and if it was less than 0.02% the time step size was increased.

4.1.3 Numerical calculations for HC and PC models

In the HC and PC models there is only one governing equation (for h), equations (2.99) and (2.91), respectively, and these are solved using a simplified version of the Matlab code described in Section 4.1.2. In this simplified code, the vector q is omitted which means that the number of grid points halves as well as the number of rows and columns of the Jacobian matrix, i.e. the size of the Jacobian matrix reduces from $2M \times 2M$ to $M \times M$. Therefore, the numerical calculations become less computationally expensive. Additionally, only the initial conditions for h (4.17) are used due to the absence of q from the governing equations.

4.1.4 Additional code

Throughout the numerical analysis of the LW, HC, and PC models, comprehensive analyses of the different behaviours are performed. In particular, $h_{\min}$ and $x_{\min}$, and $\partial^2 h/\partial x^2 \,|_{x=x_{\min}}$ are tracked during behaviours where $h_{\min} \ll 1$. In these cases there may not be many grid points around the minimum points, it is useful to interpolate around $x = x_{\min}$ to obtain more refined results, as described by the Matlab code in Listing C.5 in Appendix C. This Matlab code uses in-built functions to interpolate around $x = x_{\min}$, which makes the analysis of the system easier and more efficient.

Furthermore, there are situations in this thesis where symmetric boundary conditions are required instead of the periodic boundary conditions. As this periodic code was well-tested and validated, we implemented a symmetrisation procedure, equivalent to the imposition of symmetric boundary conditions:

1. The Matlab function "fliplr", which flips a vector around its centre, was applied to h and q.

2. This was added to the original h and q, and this result was divided by 2, symmetrising the resultant h and q.

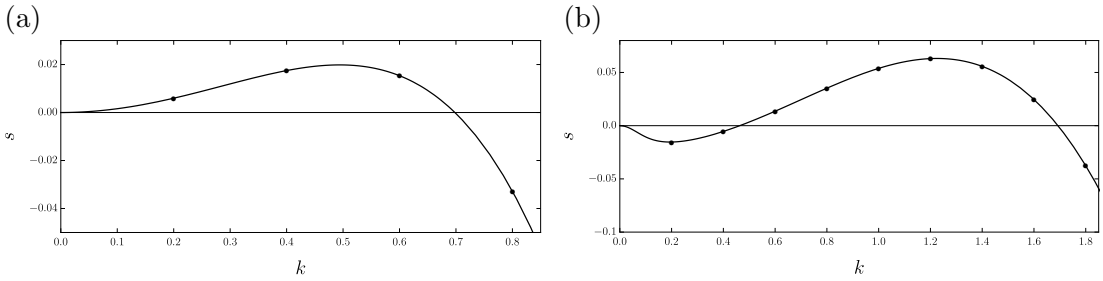

Figure 4.1: Plots of s as a function of k for the LW model where (a) $E_{\mathrm{b}} = 5$, $d = 3$, $\Sigma_{\mathrm{G}} = 1$, $\Sigma_{\mathrm{L}} = 6$, $\epsilon_{\mathrm{R}} = 4$, and $\epsilon = 1$, and (b) $E_{\mathrm{b}} = 5$, $d = 4$, $\Sigma_{\mathrm{G}} = 1$, $\Sigma_{\mathrm{L}} = 2$, $\epsilon_{\mathrm{R}} = 30$, and $\epsilon = 1$.

4.1.5 Validating the Matlab code

This Matlab code was validated against two stringent tests. Firstly, the analytically derived growth rates predicted by linear stability theory were reproduced numerically in the appropriate linear regime. Secondly, the results produced using Matlab, once the system had entered the nonlinear regime, were compared with those of other numerical solvers.

4.1.5.a Comparison with linear stability theory

The numerically calculated growth rates s_{N} at early times were compared with the linear stability predictions. The initial conditions (4.17) and (4.18) were used where $\delta = 10^{-6}$, and s_{N} was obtained using

$$s_{\mathrm{N}} = \frac{\log\left(h^{20}_{\mathrm{max}}\right) - \log\left(h^{10}_{\mathrm{max}}\right)}{t_{20} - t_{10}}, \tag{4.19}$$

where $h = h^{j}_{\mathrm{max}}$ is the maximum value of the interfacial height h^{j} at time $t = t_j$. The growth rates were calculated from the time $t = t_{10}$ since the initial conditions for h and q are out of phase, and so it takes a few time steps to readjust. This could be solved by calculating $\widetilde{h}$ and $\widetilde{q}$ from the linear stability analysis in Chapter 3 and applying them to the initial conditions. The numerically calculated growth rates s_{N} are illustrated by the filled dots on Figures 4.1, which also show plots of the linear growth rates s as a function of k. The results were compared for various

wavenumbers by changing the domain length L and obtaining the corresponding wavenumber by using the relation, $k = 2\pi/L$. These figures show excellent agreement between the linear stability predictions and the numerical results for the LW model. When the parameter δ in the initial conditions (4.17) and (4.18) was increased from from 10^{-6} to 0.1, it was observed that the agreement between the linear stability results and numerical results worsened. This is expected as the nonlinear terms, which are neglected during the linear stability analysis, begin to become important with increasing δ. Therefore, the excellent agreement of the numerical results with the linear stability results inspires confidence in this numerical code and the results that it produces.

4.1.5.b Comparison with the results of other numerical codes

The numerical results from the Matlab code was also compared with the results using other numerical solvers, specifically, the Mathematica solver "NDSolve", the finite-element solver COMSOL Multiphysics, and a pre-existing C++ code written by one of the author's supervisors (Dr Wray) which performs the calculations on a uniform grid using the Method of Lines. The results obtained using the different solvers were compared when h and q in the nonlinear regime in which the linear stability theory is not applicable.

Firstly, the Matlab code, the COMSOL and C++ codes were used to solve the LW model for h and q, and their results were compared. Figure 4.2 shows plots of (a) h and (b) q as functions of x/L. The solid, dashed and dotted lines show the results obtained using the Matlab code, the C++ code, and the COMSOL solver, respectively, and the lines are virtually indistinguishable, demonstrating the excellent agreement between the results of the different solvers. Similarly, Figure 4.3 shows plots of (a) h and (b) q as functions of x/L, where the solid, dashed and dotted lines show the results obtained using the Matlab code, the C++ code, and the COMSOL solver, respectively. At this time, $t = 885$, the

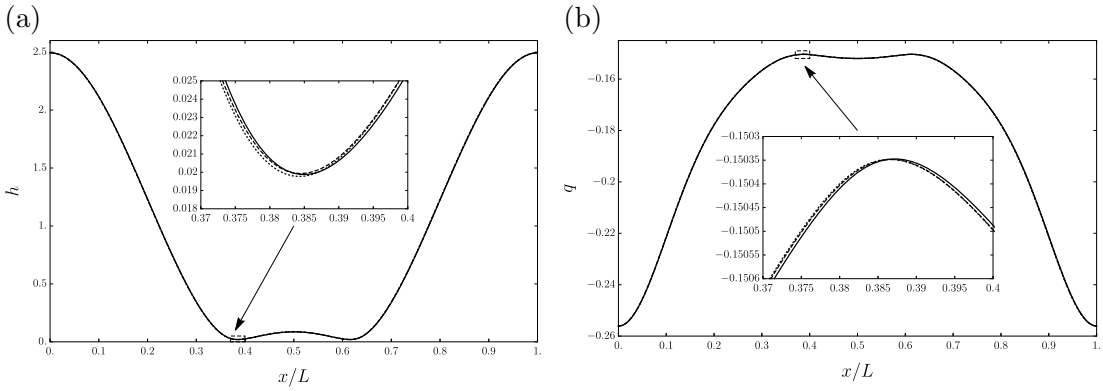

Figure 4.2: Plots of (a) h and (b) q as a function of x/L at time $t = 1000$, where the solid, dashed, and dotted lines are the results of the LW model using the Matlab code, the author's supervisor's C++ code, and COMSOL solver, respectively. The inserts show magnified views of the plots. The parameter values used are $E_{\mathrm{b}} = 20$, $d = 5$, $\Sigma_{\mathrm{R}} = 4$, $\epsilon_{\mathrm{R}} = 1$, and $L = 10$, and 1000 grid points used in all calculations and the initial conditions used are given by (4.17) and (4.18).

interface around $x/L = 0.5$ is moving very fast, and the time steps used are small. There is a difference in the results between the solvers around $x/L = 0.5$, and these discrepancies are due to the time step sizes that are used in the numerical solvers. Decreasing the step sizes would lead to smaller errors and better agreement between the solvers, however, decreasing the step-sizes must be balanced against the computational cost of an increased number of time steps required to reach the same time. Nevertheless, the results given in Figure 4.3 still show very good agreement between the results of the different solvers.

Furthermore, the simplified Matlab code used to solve the HC and PC models was compared against C++ code and the Mathematica solver "NDSolve". These were used to solve the HC model for various parameter values, and Figure 4.4 shows plots of h as a function of x/L for different parameter values. The results in Figure 4.4(a), in which the lines are virtually indistinguishable, show excellent agreement between the results of the different solvers. In Figure 4.4(b), the difference between the results is visible, however, this is again due to the interface moving quickly and the small step sizes that are required at these times.

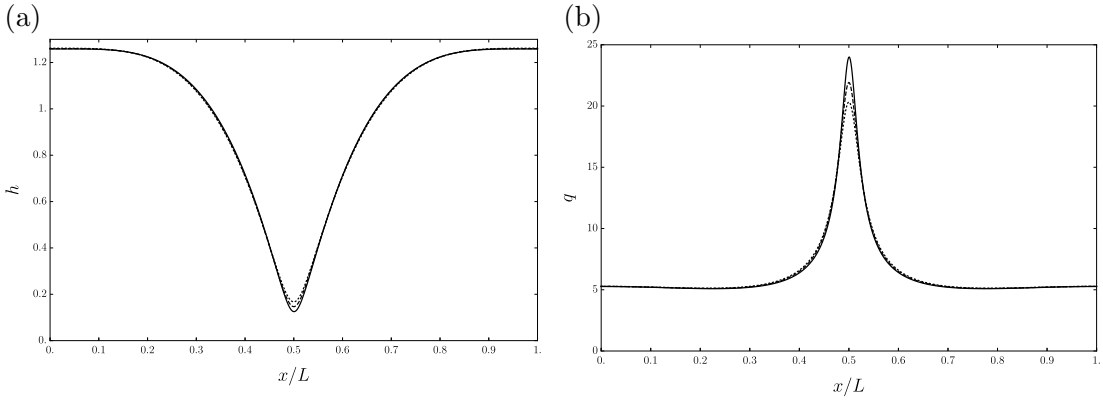

Figure 4.3: Plots of (a) h and (b) q as a function of x/L at time $t = 885$, where the solid, dashed, and dotted lines are the results of the LW model using the Matlab code, the author's supervisor's C++ code, and COMSOL solver, respectively. The parameter values used are $E_{\rm b} = 2$, $d = 5$, $\Sigma_{\rm R} = 2$, $\epsilon_{\rm R} = 60$, and $L = 10$, and 1000 grid points used in all calculations. The initial conditions used in all calculations are given by (4.17) and (4.18).

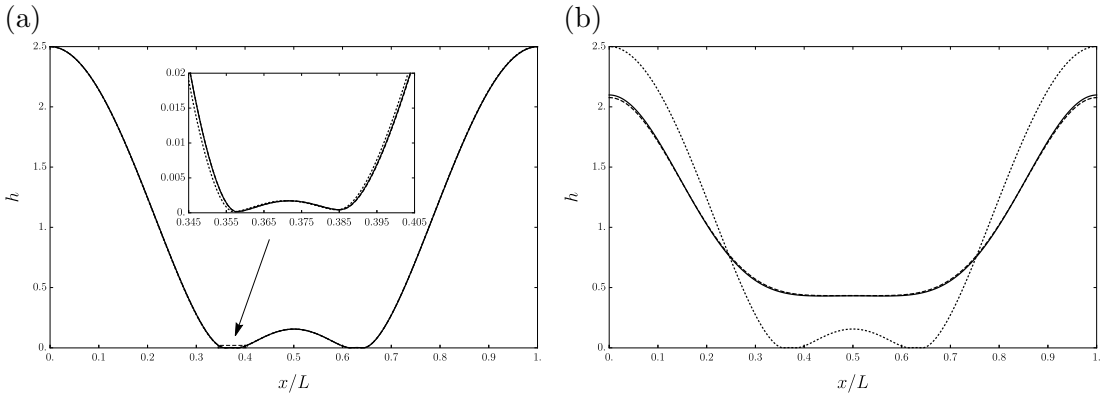

Figure 4.4: Plots of h as a function of x/L where the solid, dashed, and dotted lines are the results of the HC model using the Matlab code, the author's supervisor's C++ code, and the Mathematica solver, respectively, at times (a) $t = 10^7$ and (b) $t = 3 \times 10^4$. The insert in (a) shows a magnified view of the plots. The parameter values used are (a) $d = 5$, $\Sigma_{\rm R} = 2$, $\epsilon_{\rm R} = 1$, and $L = 50$, and (b) $d = 4$, $\Sigma_{\rm R} = 10$, $\epsilon_{\rm R} = 3$, and $L = 10$, and 1000 grid points used in all calculations. In all calculations, the initial conditions used are given by (4.17).

4.2 Shooting method for solving a BVP

In Chapter 5, the shooting method was used to solve a BVP, specifically, a fourth-order ODE (5.13) subject to the four boundary conditions (5.31)–(5.33). The shooting method involves changing a BVP into an initial value problem (IVP) and finding the initial conditions in which the solutions to the IVP also satisfy the BVP. In Section 4.2.1, we discuss the theoretical approach of solving the BVP that arises in Chapter 5 through using this shooting method. In Section 4.2.2, we discuss the Matlab routine used to implement the shooting method and hence solve the BVP.

4.2.1 Theoretical approach

Consider the following BVP,

$$f^{(4)} = F\left(\eta, f, f', f'', f'''\right), \tag{4.20}$$

on the domain $0 \leq \eta \leq \eta_{\text{end}}$, where $f = f(\eta)$, and which is subject to the boundary conditions

$$f'(0) = f'''(0) = 0, \tag{4.21}$$

at the origin $\eta = 0$, and

$$f\left(\eta_{\text{end}}\right) = F_1\left(\eta_{\text{end}}, f'\right), \tag{4.22}$$

$$f\left(\eta_{\text{end}}\right) = F_2\left(\eta_{\text{end}}, f''\right), \tag{4.23}$$

where $F_1 = F_1\left(\eta, f'\right)$ and $F_2 = F_2\left(\eta, f''\right)$ are functions of η, $f'(\eta)$, and $f''(\eta)$. The shooting method begins by changing this BVP into an IVP, specifically,

equation (4.20) subject to the boundary conditions,

$$f(0) = \alpha, \qquad f'(0) = 0, \qquad f''(0) = \beta, \qquad f'''(0) = 0, \tag{4.24}$$

where α and β are constants and the solution to this IVP is denoted by $f = f_{\mathrm{S}}(\eta)$. Therefore, an investigation of $(f(0), f''(0))$-space is required to find values of α and β such that $f_{\mathrm{S}}(\eta)$ satisfies both boundary conditions (4.22) and (4.23). Hence, for these values of α and β, $f_{\mathrm{S}}(\eta)$ is also a solution to the BVP (4.20)–(4.23). The investigation of $(f(0), f''(0))$-space is performed in two stages:

1. (a) Assign a value to α.

   (b) Search for values of β where the solution to the IVP $f = f_{\mathrm{S}}(\eta)$ satisfies equation (4.22) at $\eta = \eta_{\mathrm{end}}$.

2. (a) Assign a value to β.

   (b) Search for values of α where the solution to the IVP $f = f_{\mathrm{S}}(\eta)$ satisfies equation (4.23) at $\eta = \eta_{\mathrm{end}}$.

Once a value has been assigned to α or β, i.e. part (a) of each stage, a root-finding method, such as the NR method or Euler's method, is used in part (b) of each stage to find the solution to the IVP. An initial guess is chosen for the remaining parameter, β and α at stage 1 and 2, respectively, and β or α may converge to a different solution depending on this initial guess. Hence, for any value of α or β assigned at step (a), a different initial guess for the remaining parameter may converge to a different solution. If $f_{\mathrm{S}}(\eta)$ satisfies the required boundary condition at $\eta = \eta_{\mathrm{end}}$, the values $(f(0), f''(0)) = (\alpha, \beta)$ are stored. Lastly, the solution to the BVP is found using points in $(f(0), f''(0))$-space at which the solution to the IVP satisfies both of the boundary conditions (4.22) and (4.23).

4.2.2 Matlab code

A Matlab routine was used to solve the BVP (4.20)–(4.23). Firstly, a search of $(f(0), f''(0))$-space is performed to find values of $f(0)$ and $f''(0)$ where the solution to the IVP $f = f_{\mathrm{S}}(\eta)$ satisfies both of the boundary conditions (4.22) and (4.23). Listing C.6 gives Matlab code that performs part 1 of the $(f(0), f''(0))$-space investigation as described in Section 4.2.1, i.e. finding β, and a very similar code was used to perform stage 2 of the investigation, i.e. finding α. Secondly, the solution to the IVP $f = f_{\mathrm{S}}(\eta)$ was found using values of α and β as initial conditions that ensured the BVP was also satisfied.

This Matlab code in Listing 4.2.2 does particularly well at solving the BVP (4.20)–(4.22). The Matlab solver "ode15s" deals with stiff systems particularly well and the code is more robust in dealing with changes in the boundary sizes, i.e. changing η_{end}. Also, the regions of $(f(0), f''(0))$-space can be refined by choosing smaller step sizes.

4.3 Summary

In summary, a numerical scheme was introduced that solves the LW model (2.107)–(2.108) in Section 4.1.1. Here, the Method of Lines was used in which the PDEs were discretised into a system of nonlinear ODEs using centred finite-differences and the backwards Euler method. The NR method was then used to solve the system of ODEs. A bespoke Matlab code, which solves the LW model and imposes periodic boundary conditions, was discussed in Section 4.1.2 and is given by Listings C.1–C.4 in Appendix C. Important features of the code were highlighted and discussed. Specifically, an adaptive time stepping feature is used such that the time step size is decreased when the difference in h changes by more than 2% and increases when h changes by less than 0.02%. Also, the memory and computational costs were minimised by retaining only the time steps from the

current and previous time steps, as well as using a conservative approach to computing the Jacobian matrix and storing it as a sparse matrix, which ultimately speeds up the code. In Section 4.1.4, additional Matlab code was introduced to interpolate the results around $x = x_{\min}$, which is given by Listing C.5, and a routine to impose symmetric boundary conditions was discussed.

Furthermore, the Matlab code was validated extensively by comparing the numerically calculated growth rates with the analytically calculated linear growth rates, which showed excellent agreement. Also, the numerical results were also compared against results of other PDE solvers, showing very good agreement even when the system has entered the nonlinear regime.

In Section 4.2.1, the theoretical framework for performing the shooting method was introduced. This shooting method solves the BVP (4.20)–(4.23) by turning it into an IVP (equation (4.20) with initial conditions (4.24)). A search for initial conditions is performed in which the solution to the IVP also satisfies the BVP. The Matlab code given by Listing C.6 applies this theory, which searches for initial conditions in which the solution of the IVP satisfies the boundary condition (4.22). This code can be easily altered to search for initial conditions in which the solution to the IVP satisfies equation (4.23) instead. The solution of the BVP is subsequently found by solving the IVP using initial conditions for which its solution satisfies both boundary conditions (4.22) and (4.23).

Chapter 5

Perfectly conducting (PC) model

In this Chapter, the PC model (derived in Section 2.4.1) is investigated and three behaviours are observed, namely, levelling (LV), upper contact (UC), and thinning (TH). In Section 5.1, we investigate (L, d) parameter space, highlighting where each of these three behaviours occur. In Sections 5.2–5.4, the three different behaviours are described fully and investigated both analytically and numerically. In Section 5.5, the transition curves separating the three behaviours will be investigated, and we use linear stability theory to obtain an analytical expression for the transition curve separating UC or TH behaviour with LV behaviour.

5.1 (L, d) parameter space

The results of our numerical investigation of the PC model revealed three behaviours, namely, levelling (LV), upper contact (UC), and thinning (TH), which will be fully described in Sections 5.2, 5.3, and 5.4, respectively. However, we will briefly introduce each behaviour here:

1. LV behaviour: perturbations to the base state decay and the interface levels.

2. UC behaviour: the interface touches the upper electrode in finite time.

3. TH behaviour: the interface approaches the lower electrode asymptotically as $t \to \infty$.

The behaviour which the system adopts is dependent on the parameter values, specifically, the domain length L and the upper electrode position d. Therefore, we performed a numerical investigation of (L, d) parameter space to explore where each behaviour is observed.

5.1.1 Numerical investigation

The investigation of (L, d) parameter space was performed by solving the governing equation for h of the PC model (2.91) using a pre-existing C++ code written by one of the author's supervisors (Dr Wray) that implements the Method of Lines on a uniform grid. Note that the C++ code was used to perform the extensive parameter space investigation due to the program's speed and memory efficiency. However, later in this Chapter each behaviour is investigated further using Matlab. This is since the author is more familiar and adept in using Matlab than C++ , as well as Matlab having useful built-in functions (described in Chapter 4), which makes the analysis of each behaviour easier to perform. Furthermore, Matlab is used over C++ since a comprehensive analysis of each behaviour is not as computationally expensive as the parameter space investigation.

We performed the numerical calculations using 2048 grid points and the initial conditions given by (4.17) with $\delta = 0.01$. We explored (L, d) parameter space over the ranges $7 \leq L \leq 500$ and $1.5 \leq d \leq 20$ with step sizes of 1 and 0.05 in the L and d directions, respectively. At each point in (L, d) parameter space, the observed behaviour was classified according to the following conditions:

1. LV behaviour: When $h_{\max} - h_{\min} < 10^{-8}$.

2. UC behaviour: When the time step size $\Delta t < 10^{-4}$ (as the step size is reduced as $h \to d$).

3. TH behaviour: When $h_{\min} < 10^{-3}$.

Recall from Chapter 4 that Δt is the time step size, and that $h_{\max} = h_{\max}(t)$ is the maximum value of h, located at $x = x_{\max}(t)$. The results obtained using the C++ code were cross-referenced at several points in parameter space by using the Matlab code introduced in Chapter 4. Both codes predicted the same behaviour in all cases which inspires confidence in the results.

5.1.2 Results of the investigation of (L, d) parameter space

The results of the investigation of (L, d) parameter space are presented in Figure 5.1, which includes transition curves that separate regions of (L, d) parameter space in which UC, TH or LV behaviours occur. Figure 5.1 shows the numerically calculated transition curves (solid lines) and the analytically calculated transition curve (dashed line) given by equation (5.85) which will be discussed in Section 5.2. The numerically calculated transition curves were obtained by taking two points in (L, d) parameter space, denoted by (L_1, d_1) and (L_1, d_2), with the same value of L, between which the behaviour changes as the value for d changes, and estimating that the transition curve lies half-way between these points, i.e. $(L_1, (d_1 + d_2)/2)$, which is accurate since the step size in d, i.e. $d_2 - d_1$, is small, i.e. 0.05. Figure 5.1 also includes insets which identify the LV, UC, and TH behaviours by the dark grey, black, and light grey dots, respectively, at all the points for which numerical calculations were undertaken. The lower inset shows the transition from TH to LV behaviour as d increases, and the upper transition shows a "tongue" of UC behaviour extending into the region of TH behaviour. Also, the density of points shown in both insets shows the large number of data points used to produce this plot of (L, d) parameter space. There is also excellent agreement between the analytical transition curve and corresponding numerically calculated transition curve as these two curves are indistinguishable. Figure 5.1 also shows that below a critical value for the domain length, specifically, below

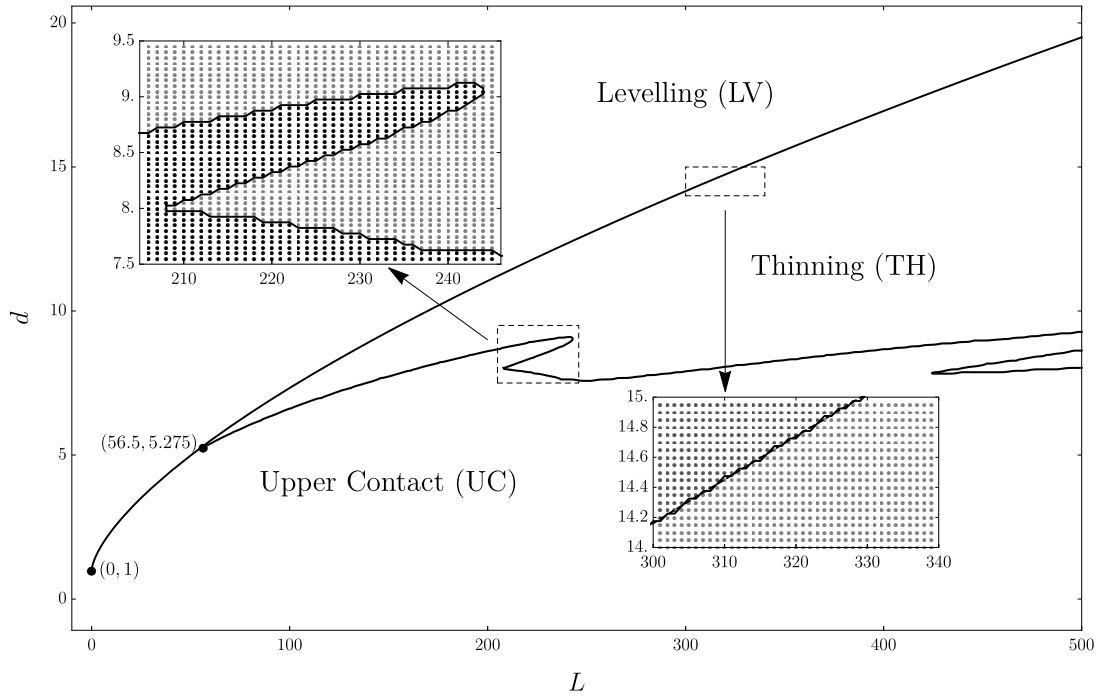

Figure 5.1: (L, d) parameter space showing the numerically calculated transition curves (solid lines) and the analytically calculated transition curve (dashed line) given by equation (5.85) separating the UC or TH, and LV behaviours. The solid and dashed curves are indistinguishable. The inset figures show the numerically calculated behaviours around the transition curves, where the dark grey, black, and light grey dots in the insets indicate LV, UC, and TH behaviours, respectively.

$L = 56.5 \pm 0.5$, the TH region disappears, which is marked by the larger black dot at $(56.5 \pm 0.5, 5.275)$ in Figure 5.1. Hence, to the left of this black dot, the behaviour goes from UC to LV as d increases. For a range of values of L to the right of $L = 56.5 \pm 0.5$, the behaviour goes from UC to TH, and then to LV as d increases. This critical value for the domain length is marked by the filled circle at $(56, 5.275)$. Furthermore, for even larger values of L, there are also regions in which the behaviour goes from TH to UC as d increases, i.e. the tongue of UC behaviour extending into the TH region, shown in the upper inset in Figure 5.1. For example, for $L = 250$ the behaviour goes from UC to TH, then from TH to UC behaviour, and finally from UC to TH then to LV behaviour as d increases.

5.2 Levelling (LV) behaviour

LV behaviour occurs when perturbations to the base state $\overline{h} = 1$ decay, as illustrated by Figure 5.2. Figure 5.2 shows plots of h as a function of x/L at equally spaced times t including a plot of the initial condition (4.17) in which $\delta = 0.01$ (shown with a dashed line).

Recall that the PC model is always linearly unstable in an unbounded domain, as discussed in Section 3.7. Therefore, LV behaviour can only occur when there are unstable wavenumbers but the corresponding wavelengths are too long (i.e. the values of k are too small) to fit into the domain. The value for $d = 7$ used in Figure 5.2 was substituted into the equation for the cutoff wavenumber k_c given by equation (3.44) in Section 3.7. This gives $k_c = 1/6^{3/2}$ which means that only domain lengths longer than $L = 6^{3/2} \times 2\pi = 12\sqrt{6}\pi$ contain any unstable wavenumbers. Since the domain length used in Figure 5.2 is $L = 10$, it is too short to contain any unstable wavenumbers and so the linear stability theory predicts LV behaviour, agreeing with the results of the numerical calculations.

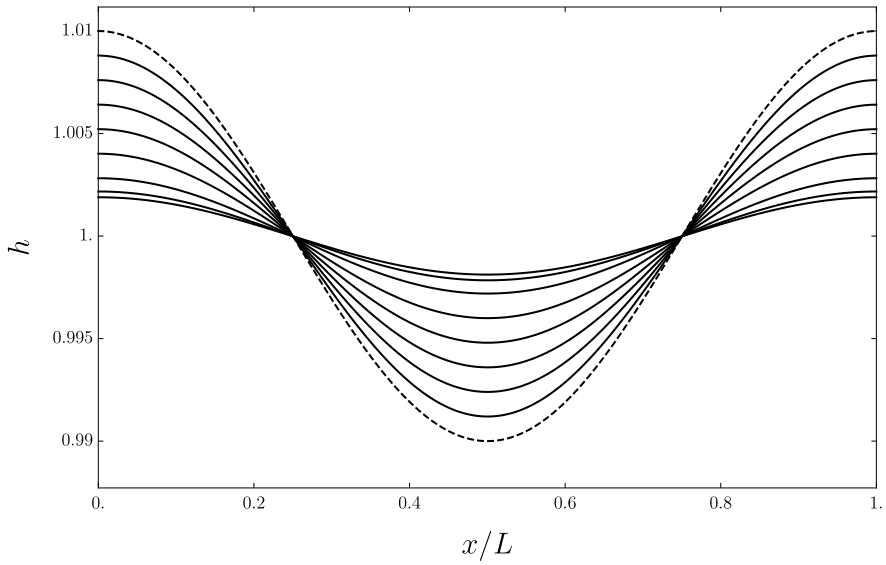

Figure 5.2: Plots of the interfacial height h as a function of x/L at equally spaced times from $t = 0$ to $t = 80$. The dashed line indicates the initial condition (4.17) where $\delta = 0.01$, and the parameters used are $L = 10$ and $d = 7$.

5.3 Upper contact (UC) behaviour

UC behaviour occurs when the interface approaches the upper electrode and touches it in finite time, as illustrated by Figure 5.3. Figure 5.3 shows plots of (a) h as a function of x/L for values of t corresponding to $d - h_{\max} = 0.1$, 0.3, 0.5, 0.7 and 0.9 (solid lines), and the initial condition (4.17) for $\delta = 0.01$ (shown by the dashed line), and (b) $\mathrm{d}h_{\max}/\mathrm{d}t$ as a function of t where the vertical axis is logarithmically scaled. Note that $\mathrm{d}h_{\max}/\mathrm{d}t = \partial h/\partial t|_{x=x_{\max}}$ which will be equal to $\partial h/\partial t(0,t)$ since the calculations are performed using the initial condition (4.17, and Figure 5.3(b) shows that this term blows up as the interface approaches the upper electrode, i.e. $\mathrm{d}h_{\max}/\mathrm{d}t \to \infty$ as $h_{\max} \to d$, showing that finite-time contact occurs. Smaller time steps are required close to contact, i.e. smaller values of Δt as $h \to d$, to resolve the behaviour when the interface moves rapidly. The evolution of h to finite-time contact corresponds to a localised singularity of the governing equation (2.91) at $h = d$, in which the third term of (2.91) diverges as h approaches d.

5.3.1 Analytical investigation of UC behaviour

Close to the time of contact with the upper electrode, i.e. when $h_{\max}$ is close to d, the interface exhibits self-similar behaviour, as we shall now describe. Firstly, we pose the similarity solution for h (close to the time of contact) to be of the form,

$$h = d - \tau^{\alpha} f(\eta), \tag{5.1}$$

in which

$$\eta = \frac{x - x_{\mathrm{c}}}{\tau^{\beta}}, \qquad \tau = t_{\mathrm{c}} - t, \tag{5.2}$$

where $t = t_{\mathrm{c}}$ and $x = x_{\mathrm{c}}$ are the time and position of contact with the upper electrode, respectively, $\tau \ll 1$, $f = f(\eta)$ is the similarity function, and α and β are the similarity exponents which are expected to be positive. Also note that $x_{\mathrm{c}} = 0$ for our numerical calculations since the initial condition (4.17) is used (and there is no symmetry breaking) which means that $h_{\max}$ (and hence contact) will occur at $x = 0$.

We will now determine the similarity exponents α and β by firstly substituting the similarity solution (5.1) into the governing equation (2.91). Firstly, the $\partial h/\partial t$ term in (2.91) is

$$\frac{\partial h}{\partial t} = -\alpha\tau^{\alpha-1} f(\eta) - \tau^{\alpha} f'(\eta)\frac{\partial \eta}{\partial \tau} = \tau^{\alpha-1}\left(-\alpha f(\eta) + \beta\eta f'(\eta)\right), \tag{5.3}$$

where the dashes represent differentiation with respect to the argument. Similarly, the h^3 term, the spatial derivative terms, and the $1/(d-h)^3$ term in (2.91)

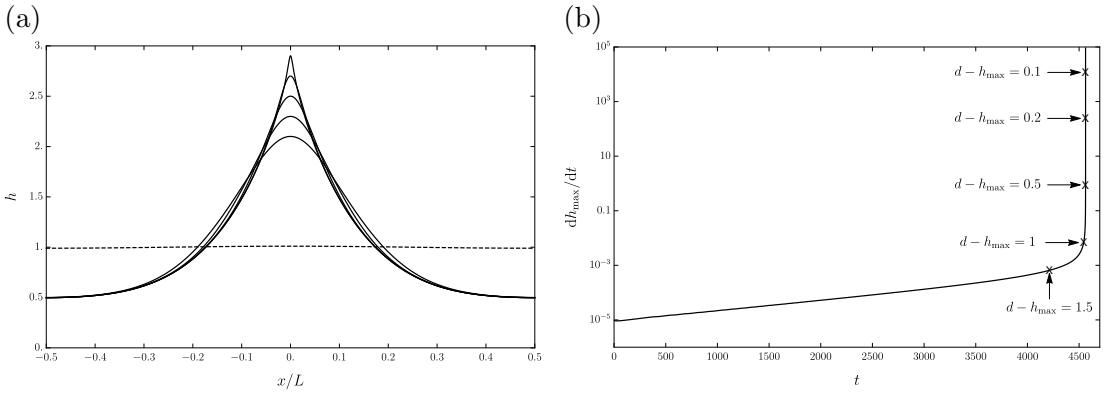

Figure 5.3: Plots of (a) h as a function of x/L for values of t corresponding to $d - h_{\max} = 0.1$, 0.3, 0.5, 0.7 and 0.9 (solid lines), and the initial condition (4.17) in for $\delta = 0.01$ (shown by the dashed line), and (b) $\mathrm{d}h_{\max}/\mathrm{d}t$ as a function of t where the vertical axis is logarithmically scaled. The parameters used are $L = 20$ and $d = 3$.

are

$$h^3 = (d - \tau^\alpha f(\eta))^3 = d^3 + O(\tau^\alpha), \tag{5.4}$$

$$\frac{\partial h}{\partial x} = -\tau^{\alpha-\beta} f'(\eta), \quad \frac{\partial^2 h}{\partial x^2} = -\tau^{\alpha-2\beta} f''(\eta), \quad \frac{\partial^3 h}{\partial x^3} = -\tau^{\alpha-3\beta} f'''(\eta), \tag{5.5}$$

$$\frac{1}{(d-h)^3} = \frac{\tau^{-3\alpha}}{(f(\eta))^3}, \tag{5.6}$$

respectively. Hence, using equations (5.4)–(5.6), the second and third terms of (2.91) become

$$\frac{\partial}{\partial x}\left(h^3 \frac{\partial^3 h}{\partial x^3}\right) = \frac{\partial}{\partial x}\left(-\tau^{\alpha-3\beta} d^3 f'''(\eta) + O\left(\tau^{2\alpha-3\beta}\right)\right) \tag{5.7}$$

$$= -\tau^{\alpha-4\beta} d^3 f^{(4)}(\eta) + O\left(\tau^{2\alpha-4\beta}\right), \tag{5.8}$$

$$\frac{\partial}{\partial x}\left(h^3 \frac{1}{(d-h)^3} \frac{\partial h}{\partial x}\right) = \frac{\partial}{\partial x}\left(-\tau^{-2\alpha-\beta} d^3 f^{-3}(\eta) f'(\eta) + O\left(\tau^{-\alpha-\beta}\right)\right) \tag{5.9}$$

$$= -\tau^{-2(\alpha+\beta)} d^3 \left(f'(\eta) f^{-3}(\eta)\right)' + O\left(\tau^{-\alpha-2\beta}\right). \tag{5.10}$$

Therefore, balancing the leading order terms of (5.3), (5.8) and (5.10) gives the balance,

$$\tau^{\alpha-1} \sim \tau^{\alpha-4\beta} \sim \tau^{-2(\alpha+\beta)}. \tag{5.11}$$

Balancing these three terms requires

$$\alpha - 1 = \alpha - 4\beta = -2(\alpha + \beta), \tag{5.12}$$

which has a unique solution for the similarity exponents, namely, $\alpha = 1/6$ and $\beta = 1/4$, which will be compared against the solutions to the governing equation (2.91) in Section 5.3.1.a. This balance means that both surface tension and electrostatic effects are important close to contact.

Furthermore, using the similarity exponents $\alpha = 1/6$ and $\beta = 1/4$, and equations (5.3), (5.8) and (5.10) at leading order in τ, we find that the similarity function f obeys the similarity ODE

$$3\eta f' - 2f = -4d^3 \left(f^{(4)} + \left(f^{-3} f' \right)' \right). \tag{5.13}$$

This ODE governs the shape of the similarity solution close to contact and includes the effects of surface tension and electrostatic effects, corresponding to the second and third terms, respectively.

In summary, close to the time of contact t_c during UC behaviour, the interface exhibits self-similar behaviour which is described by the similarity solution,

$$h = d - \tau^{1/6} f(\eta), \tag{5.14}$$

in which

$$\eta = \frac{x - x_{\mathrm{c}}}{\tau^{1/4}}, \qquad \tau = t_{\mathrm{c}} - t, \tag{5.15}$$

where $\tau \ll 1$, and f obeys the similarity ODE (5.13) which incorporates both surface tension and electrostatic effects.

5.3.1.a Comparison between the similarity solution (5.14)–(5.15) and the numerical results

We will now compare the power-law behaviour predicted by the similarity solution (5.14)–(5.15) with numerical solutions to the governing equation (2.91). In particular, we will show that log-log plots of $\mathrm{d}h_{\max}/\mathrm{d}t$ and $-\partial^2 h/\partial x^2\,|_{x=x_{\max}}$ as functions of $d - h_{\max}$ give the power-law behaviour predicted by (5.14)–(5.15). Plotting these variables as a function of $d - h_{\max}$ instead of τ leads to more robust results as it bypasses the issue of accurately calculating t_{c}, which can be quite difficult due to the small time step sizes close to the time of contact.

We used the similarity solution (5.14)–(5.15) to evaluate

$$\frac{\log(\partial h/\partial t)}{\log(d-h)} = \frac{\log\left(\tau^{-5/6}\left(-f+\eta f'\right)\right)}{\log\left(\tau^{1/6} f\right)} = -5 \times \frac{\log\left(\tau\left(-f+\eta f'\right)^{6/5}\right)}{\log\left(\tau\left(f\right)^{-1/6}\right)} \tag{5.16}$$

and

$$\frac{\log\left(-\partial^2 h/\partial x^2\right)}{\log(d-h)} = \frac{\log\left(\tau^{-1/3} f''\right)}{\log\left(\tau^{1/6} f\right)} = -2 \times \frac{\log\left(\tau\left(f''\right)^{1/3}\right)}{\log\left(\tau\left(f\right)^{-1/6}\right)}. \tag{5.17}$$

Furthermore, evaluating equations (5.16) and (5.17) at $x = x_{\max}$ yields

$$\frac{\log(\mathrm{d}h_{\max}/\mathrm{d}t)}{\log\left(d-h_{\max}\right)} = -5 \times \frac{1 + \log\left(\left(-f(0)\right)^{6/5}\right)/\log(\tau)}{1 + \log\left(\left(f(0)\right)^{-1/6}\right)/\log(\tau)} \tag{5.18}$$

and

$$\frac{\log\left(-\partial^2 h/\partial x^2\,|_{x=x_{\max}}\right)}{\log\left(d-h_{\max}\right)} = -2 \times \frac{1+\log\left(\left(f''(0)\right)^{1/3}\right)/\log\left(\tau\right)}{1+\log\left(\left(f(0)\right)^{-1/6}\right)/\log\left(\tau\right)}. \tag{5.19}$$

Hence, as the interface approaches the upper electrode, i.e. as $\tau \to 0$, we expect log-log plots of $\mathrm{d}h_{\max}/\mathrm{d}t$ and $-\partial^2 h/\partial x^2\,|_{x=x_{\max}}$ as a function of $d-h_{\max}$ to have gradients -2 and -5, respectively. Figure 5.4 shows log-log plots of $\mathrm{d}h_{\max}/\mathrm{d}t$ and $-\partial^2 h/\partial x^2\,|_{x=x_{\max}}$ as a function of $d-h_{\max}$ (solid lines) and the lines of best fit (dashed lines). We have validated across four different parameter regimes, namely, (a) $L=10$ and $d=2$, (b) $L=20$ and $d=3$, (c) $L=60$ and $d=5$, and (d) $L=80$ and $d=6$, and the lines of best fit have gradients (a) -5.01003 and -1.99581, (b) -5.00375 and -1.99531, (c) -5.0027 and -1.99059, and (d) -5.0185 and -1.99343. Hence, Figure 5.4 shows that as $h_{\max} \to d$, the solutions to the governing equation (2.91) converge to the power-law behaviour predicted by the similarity solution (5.14)–(5.15). This excellent agreement was also found for solutions to the governing equation (2.91) at other points in (L,d) parameter space. Hence, this confirms that the self-similar solutions to the governing equation (2.91) are described by the similarity solution (5.14)–(5.15) with similarity exponents $\alpha = 1/6$ and $\beta = 1/4$, and so both surface tension and electrostatic effects are important during UC behaviour. Furthermore, the intercepts of the lines of best fit were used to estimate $f(0)$ and $f''(0)$ (the theory governing this is outlined in Appendix D) and are presented in Table 5.1 in Section 5.3.3.a. We will compare these estimates against the solutions to the similarity ODE (5.13) in Section 5.3.3.

5.3.2 Asymptotic far-field behaviours

Close to the time of contact, we have found that h is described locally near $x = x_{\max}$ by the similarity solution (5.14), where f obeys the similarity ODE

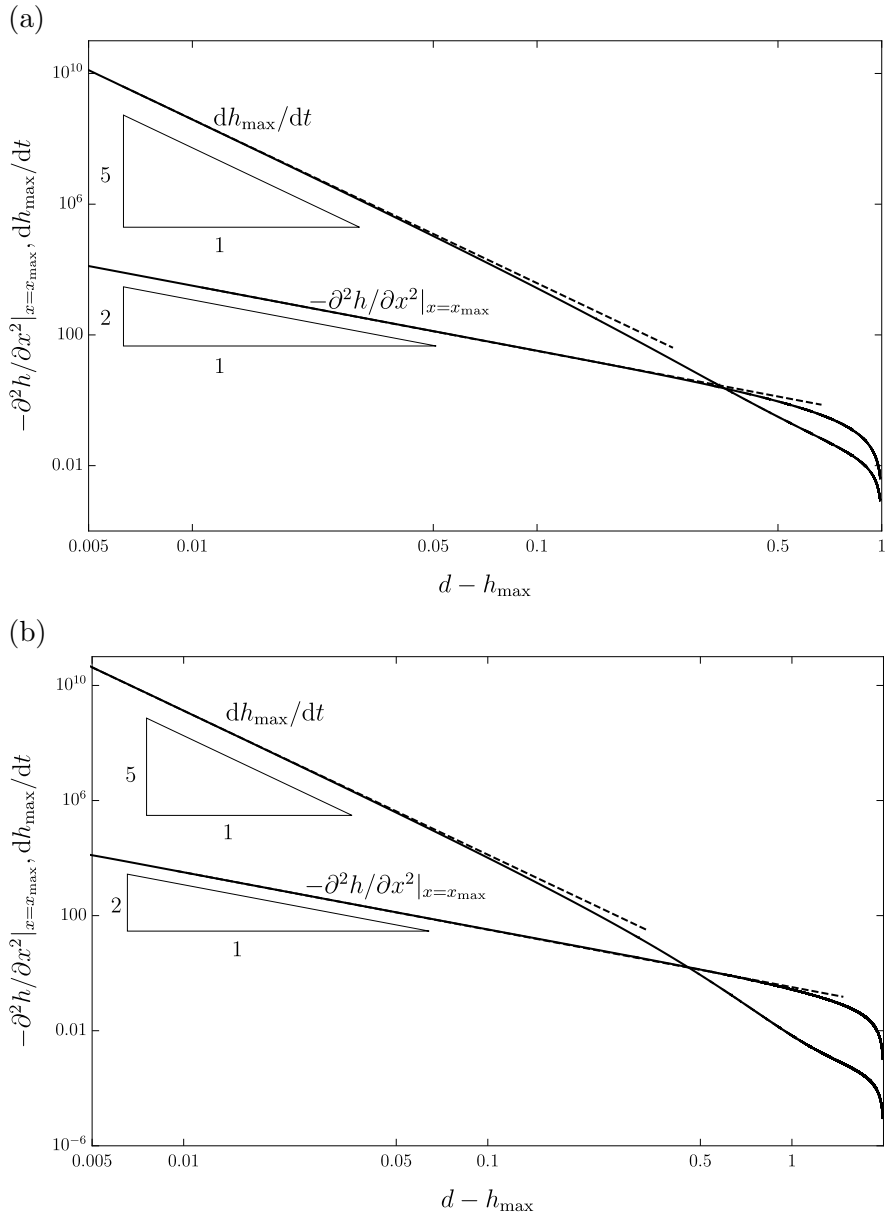

Figure 5.4: Log-log plots of $\mathrm{d}h_{\max}/\mathrm{d}t$ and $-\partial^2 h/\partial x^2\,|_{x=x_{\max}}$ as a function of $d - h_{\max}$ (solid lines) and the lines of best fit (dashed lines). The parameter values used are (a) $L = 10$ and $d = 2$, and (b) $L = 20$ and $d = 3$, and the lines of best fit have gradients (a) -5.01003 and -1.99581, and (b) -5.00375 and -1.99531.

(5.13). This local solution corresponds to an inner solution in the asymptotic sense, and we will now search for the corresponding outer solution by finding all asymptotic far-field behaviours of f as $\eta \to \infty$. These will then be compared against the far-field behaviours that are observed in the numerical solutions to the governing equation (2.91).

5.3.2.a Analytical investigation of asymptotic far-field behaviours

We look for asymptotic far-field behaviours of the similarity function f in the form

$$f \sim \eta^n \tag{5.20}$$

as $\eta \to \infty$.

Substituting (5.20) into the similarity ODE (5.13), we obtain the following balance at leading order in the limit $\eta \to \infty$,

$$\eta^n \sim \eta^{n-4} \sim \eta^{-2n-2}. \tag{5.21}$$

The first and second terms in (5.21) can never balance, however balancing the first and third terms in (5.21) yields $n = -2/3$, which gives the far-field behaviour,

$$f \sim \eta^{-2/3} \tag{5.22}$$

as $\eta \to \infty$. Therefore, using (5.14)–(5.15), this corresponds to the far-field behaviour

$$h \sim d - \tau^{1/6}\eta^{-2/3} \tag{5.23}$$

as $\eta \to \infty$.

On the other hand, balancing the second and third terms of (5.21) yields $n = 2/3$, which gives the far-field behaviour

$$f \sim \eta^{2/3} \tag{5.24}$$

as $\eta \to \infty$, and using (5.14)–(5.15) gives

$$h \sim d - \tau^{1/6}\eta^{2/3} \tag{5.25}$$

as $\eta \to \infty$. This far-field behaviour corresponds to the left hand side of the similarity ODE (5.13) being negligible in the limit $\eta \to \infty$, namely,

$$3\eta f' - 2f \sim 0, \tag{5.26}$$

which also corresponds to the time derivative term $\partial h/\partial t$ of the governing equation (2.91) being negligible. Hence (5.26) describes a quasi-steady far-field behaviour in which h is slowly-varying in time t.

5.3.2.b Numerical investigation of far-field behaviours

The similarity solution (5.14)–(5.15) can be rearranged to obtain an expression for τ, namely,

$$\tau = \left(\frac{d-h}{f(\eta)}\right)^6, \tag{5.27}$$

and this shows that, close to the time of contact at $x = x_{\max}$,

$$\tau = \left(\frac{d-h_{\max}}{f(0)}\right)^6 \ll 1. \tag{5.28}$$

This expression for τ was used in (5.14)–(5.15) evaluated at $x = x_{\max}$ to obtain

$$d - h = \frac{d - h_{\max}}{f(0)} f(\eta) \tag{5.29}$$

and

$$x - x_{\mathrm{c}} = \left(\frac{d - h_{\max}}{f(0)} \right)^{3/2} \eta \tag{5.30}$$

when $h_{\max}$ is close to d.

Equations (5.29) and (5.30) show that, close to the time of contact, $d - h \sim (d - h_{\max}) f(\eta)$ and $x - x_{\mathrm{c}} \sim (d - h_{\max})^{3/2} \eta$, which are used to plot the numerical solution to the governing equation (2.91) in appropriately rescaled coordinates, as presented in Figure 5.5. Figure 5.5 shows log-log plots of the rescaled interfacial height $(d - h)/(d - h_{\max})$ as a function of the rescaled horizontal coordinate $(x - x_{\mathrm{c}})/(d - h_{\max})^{3/2}$ (solid line) and the line of best fit (dashed line). The lines of best fit have gradients (a) 0.6620, (b) 0.6631, (c) 0.6677, and (d) 0.6730. The plots were taken at values of t where (a) $d - h_{\max} \simeq 0.02$, (b) $d - h_{\max} \simeq 0.02$, (c) $d - h_{\max} \simeq 0.05$, and (d) $d - h_{\max} \simeq 0.05$. The gradients of the lines of best fit describe the behaviour in the bulk of the domain away from the boundaries, and they suggest that the rescaled interfacial height $(d - h)/(d - h_{\max})$ varies approximately like $\left((x - x_{\mathrm{c}})/(d - h_{\max})^{3/2}\right)^{2/3} = (x - x_{\mathrm{c}})^{2/3}/(d - h_{\max})$, i.e. $f \sim \eta^{2/3}$. This shows that the quasi-steady far-field behaviour described by (5.24) and not that described by (5.22), is the one observed in the solutions to the governing equation (2.91). This means that the interface close to contact is described by the similarity ODE (5.13), and this matches to the quasi-steady behaviour described by (5.24) as $\eta \to \infty$.

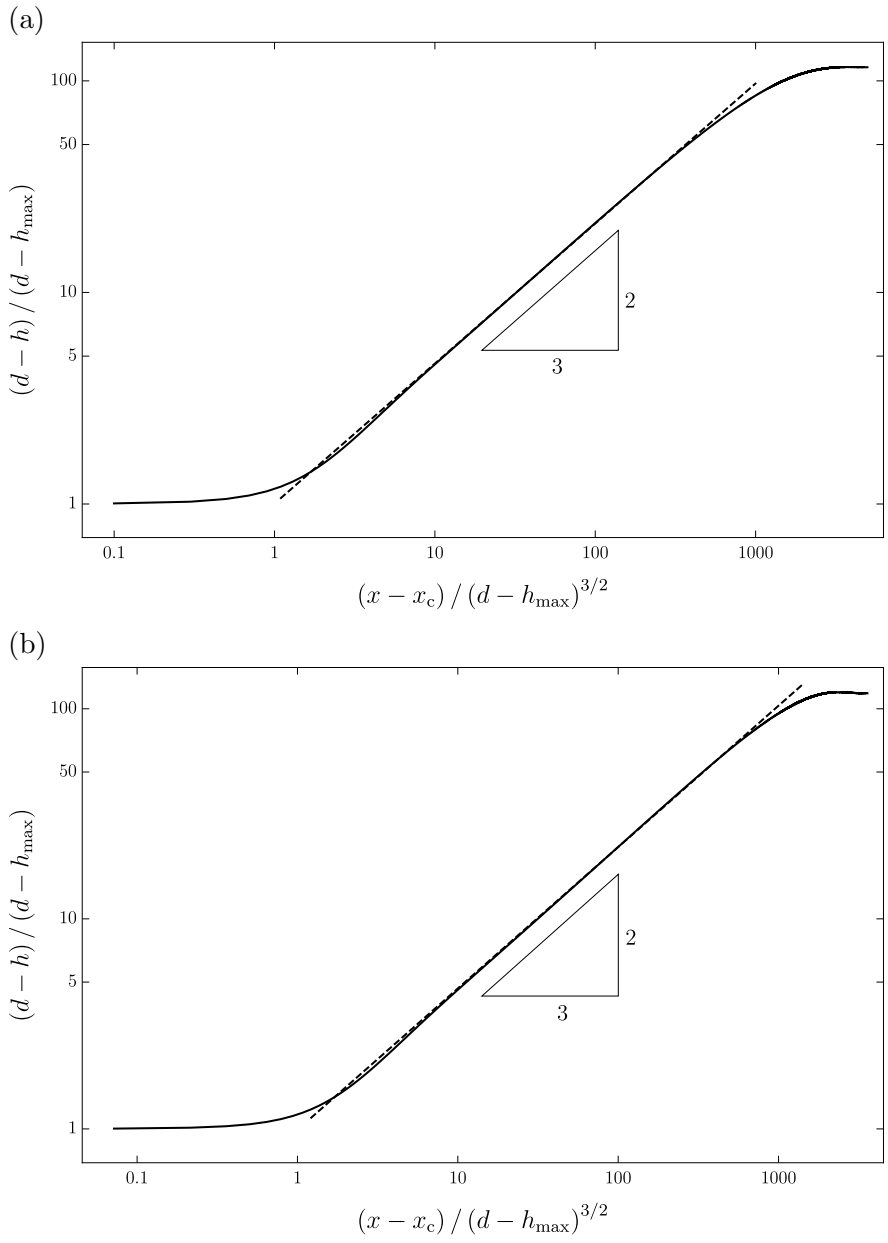

Figure 5.5: Log-log plots of the rescaled interfacial height $(d-h)/\,(d-h_{\max})$ as a function of the rescaled horizontal coordinate $(x-x_{\mathrm{c}})/(d-h_{\max})^{3/2}$ (solid line) and the line of best fit (dashed line). The lines of best fit have gradients (a) 0.6620 and (b) 0.6631. The plots were taken at values of t where $d-h_{\max} \simeq 0.02$. The parameter values used are (a) $L=10$ and $d=2$, and (b) $L=20$ and $d=3$.

5.3.3 Numerical solution of the similarity ODE (5.13)

The shooting method used to solve the similarity ODE (5.13) provides further confirmation that the solutions to the governing equation (2.91) are described by the similarity solution (5.14)–(5.15). The similarity ODE was solved over a large but finite integration interval from $\eta = 0$ to $f = \eta_{\text{end}}$. In practice, we found it sufficient to use $\eta_{\text{end}} = 10$. Furthermore, four boundary conditions are required since the ODE is fourth-order. Firstly, we imposed two boundary conditions at $\eta = 0$, namely,

$$f'(0) = f'''(0) = 0, \tag{5.31}$$

and are the symmetry boundary conditions.

The two remaining boundary conditions were imposed at the end of the integration interval, namely,

$$3\eta f'(\eta) - 2f(\eta) = 0, \tag{5.32}$$

$$9\eta^2 f''(\eta) + 2f(\eta) = 0, \tag{5.33}$$

evaluated at $\eta = \eta_{\text{end}}$. We chose equations (5.32) and (5.33) so that the quasi-steady far-field behaviour (5.24) was satisfied at $\eta = \eta_{\text{end}}$ and their solutions are independent of each other. Specifically, the solutions to equations (5.32) and (5.33) are $f = A\eta^{2/3}$ and $f = B\eta^{1/3} + C\eta^{2/3}$, respectively, where A, B, and C are constants. Hence, for both solutions, $f \propto \eta^{2/3}$ for large η, which corresponds to the quasi-steady far-field behaviour (5.24). To confirm that this far-field condition gives the correct number of boundary conditions, we may follow Zhang and Lister [71] and linearise (5.13) about $\eta = \eta^{2/3}$. We find that there are two exponentially growing modes, so that imposing this far-field condition is equivalent to requiring that the amplitudes corresponding to both these modes must vanish as $\eta \to \infty$,

which constitutes two boundary conditions.

The shooting method described in Section 4.2 is used to solve the similarity ODE (5.13) subject to the four boundary conditions (5.31)–(5.33). Recall that the shooting method is split into two parts:

1. An investigation of $(f(0), f''(0))$-space to search for points at which the solution to (5.13) satisfies both boundary conditions (5.32) and (5.33) at $\eta = \eta_{\text{end}}$.

2. Solving the similarity ODE (5.13) from $\eta = 0$ to $\eta = \eta_{\text{end}}$, subject to the initial conditions (5.31) and the points in $(f(0), f''(0))$-space found in step 1.

5.3.3.a Investigation of $(f(0), f''(0))$-space

Part 1 of the shooting method, described above, involves investigating $(f(0), f''(0))$-space to find regions where the solution to the similarity ODE (5.13) satisfies either boundary condition (5.32) or (5.33) at $\eta = \eta_{\text{end}}$. The investigation was performed in two steps using the Matlab code introduced in Section 4.2.2:

1. We fixed a value of $f(0)$, and continued on the value of $f''(0)$ in order to find parameter pairs where the solution to the similarity ODE satisfies equation (5.32).

2. We then fixed a value of $f''(0)$, and continued on the value of $f(0)$ in order to find parameter pairs where the solution to the similarity ODE satisfies equation (5.33).

The results of the investigation of $(f(0), f''(0))$-space are presented in Figure 5.6. Figure 5.6 shows the results of the investigation of $(f(0), f''(0))$-space where the black and grey dots (which are so numerous they appear to be lines) correspond to points where the solution to the similarity ODE (5.13) satisfies the boundary

conditions (5.32) and (5.33), respectively. The larger black dots show the points located at (a) $(0.7905, 0.5095)$, (b) $(0.9655, 0.3445)$, (c) $(1.2355, 0.2055)$, and (d) $(1.3655, 0.1625)$, which are estimates of $f(0)$ and $f''(0)$ for which the solution to (5.13) satisfies both boundary conditions (5.32) and (5.33). These points were estimated by drawing straight lines between the dots and finding the four data points surrounding the intersection point, denoted by (x_1, y_1), (x_1, y_2), (x_2, y_1), and (x_2, y_2). The estimate of the intersection point was obtained by calculating $((x_2 - x_1)/2, (y_2 - y_1)/2)$, which is a good approximation since $x_2 - x_1$ and $y_2 - y_1$ are small.

Figure 5.6 shows that there are many intersection points (where the solution to the similarity ODE (5.13) satisfies both boundary conditions (5.32) and (5.33) at $\eta = \eta_{\text{end}}$) and so we conclude that there is a family of solutions to the similarity ODE (5.13). As also noted by Zhang and Lister [71], the spacing between intersection points decreases as $f(0) \to 0$, suggesting that there are countably infinite solutions to (5.13). However, note that the points indicated by the larger black dots are in very good agreement with the estimates of $f(0)$ and $f''(0)$ using the numerical solutions, given in Table 5.1, and we expect that this agreement would improve even more if the numerical calculations could get closer to the time of contact. Hence, this suggests that the similarity solutions obtained using the points denoted by the larger black dots correspond to the solutions to the governing equation (2.91). Furthermore, we also searched $(f(0), f''(0))$-space for different values of η_{end} from 4 to 10, which changed its qualitative structure. However, the intersection points denoted by the larger black dots stayed roughly the same.

5.3.3.b Solving the similarity ODE (5.13)

The similarity ODE (5.13) is solved using the Matlab code introduced in Section 4.2.2 to perform the shooting method, in which the following initial conditions

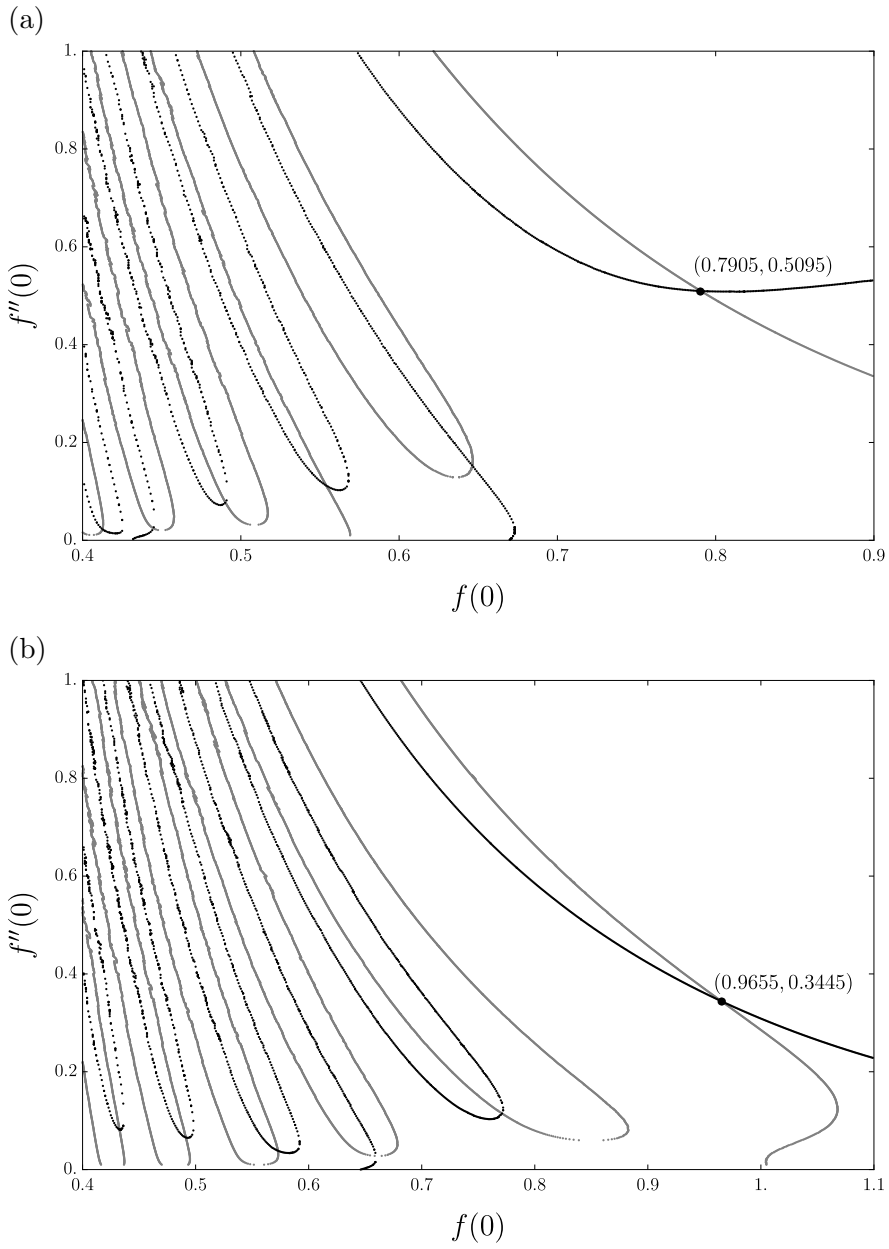

Figure 5.6: Results of the investigation of $(f(0), f''(0))$-space where the black and grey dots (which are so numerous they appear to be lines) correspond to points where the solution to the similarity ODE (5.13) satisfies the boundary conditions (5.32) and (5.33), respectively. The parameter values used are $\eta_{\text{end}} = 10$ and (a) $d = 2$ and (b) $d = 3$. The larger black dots show the points located at (a) $(0.7905, 0.5095)$ and (b) $(0.9655, 0.3445)$ that are estimates of $f(0)$ and $f''(0)$ for which the solution to the ODE satisfies both boundary conditions (5.32) and (5.33).

Figure 5.4	(a)	(b)	(c)	(d)
$f(0)$	0.7796	0.9597	1.2414	1.3446
$f''(0)$	0.5387	0.3559	0.2162	0.1820

Table 5.1: Estimated values for $f(0)$ and $f''(0)$ using the intercepts of the lines of best fit in Figure 5.4.

are used

$$f(0) = f_0, \qquad f'(0) = 0, \qquad f''(0) = f_0'', \qquad f'''(0) = 0, \tag{5.34}$$

where f_0 and f_0'' are constants. Recall that, close to contact, we obtained an expression for τ, namely, expression (5.28), which was used to give equations (5.29) and (5.30). Hence, both f and η can be expressed in terms of h and $x - x_c$, respectively, i.e.

$$f(\eta) = \frac{f(0)}{d - h_{\max}} (d - h), \tag{5.35}$$

$$\eta = \left(\frac{f(0)}{d - h_{\max}} \right)^{3/2} (x - x_c), \tag{5.36}$$

where the value of $f(0)$ corresponds to the intersection point denoted by the larger black dots in Figure 5.6. Equations (5.35) and (5.36) allow us to compare the solutions to the similarity ODE (5.13) with the corresponding solutions to the governing equation (2.91).

Figure 5.7 shows plots of the rescaled interfacial height $(f(0)/(d - h_{\max}))\,(d-h)$ as a function of the rescaled horizontal coordinate $(f(0)/(d - h_{\max}))^{3/2}\,(x-x_c)$ (solid line) and the corresponding solution to the similarity ODE (dashed line) with initial conditions (5.34) in which (a) $f_0 = 0.7905$, and $f_0'' = 0.5095$, (b) $f_0 = 0.9655$ and $f_0'' = 0.3445$, (c) $f_0 = 1.2355$ and $f_0'' = 0.2055$, and (d) $f_0 = 1.3655$ and $f_0'' = 0.1625$. The values of f_0 and f_0'' were chosen so that they correspond to the larger black dots in Figure 5.6. The plots of the solutions to the governing equa-

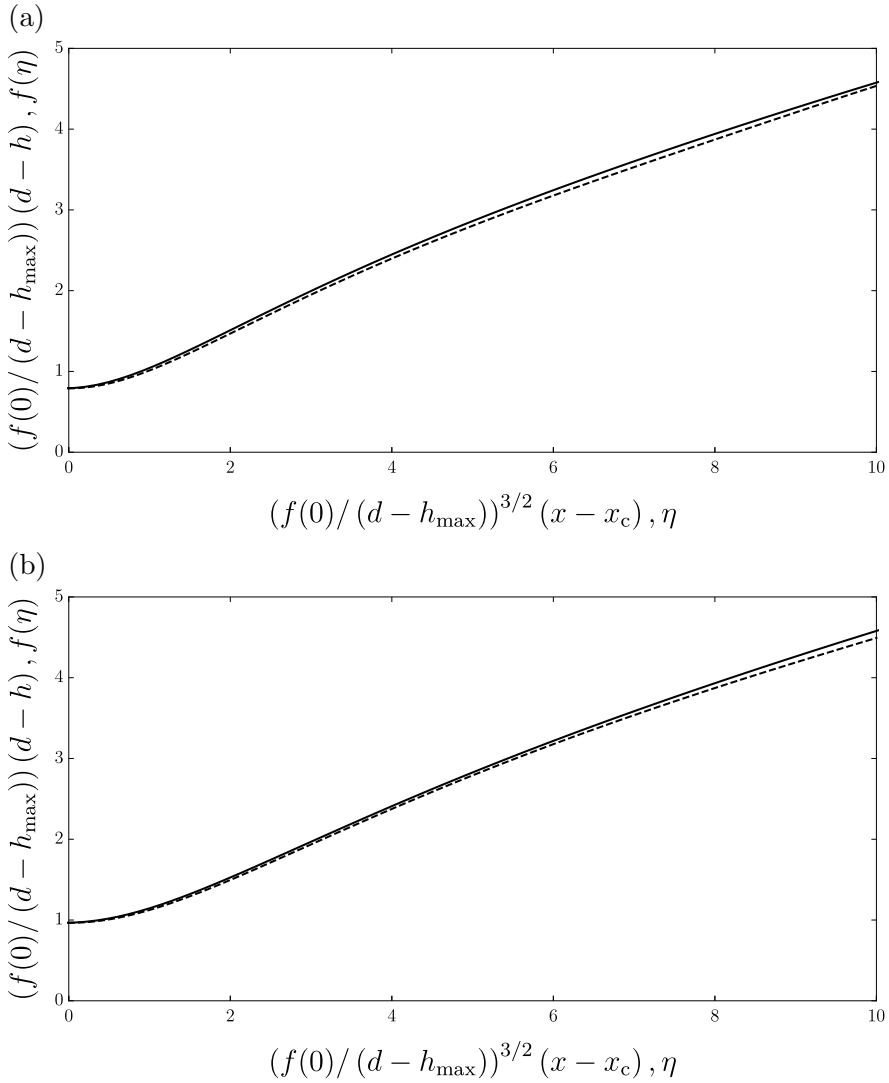

Figure 5.7: Plots of the rescaled interfacial height $(f(0)/(d-h_{\max}))\,(d-h)$ as a function of the rescaled position $(f(0)/(d-h_{\max}))^{3/2}\,(x-x_{\mathrm{c}})$ (solid line) and the corresponding solution to the similarity ODE (dashed line) with initial conditions (5.34) in which (a) $f_0 = 0.7905$, and $f_0'' = 0.5095$, and (b) $f_0 = 0.9655$ and $f_0'' = 0.3445$. The plots of the solution to (2.91) correspond to values of t where (a) $d - h_{\max} \simeq 0.02$. The parameter values are (a) $L = 10$, $d = 2$ and (b) $L = 20$, $d = 3$.

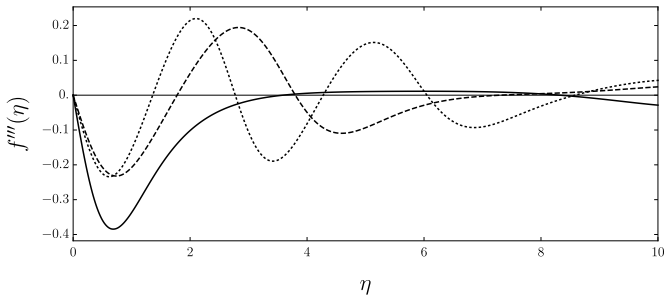

Figure 5.8: Plots of $f'''(\eta)$ as a function of η using the initial conditions (5.34) in which $f_0 = 0.7905$ and $f_0'' = 0.5095$ (solid line), $f_0 = 0.6465$ and $f_0'' = 0.1535$ (dashed line), and $f_0 = 0.554$ and $f_0'' = 0.1115$ (dotted line). The parameter values used are $\eta_{\text{end}} = 10$ and $d = 2$.

tion (2.91) correspond to values of t where (a) $d - h_{\max} \simeq 0.02$, (b) $d - h_{\max} \simeq 0.02$, (c) $d - h_{\max} \simeq 0.05$, and (d) $d - h_{\max} \simeq 0.05$.

Figure 5.7 shows very good agreement between the rescaled solutions to the governing equation (2.91) and the solutions to the similarity ODE (5.13). Specifically, the rescaled solutions to the governing equation (2.91) converge to the solutions to the similarity ODE (5.13) as $h_{\max} \to d$. However, the numerical calculations can only be computed up to around $d - h_{\max} = 0.01$ due to restrictions in the number of grid points, and so we would expect even better agreement for numerical solutions closer to contact. Together with the results in Section 5.3.1.a, this confirms that, during UC behaviour, the interface exhibits self-similar behaviour which is described by the similarity solution (5.14)–(5.15). In particular, h is described near $x = x_{\max}$ by the similarity ODE (5.13) and quasi-steady far field behaviour, as described by (5.24), at $\eta \to \infty$. As discussed in Chapter 1, Zhang and Lister [71] concluded that solutions to their governing equation corresponds to the intersection point with the largest value of $f(0)$, which gives the least oscillatory curvature profile. Also, Witelski and Bernoff [72] subsequently showed that this was the only stable similarity solution.

For the present problem, Figure 5.8 shows plots of $f'''(\eta)$ as a function of η using the initial conditions (5.34) in which $f_0 = 0.7905$ and $f_0'' = 0.5095$ (solid line), $f_0 = 0.6465$ and $f_0'' = 0.1535$ (dashed line), and $f_0 = 0.554$ and $f_0'' = 0.1115$ (dot-

ted line). These initial conditions correspond to the first three intersection points from right to left in Figure 5.6(a) (estimated using the same method described previously). Figure 5.8 shows the same structured ordering as seen by Zhang and Lister [71], where there are extra half oscillations of the $f'''(\eta)$ profile at each intersection point as $f(0)$ decreases. The same behaviour is seen for other values of η_{end} and d. Hence, following the same logic used by Zhang and Lister [71], we conclude that there are no more intersection points for values of $f(0)$ larger than those corresponding to the larger black dots in the $(f(0), f''(0))$-space plots in Figure 5.6, and the self-similar behaviour observed in the solutions to the governing equation (2.91) corresponds to the least oscillatory curvature profile. We will hypothesise that the similarity solutions obtained using smaller values of $f(0)$, that are not observed in the solutions to (2.91), are unstable, though a stability analysis has not been performed.

Lastly, we note that the similarity ODE (5.13) can be recast into canonical form using the scalings

$$f = d^{1/2} g, \qquad \eta = d^{3/4} \xi, \tag{5.37}$$

where $g = g(\xi)$, giving

$$3\xi g' - 2g = -4(g^{(4)} + (g^{-3} g')'). \tag{5.38}$$

Hence, under these rescalings, the parameter d falls out of the similarity ODE (5.13), and we find that the solutions to the similarity ODE presented in Figure 5.7 collapse onto the same curve.

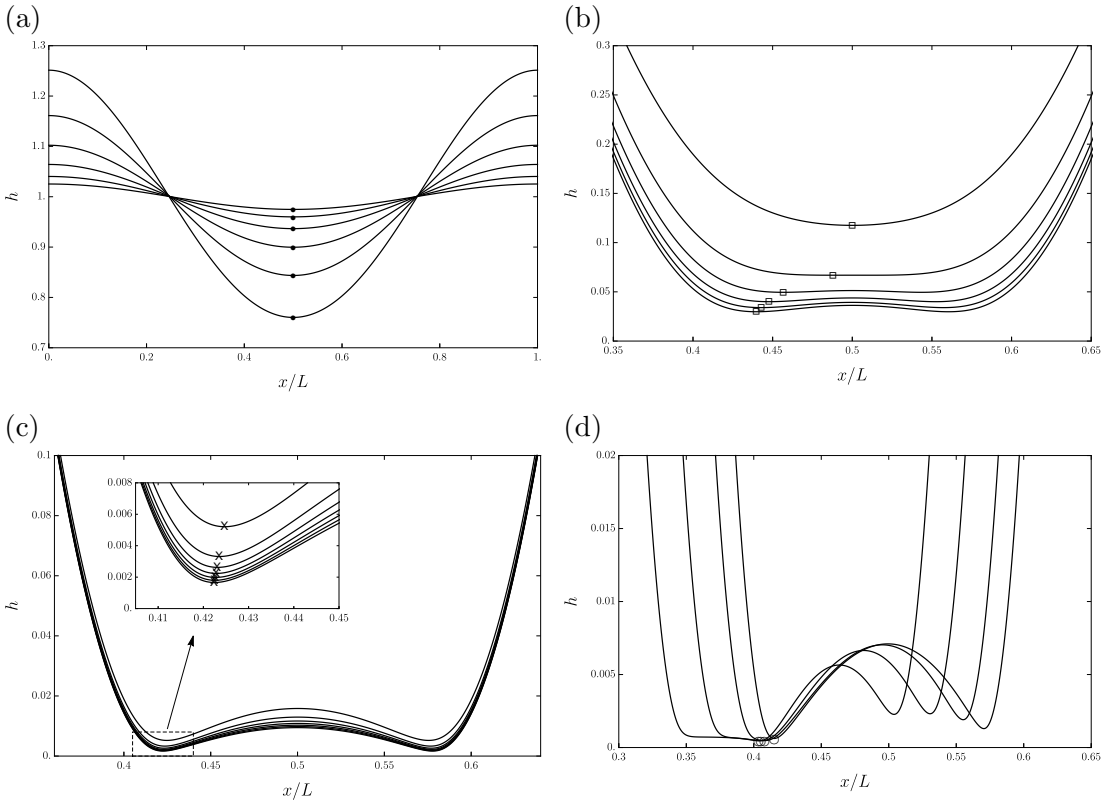

Figure 5.9: Plots of h as a function of x/L during the (a) progressive growth, (b) buckling, (c) asymptotic thinning, and (d) onset of sliding stages. The dots, squares, crosses, and circles are used to track the positions of $h_{\min}$ during the progressive growth, buckling, asymptotic thinning, and onset of sliding stages, respectively. The parameter values used are $L = 100$ and $d = 7$.

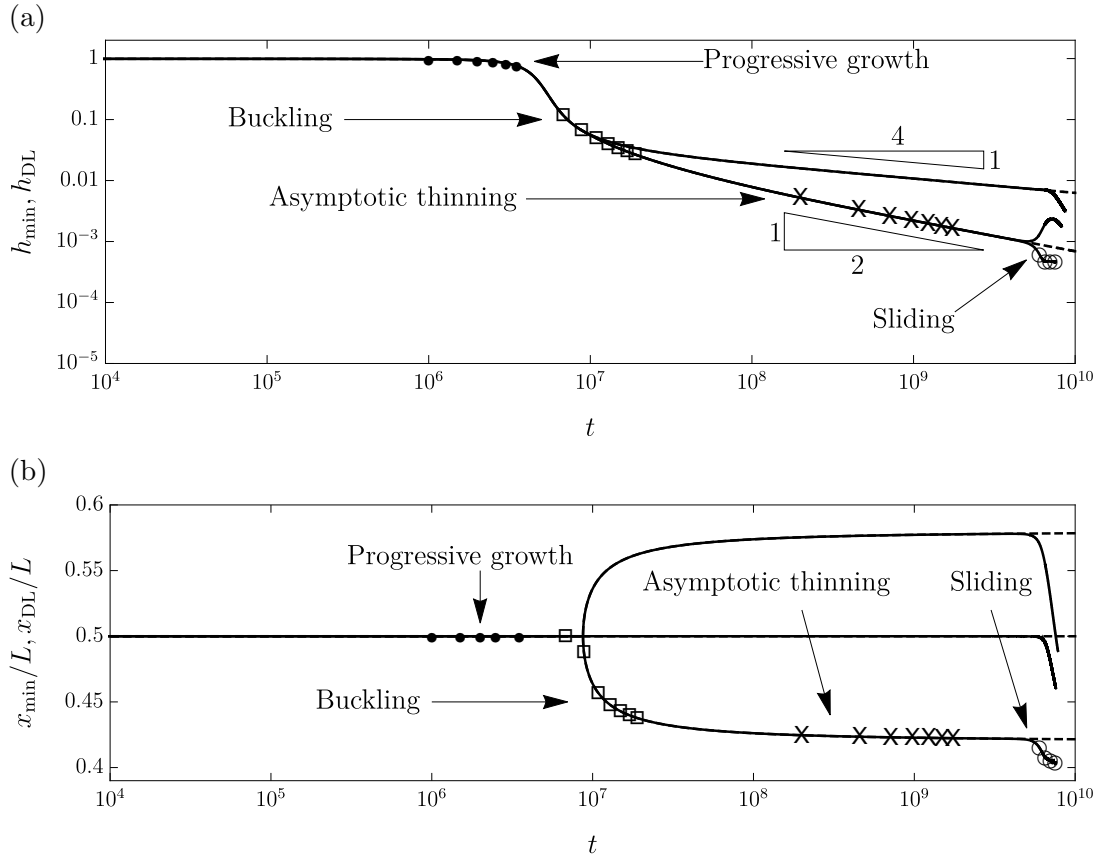

Figure 5.10: Plots of (a) $h_{\min}$ and h_{DL} as functions of t, and (b) $x_{\min}/L$ and x_{DL}/L as functions of t. Note that, in (a) the horizontal and vertical axes are logarithmically scaled, and in (b) the horizontal axes is logarithmically scaled. The dots, squares, crosses, and circles correspond to those in Figure 5.9. The solid and dashed lines correspond to the numerical calculations in which the periodic and symmetric boundary conditions are imposed, respectively, and are indistinguishable until $t \approx 6 \times 10^9$. The parameter values used are $L = 100$ and $d = 7$.

5.4 Thinning (TH) behaviour

TH behaviour occurs when the interface evolves through four different stages, which we term "progressive growth", "buckling", "asymptotic thinning", and "onset of sliding", as illustrated by Figure 5.9. Figure 5.9 shows plots of h as a function of x/L during the (a) progressive growth, (b) buckling, (c) asymptotic thinning, and (d) onset of sliding stages. The dots, squares, crosses, and circles are used to track the positions of $h_{\min}$ during the progressive growth, buckling, asymptotic thinning, and onset of sliding stages, respectively. Note that, unless otherwise stated, the periodic boundary conditions are imposed. The evolution of the interface through these four stages are the same as those found by Dietze *et al.* [86] who considered the Rayleigh–Taylor instability of a fluid film suspended from a ceiling.

During the progressive growth stage, the interface approaches the lower electrode, as shown in Figure 5.9(a). The resistance to flow increases as h approaches the lower electrode, and this is characterised by the mobility coefficient $h^3/3$ present in the governing equation (2.91), which corresponds to the effect of viscosity.

During the buckling stage, the interface flattens as it approaches the lower electrode, and ultimately the "buckling" occurs where the interface forms two trough regions (that each contain a local minimum), two filling lobes and a draining lobe, as shown in Figure 5.9(b). Note that in Figure 5.9(b), the draining lobe is located between the two trough regions, i.e. between $x/L \approx 0.44$ and $x/L \approx 0.56$, and the filling lobes are located at both ends of the domain. The liquid flows from the draining lobe into the filling lobe through the trough regions, and the local minima in the trough regions approach the lower electrode. Symmetry is imposed at $t = 0$, since the initial initial conditions (4.17) are used, and holds for some of the calculation. Hence, the height of the local minima in the trough regions have the same value, namely $y = h_{\min}$. Due to the symmetry of the interface, we only track the position of the minimum for the leftmost trough region in Figure 5.9.

The interface now enters the asymptotic thinning stage, as shown by Figure 5.9(c), where the liquid continues to drain from the draining lobe into the filling lobes through the trough regions, and the local minima located in the trough regions continue to approach the lower electrode. The interface is also in a quasi-steady regime during the asymptotic thinning stage, in which the variation of the interface in time t is small, and this will be shown analytically in Section 5.4.1. It is also observed during the asymptotic thinning stage that $h_{\min}$ and the height of the draining lobe, denoted by $h_{\rm DL} = h_{\rm DL}(t)$ at $x/L = x_{\rm DL}/L = 0.5$, approach a power-law behaviour at large times, specifically, $h_{\min} = O(t^{-1/2})$ and $h_{\rm DL} = O(t^{-1/4})$, as illustrated in Figure 5.10(a). Figure 5.10 shows plots of (a) $h_{\min}$ and $h_{\rm DL}$ as functions of t, and (b) $x_{\min}/L$ and $x_{\rm DL}/L$ as functions of t. Note that, in (a) the horizontal and vertical axes are logarithmically scaled, and in (b) the horizontal axis is logarithmically scaled. The dots, squares, crosses, and circles correspond to those in Figure 5.9. The solid and dashed lines correspond to the numerical calculations in which the periodic and symmetric boundary conditions are imposed, respectively, and are indistinguishable until $t \approx 6 \times 10^9$. Recall that the symmetric boundary conditions are imposed using the Matlab code introduced in Section 4.1.4. The parameter values used are $L = 100$ and $d = 7$. Note that $x = x_{\min}$ denotes the positions of the local minima in the trough regions.

Furthermore, the values of $h_{\min}$ and $h_{\rm DL}$ continue to decrease like $O(t^{-1/2})$ and $O(t^{-1/4})$, respectively, until asymmetric disturbances, which are seeded by small numerical noise, stimulate the onset of sliding (and this will be discussed further in Section 5.4.2). The onset of sliding stage is characterised by a loss of symmetry and the interface translates to the left, as illustrated by Figures 5.9(d) and 5.10. Note that the interface can also translate to the right, and we will show in Section 5.4.2 that the direction of translation is determined by numerical errors seeded by numerical noise. Figure 5.10(a) shows that the values of the local minima

$h_{\min}$ in the two trough regions diverge from each other, highlighting the loss of symmetry, and Figure 5.10(b) shows the positions of the local minima $x_{\min}$ and the position of the draining lobe x_{DL} moves to the left at $t \approx 6 \times 10^9$, highlighting the translation of the interface to the left. Note that the circles in Figures 5.9 and 5.10 now track the global minimum point, since symmetry is lost and the local minima values in the two trough regions diverge.

The numerical calculations of Pillai and Narayanan [118, 126], who studied this system, also show that sliding occurs. Furthermore, if the symmetric boundary conditions are used (implemented using the Matlab code introduced in Section 4.1.4), then the onset of sliding would never occur since asymmetric disturbances are removed at every time step of the numerical calculations. Therefore, the asymptotic thinning stage would continue indefinitely for increasing t, and $h_{\min}$ and h_{DL} would continue to show the power-law behaviour described earlier, i.e. $h_{\min} = O(t^{-1/2})$ and $h_{\mathrm{DL}} = O(t^{-1/4})$. The dashed lines in Figure 5.10 show that these symmetric boundary conditions do indeed stop sliding. Specifically, the dashed lines in Figure 5.10(a) show that there is no loss of symmetry in the values of the local minima in the two trough regions $h_{\min}$, and Figure 5.10 shows that the positions of the local minima and the draining lobe $x_{\min}$ and x_{DL}, respectively, do not move to the left at all. The results of the numerical calculations introduced above were observed for other values of L and d.

In Section 5.4.1, the asymptotic thinning stage is investigated analytically. In particular, a similarity solution describing the trough region (at times where $h_{\min} \ll 1$) is determined, and the time dependence of the system is then determined analytically which agrees with the numerical results. Furthermore, in Section 5.4.2, the onset of sliding is investigated by performing a frozen-time linear stability analysis (which will be introduced and discussed in Section 5.4.2), which shows that the sliding phenomenon is caused by asymmetric disturbances.

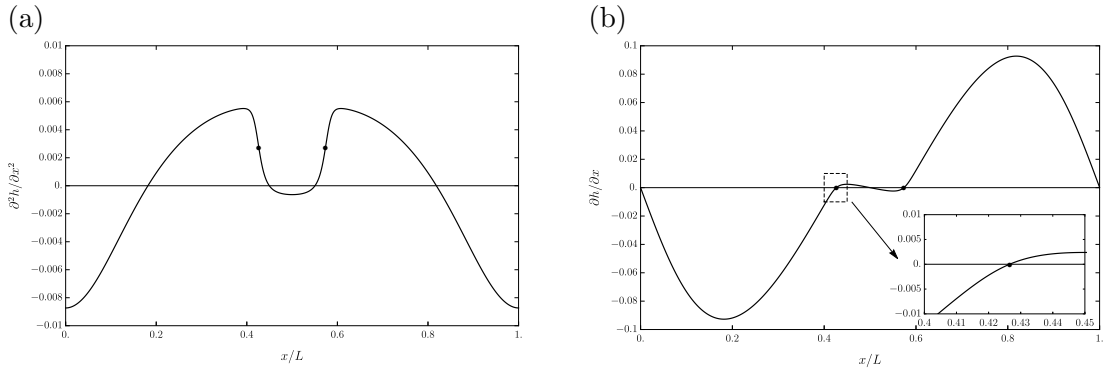

Figure 5.11: Plots of (a) $\partial^2 h/\partial x^2$, and (b) $\partial h/\partial x$ as functions of x/L. The dots indicate the positions of the local minima in the trough regions. The profiles are shown at $t \approx 9 \times 10^7$ for which $h_{\min} = 8.351 \times 10^{-3}$, and the parameter values used are $L = 100$ and $d = 7$.

5.4.1 Investigation of the asymptotic thinning stage

In this Section, we take inspiration from the work of Hammond [81], who obtained asymptotic solutions to the long-time behaviour of a draining lobe when he investigated the nonlinear evolution of an axisymmetric annular film confined within a cylindrical pipe, as discussed in Chapter 1. Specifically, we obtain a similarity solution that describes the interface in the trough regions during the asymptotic thinning stage of TH behaviour, specifically, at times when $h_{\min} \ll 1$. We consider a system of filling lobe, trough, and draining lobe regions, in which the local minima in the trough regions are located at $x = \pm x_0$, and the draining lobe is in the region $-x_0 \leq x \leq x_0$. We will consider the trough region at $x = x_0$, although, due to symmetry, a similar analysis will apply to the trough region at $x = -x_0$. Firstly, we seek a similarity solution for h in the trough region of the form,

$$h = \epsilon H(\eta), \qquad \eta = \frac{x - x_0}{\epsilon^\alpha}, \tag{5.39}$$

where $\epsilon \ll 1$ is a measure of the height of the trough region, $H = H(\eta)$ is the similarity function, and α is the similarity exponent. The numerical results,

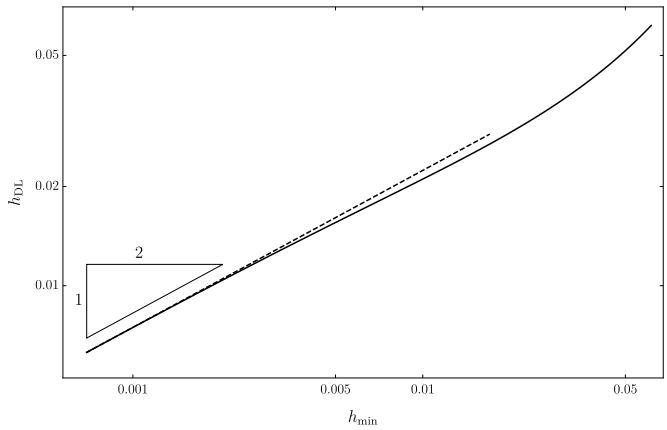

Figure 5.12: Log-log plots of h_{DL} as a function of $h_{\min}$ where the dashed line is the line of best fit with gradient 0.4764. The symmetric boundary conditions are used so that sliding does not occur, and the parameter values used are $L = 100$ and $d = 7$.

specifically the variation in curvature $\partial^2 h/\partial x^2$ across the local minima in the trough regions, shown in Figure 5.11(a), are used to determine the value for α. Figure 5.11 shows plots of (a) $\partial^2 h/\partial x^2$, and (b) $\partial h/\partial x$ as functions of x/L. The dots indicate the positions of the local minima in the trough regions. Figure 5.11(a) shows that the curvature changes by $O(1)$ across the local minimum located at $x = x_{\min}$. Motivated by these results, we infer that $\partial^2 h/\partial x^2$ is of order unity the trough region, and using the similarity solution (5.39) we obtain

$$\epsilon^{1-2\alpha} H''(\eta) = O(1), \tag{5.40}$$

and hence $\alpha = 1/2$, i.e. the appropriate lengthscale in the trough region is $x = O(\epsilon^{1/2})$, and so the similarity solution (5.39) becomes

$$h = \epsilon H(\eta), \qquad \eta = \frac{x - x_0}{\epsilon^{1/2}}. \tag{5.41}$$

In Section 5.4.1.a, the heights and lengthscales of the filling and draining lobe regions are obtained, then, in Section 5.4.1.b, the timescales in the filling lobe, trough, and draining lobe regions are determined, and we show that the interface in these regions is quasi-steady. In Sections 5.4.1.c and 5.4.1.d, the governing

equation for H in the trough region and the matching conditions to the filling and draining lobes are determined, respectively, and the resultant system is presented in Section 5.4.1.e. Furthermore, the system is used in Section 5.4.1.f to show analytically that the time dependence h in the trough and draining lobe regions are $h = O(t^{-1/2})$ and $h = O(t^{-1/4})$, respectively, agreeing with the numerical results shown in Figure 5.10(a).

5.4.1.a Obtaining the heights and lengthscales of the draining and filling lobe regions

The draining lobe is investigated first, in which the height and lengthscale are taken to be $h = O(t^{n_1})$ and $x = O(t^{n_2})$, where the exponents n_1 and n_2 are constants to be determined. Figure 5.12 shows log-log plots of h_{DL} as a function of h_{min}, where the dashed line is the line of best fit with gradient 0.4764. Symmetric boundary conditions are used so that sliding does not occur, and the parameter values used are $L = 100$ and $d = 7$. Figure 5.12 (and similar plots for other values of L and d not shown for brevity) suggests that log-log plots of h_{DL} as a function of h_{min} converge to straight lines with gradients of $1/2$ as $t \to \infty$. Since

$$\frac{\log\left(h_{\mathrm{DL}}\right)}{\log\left(h_{\mathrm{min}}\right)} \sim \frac{\log\left(\epsilon^{n_1}\right)}{\log\left(\epsilon\right)} = n_1, \tag{5.42}$$

the numerical results suggest that $n_1 = 1/2$, i.e. the height of the draining lobe is $h = O(\epsilon^{1/2})$. The lengthscale of the draining lobe can now be determined by substituting $h = O(\epsilon^{1/2})$ and $x = O(\epsilon^{n_2})$ into the governing equation (2.91). Ensuring that the surface tension and electrostatic effects are both important in the draining lobe means that the second and third terms (corresponding to surface tension and electrostatic effects, respectively) must balance, giving

$$\epsilon^{1/2-3n_2} \sim \epsilon^{1/2-n_2}. \tag{5.43}$$

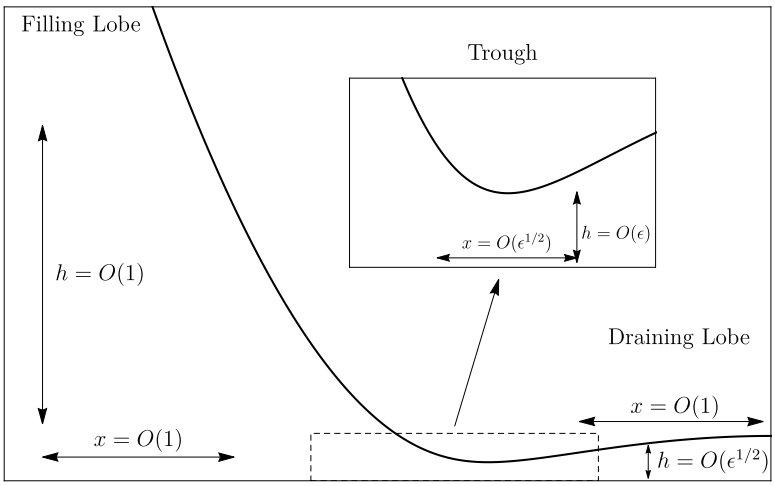

Figure 5.13: A schematic of the heights and lengthscales of the filling lobe, the trough, and the draining lobe regions.

Hence, $n_2 = 0$, and so the lengthscale of the draining lobe region is $x = O(1)$. Now considering the filling lobe regions, again motivated by the numerical results, we pose that the heights of the filling lobes are $h = O(1)$, and the lengthscale is $x = O(\epsilon^{n_3})$, where the exponent n_3 is a constant to be determined. The lengthscale is determined by substituting $h = O(1)$ and $x = O(\epsilon^{n_3})$ into the governing equation (2.91). Again, ensuring that surface tension and electrostatic effects are important in the filling lobe means that the second and third terms must balance, which gives

$$\epsilon^{-3n_3} \sim \epsilon^{-n_3}. \tag{5.44}$$

Hence, $n_3 = 0$, and so the lengthscales of the filling lobe regions are $x = O(1)$. In summary, the heights and lengthscales of the three different regions, namely, the filling lobe, trough, and draining lobe regions, have been determined, as summarised in Figure 5.13. Figure 5.13 is a schematic of the heights and lengthscales of the filling lobe, trough, and draining lobe regions.

5.4.1.b Determination of different timescales

Recall that, during the asymptotic thinning stage, the liquid flows from the draining lobe through the troughs and into the filling lobes. The heights and lengthscales in these regions are different (and shown in Figure 5.13), and so the timescales may be different too. Furthermore, an additional timescale needs to be considered, namely, the timescale for drainage, i.e. the drainage of the liquid from the draining lobe into the filling lobe. We will show that the timescale for drainage is much longer than the timescales in the filling lobe, trough, and draining lobe regions. This means that the filling lobe, trough and draining lobe regions can be treated as quasi-steady, and so time derivative terms in the differential equations describing them can be neglected.

Firstly, the timescales in the trough regions are $t = O(\epsilon^{n_4})$, where the exponent n_4 is a constant to be determined. Recall that $h = O(\epsilon)$ and $x = O(\epsilon^{1/2})$ in the trough regions, and from the governing equation (2.91) the following balance is obtained between the time derivative term and the capillary and electrostatic terms,

$$\epsilon^{1-n_4} \sim \epsilon^2. \tag{5.45}$$

Hence, $n_4 = -1$, and so the timescale in the trough regions is $t = O(\epsilon^{-1})$.

Secondly, the timescale in the draining lobe region is $t = O(\epsilon^{n_5})$, where the exponent n_5 is a constant to be determined. Recall that $h = O(\epsilon^{1/2})$ and $x = O(1)$ in the draining lobe regions, and the governing equation (2.91) gives the following balance between the time derivative and capillary terms,

$$\epsilon^{1/2-n_5} \sim \epsilon^2. \tag{5.46}$$

Hence, $n_5 = -3/2$, and so the timescale in the draining lobe region is $t = O(\epsilon^{-3/2})$. Furthermore, the timescales in the filling lobe regions are $t = O(\epsilon^{n_6})$, where the exponent n_6 is a constant to be determined. Recall that $h = O(1)$ and $x = O(1)$ in the filling lobe regions, and from the governing equation (2.91) the following balance is obtained between the time derivative term and the capillary and electrostatic terms,

$$\epsilon^{n_6} \sim \epsilon^0. \tag{5.47}$$

Hence, $n_6 = 0$, and so the timescale in the filling lobe regions is $t = O(1)$.

The timescale for the drainage of liquid from the draining lobe into the filling lobes through the trough region is now determined. We express the governing equation (2.91) as

$$\frac{\partial h}{\partial t} = -\frac{\partial Q}{\partial x}, \tag{5.48}$$

where $Q = Q(x,t)$ is the volume flux of liquid in the x-direction, namely,

$$Q = \frac{h^3}{3}\left(\frac{\partial^3 h}{\partial x^3} + \frac{1}{(d-h)^3}\frac{\partial h}{\partial x}\right). \tag{5.49}$$

Integrating equation (5.48) with respect to x between $-x_0$ and x_0, i.e. between the two trough regions, gives

$$\frac{\partial V}{\partial t} = -(Q(-x_0) - Q(x_0)) = -2Q(x_0), \tag{5.50}$$

where $V = V(t)$ is the volume of liquid in the draining lobe and the second equality comes from the symmetry of the interface. Note that equation (5.50) states that the change in volume of liquid in the draining lobe is balanced by the liquid flux through the trough regions into the filling lobes.

The timescale for drainage is $t = O(\epsilon^{n_7})$, where the exponent n_7 is a constant to be determined. Since $h = O(\epsilon)$ and $x = O(\epsilon^{1/2})$ in the trough regions, we find that $Q(x_0) = O(\epsilon^{5/2})$ from equation (5.49). Hence, equation (5.48) gives

$$\epsilon^{1/2-n_7} \sim \epsilon^{5/2}, \tag{5.51}$$

and balancing these terms gives $n_7 = -2$. Therefore, the timescale for drainage is $t = O(\epsilon^{-2})$.

In summary, the timescales in the filling lobe, trough, and draining lobe regions are $t = O(1)$, $t = O(\epsilon^{-1})$, and $t = O(\epsilon^{-3/2})$, respectively, and the timescale for drainage is $t = O(\epsilon^{-2})$. Therefore, drainage takes place on a timescale much longer than those in the three different regions, and so the interface in the filling lobe, trough, and draining lobe regions can be treated as being quasi-steady.

5.4.1.c Governing equation for $H(\eta)$ in the trough region

In order to find the equation that describes $H(\eta)$ at leading order in the trough regions, the similarity solution (5.41) is substituted into the governing equation (2.91), giving

$$\frac{H^3}{3}\left(\epsilon^{5/2}H''' + \epsilon^{7/2}\frac{H'}{(d-\epsilon H)^3}\right) = Q(x_0) = \epsilon^{5/2}\overline{Q}(x_0), \tag{5.52}$$

where $\overline{Q}(x_0) = O(1)$, where we have used the fact that the interface is quasi-steady. Hence, at leading order in ϵ, equation (5.52) becomes

$$H''' = \frac{3\overline{Q}(x_0)}{H^3}, \tag{5.53}$$

which is the same equation as that found by Hammond [81].

5.4.1.d Matching conditions to the draining and filling lobe regions

The matching conditions from the trough region to the filling and draining lobe regions are now determined, where, in an asymptotic sense, the trough region is the inner solution, and the draining and filling lobes are the outer solution. A qualitative difference is found in the matching conditions to the filling and draining lobes, namely that the trough region matches to a linear function as $\eta \to \infty$ (corresponding to the draining lobe) and matches to a quadratic function as $\eta \to -\infty$ (corresponding to the filling lobe): This is then the manifestation of the asymmetry which causes drainage. The matching condition to the draining lobe is determined first.

In the draining lobe region, recall that $h = O(\epsilon^{1/2})$ and $x = O(1)$, and so the governing equation (2.91) at leading order in ϵ becomes

$$\frac{\partial}{\partial x}\left(h^3\left(\frac{\partial^3 h}{\partial x^3} + \frac{1}{d^3}\frac{\partial h}{\partial x}\right)\right) = 0, \tag{5.54}$$

which has the solution

$$h = \epsilon^{1/2}\left(A + B\cos\left(\frac{x}{d^{3/2}}\right)\right), \tag{5.55}$$

where $A = O(1)$ and $B = O(1)$ are unknown constants of integration.

As determined in Section 5.4.1.a, the heights of the filling and draining lobe regions are much larger than the height of the trough region, and so the matching conditions $h(\pm x_0) = 0$ are used. Imposing these matching conditions on the solution given in equation (5.55) yields

$$h = \epsilon^{1/2} B\left(\cos\left(\frac{x}{d^{3/2}}\right) - \cos\left(\frac{x_0}{d^{3/2}}\right)\right). \tag{5.56}$$

Matching the trough region (inner solution) to the draining lobe region (outer solution) requires performing a Taylor expansion of equation (5.56) around $x =$

x_0, giving

$$h \sim -\epsilon^{1/2}\alpha(x - x_0) \tag{5.57}$$

as $x \to x_0^-$, where

$$\alpha = \frac{B}{d^{3/2}} \sin\left(\frac{x_0}{d^{3/2}}\right) = O(1). \tag{5.58}$$

Rewriting (5.57) in terms of $H(\eta)$ and η using the similarity solution (5.41) gives

$$H \sim -\alpha\eta \tag{5.59}$$

as $\eta \to -\infty$. Hence, the matching condition from the trough region to the draining lobe region is given by (5.59).

The matching condition from the trough region to the filling lobe region is found by firstly performing a Taylor expansion of h around $x = x_0$, which gives

$$h = h(x_0) + (x - x_0)\frac{\partial h}{\partial x}(x_0) + \frac{(x - x_0)^2}{2}\frac{\partial^2 h}{\partial x^2}(x_0) + O\left((x - x_0)^3\right) \tag{5.60}$$

as $x \to x_0^+$.

The matching conditions $h(\pm x_0) = 0$ are again used, and the numerical results suggest that $\partial h/\partial x \to 0$ as $x \to x_0^+$, and an analytical justification of this result is presented in Appendix E. Imposing $h(x_0) = \partial h/\partial x(x_0) = 0$, equation (5.60) simplifies to

$$h = \frac{(x - x_0)^2}{2}\frac{\partial^2 h}{\partial x^2}(x_0) + O\left((x - x_0)^3\right) \tag{5.61}$$

as $x \to x_0^+$.

The similarity solution (5.15) is used to rewrite the leading order term of equation

(5.61) in terms of $H(\eta)$ and η, giving

$$H \sim \frac{H''(0)}{2}\eta^2 \tag{5.62}$$

as $\eta \to \infty$. Hence, the matching condition from the trough region to the filling lobe region is given by (5.62). Recall that the qualitative difference in the matching conditions to the filling and draining lobes, namely that the trough region matches to a linear function as $\eta \to \infty$ and matches to a quadratic function as $\eta \to -\infty$, is the manifestation of the asymmetry which causes drainage.

5.4.1.e The system describing the trough region

In Sections 5.4.1.c and 5.4.1.d, the following system describing the trough region has been obtained,

$$H'''(\eta) = \frac{3\overline{Q}(x_0)}{H(\eta)^3}, \qquad H(\eta) \sim -\alpha\eta \text{ as } \eta \to -\infty, \qquad H(\eta) \sim \frac{H''(0)}{2}\eta^2 \text{ as } \eta \to \infty, \tag{5.63}$$

where the second and third equations are the matching conditions to the draining and filling lobes, respectively.

The system (5.63) can be recast in canonical form by introducing the following rescalings,

$$X = \frac{H''(0)}{2\alpha}\eta, \qquad Y(X) = \frac{H''(0)}{2\alpha^2}H(\eta), \tag{5.64}$$

where

$$\Lambda = \frac{3H''(0)\overline{Q}(x_0)}{2\alpha^5}, \tag{5.65}$$

to yield

$$Y''' = \frac{\Lambda}{Y^3}, \qquad Y \sim -X \text{ as } -X \to \infty, \qquad Y \sim X^2 \text{ as } X \to \infty. \tag{5.66}$$

This is exactly the same system as that found by Jones and Wilson [80] and Hammond [81], and its time dependence will be explored in Section 5.4.1.f to show that $h = O(t^{-1/2})$ and $h = O(t^{-1/4})$ in the trough and draining lobe regions, respectively, consistent with the numerical results presented in Section 5.4.

5.4.1.f Investigation of the time dependence of the system given by (5.66)

Recall that the timescale for drainage of liquid from the filling lobe to the draining lobe is longer than the timescales in the filling lobe, trough, and draining lobe regions, and so the time dependence for h during the asymptotic thinning stage of TH behaviour is determined by drainage. Firstly, the solution for h in the draining lobe region, i.e. (5.56), is integrated with respect to x between $-x_0$ and x_0 to obtain the expression for the volume of liquid in the draining lobe, namely,

$$V = 2\epsilon^{1/2} d^{3/2} \left(1 - x_0 \cot\left(\frac{x_0}{d^{3/2}}\right)\right) B \sin\left(\frac{x_0}{d^{3/2}}\right) = 2\epsilon^{1/2} d^{3/2} \left(1 - x_0 \cot\left(\frac{x_0}{d^{3/2}}\right)\right) \alpha. \tag{5.67}$$

The expression $Q(x_0) = \epsilon^{5/2}\overline{Q}(x_0)$ is used in equation (5.50) to yield

$$\frac{\partial V}{\partial t} = -2\epsilon^{5/2}\overline{Q}(x_0). \tag{5.68}$$

Using the definition of Λ given by (5.65), equation (5.68) becomes

$$\frac{\partial V}{\partial t} = -\frac{4\epsilon^{5/2}\Lambda\alpha^5}{3H''(0)}. \tag{5.69}$$

The expression for V, given by equation (5.67), is now used to remove ϵ from (5.69), giving

$$\frac{\partial V}{\partial t} = -\frac{\Lambda}{24d^{15/2}H''(0)}\left(1 - x_0 \cot\left(\frac{x_0}{d^{3/2}}\right)\right)^{-5} V^5 = -K_1 V^5, \tag{5.70}$$

where

$$K_1 = \frac{\Lambda}{24d^{15/2}H''(0)}\left(1 - x_0 \cot\left(\frac{x_0}{d^{3/2}}\right)\right)^{-5}. \tag{5.71}$$

Equation (5.70) shows that $\partial V/\partial t \propto d^{-15/2}$, and suggests that the distance between the two electrodes d has an important impact on the rate of drainage of liquid from the draining lobe. Specifically, as the distance between the two electrodes increases or decreases, the rate at which liquid drains from the draining lobe decreases or increases, respectively. This makes sense physically since the destabilising electric field is facilitating drainage, and its strength is decreasing as as d increases, leading to a slower rate of drainage of liquid from the draining lobe. Likewise, the strength of the electric field increases as d decreases leading to an increased rate of drainage of liquid from the draining lobe.

We solve equation (5.70) for $V(t)$ to give

$$V(t) = V(0)\left(1 + 4V(0)^4 K_1 t\right)^{-1/4}. \tag{5.72}$$

Hence, the volume of the draining lobe varies like $V = O(t^{-1/4})$, which we will now use to show that $h = O(t^{-1/2})$ and $h = O(t^{-1/4})$ in the trough and draining lobe regions, respectively.

Firstly, the time dependence of h in the trough region is determined analytically. Rearranging the second term of (5.64) for $H(\eta)$ and substituting it into the

similarity solution (5.41) gives

$$h = \epsilon H(\eta) = \frac{2\epsilon\alpha^2}{H''(0)} Y(X), \tag{5.73}$$

and using equation (5.67) to remove ϵ from (5.73) gives

$$h = \frac{Y(X)}{2d^3 H''(0)} \left(1 - x_0 \cot\left(\frac{x_0}{d^{3/2}}\right)\right)^{-2} V^2 = K_2 V^2, \tag{5.74}$$

where

$$K_2 = \frac{Y(X)}{2d^3 H''(0)} \left(1 - x_0 \cot\left(\frac{x_0}{d^{3/2}}\right)\right)^{-2}. \tag{5.75}$$

Since $V = O(t^{-1/4})$, it is clear from equation (5.74) that $h = O(t^{-1/2})$, which is consistent with the results of the numerical calculations shown in Figure 5.10(a). Secondly, the time dependence of h in the draining lobe region can be determined analytically. Recall that equation (5.56) gives the solution for h in the draining lobe, and using equation (5.67) to remove ϵ from (5.56) yields

$$h = \frac{B}{2d^{3/2}\alpha} \left(\cos\left(\frac{x}{d^{3/2}}\right) - \cos\left(\frac{x_0}{d^{3/2}}\right)\right) \left(1 - x_0 \cot\left(\frac{x_0}{d^{3/2}}\right)\right)^{-1} V = K_3 V, \tag{5.76}$$

where

$$K_3 = \frac{B}{2d^{3/2}\alpha} \left(\cos\left(\frac{x}{d^{3/2}}\right) - \cos\left(\frac{x_0}{d^{3/2}}\right)\right) \left(1 - x_0 \cot\left(\frac{x_0}{d^{3/2}}\right)\right)^{-1}. \tag{5.77}$$

Therefore, since $V = O(t^{-1/4})$, equation (5.76) shows that $h = O(t^{-1/4})$ in the draining lobe, which is in agreement with the results of the numerical calculations shown in Figure 5.10(a).

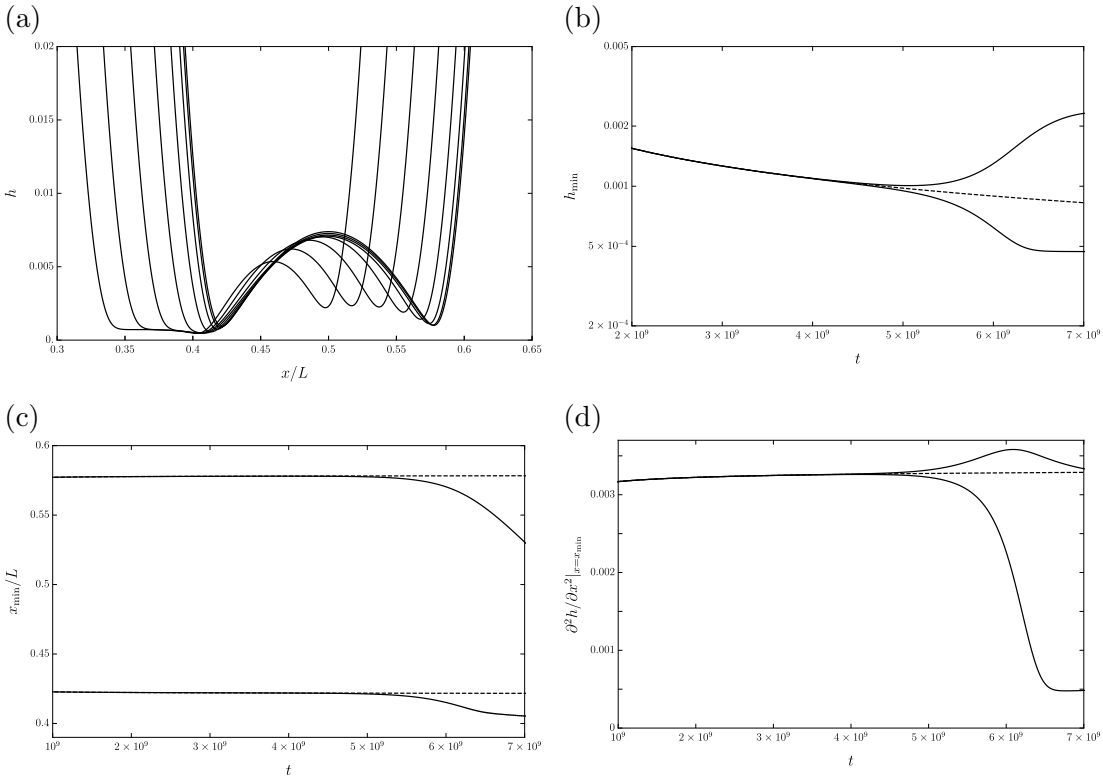

Figure 5.14: Plots of (a) h as a function of x/L at equally spaced times, (b) $h_{\min}$ as a function of t, (c) $x_{\min}$ as a function of t, and (d) $\partial^2 h/\partial x^2|_{x=x_{\min}}$ as a function of t. The solid and dashed lines in parts (b), (c) and (d) correspond to the numerical results obtained using periodic and symmetric boundary conditions, respectively, and the parameter values used are $L = 100$ and $d = 7$.

5.4.2 Investigation of the onset of sliding stage

The onset of sliding stage is characterised by a loss of symmetry and the interface translates to the left, as shown in Figure 5.14. The interface can also translate to the right, and we will show that the direction of translation is dependent on numerical errors seeded by numerical noise. Figure 5.14 shows plots of (a) h as a function of x/L at equally spaced times, (b) $h_{\min}$ as a function of t, (c) $x_{\min}$ as a function of t, and (d) $\partial^2 h/\partial x^2|_{x=x_{\min}}$ as a function of t. The solid and dashed lines in parts (b), (c) and (d) correspond to the numerical results obtained using periodic and symmetric boundary conditions, respectively. In particular, the heights of the local minima in the left and right hand trough regions decrease and increase in height, respectively, as shown in Figure 5.14(a) and (b), and the leftward translation of the interface is shown in Figure 5.14(a) and (c). Figure 5.14(d) shows that the interfacial curvature in the left and right hand trough regions decreases and increases, respectively, which corresponds to the left and right hand trough regions flattening and becoming more curved, respectively, as shown in Figure 5.14(a). The time of the onset of sliding is $t_{\rm s} = 4.849 \times 10^9$, as determined by calculating the first time step where the differences between the values of $h_{\min}$ between the numerical calculations using symmetric and periodic boundary conditions differ by more than 2%.

In Section 5.4.2.a we describe and use a frozen-time linear stability analysis to show that the onset of sliding is caused by an asymmetric disturbance. In Section 5.4.2.b we discuss the results of this analysis, which will also be used in Section 5.4.2.c to understand the interfacial dynamics during the onset of sliding.

5.4.2.a Frozen-time linear stability analysis

Recall from Section 5.4.1.b that the interface in the filling lobe, trough, and draining lobe regions is quasi-steady. Therefore, we will use a frozen-time linear stability analysis to investigate the system at $t = t_{\rm s}$. A frozen-time linear sta-

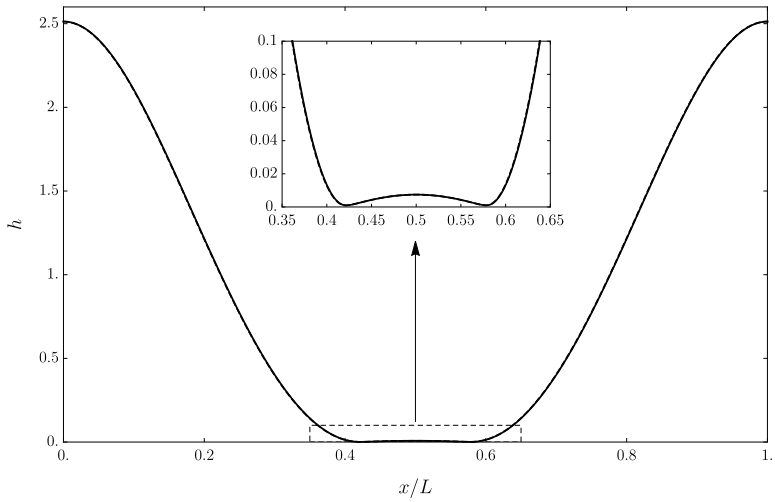

Figure 5.15: Plots of h as a function of x/L at $t = t_s$, and so is also a plot of $\overline{H}(x)$. The solid and dashed lines correspond to the results of the numerical calculations that use symmetric and periodic boundary conditions, respectively, and are indistinguishable. The parameter values used are $L = 100$ and $d = 7$.

bility analysis involves obtaining a base state, denoted by $\overline{H} = \overline{H}(x)$. In this case, it must be determined numerically as the interfacial shapes are not accessible analytically. Hence, the base state H was determined numerically (using the symmetric boundary conditions) at $t = t_s$, as shown in Figure 5.15. Figure 5.15 shows plots of h as a function of x/L at $t = t_s$, and so is also a plot of $\overline{H}$. The solid and dashed lines correspond to the results of the numerical calculations that use symmetric and periodic boundary conditions, respectively, and are indistinguishable. At the time of sliding $t = t_s$, the interface is evolving slow enough that it can be assumed to be quasi-static, and we will determine whether there is a dominant asymmetric instability. The system is then perturbed around the base state $\overline{H}$, i.e.

$$h = \overline{H}(x) + \delta\widetilde{h}\exp(st), \tag{5.78}$$

where $\delta \ll 1$ is the linearisation parameter, $\widetilde{h} = \widetilde{h}(x)$ is the amplitude of the perturbation, and s is the growth rate. The perturbed interfacial height (5.78) is substituted into the governing equation (2.91) and linearised, giving an equation

in terms of (the eigenvalue) s and (the eigenfunction) $\widetilde{h}$, namely,

$$s\widetilde{h} = -\frac{\partial}{\partial x}\left[\frac{\overline{H}^2}{A^4}\left(\left(A^4\frac{\partial^3\overline{H}}{\partial x^3} + d\frac{\partial\overline{H}}{\partial x}\right)\widetilde{h} + \frac{\overline{H}}{3}\left(A^4\frac{\partial^3\widetilde{h}}{\partial x^3} + A\frac{\partial\widetilde{h}}{\partial x}\right)\right)\right]. \tag{5.79}$$

where $A = d - \overline{H}$. To solve this equation for s and $\widetilde{h}$, a Fourier ansatz for $\widetilde{h}$ is introduced, namely,

$$\widetilde{h}(x) = \sum_{j=1}^{N} A_j \sin\left(\frac{2\pi x j}{L}\right) + B_j \cos\left(\frac{2\pi x j}{L}\right), \tag{5.80}$$

where A_j and B_j are constants for $j = 1, 2, ..., N$. The ansatz (5.80) is substituted into equation (5.79), which is solved for symmetric and antisymmetric perturbations. Specifically, setting $A_j = 0$ removes all sine functions from the Fourier series ansatz and gives a symmetric perturbation to the base state $\overline{H}$. Similarly, setting $B_j = 0$ removes all cosine functions and gives an antisymmetric perturbation to the base state $\overline{H}$. Furthermore, since the base state $\overline{H}$ is x-periodic with period L, this stability analysis is that of a Floquet-type analysis [152]. The linear stability calculations were performed using Mathematica, where Fourier transforms were used to calculate the derivatives and in-built functions were used to obtain the eigenvalues and eigenfunctions of the system. The accuracy of these calculations were explored through comparison with the numerical results, as illustrated by Figure 5.18.

5.4.2.b Frozen-time linear stability analysis results

The linear stability analysis was performed using $N = 150$ Fourier modes, and the results revealed that all symmetric eigenmodes (when $A_i = 0$ in equation (5.80)) are stable, with least stable eigenvalue $s = -5.2509 \times 10^{-10}$. Also, all antisymmetric eigenmodes (when $B_i = 0$ in equation (5.80)) except one are also stable, and the unstable eigenmode has eigenvalue $s = 5.512 \times 10^{-9}$. This is very

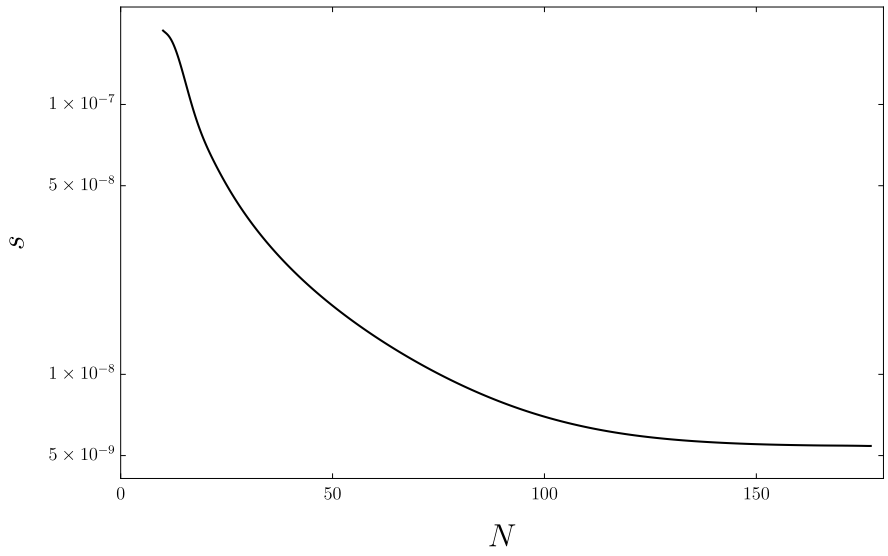

Figure 5.16: Plot of the unstable growth rate s as a function of the number of Fourier modes N. The y-axis is logarithmically scaled.

close to zero, and so a plot of the most unstable eigenvalue as a function of the number of Fourier modes N was produced, given by Figure 5.16. Figure 5.16 shows a plot of the unstable eigenvalue s as a function of the number of Fourier modes N. This shows that the unstable growth rate does indeed converge to a positive value and not zero. Furthermore, we found that this linear stability analysis produces a spectrum of N discrete eigenvalues that are all real. The least stable symmetric and unstable antisymmetric eigenfunctions are shown in Figure 5.17. Figure 5.17 shows plots of the least stable symmetric and unstable antisymmetric eigenfunctions (a) $\widetilde{h}$ and (b) $\widetilde{h}/\overline{H}$ as functions of x/L. The solid and dashed lines correspond to the antisymmetric and symmetric eigenfunctions, respectively. The dots correspond to the heights of the local minima in the trough regions. The results of this analysis suggests that the onset of sliding is caused by a single, unstable, antisymmetric eigenmode, which we will now confirm by showing that the unstable antisymmetric eigenfunction shows excellent agreement with the perturbations calculated by taking the difference between h using the symmetric and periodic boundary conditions at $t = t_{\mathrm{s}}$.

The antisymmetric perturbation was obtained by calculating the difference be-

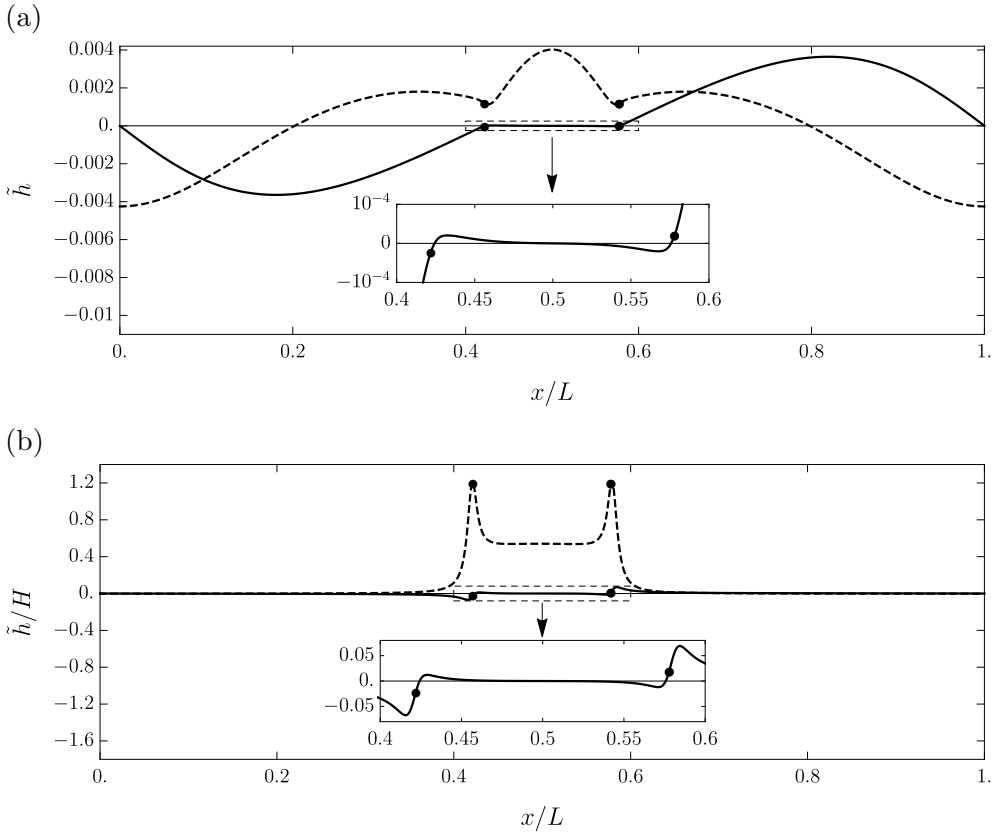

Figure 5.17: Plots of the least stable symmetric and unstable antisymmetric eigenfunctions (a) $\widetilde{h}$ and (b) $\widetilde{h}/\overline{H}$ as functions of x/L. The solid and dashed lines correspond to the antisymmetric and symmetric eigenfunctions, respectively. The dots correspond to the local minima in the trough regions, and the parameter values used are $L = 100$ and $d = 7$.

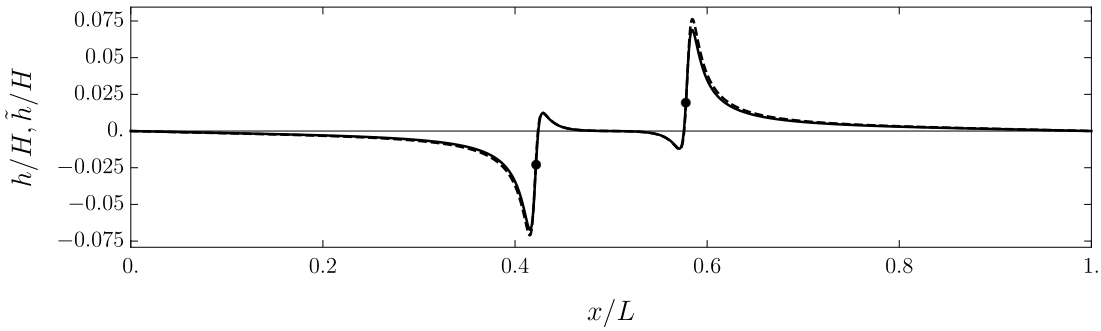

Figure 5.18: Plots of the perturbation obtained by calculating the difference between the interfaces using symmetric and periodic boundary conditions at $t = t_s$ (solid line), and the unstable asymmetric eigenfunction (dashed line), as a function of x/L. The solid and dashed lines are virtually indistinguishable. The dots correspond to the local minima in the trough regions, and the parameter values used are $L = 100$ and $d = 7$.

tween h at $t = t_s$ obtained using the symmetric and periodic boundary conditions, i.e. the difference between the solid and dashed lines in Figure 5.15. Figure 5.18 shows plots of the asymmetric perturbation obtained this way (solid line), and the unstable asymmetric eigenfunction (dashed line), as functions of x/L. The solid and dashed lines are virtually indistinguishable. The dots correspond to the local minima in the trough regions, and the parameter values used are $L = 100$ and $d = 7$. Figure 5.18 shows excellent agreement between the numerical results and the frozen-time linear stability results, confirming that the onset of sliding is caused by this asymmetric disturbance. Similar results were found in other parts of (L, d) parameter space for which TH behaviour occurs.

5.4.2.c Understanding the interfacial dynamics during the onset of sliding stage

The results of the frozen-time linear stability analysis are now used to describe the interfacial dynamics during the onset of sliding stage. In particular, we show that the unstable asymmetric eigenfunction causes the local minima in the left and right hand trough regions to decrease and increase, respectively, as shown in Figure 5.14(a) and (b). In addition, the asymmetric disturbance shown in

Figure 5.18 is used to explain the leftward translation of the interface (and, in particular, of the trough regions), as shown in Figure 5.14(a) and (c). Note that, since the eigenfunction is determined to within a $+/-$ regularisation, the eigenfunction could also translate to the right. Furthermore, the time derivative of the interfacial curvature $\partial/\partial t\,(\partial^2 h/\partial x^2)$ of the unstable asymmetric eigenfunction is used to show that the asymmetric disturbance causes the left and right hand trough regions to flatten and become more curved, respectively, as shown in Figure 5.14(a) and (d).

The perturbed interfacial height (5.78) is used to obtain

$$\frac{\partial h}{\partial t} = s\widetilde{h}\exp(st)\,, \tag{5.81}$$

where $s > 0$ and $\exp(st) > 0$ for the unstable asymmetric eigenmode, and so the sign of $\partial h/\partial t$ is determined by the sign of $\widetilde{h}$. Figure 5.15 shows that the unstable asymmetric eigenfunction $\widetilde{h}$ (and $\widetilde{h}/\overline{H}$) is negative and positive in the left and right hand trough regions, respectively. Hence, equation (5.81) shows that $\partial h/\partial t < 0$ and $\partial h/\partial t > 0$ in the left and right hand trough regions, respectively. This corresponds to the heights of the local minima in the left and right hand trough regions decreasing and increasing during the onset of sliding, in agreement with the numerical results shown in Figure 5.14(a) and (b).

Figure 5.18 can also be used to explain the leftward translation of the trough regions. Specifically, in the left hand trough region, $\widetilde{h}/\overline{H}$ is negative and positive to the left and right of the local minimum. This shows that h is decreasing and increasing to the left and right hand side of the local minimum, indicating that the local minimum in the left hand trough region is moving to the left. Likewise, for the right hand trough region, $\widetilde{h}/\overline{H}$ is negative and positive to the left and right hand sides of the local minimum. This shows that h is decreasing and increasing to the left and right hand side of the local minimum, respectively, indicating that

the local minimum in the trough region is moving to the left. Therefore, this explains the leftward translation of the local minima in the trough regions during the onset of sliding.

Note that the leftward translation of the interface is not unique, and it could equally well translate rightward. Since the numerical calculations begin with symmetric initial conditions, given by (4.17), the asymmetric disturbances must come from small numerical errors seeded by numerical noise. The numerical noise is dependent on factors such as the number of grid points used in the calculations and the accuracy of the finite-difference scheme (introduced in Section 4.1.1). Hence, numerical noise ultimately determines the direction that the interface moves during the onset of sliding which is effectively random.

Furthermore, the perturbed interfacial height (5.78) gives

$$\frac{\partial}{\partial t}\left(\frac{\partial^2 h}{\partial x^2}\right) = \frac{\partial}{\partial t}\left(\frac{\partial^2 \widetilde{h}}{\partial x^2}\exp\left(st\right)\right) = s\frac{\partial^2 \widetilde{h}}{\partial x^2}\exp\left(st\right), \tag{5.82}$$

where $s > 0$ and $\exp(st) > 0$ for the unstable asymmetric eigenmode, and so the sign of $\partial/\partial t\left(\partial^2 h/\partial x^2\right)$ is determined by the sign of $\partial^2\widetilde{h}/\partial x^2$. Figure 5.19 shows a plot of $\partial^2\widetilde{h}/\partial x^2$ as a function of x/L for the unstable asymmetric eigenmode. The dots correspond to the local minima in the trough regions. Figure 5.19 shows that, for the unstable asymmetric eigenfunction, $\partial^2\widetilde{h}/\partial x^2 < 0$ and $\partial^2\widetilde{h}/\partial x^2 > 0$ in the left and right hand trough regions, respectively. Hence, equation (5.82) shows that $\partial/\partial t\left(\partial^2 h/\partial x^2\right) < 0$ and $\partial/\partial t\left(\partial^2 h/\partial x^2\right) > 0$ in the left and right hand trough regions, respectively. This corresponds to the interface in the left and right hand trough regions flattening and becoming more curved, respectively, agreeing with the numerical results shown in Figure 5.14(a) and (c).

The results of this frozen-time linear stability analysis also agree with the results of Dietze *et al.* [86], who found that the onset of sliding for their problem was caused by an asymmetric disturbance. Recall also that Pillai and Narayanan

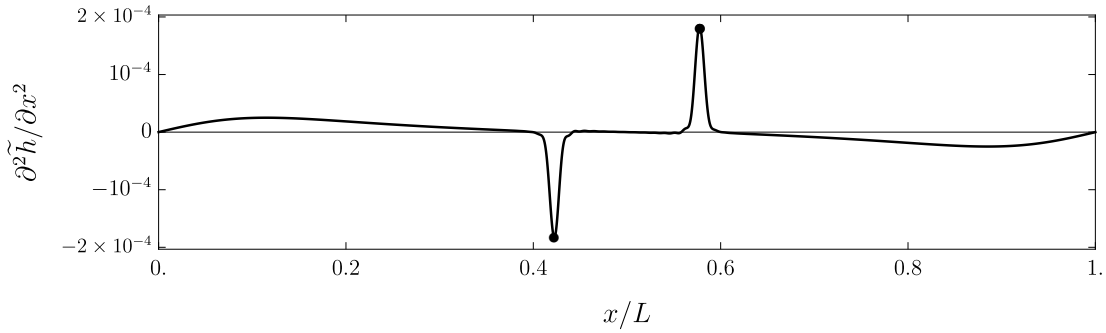

Figure 5.19: Plots of the $\partial^2\widetilde{h}/\partial x^2$ as a function of x/L, for the unstable asymmetric eigenfunction. The filled circles correspond to the local minima in the trough regions, and the parameter values used are $L = 100$ and $d = 7$.

[126], who also studied this PC model, showed that sliding occurs, and they assumed that the onset of sliding is caused by an asymmetric disturbance as found by Dietze *et al.* [86]. The results of our frozen-time linear stability analysis confirms that this is indeed the case.

5.5 Investigation of the transition curves in (L, d) parameter space

In this Section, the transition curves separating the three behaviours in (L, d) parameter space, shown in Figure 5.1, are investigated. Specifically, there are two different types of transition curve:

1. One that separates UC or TH behaviour from LV behaviour.

2. One that separates UC behaviour from TH behaviour.

The first type of transition curve is investigated in Section 5.5.1, and is obtained analytically using linear stability theory. The second type of transition curve is investigated in Section 5.5.2, and we will show that its more complex behaviour is explained using the number of filling lobes and the value of d.

5.5.1 Transition curve separating UC or TH behaviour from LV behaviour

Recall from Section 3.7 the PC model is always linearly unstable in an unbounded domain, and so LV behaviour can only occur when the domain length L is too short to contain any unstable wavenumbers. We will now calculate analytically the transition curve separating UC or TH behaviour from LV behaviour.

Recall that the cutoff wavenumber k_c, given by equation (3.44), is the value of $k > 0$ where $s = 0$. Equation (3.44) is substituted into the expression

$$k_c = \frac{2\pi}{L}, \tag{5.83}$$

giving

$$\frac{1}{(d_c - 1)^{3/2}} = \frac{2\pi}{L}, \tag{5.84}$$

where d_c is the cutoff value for d, and the system is unstable to small perturbations of wavelength L when $d < d_c$. Equation (5.84) can be rearranged to give an equation for d_c in terms of L, namely,

$$d_c = 1 + \left(\frac{L}{2\pi}\right)^{2/3}. \tag{5.85}$$

Therefore, for any given domain length L, equation (5.85) gives the value for d_c such that, when $d < d_c$ and $d \geq d_c$, the PC model will exhibit UC or TH behaviour and LV behaviour, respectively. Equation (5.85) is used to plot the analytically calculated transition curve (shown by the dashed line) in Figure 5.1 which is indistinguishable from the corresponding numerically calculated transition curve. This shows the excellent agreement between the numerically calculated and analytical transition curves. Equation (5.85) is the analytic expression for the curve separating UC or TH behaviour from LV behaviour.

5.5.2 Transition curve separating UC and TH behaviours

We will show that the transition curve separating UC behaviour from TH behaviour is determined by a complex balance between the number of filling lobes and the value of d. Recall that (L, d) parameter space shows a tongue of UC behaviour extending into the TH region, shown in the upper inset in Figure 5.1. The behaviour in this tongue is investigated by exploring Figure 5.20, which shows plots of h as a function of x/L for (a) $d = 7$, (b) $d = 7.5$, (c) $d = 8$, (d) $d = 8.5$, (e) $d = 9$, and (f) $d = 9.5$ when $L = 240$. Figure 5.20(a), (b) and (e) show UC behaviour, and Figure 5.20(c), (d) and (f) show TH behaviour. The profiles are plotted at the first time where the conditions that determine each behaviour (described in Section 5.1.1) were satisfied, and the horizontal dashed lines show the upper electrode.

In Figure 5.20:

1. Parts (a) and (b) show one filling lobe around $x/L = 0$ and two half filling lobes at the ends of the domain which, due to periodicity, means that there are essentially two full filling lobes in the domain. These plots show that h has got sufficiently close to the upper electrode for UC behaviour to occur.

2. Parts (c) and (d) still show two filling lobes in the domain, and so in this case TH behaviour will occur. The change in behaviour from UC to TH, between plots (b) and (c), occurs since the value of d is sufficiently large such that h will not evolve to be sufficiently close to the upper electrode for UC behaviour to occur.

3. Part (e) now only has one filling lobe around $x/L = 0$, into which all the liquid now drains. This means that h can now evolve close enough to the upper electrode for UC behaviour to occur.

4. Part (f) also shows one filling lobe around $x/L = 0$, and in this case TH behaviour will occur. The change in behaviour from UC to TH between

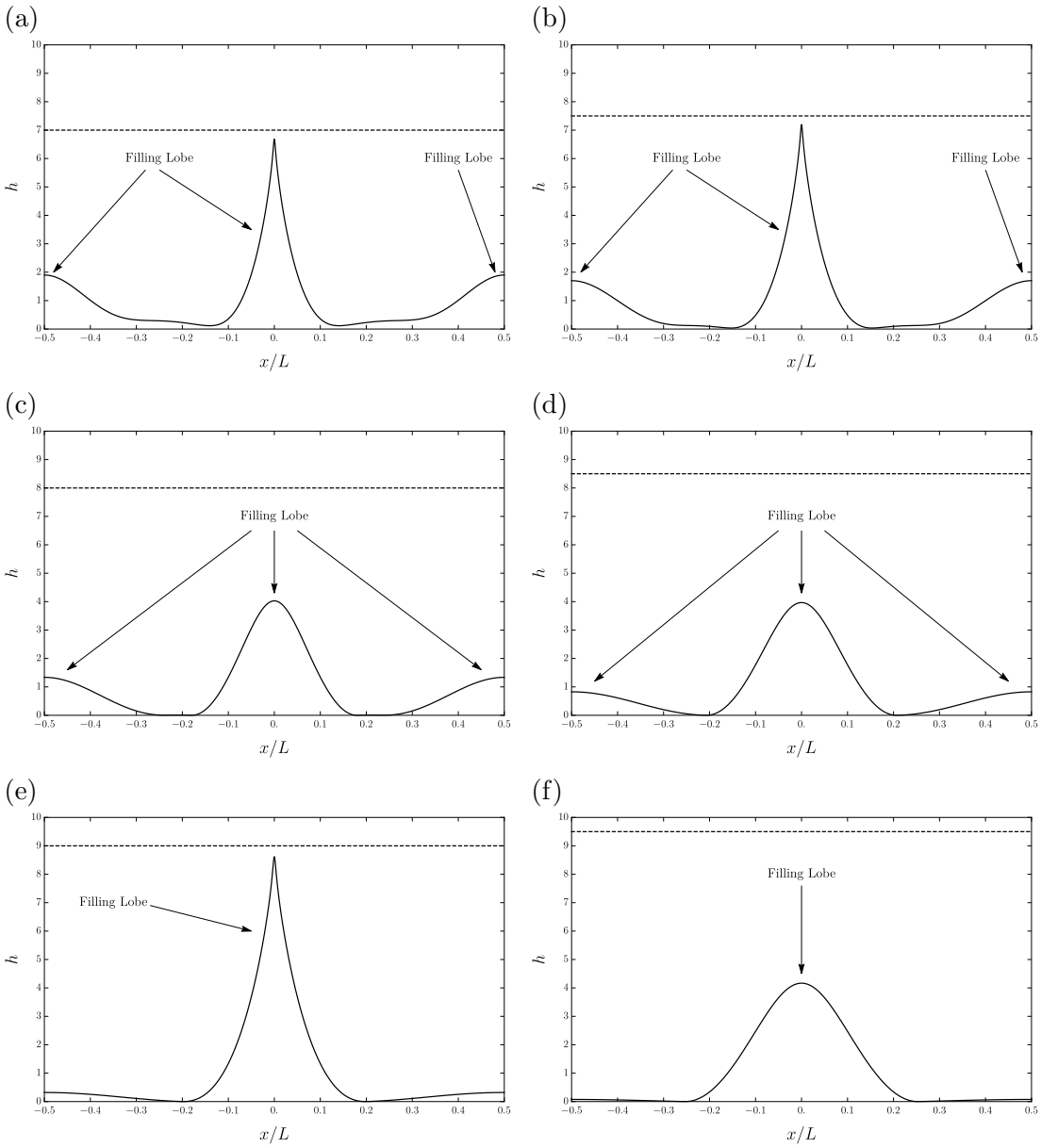

Figure 5.20: Plots of the h as a function of x/L for (a) $d = 7$, (b) $d = 7.5$, (c) $d = 8$, (d) $d = 8.5$, (e) $d = 9$, and (f) $d = 9.5$ when $L = 240$. Plots (a), (b) and (e) show UC behaviour, and plots (c), (d) and (f) show TH behaviour. The profiles are plotted at the first time where the conditions that determine each behaviour (described in Section 5.1.1) were satisfied, and the horizontal dashed lines show the upper electrode

plots (e) and (f) occurs for the same reason as that between plots (b) and (c), namely, the upper electrode is now too far away from the filling lobe such that UC behaviour cannot occur.

Hence, the transition between UC behaviour and TH behaviour is a complex balance between the number of filling lobes and the value of d. It might reasonably be anticipated that the number of lobes can be predicted by linear stability theory; in this case it would be expected that the transition from two lobes to one would take place when the linear growth rate s corresponding to the wavenumber $k = 2\pi/L$ exceeded that corresponding to $k = 2 \times 2\pi/L$. From equation (3.43) this takes place at $d = 1 + 4 \times 5^{1/3} (3/\pi)^{2/3} \approx 7.63$, which is in only approximate agreement with the actual transition from (d) to (e) which takes place at $d \approx 8.8$, reflecting the fact that the formation of lobes is at least in part a nonlinear phenomenon.

The analysis above raises the question of how close the filling lobe has to be to the upper electrode for UC behaviour to occur. We performed a detailed investigation of the interfacial height at the first time step at which the conditions that determine each behaviour were satisfied. As a general rule of thumb, the behaviour observed is determined by the maximum value of the interfacial height $h_{\max}$. Specifically, when the interface evolves to the point where $h_{\max} > d/2$, UC behaviour is observed, otherwise, if $h_{\max} < d/2$ for all t, then TH behaviour is observed. This discussion about $h_{\max}$ ties up with the number of filling lobes, since varying the number of filling lobes will influence the value of $h_{\max}$, and, therefore, influences the behaviour that is observed.

5.6 Summary

In summary, we performed an analytical and numerical investigation of the PC model that has the governing equation (2.91) for h. We found that three be-

haviours can occur, namely, LV, UC and TH. In Section 5.1, we performed a numerical investigation of (L, d) parameter space, and transition curves (which separate regions in (L, d) parameter space with different behaviours) were obtained. We described and investigated LV behaviour in Section 5.2, in which perturbations to the base state decay. Using linear stability theory, we showed that while unstable wavenumbers always exist, none are sufficiently short to fit into a domain of a given length.

In Section 5.3, UC behaviour was described and investigated, in which the interface touches the upper electrode in finite time. A similarity solution (5.14)–(5.15) was found that describes the interface close to the upper electrode, which showed excellent agreement with the numerical results. The similarity ODE (5.13) was found and solved using the shooting method, and showed good agreement with the numerical results, which is further confirmation that the interface exhibits self-similar behaviour described by the similarity solution (5.14)–(5.15). We also noted that, through the rescalings (5.37), the similarity ODE can be recast into canonical form (5.38).

A description and investigation of TH behaviour was performed in Section 5.4, where the interface evolves through four different stages, namely, the progressive growth, buckling, asymptotic thinning, and the onset of sliding stages. For the asymptotic thinning stage where the interface has evolved into filling lobe, trough, and draining lobe regions, we found a similarity solution for the trough region. In particular, the similarity solution shows that $h = O(t^{-1/2})$ and $h = O(t^{-1/4})$ in the trough and draining lobe regions, respectively, agreeing with the numerical results. Furthermore, the onset of sliding stage was investigated using a frozen-time linear stability analysis, the results of which showed that sliding is caused by asymmetric disturbances, seeded by the numerical noise.

In Section 5.5, we investigated the transition curves in (L, d) parameter space shown in Figure 5.1. In particular, linear stability theory was used to show that

the transition curves separating UC or TH behaviour from LV behaviour occurs when the domain length is too short to contain any unstable wavenumbers. We also obtained an analytical expression for the transition curve, given by equation (5.85), separating regions with UC or TH behaviour with LV behaviour. Furthermore, we found that the transition curve separating the UC and TH behaviours is determined by a complex balance between the number of filling lobes and the value of d.

Chapter 6

Highly conducting (HC) model

In this Chapter, the HC model, that has governing equation for h (2.99), is investigated. The UC, LV, and TH behaviours are again observed and, in Section 6.1, an investigation $(\Sigma_{\mathrm{R}}, \epsilon_{\mathrm{R}})$ parameter space is performed for various values of d. This investigation is made more complicated than that of the PC case due to the higher dimensionality of parameter space, as will be discussed in Section 6.1.1. Also, the specific details of the three behaviours are different from the PC case, and will be discussed and explored further in Sections 6.2–6.4. In Section 6.5, the transition curves separating the three behaviours will be investigated, and we use linear stability theory to obtain an analytical expression for the transition curve separating UC or TH behaviour with LV behaviour.

6.1 $(\Sigma_{\mathrm{R}}, \epsilon_{\mathrm{R}})$ parameter space

As mentioned above, the results of our numerical investigation of the HC model reveals three behaviours, namely, UC, LV, and TH behaviour. As in the PC case, the behaviour that the system adopts is dependent on the parameter values, specifically, the conductivity ratio Σ_{R}, the permittivity ratio ϵ_{R}, the upper electrode position d, and the domain length L. This four-dimensional parameter space is impracticably large to explore completely, and so in order to make things

more tractable, we selected values of d from 3 to 8, and the value for L was calculated explicitly at each point in parameter space which will be described fully in Section 6.1.1. In Section 6.1.1, the numerical investigation of $(\Sigma_{\mathrm{R}}, \epsilon_{\mathrm{R}})$ parameter space is described, and we give the criteria that are used to classify each behaviour. In Section 6.1.2, the results of this investigation are presented and discussed.

6.1.1 Numerical investigation of $(\Sigma_{\mathrm{R}}, \epsilon_{\mathrm{R}})$ parameter space

The investigation of $(\Sigma_{\mathrm{R}}, \epsilon_{\mathrm{R}})$ parameter space was performed by solving the governing equation for h of the HC model (2.99) using the pre-existing C++ code written by Dr Wray. We also used the Matlab code (introduced in Section 4.1.2) for cross-checking and validation of the results, which is the same as that used for the PC case. The numerical calculations were performed using 1024 grid points and the initial conditions given by (4.17) with $\delta = 0.01$. For each point in parameter space that was explored, L was chosen so that exactly one wave of the most unstable wavenumber $k_{\max}$ given by (3.41) would fit in the domain, i.e.

$$L = \frac{2\pi}{k_{\max}}. \tag{6.1}$$

Note that when there are no real solutions for $k_{\max}$, indicating that there are no unstable wavenumbers, we set $L = 2\pi$.

We explored parameter space over the ranges $1 < \Sigma_{\mathrm{R}} < 10$ and $1 < \epsilon_{\mathrm{R}} < 20$ with step sizes of 0.05 and 0.025, respectively, and d was varied from 3 to 8 in step sizes of 1. These step sizes were chosen so that an accurate picture of parameter space was obtained whilst not taking an inordinate amount of time to do so. At each point in parameter space, we used the same conditions for determining each behaviour as for the PC case (given in Section 5.1.1).

We checked points in $(\Sigma_{\mathrm{R}}, \epsilon_{\mathrm{R}})$ parameter space close to the transitions and at

extremal points, and the results were cross-referenced between the Matlab and C++ codes (which are not shown here), and predict the same behaviours in all cases.

6.1.2 Results of the investigation of (Σ_R, ϵ_R) parameter space

The results of the investigation of (Σ_R, ϵ_R) parameter space are presented in Figure 6.1. Figure 6.1 shows (Σ_R, ϵ_R) parameter space showing the numerically calculated transition curves (solid lines) and the analytically calculated transition curve (dashed line) separating the regions showing UC, TH, and LV behaviours, with (a) $d = 3$, (b) $d = 4$, (c) $d = 5$, (d) $d = 6$, (e) $d = 7$, (f) $d = 8$. The solid and dashed curves are indistinguishable and the inset figures show the numerically calculated behaviours around the transition curves, where the light grey, dark grey, and black dots in the insets indicate LV, UC, and TH behaviours, respectively, and are so numerous that they are indistinguishable and appear to be lines. The larger black dots are located at (a) $(1.225, 1.225)$, (b) $(1.425, 1.45)$, (c) $(1.475, 1.5)$, (d) $(1.525, 1.55)$, (e) $(1.725, 1.7625)$, and (f) $(1.775, 1.8125)$. To the left of the larger black dots, the behaviour goes from TH to LV as ϵ_R increases, and to the right of the larger black dots, the behaviour goes from TH to UC, then to LV behaviour as ϵ_R increases. The margin of error of the location of the larger black dots is 0.025 and 0.0125 for Σ_R and ϵ_R, respectively, since the step sizes for Σ_R and ϵ_R are 0.05 and 0.025, respectively. Figure 6.1 shows that, as d increases, the regions in (Σ_R, ϵ_R) parameter space showing TH and UC behaviours become larger and smaller, respectively. Also, the location of the larger black dots (indicating where UC behaviour first occurs) moves upwards and to the right in (Σ_R, ϵ_R) parameter space as d increases. This makes sense since, as d increases, there will be more points in parameter space for which the interface will not evolve close enough to the upper electrode, meaning that TH behaviour

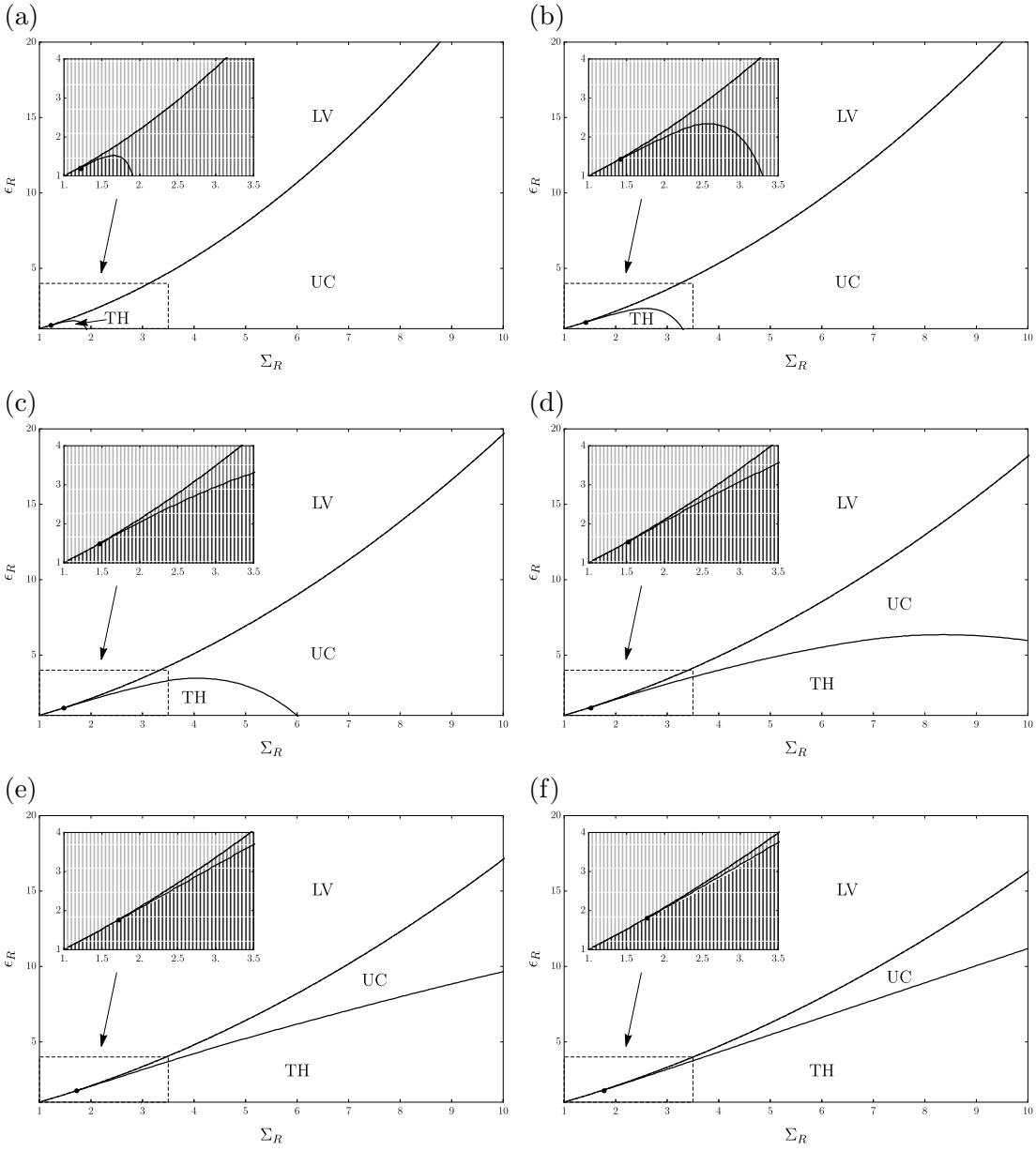

Figure 6.1: $(\Sigma_{\mathrm{R}}, \epsilon_{\mathrm{R}})$ parameter space showing the numerically calculated transition curves (solid line) and the analytically calculated transition curve (dashed line) separating the UC, TH, and LV behaviours, where (a) $d = 3$, (b) $d = 4$, (c) $d = 5$, (d) $d = 6$, (e) $d = 7$, (f) $d = 8$. The solid and dashed curves are indistinguishable, and the inset figures show the numerically calculated behaviours around the transition curves, where the light grey, dark grey, and black dots in the insets indicate LV, UC, and TH behaviours, respectively, and are so numerous that they are indistinguishable and appear to be lines. The larger black dots are located at (a) $(1.225, 1.225)$, (b) $(1.425, 1.45)$, (c) $(1.475, 1.5)$, (d) $(1.525, 1.55)$, (e) $(1.725, 1.7625)$, and (f) $(1.775, 1.8125)$.

will occur. Also, the region showing LV behaviour becomes larger for increasing d: the transition curve separating UC or TH behaviour from LV behaviour moves towards the Σ_{R}-axis as d increases. This makes sense since the strength of the electric field (which is the only source of instability in this system) decreases as d increases, and so we would expect the region showing LV behaviour to become larger.

6.2 Levelling (LV) behaviour

LV behaviour occurs when perturbations to the base state $\overline{h} = 1$ decay, as illustrated by Figure 5.2. Since the value of L in our numerical calculations corresponds to the most unstable wavenumber from linear stability theory, LV behaviour only occurs when there are no unstable wavenumbers which means that the system is always stable. This is different from the PC case where LV behaviour occurs if the domain length L is too short to contain any unstable wavelengths. In Section 7.6, we will determine analytically (using linear stability theory) the transition curve separating UC or TH behaviour from LV behaviour, which show very good agreement with the numerical results.

6.3 Upper contact (UC) behaviour

UC behaviour occurs when the interface touches the upper electrode, as shown in Figure 6.2, and unlike the PC case, the interface does not show self-similar behaviour. Figure 6.2 shows plots of (a) h as a function of x/L at equally spaced times from $t = 326.075$ to $t = 264403$, and (b) $\mathrm{d}h_{\max}/\mathrm{d}t$ as a function of t. In Figure 6.2(b) the values of $\mathrm{d}h_{\max}/\mathrm{d}t$ are small, showing that the interface does not approach the upper electrode rapidly. To show that self-similar behaviour during UC behaviour does not occur, the singularity in the governing equation

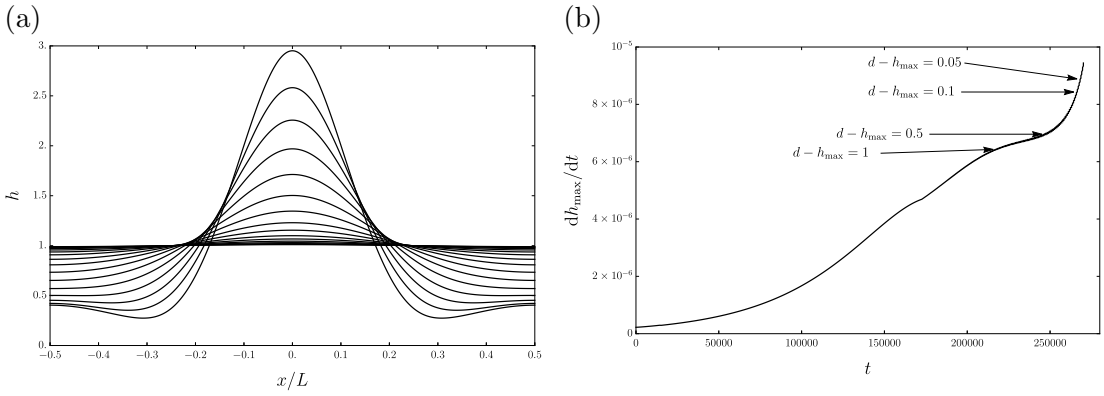

Figure 6.2: Plots of (a) h as a function of x/L at equally spaced times from $t = 326.075$ to $t = 264,403$, and (b) $\partial h_{\max}/\partial t$ as a function of t. The parameter values used are $d = 3$, $\Sigma_{\mathrm{R}} = 2$, $\epsilon_{\mathrm{R}} = 2$, and $L = 70.2481$.

(2.99) was found, which occurs when its denominator is zero, i.e. when

$$h = \frac{\Sigma_{\mathrm{R}} d}{\Sigma_{\mathrm{R}} - 1} > d. \tag{6.2}$$

Therefore, the singularity occurs at $h > d$, which does not occur physically since the interface would touch the upper electrode before reaching the singularity. Hence, self-similar behaviour or $\partial h/\partial t \to \infty$ as t increases do not occur.

6.4 Thinning (TH) behaviour

TH behaviour occurs when the interface evolves through two different stages, namely, "progressive growth" and "buckling", as described in Section 5.4. Afterwards, instead of asymptotic thinning and the onset of sliding (which is observed in the PC case), secondary buckling events occur, where each trough region splits into two trough regions that each contain a local minimum, as shown in Figure 6.3. Figure 6.3 shows plots of h as a function of x/L at equally spaced times using the symmetric boundary conditions. In fact, we will show in Section 6.4.1 that a cascade of secondary buckling events occur indefinitely as $h \to 0$, and is a consequence of the tangential Maxwell stress term that is now present in the

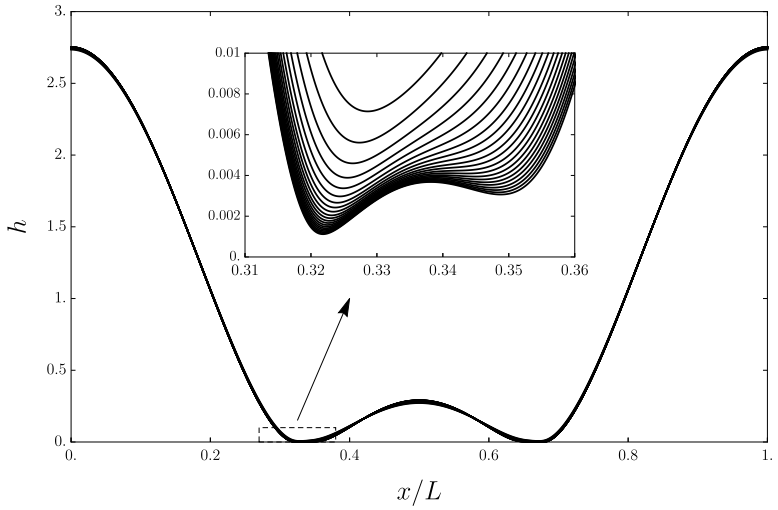

Figure 6.3: Plots of h as a function of x/L at equally spaced times from $t = 197,938$ to $t = 704,469$. The symmetric boundary conditions are imposed and the parameter values used are $d = 3$, $\Sigma_{\mathrm{R}} = 1.5$, $\epsilon_{\mathrm{R}} = 1.2$, and $L = 44.5159$.

governing equation for h (2.99).

6.4.1 Investigation of the cascade of secondary buckling events

Recall from Section 1.4 that a cascade of secondary buckling events were investigated by Dietze *et al.* [86], and found that by including Marangoni stresses in their system, secondary buckling events occur (as described above) which suppress the onset of sliding. Later, Pillai and Narayanan [126] showed that the cascade of buckling events occur for leaky dielectrics when the normal component of the Maxwell stress is zero. Drawing on the results of Dietze *et al.* [86], Pillai and Narayanan [126] briefly stated that the cascade of buckling events occur due to the presence of the tangential Maxwell stress term (which is mathematically similar to the Marangoni stress term in [86]). Hence, in this Section, we take inspiration from the work of Dietze *et al.* [86] to confirm that the cascading buckling events (in the HC case) are indeed caused by tangential component of the Maxwell stress, i.e. the third term on the right hand side of equation (2.99). To describe the secondary buckling events, we use the liquid flux Q, as well as

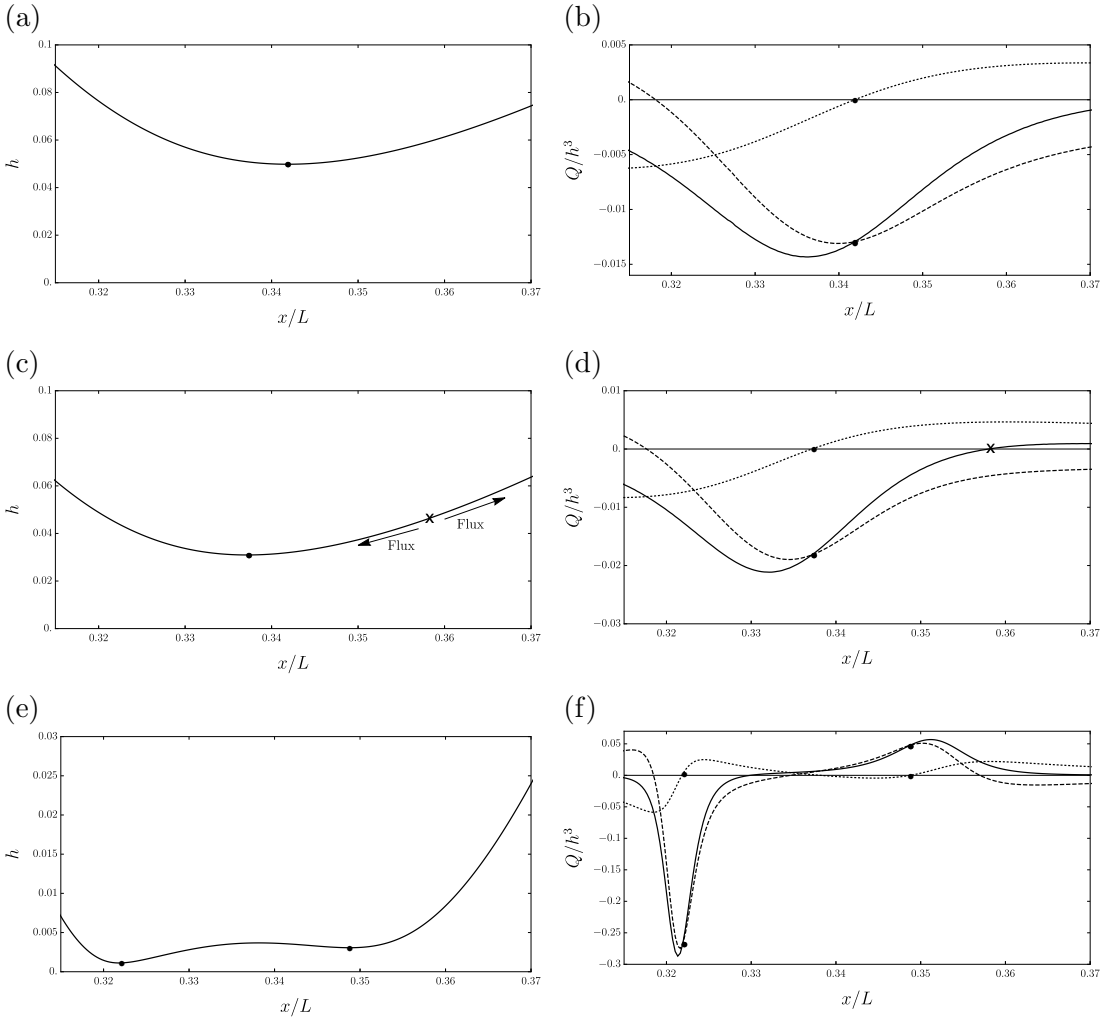

Figure 6.4: Plots of h as a function of x/L (first column) and Q (solid lines), Q_{N} (dashed lines), and Q_{T} (dotted lines) as functions of x/L (second column). The black dots indicate the positions of the local minima, and the the crosses in parts (c) and (d) indicate the position where $Q = 0$. The parameter values used are $d = 3$, $\Sigma_{\mathrm{R}} = 1.5$, $\epsilon_{\mathrm{R}} = 1.2$, and $L = 44.5159$.

the contributions to the flux arising from the normal and tangential components of the stress, Q_{N} and Q_{T}, respectively, i.e.

$$Q = Q_{\mathrm{N}} + Q_{\mathrm{T}}, \tag{6.3}$$

$$Q_{\mathrm{N}} = \frac{h^3}{3}\left(\frac{\partial^3 h}{\partial x^3} + \frac{(\Sigma_{\mathrm{R}} - 1)(\Sigma_{\mathrm{R}}^2 - \epsilon_{\mathrm{R}})}{(\Sigma_{\mathrm{R}}(d-h)+h)^3}\frac{\partial h}{\partial x}\right), \tag{6.4}$$

$$Q_{\mathrm{T}} = \frac{h^2}{2}\frac{d(\Sigma_{\mathrm{R}} - \epsilon_{\mathrm{R}})\Sigma_{\mathrm{R}}}{(\Sigma_{\mathrm{R}}(d-h)+h)^3}\frac{\partial h}{\partial x}. \tag{6.5}$$

Plots of h, Q, Q_{N}, and Q_{T} before, during and after secondary buckling, are shown in Figure 6.4. Figure 6.4 shows plots of h as a function of x/L (first column) and Q (solid lines), Q_{N} (dashed lines), and Q_{T} (dotted lines) as functions of x/L (second column). The black dots indicate the positions of the local minima of h, and the crosses in parts (c) and (d) indicate the position where $Q = 0$.

Figures 6.4(a) and (b) show that, before secondary buckling, Q_{N} is the dominant term in the trough region, and so the liquid continues to drain from the draining lobe to the filling lobe. As h approaches the lower electrode, Q_{T} begins to compete with Q_{N}, and this creates a divergence point Q (where the liquid flows away from this point) to the right of the local minimum, at the location of the crosses in Figures 6.4(c) and (d). This is explained by equations (6.3)–(6.5), where, in particular, we note the mobility coefficients of the normal and tangential terms, $h^3/3$ and $h^2/2$, respectively. These mobility coefficients are important since, as $h \to 0$, we expect Q_{T} to begin to compete with Q_{N}, and then dominate. This is shown by the numerical results in Figure 6.4(d), where the Q_{T} term creates the divergence point in Q. This means that liquid is flowing away from this point, as shown by the arrows in Figure 6.4(c), and ultimately leads to the formation of another local minimum, as shown in Figure 6.4(e). Furthermore, Figure 6.4(f) shows that the region located between the black dots is a draining lobe, and that Q_{N} is now the dominant term after the additional local minimum

has formed. However, as h continues to approach the lower electrode, Q_{T} will begin to compete again, causing more secondary buckling events, showing that there will be a cascade of buckling events that will occur indefinitely as $h \to 0$. Note that, due to symmetry, the preceding description of secondary buckling also applies to the right hand trough region. Therefore, using an analysis inspired by Dietze *et al.* [86], we have shown that the cascade of secondary buckling events are due to the tangential Maxwell stress term, confirming the statement made by Pillai and Narayanan [126].

6.5 The transition curves in $(\Sigma_{\mathrm{R}}, \epsilon_{\mathrm{R}})$ parameter space

In this Section, we will investigate the transition curves separating the three behaviours in $(\Sigma_{\mathrm{R}}, \epsilon_{\mathrm{R}})$ parameter space, shown in Figure 6.1. Specifically, there are two types of transition curve:

1. One that separates UC or TH behaviour from LV behaviour.

2. One that separates UC behaviour from TH behaviour.

The first type of transition curve is investigated in Section 6.5.1 and is obtained analytically using linear stability theory, and the second type of transition curve is investigated in Section 6.5.2.

6.5.1 Transition curve separating UC or TH behaviour from LV behaviour

Recall from Section 6.2 that LV behaviour in the HC case must occur when the growth rate $s < 0$ for all wavenumbers $k > 0$, and, equation (3.40) gives a relationship between ϵ_{R}, Σ_{R} and d in which the system is neutrally stable.

Substituting $\epsilon_{\mathrm{R}} = \epsilon_{\mathrm{c}}$ (where ϵ_{c} is the cutoff value) into equation (3.40) gives

$$\epsilon_{\mathrm{c}} = \frac{\Sigma_{\mathrm{R}}^2 \left(2\Sigma_{\mathrm{R}} + 3d - 2\right)}{\Sigma_{\mathrm{R}} \left(3d + 2\right) - 2}, \tag{6.6}$$

and the system is unstable and stable to small perturbations when $\epsilon_{\mathrm{R}} < \epsilon_{\mathrm{c}}$ and $\epsilon_{\mathrm{R}} \geq \epsilon_{\mathrm{c}}$, respectively. Therefore, when $\epsilon_{\mathrm{R}} < \epsilon_{\mathrm{c}}$ or $\epsilon_{\mathrm{R}} \geq \epsilon_{\mathrm{c}}$, the HC system will exhibit UC or TH behaviour, or LV behaviour, respectively. The analytically calculated transition curve (shown by the dashed line) in Figure 6.1, is indistinguishable from the corresponding numerically calculated transition curve (shown by the solid line), confirming that equation (6.6) is the analytic expression for the curve separating UC or TH behaviour with LV behaviour.

Furthermore, equation (6.6) shows that ϵ_{c} decreases as d increases, agreeing with the numerical results shown in Figure 6.1, where the transition curve separating UC or TH behaviour with LV behaviour tends towards the Σ_{R}-axis as d increases. This makes sense physically since the electric field is the only source of instability in this system, and increasing d weakens the influence of the electric field. Hence, the region where LV behaviour is observed is expected to become larger as d increases.

6.5.2 Transition curve separating UC and TH behaviour

Limited progress has been made in analysing the transition curve that separates UC and TH behaviour. There are additional factors involved in this system which make this curve difficult to analyse. Firstly, the position of the singularity is dependent on Σ_{R} and d, and so changes throughout parameter space. Secondly, there are now two ways in which UC behaviour is observed and, thirdly, the value for L changes at every point in parameter space. Hence, these additional factors make the system more complex and difficult to analyse. Furthermore, in contrast to the PC case, this transition curve does not show a tongue. This is since L is

calculated at each point in parameter space using $k_{\max}$, and so h always evolves to form one filling lobe and one draining lobe. Recall that, in Section 5.5.2, the tongue is associated with a change in the number of filling lobes (that ultimately form in the evolution of h) as a parameter is varied in parameter space, leading to a change in behaviour. Hence, for the HC case, the number of filling lobes will not change as a parameter is varied since L is determined using the most unstable wavenumber $k_{\max}$, and so we would not expect to see tongues as was observed in the PC case.

6.6 Summary

In summary, we have investigated the HC model, that has governing equation (2.99) for h, both analytically and numerically. We found that, as in the PC case, the LV, UC and TH behaviours are possible, albeit the details of each behaviour are different.

An investigation of $(\Sigma_{\mathrm{R}}, \epsilon_{\mathrm{R}})$ parameter space with varying values of d was performed in Section 6.1, and the transition curves separating each behaviour was obtained. In Section 6.2, we described and investigated LV behaviour, and linear stability theory showed that LV behaviour occurs when $s < 0$ for all $k > 0$.

We also described and investigated UC behaviour, where, in contrast to the PC case, self-similar behaviour does not occur. This is because the singularity in the governing equation (2.99) occurs when $h > d$, and so the interface touches the upper electrode before reaching the singularity.

TH behaviour was described and investigated in Section 6.4, and we showed that the system evolves through two stages seen in the PC case, namely, progressive growth and buckling. However, instead of the onset of sliding occurring, the interface undergoes a cascade of secondary buckling events not seen in the PC case. Here, the local minima in the trough regions split into two minima (and so into

two separate trough regions) as $h \to 0$, as shown in Figure 6.3. We showed that the presence of the tangential component of the Maxwell stress (not present in the PC model) causes the secondary buckling events.

In Section 6.5, we investigated the transition curves in $(\Sigma_{\mathrm{R}}, \epsilon_{\mathrm{R}})$ parameter space, as shown in Figure 6.1. In particular, in Section 6.5.1, linear stability theory was used to show that the transition curves separating UC or TH behaviour from LV behaviour occurs when $s < 0$ for all $k > 0$. Equation (5.85) gives an analytical expression for the transition curve separating regions with UC or TH behaviour from LV behaviour. In Section 6.5.2, limited progress was made in analysing the transition curve separating UC and TH behaviour, due to the additional factors that make investigating this curve more difficult. However, we explained that, since $k_{\max}$ was used to calculate L at every point in parameter space, no tongues will be observed (as was seen in the PC case).

Chapter 7

Long-wave (LW) model

In this Chapter, the LW model, that has governing equations (2.107)–(2.108), is investigated. An investigation $(\Sigma_{\mathrm{R}}, \epsilon_{\mathrm{R}})$ parameter space is again performed for various values of E_{b}. Since the LW model is more complex than the PC and HC models, this parameter space investigation is made more complicated, as will be discussed in Section 6.1.1. Again, the same three behaviours seen in Chapters 5 and 6, i.e. LV, UC and TH, are observed. The details of these behaviours are the same as the HC case, as will be discussed in Sections 7.2–7.4. However, an additional behaviour is observed, which does not occur in the PC and HC cases, which we call touchdown (TD). During TD, the interface approaches the lower electrode and touches it in finite time, and will be described and investigated fully in Section 7.5. In Section 7.6, the transition curves separating the four behaviours are investigated and linear stability theory is used to obtain the transition curves analytically.

7.1 $(\Sigma_{\mathrm{R}}, \epsilon_{\mathrm{R}})$ parameter space

As mentioned above, for the LW model there are four possible behaviours, namely, UC, LV, TH, and TD. The behaviour that the system adopts is dependent on the parameters Σ_{R}, ϵ_{R}, d, E_{b}, and L. This five-dimensional parameter space is

impracticably large to explore completely, and so in order to make things more tractable, we set $d = 5$ and $L = 150$, and investigated $(\Sigma_{\mathrm{R}}, \epsilon_{\mathrm{R}})$ parameter space for various values of E_{b}. Our investigation of $(\Sigma_{\mathrm{R}}, \epsilon_{\mathrm{R}})$ parameter space for the HC case shows that qualitatively similar behaviours occur for other values of d. Hence, we hypothesise that this is the case for the LW model, however, our subsequent investigation of $(\Sigma_{\mathrm{R}}, \epsilon_{\mathrm{R}})$ parameter space is performed for $d = 5$.

Unlike the PC and HC models, where we obtained explicit expressions for $k_{\max}$ (given by equations (3.45) and (3.41), respectively), it is impossible to obtain a closed-form expression for $k_{\max}$ for the LW model. This is because the expression for s is of degree 8 in the variable k, and the Abel-Ruffini Theorem [153, 154] states that there are no closed-form expressions for the solutions of equations with arbitrary coefficients of degree 5 or higher. The value $L = 150$ was chosen in our numerical calculations (except where noted otherwise) so that the domain length is large enough to contain waves of small wavenumber k where $s > 0$, while not requiring an excessive number of grid points to resolve h and q. In Section 7.1.1, the numerical investigation of $(\Sigma_{\mathrm{R}}, \epsilon_{\mathrm{R}})$ parameter space is described, and we describe the criteria that are used to classify each behaviour. In Section 7.1.2, the results of this investigation are presented and discussed.

7.1.1 Numerical investigation of $(\Sigma_{\mathrm{R}}, \epsilon_{\mathrm{R}})$ parameter space

The investigation of $(\Sigma_{\mathrm{R}}, \epsilon_{\mathrm{R}})$ parameter space was performed by solving the governing equations for h and q of the LW model (equations (2.107) and (2.112), respectively) using Dr Wray's C++ code. As discussed in Chapter 4, this code is different from that used in the PC and HC cases (described in Section 4.1.2) as it also solves two coupled PDEs for h and q instead of one for h. The numerical calculations were performed using 1024 grid points and the initial conditions given by (4.17) with $\delta = 0.01$. Using 1024 grid points meant that the numerical calculations took approximately 4 weeks to produce the results of $(\Sigma_{\mathrm{R}}, \epsilon_{\mathrm{R}})$ parameter

space that are shown in Figure 7.1 in Section 7.1.2 (which contains approximately 700000 data points). Investigating more of parameter space was impractical given the restrictions on both time and computing power available. The investigation of parameter space was performed over the ranges $1 < \Sigma_{\mathrm{R}} < 10$, $1 < \epsilon_{\mathrm{R}} < 60$, and $E_{\mathrm{b}} = \{1, 2, 3, 4, 5, 6\}$. The step sizes for Σ_{R} and E_{b} were 0.05 and 1, respectively. To speed up the investigation, the step size of ϵ_{R} was varied from 0.05 closer to the transition curves to 0.2 further away from them. These step sizes were chosen so that an accurate picture of parameter space was obtained whilst not taking an inordinate amount of time to do so. At each point in parameter space, the behaviour was classified according to the following conditions:

1. LV behaviour: When $h_{\max} - h_{\min} < 10^{-9}$.
2. UC behaviour: When $\Delta t < 10^{-4}$ and $d - h_{\max} < 10^{-2}$.
3. TH behaviour: When $h_{\min} < 10^{-3}$ and $\Delta t > 10^{-2}$.
4. TD behaviour: When $h_{\min} < 10^{-4}$ and $\Delta t < 10^{-6}$ (as smaller step sizes are required to resolve the rapidly moving interface as $h_{\min} \to 0$).

The Δt condition used to determine UC acts as an extra condition since the time step was halved whenever $h > d$ in the numerical calculations. These conditions are different from those used in the PC and HC cases due to the occurrence of the additional TD behaviour, which makes it difficult to correctly determine which behaviour is occurring. Specifically, $h_{\min} \to 0$ for increasing t for both TH and TD behaviour, and so we require an additional criteria involving Δt to correctly determine which behaviour is occurring (since $\Delta t \to 0$ for UC behaviour and Δt becomes large at late times for TH behaviour). Also, $\Delta t \to 0$ as t increases for both UC and TD behaviour, and so we require an additional criteria involving $d - h_{\max}$ and $h_{\min}$ to correctly determine which behaviour is occurring. The results obtained using the C++ code were cross-referenced with those of the

Matlab code introduced in Chapter 4. In particular, the results of the two codes were compared in order to determine whether the same behaviour is predicted, as well as comparing the final interfacial profiles. We checked points in $(\Sigma_{\mathrm{R}}, \epsilon_{\mathrm{R}})$ parameter space close to the transitions, and the results are not presented here but the same behaviours were predicted in all cases.

7.1.2 Results of the investigation of $(\Sigma_{\mathrm{R}}, \epsilon_{\mathrm{R}})$ parameter space

The results of the investigation of $(\Sigma_{\mathrm{R}}, \epsilon_{\mathrm{R}})$ parameter space are presented in Figure 7.1, together with the numerically and analytically calculated transition curves (which are analysed in Sections 7.6.1 and 7.6.2). Figure 7.1 shows $(\Sigma_{\mathrm{R}}, \epsilon_{\mathrm{R}})$ parameter space together with numerically and analytically calculated transition curves, given by the solid and dashed lines (of which there are two sets in parts (a)–(f)), respectively, separating regions with UC, TH, LV, and TD behaviours. There is evidently excellent agreement between the solid and dashed lines, which are virtually indistinguishable. The insets show the numerically calculated behaviours, where the light grey, dark grey, and black dots indicate LV, UC, and TH behaviour, respectively. Note that the dots are so numerous that they are indistinguishable, and so the regions appear to be shaded. The parameter values used are $d = 5$, and (a) $E_{\mathrm{b}} = 1$, (b) $E_{\mathrm{b}} = 2$, (c) $E_{\mathrm{b}} = 3$, (d) $E_{\mathrm{b}} = 4$, (e) $E_{\mathrm{b}} = 5$, and (f) $E_{\mathrm{b}} = 6$.

Figure 7.1 shows that, as E_{b} increases, there are regions of $(\Sigma_{\mathrm{R}}, \epsilon_{\mathrm{R}})$ parameter space which go from LV behaviour to TD behaviour; this makes sense since the electric field is the only destabilising effect in this system (and so E_{b} increases with increasing field strength). Figure 7.1 also shows the transition between UC and TH behaviour becomes increasingly complicated as E_{b} increases, as shown by the insets, as more tongues and "islands" of TH behaviour form. It was not possible to draw the transition curves between UC and TH behaviour in Figure

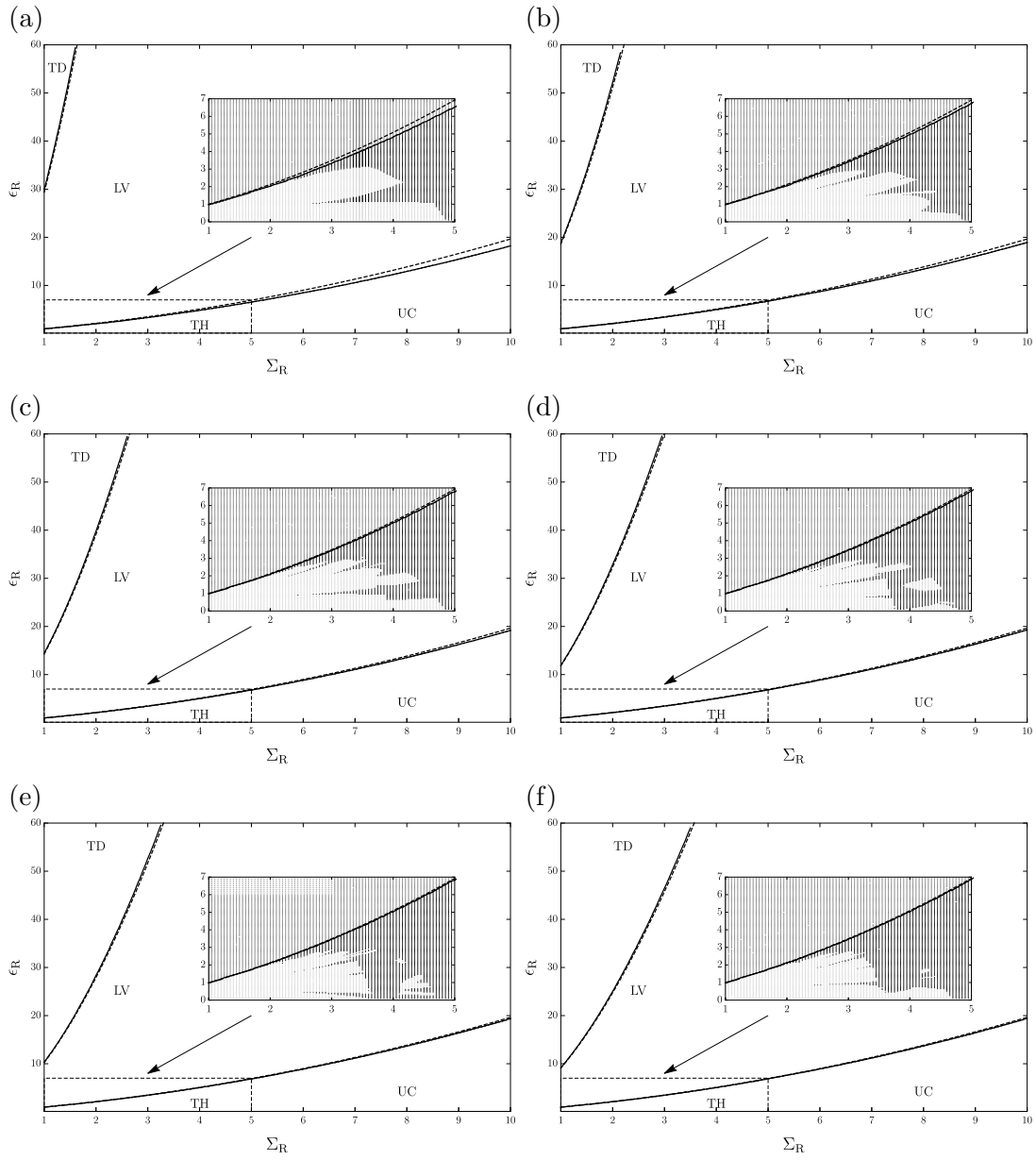

Figure 7.1: Plots of (Σ_R, ϵ_R) parameter space for the LW model, with numerically and analytically calculated transition curves, given by the solid and dashed lines, respectively, separating regions with UC, TH, LV, and TD behaviours, and are virtually indistinguishable. The insets show the numerically calculated behaviours, where the light grey, dark grey, and black dots indicate LV, UC, and TH behaviour, respectively, and are so numerous that they are indistinguishable and so the region appears to be shaded. The parameter values used are $d = 5$, and (a) $E_b = 1$, (b) $E_b = 2$, (c) $E_b = 3$, (d) $E_b = 4$, (e) $E_b = 5$, and (f) $E_b = 6$.

7.1 due to their complicated nature as shown in the insets of Figure 7.1.

7.2 Levelling (LV) behaviour

LV behaviour occurs when perturbations to the base state ($\overline{h} = 1$ and $\overline{q}$ given by equation (3.2)) decay, as illustrated by Figure 5.2. Since the domain length is held constant in our numerical calculations, namely, $L = 150$, LV behaviour occurred for one of three reasons. Firstly, there are unstable wavenumbers but the corresponding wavelengths are too long (i.e. the values of k are too small) to fit into the domain. Secondly, there are no unstable wavenumbers and so the system is always stable. Thirdly, there are unstable wavenumbers that are short wavelength (large values of k) but, as energy is transferred from small (stable) to large (unstable) wavenumbers, the interface levels to the point where the condition for LV behaviour (set in our numerical code) is satisfied. Note that the third reason for LV behaviour is not valid in the PC and HC cases since any instabilities in these systems are always LW. In Section 7.6, we will determine analytically (using linear stability theory) the transition curves separating UC or TH, and TD behaviour from LV behaviour, which show very good agreement with the numerical results.

7.3 Upper contact (UC) behaviour

UC behaviour occurs when the interface touches the upper electrode, as shown in Figure 6.2, and, like the HC case (but unlike the PC case), the interface does not show self-similar behaviour. The singularity in the LW model occurs where the denominator in the ϕ^{G} and ϕ^{L} terms in equations (2.111) and (2.110), respectively,

are zero, i.e. where

$$h = \frac{\epsilon_{\mathrm{R}} d}{\epsilon_{\mathrm{R}} - 1} > d. \tag{7.1}$$

Therefore, as in the HC case, the singularity occurs at $h > d$, which does not occur physically since the interface touches the upper electrode before reaching the singularity. Hence, we do not observe self-similar behaviour and $\partial h/\partial t \to \infty$ as t increases.

7.4 Thinning (TH) behaviour

TH behaviour occurs when the interface approaches the lower electrode but only touches it in infinite time. The interface evolves through the same three stages that occur during TH behaviour in the HC case, namely, "progressive growth", "buckling", and a "cascade of secondary buckling events".

In order to describe this behaviour, we express the charge transport equation (2.108) in the form

$$\frac{\partial q}{\partial t} + \frac{\partial C_v}{\partial x} = C_d, \tag{7.2}$$

where

$$C_v = C_{\mathrm{N}} + C_{\mathrm{T}}, \qquad C_d = \Sigma_{\mathrm{G}} \phi_y^{\mathrm{G}} - \Sigma_{\mathrm{L}} \phi_y^{\mathrm{L}}, \tag{7.3}$$

are the convection and ion conduction terms, respectively,

$$C_{\mathrm{N}} = \frac{1}{2} q h^2 \frac{\partial p}{\partial x}, \qquad C_{\mathrm{T}} = E_{\mathrm{b}} q^2 h \frac{\partial \phi^{\mathrm{L,G}}|_{y=h}}{\partial x}, \tag{7.4}$$

are the terms due to the normal and tangential stress, respectively, and p, ϕ^{L}, and ϕ^{G} are given by equations (2.109), (2.110), and (2.111), respectively. Figure

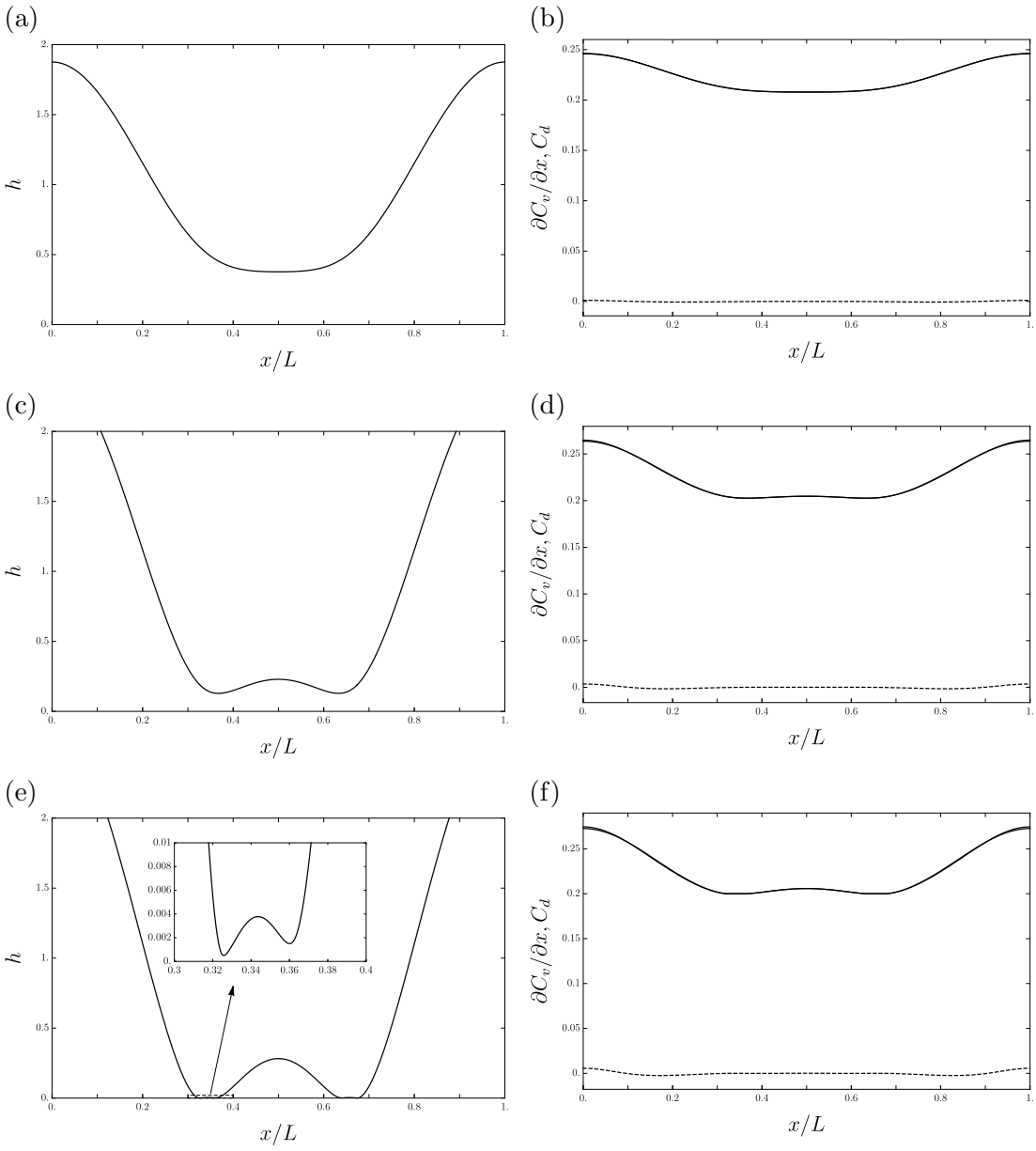

Figure 7.2: Plots of h as a function of x/L (first column), and $\partial C_v/\partial x$ (dashed line) and the first and second parts of C_d (given by the solid lines which are indistinguishable) as functions of x/L (second column). The parameter values used are $E_\mathrm{b} = 5$, $d = 5$, $\Sigma_\mathrm{R} = 2$, $\epsilon_\mathrm{R} = 1$, and $L = 25$.

7.2 shows plots of h as a function of x/L (first column), and $\partial C_v/\partial x$ (dashed line) and the two parts of C_d (given by the two indistinguishable solid lines) as functions of x/L (second column). Figures 7.2 (b), (d), and (f) show that, during TH behaviour, the $\partial C_v/\partial x$ terms are negligible compared to the C_d terms. Hence, the charge transport equation (7.2) reduces to a statement of the continuity of current at $y = h$, namely,

$$\phi_y^{\mathrm{G}} = \Sigma_{\mathrm{R}} \phi_y^{\mathrm{L}}, \tag{7.5}$$

and so the LW model simplifies to that of the HC limiting case, where the governing equation for h is given by equation (2.99). We do not say anymore about TH behaviour since it is identical to the TH behaviour in the HC case (and this was confirmed numerically).

7.5 Touchdown (TD) behaviour

TD behaviour occurs when the interface touches the lower electrode in finite time, as shown in Figure 7.3. Figure 7.3 shows plots of h in (a,c) and q in (b,d) as functions of x/L. The dashed lines in parts (a)–(d) correspond to the same time, which is the last time shown in parts (a,b) and the first time shown in parts (c,d). The positions of the minimum value of h and the maximum value of q are denoted by $x = x_{\min}$ and $x = x_{\max}$, respectively, and part (e) shows plots of $x_{\min}/L$ (solid lines) and $x_{\max}/L$ (dashed lines) as functions of t. Figures 7.3(a,b) show that $q \to \infty$ and $h \to 0$ as t increases. When h is close to the lower electrode, a new phenomenon occurs, namely, the minimum value of h splits into two local minima and the maximum value of q splits into two local maxima, as shown in Figures 7.3(c,d). We will call this new phenomenon "tip splitting" and we note that it has not previously been reported in the literature. Figure 7.3(e) shows that tip splitting for q occurs just prior to tip splitting for h. For the Matlab code,

numerically resolving the interface during tip splitting proved to be challenging, as resolving tip splitting on a uniform grid required a large number of grid points: for the numerical calculations shown in Figure 7.3, we used 4×10^4 grid points and so the grid step size was $\Delta x = 1.5708 \times 10^{-4}$.

7.5.1 Investigation of tip splitting

As we have already seen, during tip splitting, q splits at $t = t_1$ and h splits at $t = t_2$ (where $t_1 < t_2$), and so we can divide it into three stages, namely, $t < t_1$, $t_1 \leq t < t_2$, and $t \geq t_2$. To gain insight into the mechanisms of splitting, these three stages were investigated by analysing the contributions to the liquid flux Q arising from the normal and tangential stresses, denoted by Q_{N} and Q_{T}, respectively, i.e.

$$Q = Q_{\mathrm{N}} + Q_{\mathrm{T}}, \tag{7.6}$$

where

$$Q_{\mathrm{N}} = \frac{h^3}{3}\frac{\partial p}{\partial x}, \qquad Q_{\mathrm{T}} = \frac{E_{\mathrm{b}}}{2} q h^2 \frac{\partial \phi^{\mathrm{L,G}}|_{y=h}}{\partial x}, \tag{7.7}$$

and p, ϕ^{L}, and ϕ^{G} are given by equations (2.109), (2.110), and (2.111), respectively. Also, the numerical calculations reveal that, as shown in Figure 7.4, at points in $(\Sigma_{\mathrm{R}}, \epsilon_{\mathrm{R}})$ parameter space where TD behaviour occurs, the $\partial C_v/\partial x$ terms (the convection terms) in the charge transport equation (7.2) dominate and C_d terms (the ion conduction terms) are negligible. Specifically, Figure 7.4 shows (a) a plot of h as a function of x/L, and (b) the corresponding plots of $\partial C_v/\partial x$ (solid line), $\Sigma_{\mathrm{G}}\phi_y^{\mathrm{G}}$, and $\Sigma_{\mathrm{L}}\phi_y^{\mathrm{L}}$, i.e. the first and second terms of C_d (7.3) (given by the indistinguishable dashed lines), as functions of x/L. Hence, for our investigation of tip splitting, we set $C_d = 0$ in equation (7.2), i.e. neglect the ion conduction terms, which yields

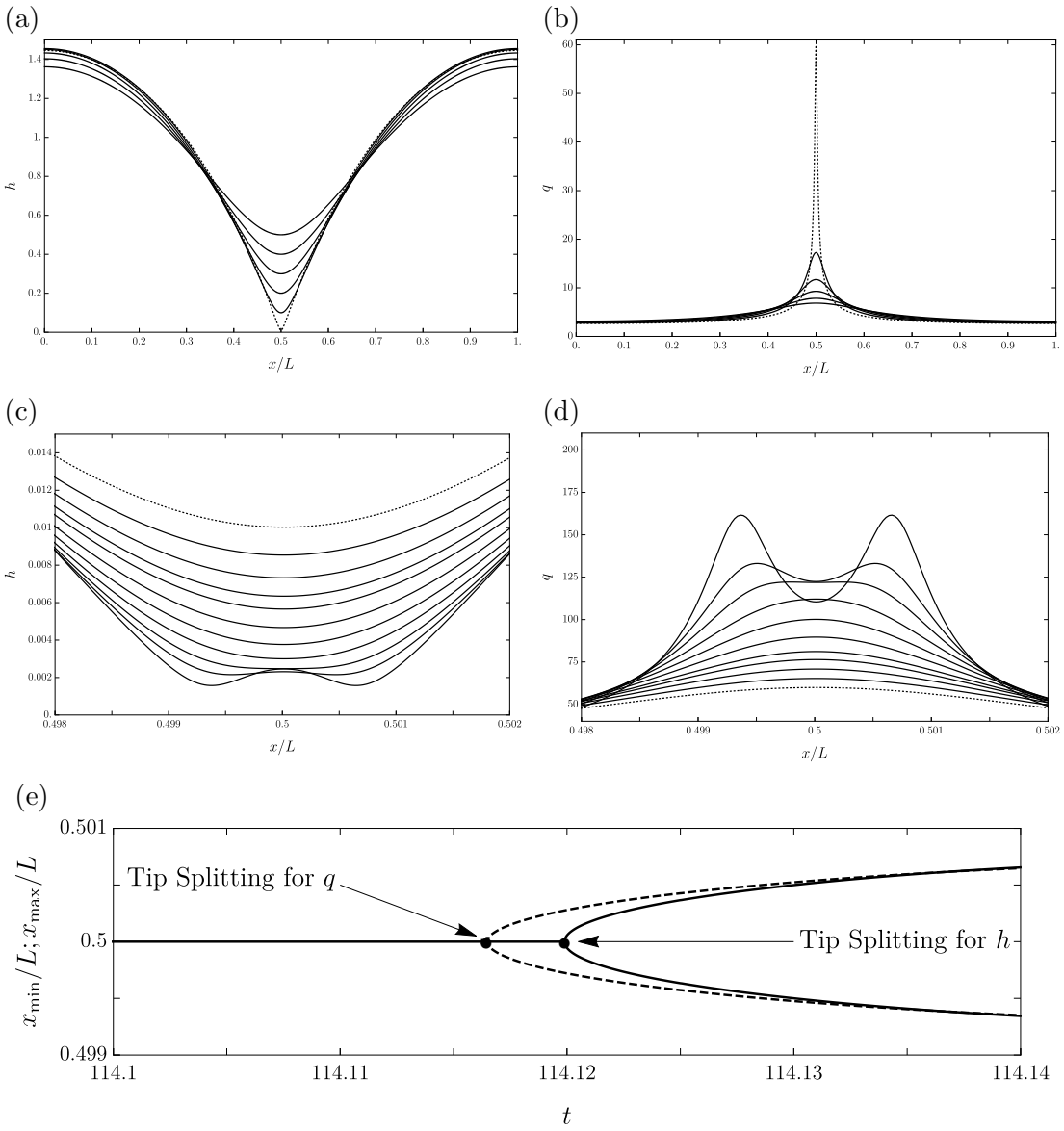

Figure 7.3: Plots of h in (a,c) and q in (b,d) as functions of x/L. The dashed lines in parts (a)–(d) correspond to the same time, which is the last time shown in parts (a,b) and the first time shown in parts (c,d). Part (e) shows plots of $x_{\min}/L$ (solid lines) and $x_{\max}/L$ (dashed lines) as functions of t, and the dots indicate where tip splitting occurs for h and q. The parameter values used are $E_{\rm b} = 5$, $d = 5$, $\Sigma_{\rm R} = 2$, $\epsilon_{\rm R} = 40$, and $L = 2\pi$.

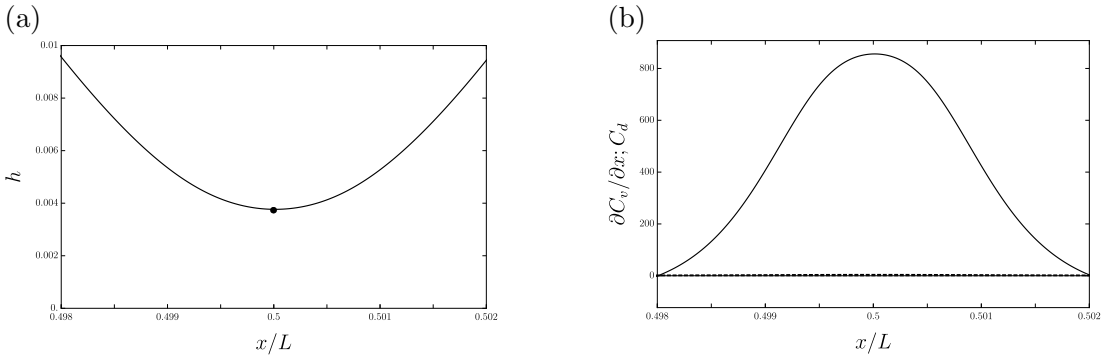

Figure 7.4: Plot of (a) h as a function of x/L, and the corresponding plots of (b) $\partial C_v/\partial x$ (solid line) and the first and second parts of C_d (given by the dashed lines which are indistinguishable) as functions of x/L. The dot in (a) indicates the position of the minimum point. The parameter values used are $E_\mathrm{b} = 5$, $d = 5$, $\Sigma_\mathrm{R} = 2$, $\epsilon_\mathrm{R} = 40$, and $L = 2\pi$.

$$\frac{\partial q}{\partial t} + \frac{\partial C_v}{\partial x} = 0. \tag{7.8}$$

Figure 7.5 shows plots of h ((a)–(c)), q ((d)–(f)), Q ((g)–(i)), and C_v ((j)–(l)) as functions of x/L. In the third/fourth rows, the solid, dashed, and dotted lines denote Q/C_v, $Q_\mathrm{N}/C_\mathrm{N}$, and $Q_\mathrm{T}/C_\mathrm{T}$, respectively. The first column ((a), (d), (g), (j)) shows plots at a time t before t_1 (i.e. the first stage of tip splitting), the second column ((b), (e), (h), (k)) shows plots at a time t such that $t_1 \leq t < t_2$ (i.e. the second stage of tip splitting), and the third column ((c), (f), (i), (l)) shows plots at a time t after t_2 (i.e. the third stage of tip splitting).

7.5.1.a First stage of tip splitting ($t < t_1$)

During this stage, tip splitting has not occurred for either h or q. Figure 7.5(g) shows that $Q = 0$ at $x/L = x_\mathrm{min}/L = 1/2$: Q is negative and positive to the left and right of $x = x_\mathrm{min}$, respectively. This corresponds to liquid draining away from the interface at $x = x_\mathrm{min}$, and so h decreases at $x = x_\mathrm{min}$. Figure 7.5(j) shows that $C_v = 0$ at $x/L = x_\mathrm{max}/L = 1/2$: C_v is positive and negative to the left and right of $x = x_\mathrm{max}$, respectively. This corresponds to charge moving towards $x = x_\mathrm{max}$, and so q increases near $x = x_\mathrm{max}$.

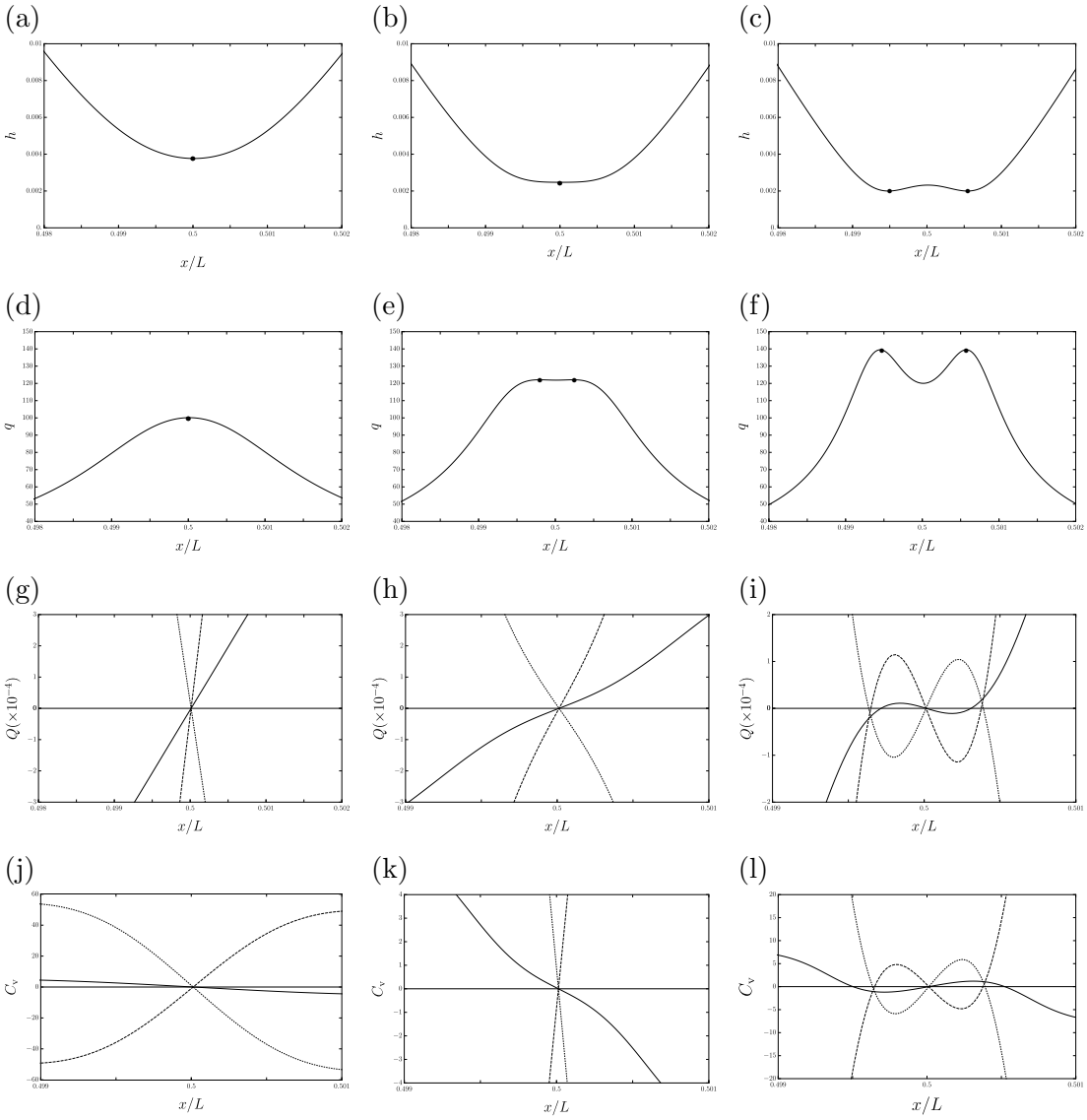

Figure 7.5: Plots of h (first row), q (second row), Q (third row), and C_v (fourth row) as functions of x/L. In the third/fourth rows, the solid, dashed, and dotted lines denote Q/C_v, $Q_\mathrm{N}/C_\mathrm{N}$, and $Q_\mathrm{T}/C_\mathrm{T}$, respectively. The first column ((a), (d), (g), (j)) shows plots at a time t before t_1, the second column ((b), (e), (h), (k)) shows plots at a time t such that $t_1 \leq t < t_2$, and the third column ((c), (f), (i), (l)) shows plots at a time t after t_2. The dots in (a)–(f) indicate the positions of the minimum points, i.e. where $x = x_\mathrm{min}$. The parameter values used are $E_\mathrm{b} = 5$, $d = 5$, $\Sigma_\mathrm{R} = 2$, $\epsilon_\mathrm{R} = 40$, and $L = 2\pi$.

7.5.1.b Second stage of tip splitting ($t_1 \leq t < t_2$)

During this stage, tip splitting has occurred for q but not for h. Figure 7.5(h) shows that $Q = 0$ at $x/L = x_{\min}/L = 1/2$: Q is negative and positive to the left and right of $x = x_{\min}$, respectively. This corresponds to liquid draining away from the interface at $x = x_{\min}$, and so h decreases there. To the left and right of $x/L = 1/2$, there are values of x for which the slope of Q steepens. This corresponds to liquid draining away from these values of x faster than the liquid draining in; hence, the value of h is decreasing faster at these values of x, showing that new minima for h will form. Figure 7.5(k) shows that $C_v = 0$ at $x/L = x_{\max}/L = 1/2$: C_v is positive and negative to the left and right of $x = x_{\max}$, respectively. This corresponds to charge moving towards $x = x_{\max}$, and so q increases near $x = x_{\max}$. However, C_v is steeper at one side of the new maxima points for q than the other side. This corresponds to extra charge accumulating at these new maxima points, and so q increases near these points.

7.5.1.c Third stage of tip splitting ($t \geq t_3$)

At this stage, tip splitting has occurred for both h and q. Figure 7.5(i) shows that there are three points where $Q = 0$. This corresponds to liquid draining into the region between the two minima, shown in Figure 7.5(c), and so h increases in the vicinity of $x/L = 1/2$. Figure 7.5(i) corresponds to liquid draining away from the interface at the two minimum points for h, and so the interface decreases at the minimum points. Figure 7.5(l) shows that there are now three points where $C_v = 0$. This corresponds to charge moving towards the points where the two local maxima are located, and so q increases at these maximum points. Also, C_v is negative and positive immediately to the left and right of $x/L = 1/2$, corresponding to charge moving away from $x/L = 1/2$. Hence, q decreases in the vicinity of $x/L = 1/2$.

7.5.2 Discussion of the time difference between the onset of tip splitting for h and q

In this subsection, we discuss the time difference between the onset of tip splitting for h and q. The driving terms in the governing equations during tip splitting, i.e. $Q_{\mathrm{N}} + Q_{\mathrm{T}}$ and $C_{\mathrm{N}} + C_{\mathrm{T}}$, are structurally almost identical, as can be seen from the full governing equations for h and q (equations (2.107) and (2.112), respectively), which makes the time difference between the onset of tip splitting for h and q perhaps slightly unexpected. However, the relative significance of the tangential component compared to the normal component is slightly different in the governing equation for q (i.e. $C_{\mathrm{T}}/C_{\mathrm{N}}$) compared to that for h (i.e. $Q_{\mathrm{T}}/Q_{\mathrm{N}}$). In particular,

$$\frac{C_{\mathrm{T}}}{C_{\mathrm{N}}} \Big/ \frac{Q_{\mathrm{T}}}{Q_{\mathrm{N}}} = \frac{4}{3}, \tag{7.9}$$

i.e. the tangential component is a third stronger (compared to the normal component) in the governing equation for q than it is for h. This accounts for the slightly earlier onset of tip splitting for q. It is informative to examine why this happens. The evolution of h and q is determined, respectively, by

$$\frac{\partial h}{\partial t} = -\frac{\partial}{\partial x} \int_0^h u \, \mathrm{d}y, \tag{7.10}$$

$$\frac{\partial q}{\partial t} = -\frac{\partial}{\partial x} \left(q u|_{y=h} \right), \tag{7.11}$$

where the streamwise velocity u is

$$u = \frac{1}{2} \frac{\partial p}{\partial x} \left(y^2 - 2hy \right) - E_{\mathrm{b}} q \frac{\partial \phi|_{y=h}}{\partial x} y, \tag{7.12}$$

and ion conduction terms have been omitted as their effects are negligible, as discussed in Section 7.5.1. Thus the relative significance of the tangential and normal components for h is determined by their relative depth-averaged values

$\left(\int_0^h u \, \mathrm{d}y\right)$, whereas that for q is determined by their relative interfacial values ($u|_{y=h}$). This introduces a disparity because the normal terms are quadratic in y, whereas the tangential terms are linear in y. This disparity is ultimately the source of the time difference between the onset of sliding for h and q: that one governing equation (equation (7.10)) is incorporated as a body force, while the other (equation (7.11)) is a tangential interfacial stress, resulting in a difference in their effect on the liquid flux and on interfacial flux for charge.

7.6 The transition curves in $(\Sigma_{\mathrm{R}}, \epsilon_{\mathrm{R}})$ parameter space

In this Section, we will investigate the transitions in $(\Sigma_{\mathrm{R}}, \epsilon_{\mathrm{R}})$ parameter space between UC or TH behaviour and LV behaviour, and between LV behaviour and TD behaviour. We note that for the LW model, there are three possible plots of the linear growth rate s as a function of k (i.e. the dispersion curves), as shown in Figure 7.6, which are:

1. $s < 0$ for all $k > 0$, as illustrated by Figure 7.6(a).

2. $s > 0$ for a range of unstable wavenumbers $0 < k < k_{\mathrm{c}}$, where $s = 0$ when $k = k_{\mathrm{c}}$, as illustrated by Figure 7.6(b).

3. $s > 0$ for a range of unstable wavenumbers $0 < k_1 < k < k_2$, where $s = 0$ when $k = k_1$ or $k = k_2$, as illustrated by Figure 7.6(c).

In Sections 7.6.1 and 7.6.2, we investigate the points in $(\Sigma_{\mathrm{R}}, \epsilon_{\mathrm{R}})$ parameter space where there is a qualitative change in the dispersion curves, and use these points to obtain an analytical expression for some of the transition curves.

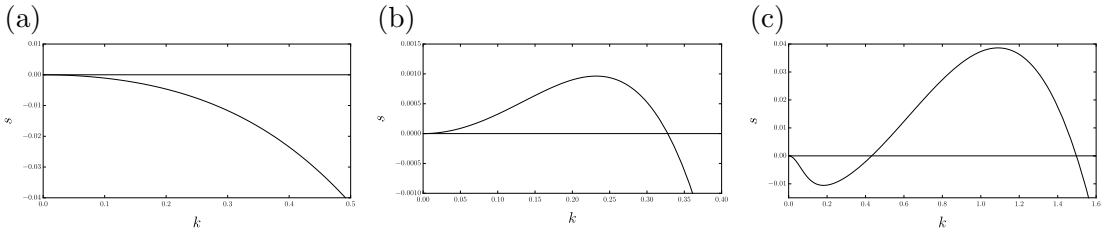

Figure 7.6: Plots of s as a function of k. The parameter values used are $E_{\mathrm{b}} = 5$, $d = 5$, and (a) $\Sigma_{\mathrm{R}} = 2$ and $\epsilon_{\mathrm{R}} = 5$, (b) $\Sigma_{\mathrm{R}} = 10$ and $\epsilon_{\mathrm{R}} = 2$, and (c) $\Sigma_{\mathrm{R}} = 2$ and $\epsilon_{\mathrm{R}} = 40$.

7.6.1 Transition curve separating UC or TH behaviour from LV behaviour

In this Section, we will show that UC or TH behaviour occurs at points in $(\Sigma_{\mathrm{R}}, \epsilon_{\mathrm{R}})$ parameter space where the dispersion curve is of the form shown in Figure 7.6(b), and we will calculate where in $(\Sigma_{\mathrm{R}}, \epsilon_{\mathrm{R}})$ parameter space there is a qualitative change in the dispersion curves between those shown in Figures 7.6(a) and (b). After investigating dispersion curves throughout $(\Sigma_{\mathrm{R}}, \epsilon_{\mathrm{R}})$ parameter space, we found that they cannot change directly between those of the form shown in Figures 7.6(b) and (c). Hence, a transition in the sign of $\partial^2 s/\partial k^2$ at $k = 0$ must correspond to a transition between curves of type (a) and type (b). This transition is determined to be

$$\epsilon_{\mathrm{R}} = \frac{\Sigma_{\mathrm{R}}^2 \left(2\Sigma_{\mathrm{R}} + 3d - 2\right)}{2\Sigma_{\mathrm{R}} + 3d\Sigma_{\mathrm{R}} - 2}. \tag{7.13}$$

Recall that the solid and dashed lines in Figure 7.1 correspond to the numerically and analytically calculated transition curves, respectively, and equation (7.13) also provides the expression for the analytically calculated transition curves (dashed lines) in Figure 7.1. There is good agreement between the lower solid and dashed lines in Figure 7.1. The differences between the solid and dashed curves are due to the restrictions of having a finite domain length in our numerical calculations, i.e. close to the transition curves, the domain was not long enough to

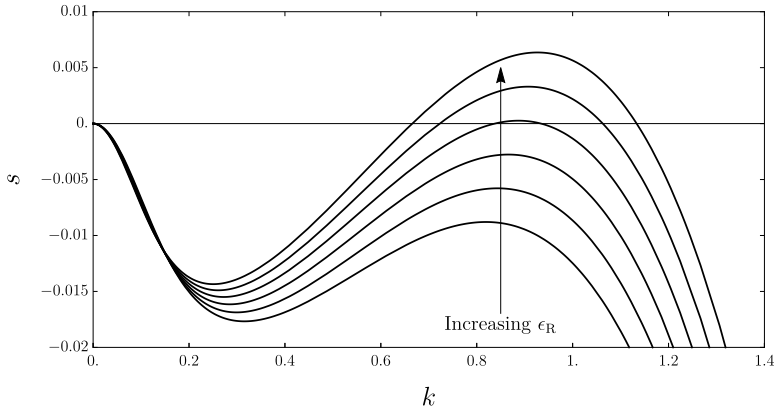

Figure 7.7: Plots of s as a function of k. The parameter values used are $E_b = 5$, $d = 5$, $\Sigma_R = 2$, and $\epsilon_R = \{25, 26, 27, 28, 29, \text{and } 30\}$.

contain any unstable wavenumbers and so LV behaviour was observed.

7.6.2 Transition curve separating LV behaviour from TD behaviour

We will not show that TD behaviour occurs at points in parameter space where the dispersion curve is of the form shown in Figure 7.6(c), and will calculate where this occurs. The transition between the dispersion curves shown in Figures 7.6(a) and (c) occurs when $s > 0$ at some finite, non-zero wavenumber $k > 0$ as shown in Figure 7.7. Figure 7.7 shows representative plots of s as a function of k for varying values of ϵ_R. Hence, this change in behaviour is caused by a finite-wavelength instability, and so an analytical expression that captures this transition curve could not be obtained. Therefore, we calculated this transition curve numerically by choosing a value for Σ_R and increasing ϵ_R until $s > 0$ (for values of k in the range $0.5 < k < 2$ due to the finite-wavelength instability). In order to perform these calculations, the wavenumber k is discretised from $k = 0$ to $k = 2$ in step sizes of 10^{-2}, Σ_R increased from $\Sigma_R = 1$ to $\Sigma_R = 10$ in step sizes of 10^{-2}, ϵ_R is increased in step sizes of 10^{-2}, and we calculate the transition curves for $E_b = \{1, 2, 3, 4, 5, 6\}$. The results are given by the upper dashed lines (analytical results) in Figure 7.1, which are virtually indistinguishable from the

upper solid lines (numerical results). The small difference between the upper solid and dashed lines is because we have to choose a cutoff criteria for each behaviour in our numerical calculations, and so the criteria for LV behaviour (described in Section 7.1.1) is satisfied before energy in the system is transferred from small (stable) wavenumbers to large (unstable) wavenumbers.

7.7 Summary

In summary, an investigation of the LW model revealed four possible behaviours, i.e. LV, UC, TH and TD. The dynamics of the LV, UC and TH behaviours were the same as the HC model. In Section 7.1, a numerical investigation of parameter space was performed, and the transition curves separating the different behaviour were calculated. In Section 7.2, we described and investigated LV behaviour, and found that it occurs due to one of three reasons: when $s < 0$ for all $k > 0$, when the domain length is not large enough to contain any unstable wavenumbers, or when there are short-wavelength instabilities but the criteria for LV is satisfied before energy can be transferred from small (stable) wavenumbers to large (unstable) wavenumbers. In Section 7.3, we described and investigated UC behaviour, and showed that self-similar behaviour does not occur since the singularity in the LW model occurs at $h > d$, which is similar to the HC case. Furthermore, TH behaviour was explored in Section 7.4, and we showed numerically that the governing equations for h and q, (2.107) and (2.108), respectively, reduce to that of the HC case, namely, the governing equation (2.99) for h.

In Section 7.5, we described and investigated the additional TD behaviour, where the interface approaches the lower electrode and touches it in finite time. We showed that a new phenomenon occurs, namely the minimum and maximum of h and q, respectively, split into two minima and maxima, and we called this "tip splitting". Tip splitting for q occurs just before it does for h. We showed that a

possible reason for this difference is that one governing equation (equation (7.10)) is incorporated as a body force, while the other (equation (7.11)) is a tangential interfacial stress, resulting in a difference in their effect on the liquid flux and on interfacial flux for charge.

In Section 7.6, we investigated the two transition curves in (Σ_R, ϵ_R) parameter space, shown in Figure 7.1. For the LW model, there are three qualitatively different dispersion curves, shown in Figure 7.6. We showed that different regions of (Σ_R, ϵ_R) parameter space where LV, UC or TH, and TD behaviours occur correspond to dispersion curves of the form shown in Figures 7.6(a), (b), and (c), respectively.

Chapter 8

Conclusions and future work

8.1 Conclusions

In this thesis, we have investigated the behaviour of a two-dimensional bilayer of leaky-dielectric liquid and gas contained between two planar electrodes. In Chapter 1 we discussed relevant work by previous authors on thin-film and EHD flows, and in Chapter 2 we derived the mathematical models of the system under investigation, including the limiting cases, specifically, the SF, LW, HC, PC and PD models. Linear stability analyses of the SF, LW, HC, and PC models were performed in Chapter 3. This allowed us to show that, for small perturbations of sufficiently long wavelength, the linear stability results of the SF model showed good agreement with the LW, HC, and PC models. In Chapter 4, we introduced and described the numerical schemes used to solve the initial value PDEs for h and q, and for the Shooting Method used to solve the BVP (4.20)–(4.23).

We investigated the PC case in Chapter 5, and found that three behaviours can occur, namely, LV, UC, or TH behaviour. The transition curve separating UC or TH behaviour and LV behaviour was calculated analytically using linear stability theory. The three behaviours were also investigated further. The occurrence of LV behaviour was explained using linear stability theory. For UC behaviour,

similarity solutions were obtained that describe the interface close in time and position to the point of contact with the upper electrode. For TH behaviour, similarity solutions were obtained describing the interface at late times and the sliding phenomenon was shown to occur due to asymmetric perturbations that arise from numerical noise.

In Chapter 6, we investigated the HC case and again found that the LV, UC, and TH behaviours can occur. A systematic investigation of $(\Sigma_{\mathrm{R}}, \epsilon_{\mathrm{R}})$ parameter space was performed, for values of d from 2 to 6, showing where these behaviours occurred and the transition curves separating the different regions were determined. The transition curve separating UC or TH behaviour and LV behaviour was calculated analytically using linear stability theory. The three behaviours were investigated further. The occurrence of LV behaviour was explained using linear stability theory. For UC behaviour, the interface does not show self-similar behaviour, unlike the PC case. For TH behaviour, a new phenomenon occurs that is not present in the PC case, namely, a cascade of buckling events.

In Chapter 7, the LW model was investigated and it was found that four behaviours can occur, namely, LV, UC, TH, and TD behaviour. A systematic investigation of $(\Sigma_{\mathrm{R}}, \epsilon_{\mathrm{R}})$ parameter space was performed with $d = 5$, $L = 150$, and values of E_{b} from 1 to 6, showing where each behaviour occurs. Transitions between LV behaviours and other behaviours were determined analytically using linear stability theory. The four behaviour were investigated further. The occurrence of LV behaviour was explained using linear stability theory. For TH and UC behaviour, the interfacial dynamics were the same as in the HC case. For TD behaviour, the interface touched the lower electrode in finite time, during which the minimum of h split into two minima as it approached the lower electrode (which we termed "tip splitting"), and the corresponding maximum point of q split into two maxima.

Throughout this thesis, we have performed systematic parametric investigations

of each model we have investigated, determining the regions in which different behaviours occur. Coupled with an investigation of the interfacial dynamics of the different behaviours, this has allowed us to obtain a more complete understanding of how varying different parameter values affects what behaviour occurs, and so we have obtained a deeper understanding of this system.

8.2 Further Work

There are many potential avenues that provide an opportunity for future work that builds on the work described in this thesis.

The system investigated in this thesis could be made more general by making the gas a viscous fluid 1.4, so that the hydrodynamics in the upper layer are now important. In particular, the presence of an upper layer may affect the behaviours that occur as well as the structure of parameter space.

It is known that the geometry of the present system influences its behaviour [116]. It would therefore be interesting to investigate what behaviours occur for different geometries and to explore where in parameter space each behaviour occurs. The differences in the behaviours seen in the planar system discussed in this thesis could be compared with those for systems with different geometries, as well as trying to form a physical understanding behind why these differences occur. One possible change in the geometry is to extend the system explored in this thesis to three dimensions, and there has been some previous work exploring this case [76, 117]. Any investigation of such a system would probably have to be numerical: all of the possible behaviours, and their differences with the two-dimensional case, could be determined. A systematic parametric investigation of where they occur is possible, though would be a lot more computationally expensive. We could also investigate the axisymmetric case of a liquid coating the outside of a cylindrical electrode and bounded outside by an outer electrode, similar to the

systems investigated in previous studies [74, 116, 119]. In this situation there is an additional destabilising surface tension term compared to the analogous two-dimensional case in which surface tension is always stabilising. This system has been investigated in previous studies [70, 74, 116, 119], and has exhibited additional behaviours that are different to those described earlier in this thesis. However, there have been few systematic investigations of where these different behaviours occur, and it would therefore be interesting to see how the qualitative structure of parameter space compares with the parameter space of the analogous two-dimensional system

Another potential route for future work is to examine the WRIBL formulation of this system. We applied the method of weighted residuals to the full leaky dielectric problem, as outlined in Appendix F. Due to time constraints, we have only performed a preliminary investigation of the linear stability of the problem according to this formulation, as illustrated by Figure 8.1. Figure 8.1 shows plots of the growth rate s as a function of k, using parameter values $E_{\mathrm{b}} = 5$, $d = 3$, (a) $\epsilon_{\mathrm{R}} = 2$ and $\Sigma_{\mathrm{R}} = 10$, and (b) $\epsilon_{\mathrm{R}} = 30$ and $\Sigma_{\mathrm{R}} = 4$. These parameter values were used to show two plots that are qualitatively different. The solid, dashed and dotted lines denote the SF, WRIBL and LW results, respectively. Figure 8.1 shows that the linear stability results derived using the WRIBL technique are in better agreement with the results of the SF model than are those of the LW model. It would be interesting to see whether the WRIBL formulation captures the same behaviours, or whether new ones occur, like the short-wave behaviour of UC and TD.

Lastly, we could compare our results with those from DNS calculations. Systematic parametric investigations would be impractical, but each individual behaviour could be explored in more detail using DNS. The similarities and differences between the results in this thesis and the DNS calculations could be explored. In particular, it would be interesting to see whether the DNS calcu-

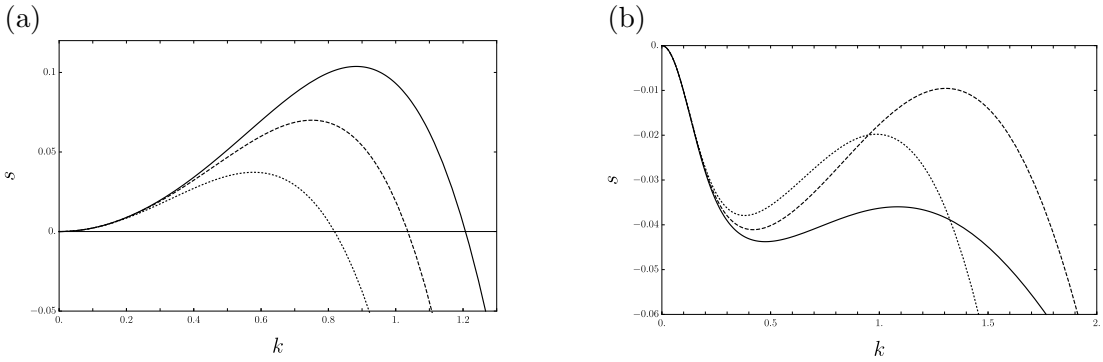

Figure 8.1: Plots of the growth rate s as a function of k, using parameter values $E_{\mathrm{b}} = 5$, $d = 3$, (a) $\epsilon_{\mathrm{R}} = 2$ and $\Sigma_{\mathrm{R}} = 10$, and (b) $\epsilon_{\mathrm{R}} = 30$ and $\Sigma_{\mathrm{R}} = 4$. The solid, dashed and dotted lines denote the results of the SF, WRIBL and LW models, respectively.

lations show the same qualitative behaviour when the LW approximation is no longer valid, e.g. during UC behaviour. In summary, there has been considerable insight gained into the dynamics of EHD flows in this thesis. However, there are still many open challenges in this interesting and surprisingly complicated problem.

Appendix A

SF linear stability matrix

The linearised SF system is described by $A\mathbf{x} = \mathbf{0}$, where $\mathbf{x} = \left(\widetilde{h}, C_1, C_2, C_3, C_4, C_\mathrm{L}, C_\mathrm{G}, D_\mathrm{L}, D_\mathrm{G}\right)^\mathrm{T}$ and A is the 9×9 stability matrix, namely,

$$A = \begin{pmatrix} 0 & k & 1 & -k & 1 & 0 & 0 & 0 & 0 \\ 0 & 1 & 1 & 0 & 0 & 0 & 0 & 0 & 0 \\ 0 & 0 & 0 & 0 & 0 & 1 & 1 & 0 & 0 \\ 0 & 0 & 0 & 0 & 0 & 0 & 0 & \mathrm{e}^{-kd} & \mathrm{e}^{kd} \\ s & ik\mathrm{e}^{k} & ik\mathrm{e}^{k} & ik\mathrm{e}^{-k} & ik\mathrm{e}^{-k} & 0 & 0 & 0 & 0 \\ 0 & A_{62} & A_{63} & A_{64} & A_{65} & A_{66} & A_{67} & A_{68} & A_{69} \\ A_{71} & 2k^2\mathrm{e}^{k} & 2(k^2+k)\mathrm{e}^{k} & 2k^2\mathrm{e}^{-k} & 2(k^2-k)\mathrm{e}^{-k} & 0 & 0 & A_{78} & A_{79} \\ k^2/\mathrm{Ca} & -2k^2\mathrm{e}^{k}i & -2\mathrm{e}^{k}i & 2k^2\mathrm{e}^{-k}i & 2\mathrm{e}^{-k}i & A_{86} & A_{87} & A_{88} & A_{89} \\ A_{91} & 0 & 0 & 0 & 0 & \mathrm{e}^{-k} & \mathrm{e}^{k} & -\mathrm{e}^{-k} & -\mathrm{e}^{k} \end{pmatrix},$$

where

$$A_{62} = \frac{\left(\epsilon_\mathrm{R}\Sigma_\mathrm{G} - \Sigma_\mathrm{L}\right)\mathrm{e}^{k}k^2}{\Sigma_\mathrm{L}(d-1) + \Sigma_\mathrm{G}}i,$$
$$A_{63} = \frac{\left(\epsilon_\mathrm{R}\Sigma_\mathrm{G} - \epsilon_\mathrm{G}\Sigma_\mathrm{L}\right)(k+k^2)\mathrm{e}^{k}}{\Sigma_\mathrm{L}(d-1) + \Sigma_\mathrm{G}}i,$$
$$A_{64} = -\frac{\left(\epsilon_\mathrm{R}\Sigma_\mathrm{G} - \Sigma_\mathrm{L}\right)k^2\mathrm{e}^{-k}}{\Sigma_\mathrm{L}(d-1) + \Sigma_\mathrm{G}}i,$$

$$A_{65} = \frac{(\epsilon_{\mathrm{R}}\Sigma_{\mathrm{G}} - \Sigma_{\mathrm{L}})\,(k - k^2)\mathrm{e}^{-k}}{\Sigma_{\mathrm{L}}(d-1) + \Sigma_{\mathrm{G}}} i,$$

$$A_{66} = -k\,(s\epsilon_{\mathrm{R}} + \Sigma_{\mathrm{L}})\,\mathrm{e}^{-k},$$

$$A_{67} = k\,(s\epsilon_{\mathrm{R}} + \Sigma_{\mathrm{L}})\,\mathrm{e}^{k},$$

$$A_{68} = k\,(s\epsilon_{\mathrm{G}} + \Sigma_{\mathrm{G}})\,\mathrm{e}^{-k},$$

$$A_{69} = -k\,(s\epsilon_{\mathrm{G}} + \Sigma_{\mathrm{G}})\,\mathrm{e}^{k},$$

$$A_{71} = \frac{E_{\mathrm{b}}\,(\epsilon_{\mathrm{R}}\Sigma_{\mathrm{G}} - \Sigma_{\mathrm{L}})\,\Sigma_{\mathrm{L}} k}{(\Sigma_{\mathrm{L}}(d-1) + \Sigma_{\mathrm{G}})^2} i,$$

$$A_{78} = \frac{E_{\mathrm{b}}\,(\epsilon_{\mathrm{L}}\Sigma_{\mathrm{G}} - \epsilon_{\mathrm{G}}\Sigma_{\mathrm{L}})\,k\mathrm{e}^{-k}}{\Sigma_{\mathrm{L}}(d-1) + \Sigma_{\mathrm{G}}} i,$$

$$A_{79} = \frac{E_{\mathrm{b}}\,(\epsilon_{\mathrm{R}}\Sigma_{\mathrm{G}} - \Sigma_{\mathrm{L}})\,k\mathrm{e}^{k}}{\Sigma_{\mathrm{L}}(d-1) + \Sigma_{\mathrm{G}}} i,$$

$$A_{86} = -\frac{E_{\mathrm{b}}\epsilon_{\mathrm{R}}\Sigma_{\mathrm{G}} k\mathrm{e}^{-k}}{\Sigma_{\mathrm{L}}(d-1) + \Sigma_{\mathrm{G}}},$$

$$A_{87} = \frac{E_{\mathrm{b}}\epsilon_{\mathrm{R}}\Sigma_{\mathrm{G}} k\mathrm{e}^{k}}{\Sigma_{\mathrm{L}}(d-1) + \Sigma_{\mathrm{G}}},$$

$$A_{88} = \frac{E_{\mathrm{b}}\Sigma_{\mathrm{L}} k\mathrm{e}^{-k}}{\Sigma_{\mathrm{L}}(d-1) + \Sigma_{\mathrm{G}}},$$

$$A_{89} = \frac{E_{\mathrm{b}}\epsilon_{\mathrm{G}}\Sigma_{\mathrm{L}} k\mathrm{e}^{k}}{\Sigma_{\mathrm{L}}(d-1) + \Sigma_{\mathrm{G}}},$$

$$A_{91} = \frac{\Sigma_{\mathrm{G}} - \Sigma_{\mathrm{L}}}{\Sigma_{\mathrm{L}}(d-1) + \Sigma_{\mathrm{G}}}.$$

Appendix B

LW linear stability matrix

The linearised LW system is described by $B\mathbf{x} = \mathbf{0}$, where $\mathbf{x} = \left(\widetilde{h}, \widetilde{q}\right)^{\mathrm{T}}$ and B is the 2×2 stability matrix, namely,

$$B = \begin{pmatrix} B_{11} - s & B_{12} \\ B_{21} & B_{22} - s \end{pmatrix},$$

where

$$B_{11} = \frac{A}{6\left(\epsilon_{\mathrm{R}}(d-1)+1\right)\left(\Sigma_{\mathrm{R}}(d-1)+1\right)^2},$$

in which

$$A = -2\left(\epsilon_{\mathrm{R}}(d-1)+1\right)\left(\Sigma_{\mathrm{R}}(d-1)+1\right)k^4 + E_{\mathrm{b}}\left(3\Sigma_{\mathrm{R}}^2 - 3(d-1)\epsilon_{\mathrm{R}}^2 + \epsilon_{\mathrm{R}}\left(2 + 3d\Sigma_{\mathrm{R}} + 2\left(\Sigma_{\mathrm{R}} - 5\right)\Sigma_{\mathrm{R}}\right)\right)k^2,$$

and

$$B_{12} = \frac{E_{\mathrm{b}}\left(\Sigma_{\mathrm{R}}\left(3d-5\right) - 5\epsilon_{\mathrm{R}}(d-1)\right)}{6\left(\epsilon_{\mathrm{R}}(d-1)+1\right)\left(\Sigma_{\mathrm{R}}(d-1)+1\right)^2}k^2,$$

$$B_{21} = \frac{\left(\Sigma_{\mathrm{R}} - \epsilon_{\mathrm{R}}\right)\left(\left(\left(\Sigma_{\mathrm{R}}(d-1)+1\right)^2\left(\epsilon_{\mathrm{R}}(d-1)+1\right)k^4 + 2\left(1-\Sigma_{\mathrm{R}}\right)\right)\right)}{\left(\epsilon_{\mathrm{R}}(d-1)+1\right)\left(\Sigma_{\mathrm{R}}(d-1)+1\right)^3}$$

$$+\frac{E_{\mathrm{b}}\left(2\Sigma_{\mathrm{R}}^{2}(d-1)-\epsilon_{\mathrm{R}}\left(\Sigma_{\mathrm{R}}^{2}+2\Sigma_{\mathrm{R}}(d-3)+1\right)-2\Sigma_{\mathrm{R}}^{2}\right)k^{2}}{\left(\epsilon_{\mathrm{R}}(d-1)+1\right)\left(\Sigma_{\mathrm{R}}(d-1)+1\right)^{3}},$$

$$B_{22}=\frac{E_{\mathrm{b}}\left(\Sigma_{\mathrm{R}}-\epsilon_{\mathrm{R}}\right)\left(3\Sigma_{\mathrm{R}}(d-1)+\Sigma_{\mathrm{R}}(3-2d)\right)k^{2}+2\left(\Sigma_{\mathrm{R}}(d-1)+1\right)^{3}}{2\left(\epsilon_{\mathrm{R}}(d-1)+1\right)\left(\Sigma_{\mathrm{R}}(d-1)+1\right)^{2}}.$$

Appendix C

Examples of numerical schemes implemented using Matlab

The numerical schemes introduced in Chapter 4 were implemented using Matlab, and this Appendix gives examples of the code. Firstly, the Matlab code that implements the Method of Lines, introduced and described in Section 4.1, to solve the LW model is given by Listings C.1–C.5. Secondly, the code that implements the Shooting method, described in Section 4.2, is given by Listing C.6.

Listing C.1: Main function for solving the LW model (2.107)–(2.108)

```
function LW_Model
 %%% Set parameter values: %%%
 d=5; Eb=5; sr=2; epr=40;
 %%% Choose grid: %%%
 DomainLength=2*pi/1; nPts=1000; dx=DomainLength/nPts;
 x=0:dx:DomainLength-dx;
 %%% Choose initial conditions: %%%
 qBar=(epr-sr)/(sr*(d-1)+1);
 delta=1e-2;
 H=1+delta*cos(2.*pi.*x./DomainLength);
 Q=qBar+delta*cos(2.*pi.*x./DomainLength);
 HQ=[H,Q];

 Time=0;    %%%     Initial time     %%%
 dt=0.002; %%% and time-step size %%%
 %%% Compute Jacobian: %%%
[J]=Jacobian(H,Q,d,Eb,sr,epr,dt,dx);
RecomputeJ=false; %%% If true: recompute Jacobian %%%

while Time<=tEnd
 %%% Implement NR method: %%%
[HNew,QNew,J,RecomputeJ]=Newton_Raphson(H,Q,Eb,d,sr,epr,dt,dx,
    J);

maxdiff=max(abs(H-HNew)./(HNew));              %%% Conditions to
        %%%
Cond1=(min(HNew)>0); Cond2=(max(HNew)<=d); %%% accept new
    values %%%
if maxdiff<0.1 && Cond1 && Cond2 && RecomputeJ==0
H=HNew; Q=QNew;
Time=Time+dt;
     if maxdiff<0.01
     dt=dt*1.2;       %%% Increasing time-step size %%%
     end
else
dt=dt/2;      %%% Halve time-step size if conditions not met
   %%%
end
%%% Recompute Jacobian if statement is true: %%%
if RecomputeJ
[J]=jacobian(H,Q,Eb,d,sr,epr,dt,dx);
RecomputeJ=false;
end
end
end
```

Listing C.2: Matlab function for calculating the governing equations.

```
function [rhs]=eqnrhsH(H,Q,Eb,d,sr,epr,dx)
%%% Defintions for derivatives of phi and pressure: %%%
pgx=( ( d*epr +( d^2 * epr - 2*d*epr.*H +(epr-1).*H.^2).*Q).*
    diff(H,dx)+ (d-H).*H.*(d*epr-(epr-1).*H).*diff(Q,dx) )./((H
    +epr.*(d-H)).^2);
pgy=(    (epr-(H.*Q)) ) ./ ( H + epr.*(d-H) );
ply=( (1+ ( Q.*(d-H) ) ) ./ ( H+epr.*(d-H)));
px=diff(-diff2(H,dx)-(Eb./2).*((pgy.^2) - epr.*( ply.^2)),dx);
%%% Computing RHS of h governing equation: %%%
rhs=-diff((px ./3 ).*(H.^3 ) + (Eb/2).*Q.*(H.^2).*(pgx),dx);
end
function [rhs]=eqnrhsQ(H,Q,Eb,d,sr,epr,dx)
%%% Defintions for derivatives of phi and pressure: %%%
pgx=( ( d*epr +( d^2 * epr - 2*d*epr.*H +(epr-1).*H.^2).*Q).*
    diff(H,dx) + (d-H).*H.*(d*epr-(epr-1).*H).*diff(Q,dx) )./((
    H+epr.*(d-H)).^2);
pgy=(    (epr-(H.*Q)) ) ./ ( H + epr.*(d-H) );
ply=( (1+ ( Q.*(d-H) ) ) ./ ( H+epr.*(d-H)));
px=diff(-diff2(H,dx)-(Eb./2).*((pgy.^2) - epr.*( ply.^2)),dx);
%%% Computing RHS of q governing equation: %%%
rhs=-((diff((px ./2).*Q.*(H.^2) +(Eb).*(Q.^2).*H.*(pgx),dx))+
    pgy-sr.*ply);
end
function [D]=diff(u,dx)
%%% Computing first derivative: %%%
D=(circshift(u,-1)-circshift(u,1))/(2*dx);
end
function [D]=diff2(u,dx)
%%% Computing second derivative: %%%
D=(circshift(u,-1)-2*u+circshift(u,1))/(dx^2);
end
```

Listing C.3: Matlab function for creating the Jacobian matrix.

```
function [J]=Jacobian(H,Q,d,Eb,sr,epr,dt,dx)
    pert=1.e-10; %%% Perturbation used for calculating
        derivative %%%
    %%% Create combined RHS vector: %%%
    RHS=[eqnrhsH(H,Q,Eb,d,sr,epr,dx),eqnrhsQ(H,Q,Eb,d,sr,epr,
        dx)];
    %%% Create sparse matrix: %%%
    J=sparse(2*n,2*n);
for i=1:length(H)
    %%% Perturb ith element of h: %%%
    H(i)=H(i)+pert;
    %%% Create new RHS: %%%
    NewRHS=[eqnrhsH(H,Q,Eb,d,sr,epr,dx), eqnrhsQ(H,Q,Eb,d,sr,
        epr,dx)];
    %%% Compute ith column of Jacobian: %%%
    J(:,i)=dt*(NewRHS-RHS)/pert;
    %%% Reverse perturbation on h. Now perturb ith element of
        q: %%%
    H(i)=H(i)-pert; Q(i)=Q(i)+pert;
    %%% Create new RHS: %%%
    NewRHS=[eqnrhsH(H,Q,Eb,d,sr,epr,dx), eqnrhsQ(H,Q,Eb,d,sr,
        epr,dx)];
    %%% Compute i+1th element of Jacobian: %%%
    J(:,i+n)=dt*(NewRHS-RHS)/pert;
    %%% Reverse perturbation on h: %%%
    Q(i)=Q(i)-pert;
    %%% Add 1 across diagonal: %%%
    J(i,i)=1+J(i,i); J(i+n,i+n)=1+J(i+n,i+n);
end
end
```

Listing C.4: Matlab function for performing the NR method.

```
function [H,Q,J,RecomputeJ]=Newton_Raphson(H,Q,Eb,d,sr,epr,dt,
    dx,J)
    numIts=0; check=0;                                  %%% Setup for
        %%%
    nPts=length(H); dh=ones(1,nPts); dh1=dh;    %%%     NR
        %%%
    HQ=[H,Q]; hqNR=[H,Q];                               %%%  Method
        %%%

while  max(abs(dh))>1e-10  %%% Condition to stop NR iterations
    %%%
    %%% Create RHS of PDEs and combine then into one vector:
        %%%
    RhsH=eqnrhsH(h,q,dx,d,sr,epr,Eb); RhsQ=eqnrhsQ(h,q,dx,d,sr
        ,epr,Eb);
    EqnRHS=[RhsH, RhsQ];
    %%% Solving equation for correction term: %%%
    dh=(J\(HQ-(hqNR+dt*EqnRHS))')';
    %%% Is the correction term growing? %%%
 if    abs(norm(dh1))-abs(norm(dh))<0
if check==3          %%% Jacobian recomputed three times
    already? %%%
RecomputeJ=true;              %%%   Then  stop the  %%%
break                         %%%     NR method     %%%
end
      %%% If Jacobian hasn't been computed three times %%%
      %%%                  then do this:                  %%%
      [J]=jacobian(hqNR(1:nPts),hqNR(nPts+1:end),Eb,d,sr,epr,dt
          ,dx);
    check=check+1;
 else
    hqNR=hqNR+dh;        %%% If the correction term decreases
        %%%
    dh1=dh;              %%%    then calculate new h and q
        %%%
    numIts=numIts+1;
 end
  if numIts==50        %%%   Have there been 50 iterations?
     %%%
    RecomputeJ=true;  %%%   Then set 'RecomputeJ' to true
        %%%
    break             %%%       and stop the NR method
        %%%
  end
end
end
```

Listing C.5: Additional Matlab code

```
%%% Compute curvature, i.e. h_xx %%%
hxx=diff2(NewH,dx);
%%% Set up vectors: %%%
mins=[]; minp=[]; minhxx=[];
for i =3:length(NewH)-2
 %%% Is this grid point of h a minima point? %%%
  if NewH(i-1)>=NewH(i) && NewH(i+1)>=NewH(i)
 %%% Take two grid points at either side and create  %%%
 %%%      a new vector 'xInt' with 100000 points:     %%%
      dxInt=((x(i+2)-x(i-2))/100000); xInt = x(i-2):dxInt:x(i
          +2);
 %%% Interpolate h and h_xx at 'xInt: %%%
      HInt=interp1(x,NewH,xInt,'spline');
      HxxInt=interp1(x,hxx,xInt,'spline');
 %%% Calculate the minimum height and position 'HInt': %%%
      [MinVal, MinPos]=min(HInt);
 %%%      Add the value of the minima, it's position       %%%
 %%% and h_xx at the minima to the corresponding vectors: %%%
MinH=[MinH, MinVal];
PosH=[PosH, xInt(MinPos)];
Hxx=[minhxx, HxxInt(MinPos)];
 end
end
```

Listing C.6: Matlab code for investigating $(f(0), f''(0))$-space.

```
function ShootSpace
SaveName=sprintf('(f(0),f''(0))-space where d=3-Assigning f.txt');
for f0=0.4:0.001:1.1 %%% Assigning f(0) %%%
Space=[]; %%% Reset this when f(0) changes %%%
%%% Use function 'solver' in lines 27-31 to assign %%%
%%%     f0 and create a function of one variable: %%%
solver2=@(x) solver(f0,x);
for fD=0.2:0.001:1.2 %%% Initial guess for f''(0) %%%
%%% Root-solver using fD as the initial guess %%%
NewVal=fzero(solver2,fD);
Coord=[f0,NewVal]; %%% Create coordinate in (f(0),f''(0))-space %%%
if isempty(Space) %%% Is this the first solution? %%%
Space=[Space NewVal]; %%% Remeber this solution %%%
%%% Write coordinate into a file: %%%
dlmwrite(SaveName,Coord,'Delimiter','\t','-append','precision','%.10f')
%%% Are there already solutions? %%%
%%%    And are they different?  %%%
elseif ~isempty(Space) && min(abs(Space-NewVal))>1e-5
Space=[Space, NewVal]; %%% Remember this solution %%%
%%% Write coordiante into a file: %%%
dlmwrite(SaveName,Coord,'Delimiter','\t','-append','precision','%.10f')
end
end
end
end
function F=solver(f0,fD)
EtaEnd=10; %%% Assign Eta_end %%%
%%% Solve the ODE defined in lines 34-40: %%%
[~,f]=ode15s(@f2,[0 EtaEnd],[f0 0 fD 0]);
%%% The boundary condition at Eta=Eta_end: %%%
F=f(end,1)-(3/2)*EtaEnd*f(end,2);
end
function u=f2(Eta,f)
d=3; %%% Assign parameter d %%%
u=zeros(4,1);
u(1)=f(2); u(2)=f(3); u(3)=f(4); %%% u1=f,u2=f', u3=f'' %%%
%%% Create ODE to be solved: %%%
u(4)=(3*f(2)^2)/(f(1)^4)-(f(3)/f(1)^3)+(2*f(1)-3*Eta*f(2))/(4*d^3);
end
```

Appendix D

Estimating the values of $f(0)$ and $f''(0)$ using the lines of best fit

In this Appendix, we estimate the values of $f(0)$ and $f''(0)$ by fitting a straight line to the results of the numerical calculations close to the time of contact given by Figure 5.4. The intercept of these straight lines are then used to obtain the values of $f(0)$ and $f''(0)$.

We firstly find $f(0)$ by investigating the straight line with gradient -5 and intercept C_1 given by

$$\log\left(\mathrm{d}h_{\max}/\mathrm{d}t\right) = -5\log\left(d - h_{\max}\right) + C_1, \tag{D.1}$$

and using (5.3) evaluated at $y = h_{\max}$ gives

$$\log\left(\tau^{-5/6}\frac{1}{6}f(0)\right) = -5\log\left(\tau^{1/6}f(0)\right) + C_1. \tag{D.2}$$

Rearranging (D.2) gives

$$\log\left(\tau^{-5/6}\right) + \log\left(\frac{1}{6}f(0)\right) = \log\left(\tau^{-5/6}\right) + \log\left((f(0))^{-5}\right) + C_1, \tag{D.3}$$

which is then simplified by cancelling the τ terms and collecting the terms involving $f(0)$, namely,

$$\log\left(\frac{1}{6}\left(f(0)\right)^6\right) = C_1. \tag{D.4}$$

An expression for $f(0)$ was obtained by taking the exponential of both sides of the equation and rearranging for $f(0)$, namely,

$$f(0) = \left(6\mathrm{e}^{C_1}\right)^{1/6}. \tag{D.5}$$

Similarly, we obtain $f''(0)$ by investigating the straight line with gradient -2 and intercept C_2 given by

$$\log\left(-\left.\frac{\partial^2 h}{\partial x^2}\right|_{y=h_{\max}}\right) = -2\log\left(d - h_{\max}\right) + C_2, \tag{D.6}$$

and using (5.5) evaluated at $y = h_{\max}$ gives

$$\log\left(\tau^{-1/3} f''(0)\right) = -2\log\left(\tau^{1/6} f(0)\right) + C_2. \tag{D.7}$$

Rearranging (D.7) gives

$$\log\left(\tau^{-1/3}\right) + \log\left(f''(0)\right) = \log\left(\tau^{1/3}\right) + \log\left(\left(f(0)\right)^{-2}\right) + C_2, \tag{D.8}$$

and cancelling the τ terms yields

$$\log\left(f''(0)\right) - \log\left(\left(f(0)\right)^{-2}\right) = C_2. \tag{D.9}$$

This equation can be rearranged to give

$$f''(0)\left(f(0)\right)^2 = \mathrm{e}^{C_2}, \tag{D.10}$$

and an expression for $f''(0)$ is obtained, namely,

$$f''(0) = (f(0))^{-2}\, \mathrm{e}^{C_2}, \tag{D.11}$$

where the $f(0)$ is determined using (D.5).

Appendix E

Analytical justification of $\partial h/\partial x \to 0$ as $x \to x_0^+$ in the filling lobe regions

During the asymptotic thinning stage of thinning (TH) behaviour, the numerical calculations suggest that $\partial h/\partial x \to 0$ as $x \to x_0^+$ in the filling lobe regions. In this Appendix we provide an analytical justification of this result.

Recall that the interface in the filling lobe region is quasi-steady, and so the time derivative term $\partial h/\partial t$ is negligible. Hence, the governing equation (2.91) reduces to

$$\frac{h^3}{3}\left(\frac{\partial^3 h}{\partial x^3} + \frac{1}{(d-h)^3}\frac{\partial h}{\partial x}\right) = Q(x_0). \tag{E.1}$$

The matching conditions with the filling lobe regions are $h(\pm x_0) = 0$, and so $Q(x_0)$ must be zero. Hence, equation (E.1) becomes

$$\frac{\partial^3 h}{\partial x^3} + \frac{1}{(d-h)^3}\frac{\partial h}{\partial x} = 0. \tag{E.2}$$

Integrating equation (E.2) with respect to x and multiplying throughout by $2\partial h/\partial x$ yields

$$\frac{\partial}{\partial x}\left(\frac{\partial h}{\partial x}\right)^2 = \left(2C - \frac{1}{(d-h)^2}\right)\frac{\partial h}{\partial x}, \tag{E.3}$$

where C is a constant of integration.

Setting $D = 2C$ and evaluating equation (E.3) at $x = x_0$ yields

$$2\left.\frac{\partial h}{\partial x}\right|_{x=x_0}\left.\frac{\partial^2 h}{\partial x^2}\right|_{x=x_0} = D\left.\frac{\partial h}{\partial x}\right|_{x=x_0} - \frac{1}{d}\left.\frac{\partial h}{\partial x}\right|_{x=x_0}, \tag{E.4}$$

where the matching condition $h(x_0) = 0$ has been used.

Equation (E.4) can be rearranged to give

$$\left.\frac{\partial h}{\partial x}\right|_{x=x_0}\left(2\left.\frac{\partial^2 h}{\partial x^2}\right|_{x=x_0} + \frac{1}{d} - D\right) = 0. \tag{E.5}$$

Therefore, there are two solutions to equation (E.5), namely,

$$\left.\frac{\partial h}{\partial x}\right|_{x=x_0} = 0$$

and

$$D = \frac{1}{d} + 2\left.\frac{\partial^2 h}{\partial x^2}\right|_{x=x_0}.$$

However, for equation (E.5) to be true for arbitrary D, then it must be that $\partial h/\partial x = 0$ at $x = x_0$. This shows analytically that $\partial h/\partial x = 0$ at $x = x_0$ in the filling lobe regions.

Appendix F

Application of the WRIBL method to the leaky dielectric problem

In this Appendix, we use the WRIBL method to obtain a model for the system when the liquid and gas are leaky dielectrics. In Section 2.3.4, we found explicit expressions for the voltage potential in the liquid and gas (given by (2.70)), namely,

$$\phi^{\mathrm{L}}(x,y,t) = \frac{((d-h)q+1)\,y}{\epsilon_{\mathrm{R}}(d-h)+h}, \qquad \phi^{\mathrm{G}}(x,y,t) = \frac{(\epsilon_{\mathrm{R}}-hq)(y-d)}{\epsilon_{\mathrm{R}}(d-h)+h} + 1. \tag{F.1}$$

Therefore, this suggests projecting onto polynomials of the form

$$\phi^{\mathrm{L}} = a_0(x,t)y + \epsilon^2 \sum_{n=2}^{N_1} a_n(x,t)y^n, \tag{F.2}$$

$$\phi^{\mathrm{G}} = 1 + b_0(x,t)(y-d) + \epsilon^2 \sum_{n=2}^{N_2} b_n(x,t)(y-d)^n, \tag{F.3}$$

where $a_n = a_n(x,t)$ $(n = 0,1,...,N_1)$ and $b_n = b_n(x,t)$ $(n = 0,1,...,N_2)$ are unknown functions, ϵ is the small aspect ratio, and N_1 and N_2 are constants.

Substituting (F.2) into the governing equation for ϕ^{L}, i.e. equation (2.49), yields

$$\epsilon^2 \left(\frac{\partial^2 a_0}{\partial x^2} y + \sum_{n=2}^{N_1} n(n-1) a_n y^{n-2} \right) = 0. \tag{F.4}$$

Equating powers of y, the nonzero coefficient terms only appear when $n = 3$, which yields

$$\phi^{\mathrm{L}} = a_0 y - \epsilon^2 \frac{1}{6} \frac{\partial^2 a_0}{\partial x^2} y^3. \tag{F.5}$$

Similarly, substituting (F.3) into the governing equation for ϕ^{G}, i.e. equation (2.50), and equating powers of y, we also obtain an expression for ϕ^{G}, namely

$$\phi^{\mathrm{G}} = 1 + b_0 (y - d) - \epsilon^2 \frac{1}{6} \frac{\partial^2 b_0}{\partial x^2} (y - d)^3. \tag{F.6}$$

Expressions (F.5) and (F.6) automatically satisfy the boundary conditions at the upper and lower electrodes.

Substituting (F.5) and (F.6) into the continuity of potential and Gauss' law at $y = h$, i.e. equations (2.69) and (2.68), respectively, gives

$$a_0 h - \epsilon^2 \frac{1}{6} \frac{\partial^2 a_0}{\partial x^2} h^3 - 1 - b_0 (h - d) + \epsilon^2 \frac{1}{6} \frac{\partial^2 b_0}{\partial x^2} (h - d)^3 = 0, \tag{F.7}$$

$$- \left(1 + \epsilon^2 \frac{\partial h}{\partial x}^2 \right)^{3/2} q - b_0 + \frac{\partial}{\partial x} \left[\epsilon^2 \left(\frac{1}{2} \frac{\partial b_0}{\partial x} (h - d)^2 \right) + \epsilon_{\mathrm{R}} \left(a_0 - \epsilon^2 \left[\frac{1}{2} \frac{\partial a_0}{\partial x} h^2 \right] \right) \right] = 0. \tag{F.8}$$

In summary, in this Appendix we have used the WRIBL method to obtain a model for the system when the liquid and gas are leaky dielectrics. It consists of the governing equations for h and q, i.e. equations (2.107) and (2.108), respectively, and two equations for a_0 and b_0, equations (F.7) and (F.8), respectively. For the purposes of comparison in Fig 8.1, we undo the long-wave scaling, i.e. set $\epsilon = 1$.

Bibliography

[1] J. Liu, J.B. Schneider, and J.P. Gollub. Three-dimensional instabilities of film flows. *Physics of Fluids*, 7(1):55–67, 1995.

[2] L. Rockford, Y. Liu, P. Mansky, T.P. Russell, M. Yoon, and S.G.J. Mochrie. Polymers on nanoperiodic, heterogeneous surfaces. *Physical Review Letters*, 82(12):2602–2605, 1999.

[3] E. Schäffer, T. Thurn-Albrecht, T.P. Russell, and U. Steiner. Electrically induced structure formation and pattern transfer. *Nature*, 403(6772):874–877, 2000.

[4] E. Schäffer, T. Thurn-Albrecht, T.P. Russell, and U. Steiner. Electrohydrodynamic instabilities in polymer films. *EPL (Europhysics Letters)*, 53(4):518–524, 2001.

[5] J. Eggers. Universal pinching of 3D axisymmetric free-surface flow. *Physical Review Letters*, 71(21):3458, 1993.

[6] D.T. Papageorgiou. On the breakup of viscous liquid threads. *Physics of Fluids*, 7(7):1529–1544, 1995.

[7] M.P. Brenner, J.R. Lister, and H.A. Stone. Pinching threads, singularities and the number 0.0304... *Physics of Fluids*, 8(11):2827–2836, 1996.

[8] J.R. Lister and H.A. Stone. Capillary breakup of a viscous thread surrounded by another viscous fluid. *Physics of Fluids*, 10(11):2758–2764, 1998.

[9] H.E. Huppert. Flow and instability of a viscous current down a slope. *Nature*, 300(5891):427–429, 1982.

[10] R.W. Griffiths. The dynamics of lava flows. *Annual Review of Fluid Mechanics*, 32:477–518, 2000.

[11] H.E. Huppert and J.E. Simpson. The slumping of gravity currents. *Journal of Fluid Mechanics*, 99(4):785–799, 1980.

[12] H.E. Huppert. Gravity currents: A personal perspective. *Journal of Fluid Mechanics*, 554:299–322, 2006.

[13] J. B. Grotberg. Pulmonary flow and transport phenomena. *Annual Review of Fluid Mechanics*, 26:529–571, 1994.

[14] A. Sharma and E. Ruckenstein. An analytical nonlinear theory of thin film rupture and its application to wetting films. *Journal of Colloid and Interface Science*, 113(2):456–479, 1986.

[15] H. Wong, I. Fatt, and C.J. Radke. Deposition and thinning of the human tear film. *Journal of Colloid and Interface Science*, 184(1):44–51, 1996.

[16] S. Kalliadasis, A. Kiyashko, and E. A. Demekhin. Marangoni instability of a thin liquid film heated from below by a local heat source. *Journal of Fluid Mechanics*, 475:377–408, 2003.

[17] O.K. Matar, C.J. Lawrence, and G.M. Sisoev. The flow of thin liquid films over spinning disks: Hydrodynamics and mass transfer. *Physics of Fluids*, 17(5):052–102, 2005.

[18] A. Oron, S.H. Davis, and S.G. Bankoff. Long-scale evolution of thin liquid films. *Reviews of Modern Physics*, 69(3):930–981, 1997.

[19] R.V. Craster and O.K. Matar. Dynamics and stability of thin liquid films. *Reviews of Modern Physics*, 81(3):1131–1198, 2009.

[20] S.H. Davis. The importance of being thin. *Journal of Engineering Mathematics*, 105(1):3–30, 2017.

[21] A. Sharma and R. Khanna. Pattern formation in unstable thin liquid films. *Physical Review Letters*, 81(16):3463–3466, 1998.

[22] R. Konnur, K. Kargupta, and A. Sharma. Instability and morphology of thin liquid films on chemically heterogeneous substrates. *Physical Review Letters*, 84(5):931, 2000.

[23] M.D. Morariu, N.E. Voicu, E. Schäffer, Z. Lin, T.P. Russell, and U. Steiner. Hierarchical structure formation and pattern replication induced by an electric field. *Nature Materials*, 2(1):48–52, 2003.

[24] K. Kargupta and A. Sharma. Templating of thin films induced by dewetting on patterned surfaces. *Physical Review Letters*, 86(20):4536, 2001.

[25] R. Mukherjee and A. Sharma. Instability, self-organization and pattern formation in thin soft films. *Soft Matter*, 11(45):8717–8740, 2015.

[26] S.Y. Chou and L. Zhuang. Lithographically induced self-assembly of periodic polymer micropillar arrays. *Journal of Vacuum Science & Technology B: Microelectronics and Nanometer Structures Processing, Measurement, and Phenomena*, 17(6):3197–3202, 1999.

[27] H. Lin, B.D. Storey, M.H. Oddy, C-H Chen, and J.G. Santiago. Instability of electrokinetic microchannel flows with conductivity gradients. *Physics of Fluids*, 16(6):1922–1935, 2004.

[28] A.O. El Moctar, N. Aubry, and J. Batton. Electro-hydrodynamic microfluidic mixer. *Lab on a Chip*, 3(4):273–280, 2003.

[29] I. Glasgow, J. Batton, and N. Aubry. Electroosmotic mixing in microchannels. *Lab on a Chip*, 4(6):558–562, 2004.

[30] M.M. Hohman, M. Shin, G. Rutledge, and M.P. Brenner. Electrospinning and electrically forced jets. I. Stability theory. *Physics of Fluids*, 13(8):2201–2220, 2001.

[31] D.H. Reneker, A.L. Yarin, E. Zussman, and H. Xu. Electrospinning of nanofibers from polymer solutions and melts. *Advances in Applied Mechanics*, 41:43–346, 2007.

[32] D.H. Reneker and A.L. Yarin. Electrospinning jets and polymer nanofibers. *Polymer*, 49(10):2387–2425, 2008.

[33] N. Arun, A. Sharma, P.S.G. Pattader, I. Banerjee, H.M. Dixit, and K.S. Narayan. Electric-field-induced patterns in soft viscoelastic films: From long waves of viscous liquids to short waves of elastic solids. *Physical Review Letters*, 102(25):254502, 2009.

[34] N. Wu and W.B. Russel. Micro-and nano-patterns created via electrohydrodynamic instabilities. *Nano Today*, 4(2):180–192, 2009.

[35] D.A. Saville. Electrohydrodynamics: The Taylor–Melcher leaky dielectric model. *Annual Review of Fluid Mechanics*, 29:27–64, 1997.

[36] D.T. Papageorgiou. Film flows in the presence of electric fields. *Annual Review of Fluid Mechanics*, 51:155–187, 2019.

[37] L. Wu and S.Y. Chou. Dynamic modeling and scaling of nanostructure formation in the lithographically induced self-assembly and self-construction. *Applied Physics Letters*, 82(19):3200–3202, 2003.

[38] D.J. Benney. Long waves on liquid films. *Journal of Mathematics and Physics*, 45(1-4):150–155, 1966.

[39] D.J. Acheson. Elementary Fluid Dynamics. Oxford University Press, 1991.

[40] A. Pumir, P. Manneville, and Y. Pomeau. On solitary waves running down an inclined plane. *Journal of Fluid Mechanics*, 135:27–50, 1983.

[41] P. Rosenau, A. Oron, and J.M. Hyman. Bounded and unbounded patterns of the Benney equation. *Physics of Fluids A: Fluid Dynamics*, 4(6):1102–1104, 1992.

[42] T.R. Salamon, R.C. Armstrong, and R.A. Brown. Traveling waves on vertical films: Numerical analysis using the finite element method. *Physics of Fluids*, 6(6):2202–2220, 1994.

[43] B. Ramaswamy, S. Chippada, and S.W. Joo. A full-scale numerical study of interfacial instabilities in thin-film flows. *Journal of Fluid Mechanics*, 325:163–194, 1996.

[44] N.A. Malamataris, M. Vlachogiannis, and V. Bontozoglou. Solitary waves on inclined films: Flow structure and binary interactions. *Physics of Fluids*, 14(3):1082–1094, 2002.

[45] K. Argyriadi, K. Serifi, and V. Bontozoglou. Nonlinear dynamics of inclined films under low-frequency forcing. *Physics of Fluids*, 16(7):2457–2468, 2004.

[46] G.I. Sivashinsky. Nonlinear analysis of hydrodynamic instability in laminar flames—I. derivation of basic equations. *Acta Astronautica*, 4(11):1177–1206, 1977.

[47] Y. Kuramoto and T. Tsuzuki. On the formation of dissipative structures in reaction-diffusion systems: Reductive perturbation approach. *Progress of Theoretical Physics*, 54(3):687–699, 1975.

[48] Y. Kuramoto and T. Tsuzuki. Persistent propagation of concentration waves in dissipative media far from thermal equilibrium. *Progress of Theoretical Physics*, 55(2):356–369, 1976.

[49] B.I. Cohen, J.A. Krommes, W.M. Tang, and M.N. Rosenbluth. Non-linear saturation of the dissipative trapped-ion mode by mode coupling. *Nuclear Fusion*, 16(6):971–992, 1976.

[50] J. Goodman. Stability of the Kuramoto-Sivashinsky and related systems. *Communications on Pure and Applied Mathematics*, 47(3):293–306, 1994.

[51] M.S. Jolly, R. Rosa, and R. Temam. Evaluating the dimension of an inertial manifold for the Kuramoto-Sivashinsky equation. *Advances in Differential Equations*, 5(1-3):31–66, 2000.

[52] G.I. Sivashinsky and D.M. Michelson. On irregular wavy flow of a liquid film down a vertical plane. *Progress of Theoretical Physics*, 63(6):2112–2114, 1980.

[53] I.G. Kevrekidis, B. Nicolaenko, and J.C. Scovel. Back in the saddle again: A computer assisted study of the Kuramoto–Sivashinsky equation. *SIAM Journal on Applied Mathematics*, 50(3):760–790, 1990.

[54] D.T. Papageorgiou and Y.S. Smyrlis. The route to chaos for the Kuramoto–Sivashinsky equation. *Theoretical and Computational Fluid Dynamics*, 3(1):15–42, 1991.

[55] Y.S. Smyrlis and D.T. Papageorgiou. Predicting chaos for infinite dimensional dynamical systems: The Kuramoto-Sivashinsky equation, a case study. *Proceedings of the National Academy of Sciences*, 88(24):11129–11132, 1991.

[56] O. Takeshi. Surface equation of falling film flows with moderate Reynolds number and large but finite Weber number. *Physics of Fluids*, 11(11):3247–3269, 1999.

[57] S. Kalliadasis, C. Ruyer-Quil, B. Scheid, and M.G. Velarde. Falling Liquid Films. Springer Science & Business Media, 2011.

[58] C. Ruyer-Quil and P. Manneville. Improved modeling of flows down inclined planes. *The European Physical Journal B-Condensed Matter and Complex Systems*, 15(2):357–369, 2000.

[59] C. Ruyer-Quil and P. Manneville. Further accuracy and convergence results on the modeling of flows down inclined planes by weighted-residual approximations. *Physics of Fluids*, 14(1):170–183, 2002.

[60] B. Scheid, C. Ruyer-Quil, and P. Manneville. Wave patterns in film flows: Modelling and three-dimensional waves. *Journal of Fluid Mechanics*, 562:183–222, 2006.

[61] S. Chakraborty, P.K. Nguyen, C. Ruyer-Quil, and V. Bontozoglou. Extreme solitary waves on falling liquid films. *Journal of Fluid Mechanics*, 745:564–591, 2014.

[62] S. Kalliadasis, E.A. Demekhin, C. Ruyer-Quil, and M.G. Velarde. Thermocapillary instability and wave formation on a film falling down a uniformly heated plane. *Journal of Fluid Mechanics*, 492:303–338, 2003.

[63] C. Ruyer-Quil, P. Treveleyan, F. Giorgiutti-Dauphiné, C. Duprat, and S. Kalliadasis. Modelling film flows down a fibre. *Journal of Fluid Mechanics*, 603:431–462, 2008.

[64] A.B. Thompson, D. Tseluiko, and D.T. Papageorgiou. Falling liquid films with blowing and suction. *Journal of Fluid Mechanics*, 787:292–330, 2016.

[65] A.W. Wray, D.T. Papageorgiou, and O.K. Matar. Reduced models for thick liquid layers with inertia on highly curved substrates. *SIAM Journal on Applied Mathematics*, 77(3):881–904, 2017.

[66] A.W. Wray and R. Cimpeanu. Reduced-order modelling of thick inertial flows around rotating cylinders. *Journal of Fluid Mechanics*, 898:A1, 2020.

[67] D. Tseluiko and D.T. Papageorgiou. Wave evolution on electrified falling films. *Journal of Fluid Mechanics*, 556:361–386, 2006.

[68] D. Tseluiko, M.G. Blyth, D.T. Papageorgiou, and J.-M. Vanden-Broeck. Electrified viscous thin film flow over topography. *Journal of Fluid Mechanics*, 597:449–475, 2007.

[69] O.K. Matar, R.V. Craster, and S. Kumar. Falling films on flexible inclines. *Physical Review E*, 76(5):056301, 2007.

[70] A.W. Wray, O.K. Matar, and D.T. Papageorgiou. Accurate low-order modeling of electrified falling films at moderate Reynolds number. *Physical Review Fluids*, 2(6):063701, 2017.

[71] W.W. Zhang and J.R. Lister. Similarity solutions for van der Waals rupture of a thin film on a solid substrate. *Physics of Fluids*, 11(9):2454–2462, 1999.

[72] T.P. Witelski and A.J. Bernoff. Stability of self-similar solutions for van der Waals driven thin film rupture. *Physics of Fluids*, 11(9):2443–2445, 1999.

[73] D. Vaynblat, J.R. Lister, and T.P. Witelski. Rupture of thin viscous films by van der Waals forces: Evolution and self-similarity. *Physics of Fluids*, 13(5):1130–1140, 2001.

[74] Q. Wang and D.T. Papageorgiou. Using electric fields to induce patterning in leaky dielectric fluids in a rod-annular geometry. *IMA Journal of Applied Mathematics*, 83(1):24–52, 2018.

[75] R.V. Craster and O.K. Matar. Electrically induced pattern formation in thin leaky dielectric films. *Physics of Fluids*, 17(3):032104, 2005.

[76] N. Wu, L.F. Pease, and W.B. Russel. Electric-field-induced patterns in thin polymer films: Weakly nonlinear and fully nonlinear evolution. *Langmuir*, 21(26):12290–12302, 2005.

[77] D. Bandyopadhyay, A. Sharma, U. Thiele, and P.D.S. Reddy. Electric-field-induced interfacial instabilities and morphologies of thin viscous and elastic bilayers. *Langmuir*, 25(16):9108–9118, 2009.

[78] J.S. Allen and Kevin P. Hallinan. Liquid blockage of vapor transport lines in low bond number systems due to capillary-driven flows in condensed annular films. *International Journal of Heat and Mass Transfer*, 44(20):3931–3940, 2001.

[79] D. Quéré. Fluid coating on a fiber. *Annual Review of Fluid Mechanics*, 31:347–384, 1999.

[80] A.F. Jones and S.D.R. Wilson. The film drainage problem in droplet coalescence. *Journal of Fluid Mechanics*, 87(2):263–288, 1978.

[81] P.S. Hammond. Nonlinear adjustment of a thin annular film of viscous fluid surrounding a thread of another within a circular cylindrical pipe. *Journal of Fluid Mechanics*, 137:363–384, 1983.

[82] S.G. Yiantsios and B.G. Higgins. Rayleigh–Taylor instability in thin viscous films. *Physics of Fluids A: Fluid Dynamics*, 1(9):1484–1501, 1989.

[83] J.R. Lister, J.M. Rallison, A.A. King, L.J. Cummings, and O.E. Jensen. Capillary drainage of an annular film: The dynamics of collars and lobes. *Journal of Fluid Mechanics*, 552:311–343, 2006.

[84] J.R. Lister, N.F. Morrison, and J.M. Rallison. Sedimentation of a two-dimensional drop towards a rigid horizontal plane. *Journal of Fluid Mechanics*, 552:345–351, 2006.

[85] K.B. Glasner. The dynamics of pendant droplets on a one-dimensional surface. *Physics of Fluids*, 19(10):102104, 2007.

[86] G.F. Dietze, J.R. Picardo, and R. Narayanan. Sliding instability of draining fluid films. *Journal of Fluid Mechanics*, 857:111–141, 2018.

[87] E.O. Tuck and L.W. Schwartz. A numerical and asymptotic study of some third-order ordinary differential equations relevant to draining and coating flows. *SIAM Review*, 32(3):453–469, 1990.

[88] T.G. Myers. Thin films with high surface tension. *SIAM Review*, 40(3):441–462, 1998.

[89] B.R. Duffy and S.K. Wilson. A third-order differential equation arising in thin-film flows and relevant to Tanner's law. *Applied Mathematics Letters*, 10(3):63–68, 1997.

[90] D.E. Kataoka and S.M. Troian. A theoretical study of instabilities at the advancing front of thermally driven coating films. *Journal of Colloid and Interface Science*, 192(2):350–362, 1997.

[91] T.A. Kowalewski. On the separation of droplets from a liquid jet. *Fluid Dynamics Research*, 17(3):121–145, 1996.

[92] R.J. Donnelly and W. Glaberson. Experiments on the capillary instability of a liquid jet. *Proceedings of the Royal Society of London. Series A. Mathematical and Physical Sciences*, 290(1423):547–556, 1966.

[93] E.F. Goedde and M.C. Yuen. Experiments on liquid jet instability. *Journal of Fluid Mechanics*, 40(3):495–511, 1970.

[94] W.D. Harkins and F.E. Brown. The determination of surface tension (free surface energy), and the weight of falling drops: The surface tension of water and benzene by the capillary height method. *Journal of the American Chemical Society*, 41(4):499–524, 1919.

[95] X.D. Shi, M.P. Brenner, and S.R. Nagel. A cascade of structure in a drop falling from a faucet. *Science*, 265(5169):219–222, 1994.

[96] X. Zhang and O.A. Basaran. Dynamic surface tension effects in impact of a drop with a solid surface. *Journal of Colloid and Interface Science*, 187(1):166–178, 1997.

[97] M.P. Ida and M.J. Miksis. Thin film rupture. *Applied Mathematics Letters*, 9(3):35–40, 1996.

[98] T.F. Dupont, R.E. Goldstein, L.P. Kadanoff, and S-M Zhou. Finite-time singularity formation in Hele-Shaw systems. *Physical Review E*, 47(6):4182, 1993.

[99] R.E. Goldstein, A.I. Pesci, and M.J. Shelley. Topology transitions and singularities in viscous flows. *Physical Review Letters*, 70(20):3043–3046, 1993.

[100] R. Almgren, A. Bertozzi, and M.P. Brenner. Stable and unstable singularities in the unforced Hele-Shaw cell. *Physics of Fluids*, 8(6):1356–1370, 1996.

[101] P. Constantin, T.F. Dupont, R.E. Goldstein, L.P. Kadanoff, M.J. Shelley, and S-M Zhou. Droplet breakup in a model of the Hele-Shaw cell. *Physical Review E*, 47(6):4169, 1993.

[102] M.B. Williams and S.H. Davis. Nonlinear theory of film rupture. *Journal of Colloid and Interface Science*, 90(1):220–228, 1982.

[103] J.P. Burelbach, S.G. Bankoff, and S.H. Davis. Nonlinear stability of evaporating/condensing liquid films. *Journal of Fluid Mechanics*, 195:463–494, 1988.

[104] R.S. Allan and S.G. Mason. Particle behaviour in shear and electric fields I. deformation and burst of fluid drops. *Proceedings of the Royal Society of London. Series A. Mathematical and Physical Sciences*, 267(1328):45–61, 1962.

[105] G.I. Taylor. Studies in electrohydrodynamics. I. The circulation produced in a drop by an electric field. *Proceedings of the Royal Society of London. Series A. Mathematical and Physical Sciences*, 291(1425):159–166, 1966.

[106] J.R. Melcher and G.I. Taylor. Electrohydrodynamics: A review of the role of interfacial shear stresses. *Annual Review of Fluid Mechanics*, pages 111–146, 1969.

[107] R. Feynman, R.B. Leighton, and M. Sands. The Feynman Lectures on Physics Vol. 2, 1964.

[108] L.D. Landau and E. Lifshitz. Electrodynamics of Continuous Media, 1960.

[109] L.F. Pease III and W.B. Russel. Linear stability analysis of thin leaky dielectric films subjected to electric fields. *Journal of Non-Newtonian Fluid Mechanics*, 102(2):233–250, 2002.

[110] V. Shankar and A. Sharma. Instability of the interface between thin fluid films subjected to electric fields. *Journal of Colloid and Interface Science*, 274(1):294–308, 2004.

[111] D.T. Papageorgiou and P.G. Petropoulos. Generation of interfacial instabilities in charged electrified viscous liquid films. *Journal of Engineering Mathematics*, 50(2):223–240, 2004.

[112] R.M. Thaokar and V. Kumaran. Electrohydrodynamic instability of the interface between two fluids confined in a channel. *Physics of Fluids*, 17(8):084104, 2005.

[113] O. Ozen, N. Aubry, D.T. Papageorgiou, and P.G. Petropoulos. Electrohydrodynamic linear stability of two immiscible fluids in channel flow. *Electrochimica Acta*, 51(25):5316–5323, 2006.

[114] F. Li, O. Ozen, N. Aubry, D.T. Papageorgiou, and P.G. Petropoulos. Linear stability of a two-fluid interface for electrohydrodynamic mixing in a channel. *Journal of Fluid Mechanics*, 583:347–377, 2007.

[115] A.K. Uguz, O. Ozen, and N. Aubry. Electric field effect on a two-fluid interface instability in channel flow for fast electric times. *Physics of Fluids*, 20(3):031702, 2008.

[116] A.W. Wray, D.T. Papageorgiou, and O.K. Matar. Electrified coating flows on vertical fibres: Enhancement or suppression of interfacial dynamics. *Journal of Fluid Mechanics*, 735:427–456, 2013.

[117] R. Verma, A. Sharma, K. Kargupta, and J. Bhaumik. Electric field induced instability and pattern formation in thin liquid films. *Langmuir*, 21(8):3710–3721, 2005.

[118] D.S. Pillai and R. Narayanan. Nonlinear dynamics of electrostatic Faraday instability in thin films. *Journal of Fluid Mechanics*, 855:R4, 2018.

[119] Q. Wang, S. Mählmann, and D.T. Papageorgiou. Dynamics of liquid jets and threads under the action of radial electric fields: Microthread formation and touchdown singularities. *Physics of Fluids*, 21(3):032109, 2009.

[120] Q. Wang and D.T. Papageorgiou. Dynamics of a viscous thread surrounded by another viscous fluid in a cylindrical tube under the action of a radial

electric field: Breakup and touchdown singularities. *Journal of Fluid Mechanics*, 683:27–56, 2011.

[121] D.T. Conroy, R.V. Craster, O.K. Matar, and D.T. Papageorgiou. Dynamics and stability of an annular electrolyte film. *Journal of Fluid Mechanics*, 656:481–506, 2010.

[122] D.T. Conroy, O.K. Matar, R.V. Craster, and D.T. Papageorgiou. Breakup of an electrified viscous thread with charged surfactants. *Physics of Fluids*, 23(2):022103, 2011.

[123] D.T. Conroy, O.K. Matar, R.V. Craster, and D.T. Papageorgiou. Breakup of an electrified, perfectly conducting, viscous thread in an AC field. *Physical Review E*, 83(6):066314, 2011.

[124] D.T. Conroy, O.K. Matar, R.V. Craster, and D.T. Papageorgiou. Compound viscous thread with electrostatic and electrokinetic effects. *Journal of Fluid Mechanics*, 855:171–200, 2012.

[125] L.L. Barannyk, D.T. Papageorgiou, P.G. Petropoulos, and J.-M. Vanden-Broeck. Nonlinear dynamics and wall touch-up in unstably stratified multilayer flows in horizontal channels under the action of electric fields. *SIAM Journal on Applied Mathematics*, 75(1):92–113, 2015.

[126] D.S. Pillai and R. Narayanan. Electrostatic forcing of thin leaky dielectric films under periodic and steady fields. *Journal of Fluid Mechanics*, 890:A20, 2020.

[127] R.J. Tomlin, R. Cimpeanu, and D.T. Papageorgiou. Instability and dripping of electrified liquid films flowing down inverted substrates. *Physical Review Fluids*, 5(1):013703, 2020.

[128] W. Rohlfs, L.M.F. Cammiade, M. Rietz, and B. Scheid. On the effect of electrostatic surface forces on dielectric falling films. *Journal of Fluid Mechanics*, 906:A18, 2021.

[129] A.W. Wray. Interfacial fluid dynamics in the presence of electric fields. PhD thesis, Imperial College London, 2014.

[130] D.T. Papageorgiou, P.G. Petropoulos, and J.-M. Vanden-Broeck. Gravity capillary waves in fluid layers under normal electric fields. *Physical Review E*, 72(5):051601, 2005.

[131] H. Gleeson, P. Hammerton, D.T. Papageorgiou, and J.-M. Vanden-Broeck. A new application of the Korteweg–de Vries Benjamin-Ono equation in interfacial electrohydrodynamics. *Physics of Fluids*, 19(3):031703, 2007.

[132] D.T. Papageorgiou and J.-M. Vanden-Broeck. Numerical and analytical studies of non-linear gravity–capillary waves in fluid layers under normal electric fields. *IMA Journal of Applied Mathematics*, 72(6):832–853, 2007.

[133] D.T. Papageorgiou and J.-M. Vanden-Broeck. Numerical and analytical studies of non-linear gravity–capillary waves in fluid layers under normal electric fields. *IMA Journal of Applied Mathematics*, 72(6):832–853, 2007.

[134] D. Tseluiko, M.G. Blyth, D.T. Papageorgiou, and J.-M. Vanden-Broeck. Electrified falling-film flow over topography in the presence of a finite electrode. *Journal of Engineering Mathematics*, 68(3-4):339–353, 2010.

[135] D. Tseluiko, M.G. Blyth, D.T. Papageorgiou, and J.-M. Vanden-Broeck. Effect of an electric field on film flow down a corrugated wall at zero Reynolds number. *Physics of Fluids*, 20(4):042103, 2008.

[136] D. Tseluiko, M.G. Blyth, D.T. Papageorgiou, and J.-M. Vanden-Broeck. Viscous electrified film flow over step topography. *SIAM Journal on Applied Mathematics*, 70(3):845–865, 2009.

[137] D. Tseluiko, M.G. Blyth, D.T. Papageorgiou, and J.-M. Vanden-Broeck. Electrified film flow over step topography at zero Reynolds number: An analytical and computational study. *Journal of Engineering Mathematics*, 69(2-3):169–183, 2011.

[138] V.A. Briskman and G.F. Shaidurov. Parametric instability of a fluid surface in an alternating electric field. *Soviet Physics Doklady*, 13:540, 1968.

[139] C.-S. Yih. Stability of a horizontal fluid interface in a periodic vertical electric field. *Physics of Fluids*, 11(7):1447–1449, 1968.

[140] S.A. Roberts and S. Kumar. AC electrohydrodynamic instabilities in thin liquid films. *Journal of Fluid Mechanics*, 631:255–279, 2009.

[141] P. Gambhire and R.M. Thaokar. Electrohydrodynamic instabilities at interfaces subjected to alternating electric field. *Physics of Fluids*, 22(6):064103, 2010.

[142] A. Bandopadhyay and S. Hardt. Stability of horizontal viscous fluid layers in a vertical arbitrary time periodic electric field. *Physics of Fluids*, 29(12):124101, 2017.

[143] K Ward, S. Matsumoto, and R. Narayanan. The electrostatically forced Faraday instability: Theory and experiments. *Journal of Fluid Mechanics*, 862:696–731, 2019.

[144] G.K. Batchelor. An Introduction to Fluid Dynamics. Cambridge University Press, 1967.

[145] L.E. Johns. The diffusion equation for a solute confined to a moving surface. *Physics of Fluids*, 28(3):032107, 2016.

[146] E. Seran, M. Godefroy, E. Pili, N. Michielsen, and S. Bondiguel. What we can learn from measurements of air electric conductivity in 222Rn-rich atmosphere. *Earth and Space Science*, 4(2):91–106, 2017.

[147] J.W. Thomas. Numerical Partial Differential Equations: Finite Difference Methods. Springer, 1995.

[148] R.J. Leveque. Finite Difference Methods for Ordinary and Partial Differential Equations. SIAM, 2008.

[149] J.C. Strikwerda. Finite Difference Schemes and Partial Differential Equations. SIAM, 2004.

[150] E.J. Hinch. Tink Before You Compute. Cambridge University Press, 2020.

[151] COMSOL Multiphysics v. 5.4. COMSOL Ltd., COMSOL AB, Stockholm, Sweden. www.comsol.com.

[152] C. Chicone. Ordinary Differential Equations with Applications. Springer, 1999.

[153] M.I. Rosen. Niels Hendrik Abel and Equations of the Fifth Degree. *The American Mathematical Monthly*, 102(6):495–505, 1995.

[154] J.-P. Tignol. Galois theory of algebraic equations. 2nd edition. Singapore: World Scientific, 2nd edition edition, 2016.